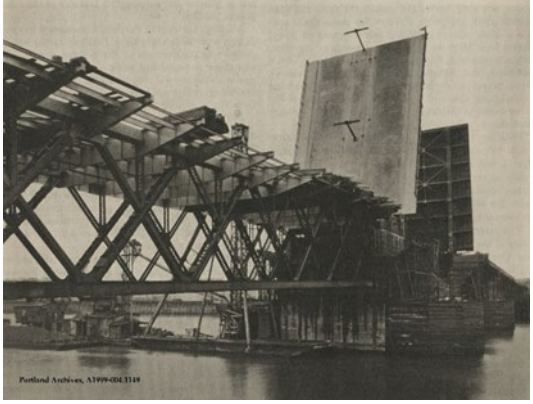

SUBMITTED TO:
HDR Engineering, Inc.
1050 SW 6th Avenue, Suite 1800
Portland, Oregon 97204

BY:
Shannon & Wilson, Inc.
3990 Collins Way, Suite 100
Lake Oswego, Oregon 97035

(503) 210-4750
www.shannonwilson.com

FINAL NEPA GEOTECHNICAL REPORT

Earthquake Ready Burnside Bridge

PORTLAND, OREGON

SHANNON & WILSON

April 2022

Shannon & Wilson No: 102636-009

PAGE INTENTIONALLY LEFT BLANK FOR DOUBLE-SIDED PRINTING

Submitted To: HDR Engineering, Inc.
1050 SW 6th Avenue, Suite 1800
Portland, Oregon 97204
Attn: Steve Drahota, PE

Subject: FINAL NEPA GEOTECHNICAL REPORT, EARTHQUAKE READY BURNSIDE BRIDGE, PORTLAND, OREGON

Shannon & Wilson, Inc. (Shannon & Wilson) prepared this report and participated in this project as a subconsultant to HDR Engineering, Inc (HDR). Our scope of services was specified in the Geotech Subconsultant Agreement with HDR dated January 24, 2019, and Amendments No. 1, 3, 4, and 5, dated February 2020, November 24, 2020, July 21, 2021, and August 25, 2021, respectively, and our Master Subconsultant Agreement with HDR, dated October 20, 2014. This report presents the results of our field explorations, laboratory testing, geotechnical design evaluations and recommendations, and geotechnical construction considerations to support the Burnside Bridge National Environmental Policy Act (NEPA) and Type Selection Phase and was prepared by the undersigned.

We appreciate the opportunity to be of service to you on this project. If you have questions concerning this report, or we may be of further service, please contact us.

Sincerely,

SHANNON & WILSON, INC.

EXPIRES: 6/30/2022

Sam Sideras, PhD, PE
Senior Engineer

Risheng "Park" Piao, PE, GE
Vice President | Geotechnical Engineer

AEH:PTO:EAB:SSS:AAS:RPP:WJP/aeh:mmb

CONTENTS

CONTENTS

CONTENTS

CONTENTS

CONTENTS

Exhibits

CONTENTS

CONTENTS

Tables

Figures

CONTENTS

CONTENTS

Appendices

ACRONYMS

1D	one-dimensional
2D	two-dimensional
3D	three-dimensional
AASHTO	American Association of State Highway and Transportation Officials
AG20	Abrahamson and Gülerce (2020)
ARS	acceleration response spectrum
ASCE	American Society of Civil Engineers
ASK14	Abrahamson and others (2014)
ASTM	American Society for Testing and Materials
BDM	Bridge Design Manual
BES	Bureau of Environmental Services
BF	Bolton fault
BFZ	Beaverton fault zone
bgs	below ground surface
bpf	blows per foot
BRF	Blue Ridge fault
BSSA14	Boore and others (2014)
CB14	Campbell and Bozorgnia (2014)
CDSS	cyclic direct simple shear
cm/yr	centimeter per year
CMS	conditional mean spectrum
CPT	Cone Penetration Test
CRBG	Columbia River Basalt Group
COP	City of Portland
CRR	cyclic resistance ratio
CSO	combined sewer overflow
CSR	cyclic stress ratio
CSZ	Cascadia Subduction Zone
CVM	community velocity model
CY14	Chiou and Youngs (2014)
DOGAMI	Oregon Department of Geology and Mineral Industries
DSHA	Deterministic Seismic Hazard Analysis
DSM	deep soil mixing
EBF	East Bank fault
EIS	Environmental Impact Statement
EPRI	Electrical Power Research Institute
EQRB	Earthquake Ready Burnside Bridge Project
ISM	improved soil mass
FHWA	Federal Highway Administration

ACRONYMS

FLAC	Fast Lagrangian Analysis of Continua (Itasca, 2019)
FODE	Full Operation Design Earthquake
fps	feet per second
FS	Factor of Safety
GBFZ	Grant Butte fault zone
GCF	Gate Creek fault
GCFZ	Gales Creek fault zone
g	acceleration due to gravity
GDM	Geotechnical Design Manual
GI	ground improvement
G_{max}	initial, or small strain, shear modulus
GMM	ground motion model
KBCG20	Kuehn and others (2020)
H	Horizontal
HDR	HDR Engineering, Inc.
HF	Helvetia fault
Hz	Hertz
I-5	Interstate 5
I.D.	inside diameter
ISM	improved soil mass
ka	"Kilo-annum" or one thousand years ago
km	kilometers
km/sec	kilometers per second
ksf	kips per square foot
LiDAR	light detection and ranging
LRFD	Load and Resistance Factor Design
LODE	Limited Operation Design Earthquake
M	Magnitude
m/sec	meters per second
Ma	"Mega-annum" or million years ago
MAF	Mount Angel fault
M_L	"Richter" or local magnitude
Mw	Moment magnitude
mm	millimeters
mm/yr	millimeters per year
M_{max}	maximum magnitude
M_{min}	minimum magnitude
M_W	Moment Magnitude
NAVD88	North American Vertical Datum of 1988

ACRONYMS

NEPA	National Environmental Policy Act
NGA-Sub	Next Generation Attenuation-Subduction project
NGA-West2	2nd Next Generation Attenuation for Western US
NGVD29	National Geodetic Vertical Datum of 1929
NLTH	Nonlinear Time History Analysis
NSHM	National Seismic Hazard Model
NSHM14	2014 National Seismic Hazard Model
NSHM23	2023 (Preliminary) National Seismic Hazard Model
OCR	overconsolidation ratio
O.D.	outside diameter
ODOT	Oregon Department of Transportation
ohm-cm	ohm-centimeters
OHW	Ordinary High Water
OR	Oregon
OSHA	Occupational Safety and Health Administration
OSSC	Oregon Standard Specifications for Construction
pcf	pounds per cubic foot
PEER	Pacific Earthquake Engineering Research Center
PGA	peak ground acceleration
PHF	Portland Hills fault
PMT	pressuremeter test
PNW	Pacific Northwest
ppm	parts per million
PSA	pseudo-spectral acceleration
PSBAH20	Parker and others (2020)
psf	pounds per square foot
PSHA	Probabilistic Seismic Hazard Analysis
psi	pounds per square inch
QFFD	U.S. Geological Survey Quaternary Fold and Fault Database
R_{epi}	distance to epicenter
R_{hyp}	hypocentral distance
R_{jb}	Joyner-Boore distance
RotD50	50th percentile (median) of the orientation-independent, period-dependent, of two orthogonal rotated horizontal components
R_{rup}	source-to-site rupture distance
SMK20	Si and others (2020)
SOF	Sylvan-Oatfield fault
SPT	Standard Penetration Test
SRF	Sandy River fault

ACRONYMS

SRM	Sandy River Mudstone
S.U.	Standard Units
T	spectral period in seconds
TLF	Twin Lakes fault
UCS	unconfined compressive strength
UHS	Uniform Hazard Spectrum
UPRR	Union Pacific Railroad
USCS	Unified Soil Classification System
USGS	United States Geological Survey
V	Vertical
Vs	shear wave velocity
V_{S30}	time-averaged shear wave velocity for 100 feet of subsurface soils
VWP	vibrating wire piezometer
WA	Washington
yr	year
$Z_{1.0}$	depth to shear wave velocity of 1 km/sec
$Z_{2.5}$	depth to shear wave velocity of 2.5 km/sec
σ_{ε}	epistemic uncertainty

1 INTRODUCTION

1.1 Project Overview

This report presents the results of field explorations, laboratory testing, preliminary geotechnical design evaluations and recommendations, and geotechnical construction considerations for the Multnomah County Burnside Bridge NEPA and Type Selection Phase in Portland, Oregon. The project is part of Multnomah County's larger effort to address the condition of its critical transportation infrastructure. After a review of the County's four downtown Portland bridges, it was determined the Burnside Bridge was a top priority due to its designation as the only Priority 1 lifeline route across the Willamette River in downtown Portland. The location of the bridge site is shown on the Vicinity Map, Figure 1-1.

As currently built, the bridge is not expected to withstand a major seismic event. Therefore, the County has taken on the responsibility to seek ways to improve the bridge in order to meet the region's needs for seismic resiliency. As part of the Burnside Bridge NEPA and Type Selection Phase, the County and their consulting team, led by HDR, are performing an environmental review in compliance with the NEPA of the alternatives presented in the Earthquake Ready Burnside Bridge (EQRB) Project Feasibility Study. The preferred alternative, as identified in the Draft Environmental Impact Statement (EIS) step of the NEPA process, has been refined for evaluation in the Supplemental Draft EIS and the selected refined bridge design will be further developed to result in the bridge type selection. Shannon & Wilson, as a subconsultant to HDR, is providing geotechnical services to support the project.

This report presents the subsurface investigations, laboratory testing, engineering studies, and geotechnical recommendations that were performed to support the NEPA and Type Selection Phase of the project. Refinements to the engineering studies and geotechnical recommendations presented in this report will be performed and documented in a subsequent report that supports the structural Nonlinear Time History (NLTH) Analysis phase of the project.

We have prepared this geotechnical report in accordance with our scope of services for the project. We understand that the bridge will be evaluated in accordance with the following guidance documents:

- Earthquake Ready Burnside Bridge Revised Seismic Design Criteria – December 2021;

- AASHTO LRFD Movable Highway Bridge Design Specifications – Second Edition (with Interim Revisions, 2018);
- AASHTO Guide Specifications for LRFD Seismic Bridge Design – Second Edition (with Interim Revisions, 2015);
- AASHTO LRFD Bridge Design Specifications – Ninth Edition (2020 with 2021 Errata);
- ODOT Bridge Design Manual (BDM) – May 2021;
- ODOT Geotechnical Design Manual (GDM) – May 2019.

Geotechnical analyses and recommendations presented in this report expand on and update the preliminary geotechnical work performed during the EQRB Feasibility Study and presented in our Geotechnical Report: Burnside Bridge Environmental Impact Study, dated February 2021 (Shannon & Wilson, 2021), for the EQRB Draft EIS (issued on February 5, 2021). The recommendations herein are more focused on the preferred "Refined Long-span" alternative discussed in Section 2.2 and incorporate additional project-specific explorations and laboratory testing, in addition to the previously available explorations and substructure components as depicted in the as-constructed plans provided by HDR.

1.2 Scope of Services

Shannon & Wilson's services were conducted in accordance with the Scope of Work defined in the Geotech Subconsultant Agreement with HDR, dated January 24, 2019, Amendments No. 1, 3, 4, and 5, dated February 2020, November 24, 2020, July 21, 2021, and August 25, 2021, respectively, and our Master Subconsultant Agreement with HDR, dated October 20, 2014. The completed geotechnical design services for the project consisted of the following tasks:

- Reviewed available existing information and visit the site to observe existing site conditions, geologic hazards, site access for the field explorations, and marked proposed exploration locations;
- Developed a field exploration work plan and obtained drilling permits;
- Explored the subsurface conditions with 30 additional geotechnical borings including vibrating wire piezometer (VWP) installations in four of the boreholes, eight Cone Penetrometer Test probes (CPTs), and collected soil samples;
- Performed in situ downhole shear wave velocity measurements in 11 of the geotechnical borings;
- Performed in situ pressuremeter testing in four of the geotechnical borings;
- Conducted laboratory testing on selected samples to characterize soil and develop static material properties for evaluation;

- Developed and implemented a specialized dynamic laboratory testing program for selected samples to evaluate the cyclic and post-cyclic behavior of the fine-grained soils susceptible to liquefaction and cyclic strength degradation;
- Refined the geologic profile and developed geologic cross sections;
- Performed refined analyses to update seismic and acceleration response spectrum (ARS) curves for the bridge seismic evaluations;
- Performed probabilistic and deterministic seismic hazard analyses, developed target spectra and time histories, and performed site-specific ground response analyses;
- Evaluated foundation alternatives and proposed conceptual mitigation measures for geotechnical hazard impacts from each alternative;
- Performed a conceptual engineering study for caisson foundations supporting the bridge in-water piers;
- Developed axial compressive and uplift resistances for drilled shafts;
- Developed p-y curves at representative depth increments for lateral shaft resistance analysis;
- Developed side resistance (t-z) and tip resistance (Q-u) curves at representative depth increments for axial shaft resistance;
- Evaluated potential influence of seismic lateral spreading or flow failure on drilled shafts for the near-shore piers using analytical methods;
- Reviewed the individual pier results and grouped the piers with similar design and construction criteria to consolidate geotechnical recommendations for structural design;
- Developed conceptual mitigation alternatives for geotechnical hazards on both sides of the Willamette River, as needed;
- Evaluated constructability and developed construction considerations for the earthwork, drilled shafts, and ground improvement;
- Assessed geologic implications or impacts to each alternative; and
- Prepared this Final NEPA Geotechnical Report based on our additional explorations, laboratory testing, and refined analyses.

2 PROJECT UNDERSTANDING

2.1 Site Description

The Burnside Bridge is located in the Portland central business district as shown on the Vicinity Map, Figure 1-1, Published Geologic Mapping, Figure 2-1, and the Site and Exploration Plan and Interpretive Subsurface Profile A-A', Figure 2-2. The bridge conveys

Burnside Street across the Willamette River and connects SW 2nd Avenue on the west side of the river to Martin Luther King Jr. Boulevard (Highway 99E) on the east side of the river. The existing bridge consists of three major structures: the West Approach Bridge (ODOT Bridge No. 00511A), the Main Span River Bridge (ODOT Bridge No. 00511), and the East Approach Bridge (ODOT Bridge No. 00511B). The West Approach consists of 19 reinforced concrete spans ranging in length from 22 to 62 feet with an overall bridge length of 604 feet and spans SW 1st Avenue, the TriMet MAX Blue/Red lines, Naito Parkway, and Tom McCall Waterfront Park. The Main Span consists of two 268-foot-long fixed steel spans flanking a 252-foot-long double leaf bascule draw span with an overall bridge length of 856 feet that spans the Willamette River and the Eastbank Esplanade. The East Approach consists of eight steel plate girder spans ranging in length from 75 to 106 feet and seven reinforced concrete spans ranging in length from 22 to 40 feet, with an overall bridge length of 849 feet. The East Approach spans Interstate 5 (I-5) and ramps, the Union Pacific Railroad (UPRR), SE 2nd Avenue, and SE 3rd Avenue. The overall bridge structure is approximately 86 feet wide, aligned in a west-east direction, and accommodates five travel lanes (two westbound and three eastbound).

Embankment fills for both the west and east approaches are approximately 15 feet high and are retained by abutment walls at each approach. The Willamette River runs within a wide channel about 60 feet below the bridge in the vicinity of the Main Span Bridge crossing. The section of the riverbed beneath the bridge is typically at an elevation of about -40 to -60 feet (North American Vertical Datum of 1988 [NAVD88]). The west riverbank is retained by a pile-supported concrete retaining wall with a level fill surface at about elevation 35 feet behind the wall (Tom McCall Waterfront Park). The east riverbank slopes up at about 2 horizontal to 1 vertical (2H:1V) to an elevation of about 10 feet, east of which the topography has a gentle uphill slope.

2.2 Project Description

The purpose of the Burnside Bridge NEPA and Type Selection Phase is to perform an environmental review of the seismic retrofit and bridge replacement alternatives developed during the EQRB Feasibility Study, in accordance with the NEPA. We understand that a preferred alternative was identified through the Draft EIS step of the NEPA process. The preferred alternative with potential refinements will be evaluated in a Supplemental Draft EIS and the selected alternative will be further developed to result in the bridge type selection.

We understand a "no-build" alternative and the following four "build" alternatives were considered in the Draft EIS issued in February 2021 (HDR, 2021a):

1. Enhanced Seismic Retrofit (aka, Retrofit);

2. Replacement Alternative with Short-span Approach (aka, Short-span Alternative);
3. Replacement Alternative with Long-span Approach (aka, Long-span Alternative); and
4. Replacement Alternative with Couch Extension (aka, Couch Extension).

The Draft EIS process resulted in the selection of the Long-span Alternative as the Preferred Alternative. Potential refinements to the Long-span Alternative were developed and are collectively referred to as the "Refined Long-span Alternative (Four-lane Version)" or the "Refined Long-span" for short. These refinements will be evaluated in a Supplemental Draft EIS and are the basis for the geotechnical evaluations and recommendations in this report. Geotechnical evaluations and recommendations for the non-preferred alternatives are not included in this report.

Based on current design plans and as shown on Figure 2-2, the Refined Long-span Alternative includes 10 bents along the existing bridge alignment that will be supported on a drilled shaft foundation system. A girder bridge is being evaluated for the west approach and a bascule bridge for the center movable span. For the east approach, both long-span cable-stay and tied-arch options are being evaluated. The east approach also includes a girder bridge between the long-span structure and the east abutment. Retaining walls are anticipated at both abutments, which will be addressed during a future design phase.

Based on information provided by HDR, we understand that the Average High Stage (annual average high) river level is at Elevation 11.43 feet (NAVD88) at the bridge site. The Ordinary High-Water level (OHW) is at Elevation 20.1 feet (NAVD88). The 100-year flood river level is at Elevation 32 feet (NAVD88). We further understand that the project construction will remove portions of the existing river piers, riprap, and riverbed sediments. The post bridge construction mudline will be relatively flat and will likely vary between approximate elevations -55 to -60 in the river channel. However, the actual post bridge construction mudline is still under design development.

The project scope of services specifies two earthquake ground motion performance levels for evaluation and retrofit or replacement of the bridge:

- LODE - Limited Operation Design Earthquake level (ground motion level referred to as "Life Safety" in the ODOT BDM and GDM and referred to as "Limited Operation") for probabilistic 1,000-year return period ground motions; and
- FODE - Full Operation Design Earthquake level (roughly equivalent to the "Operational" ground motion level in the ODOT BDM and GDM) for deterministic Cascadia Subduction Zone (CSZ) event ground motions.

3 REVIEW OF EXISTING DATA

3.1 Existing Foundation System

Based on As-Constructed Drawing No. T2, the existing bridge was originally constructed in the mid-1920s, replacing an earlier bridge built in 1894. This drawing is included in Appendix A, Existing Information. Preliminary ground surface and subsurface information was taken from the As-Constructed Record of Borings, dated 1924 (drawing included in Appendix A). Foundation configurations were taken from As-Constructed Drawing Nos. 7, T8, T10, T16, 18, and 48, dated February 1924, As-Constructed Drawing No. L-75 dated April 1925, and the Foundation Piling Summary (all drawings and piling summary included in Appendix A). All as-constructed drawings were prepared by Hedrick & Kremers Consulting Engineers.

According to the drawings provided by HDR, the Burnside Bridge has 37 spans supported by 34 bents and four piers. The bents supporting the West Approach Bridge are designated Bent 1 through Bent 19, the piers supporting the Main Span Bridge are designated Pier 1 through Pier 4, and the bents supporting the East Approach Bridge are designated Bent 21 through Bent 35. The west abutment of the West Approach Bridge is designated Bent 1, and the east abutment of the East Approach Bridge is designated Bent 35. The west abutment of the Main Span Bridge is designated Pier 1, and the east abutment of the Main Span Bridge is designated Pier 4. The overcrossing configuration is shown on As-Constructed Drawing No. T2.

Bents 1 and 35 are supported on abutment walls with a continuous footing. Bents 2 through 17 and Bents 28 through 34 are supported on spread footings. Based on our review of the provided drawings, we developed Exhibit 3-1, which provides a summary of the existing footing dimensions, number of footings at each bent, footing embedment and elevations, and bearing material. The design bearing pressures for the footings are not indicated on the plans. The spread footing foundation configurations are also shown on the drawings included in Appendix A.

Bents 18 and 19, Piers 1 through 4, and Bents 21 through 27 are supported on driven timber piles. Based on our review of the provided drawings and foundation piling summary, we developed Exhibit 3-2, which provides a summary of the existing pile cap dimensions, number of piles at each bent or pier, pile type and section, pile length and tip elevations, and bearing material. The required pile bearing capacities and pile diameters are not indicated on the plans. A 16-inch pile diameter (butt diameter) is assumed based on typical

timber pile sections available at the time the bridge was constructed. The driven pile foundation configurations are also shown on the drawings included in Appendix A.

The bearing materials for the spread footings and driven piles are not clearly defined in the as-constructed drawings and are interpreted based on information in the drawings, existing subsurface explorations at the site, and our subsurface explorations. In addition, elevations obtained from the as-constructed drawings were converted from City of Portland (COP) Datum to NAVD88 by adding 2.1 feet to the elevations shown on the drawings.

Exhibit 3-1: As-Constructed Foundation Summary of Spread Footings

Location	Number of Footings	Footing Dimensions (W x L x H) (ft)	[1]Approximate Bottom of Footing Elevation (ft)	Approximate Footing Embedment (ft)	[2]Bearing Material
Bent 1	1	10’ x 110’	24.5	5	Fine-grained Alluvium
Bent 2	4	Exterior: 6.5’ x 6.5’ x 3’ Interior: 7.5’ x 7.5’ x 3’	22	7	Fine-grained Alluvium
Bent 3	4	Exterior: 6.5’x 6.5’ x 3’ Int. North: 8’ x 8’ x 8’ Int. South: 7.5’ x 7.5’ x 3’	Exterior: 22 Interior North: 17 Interior South: 22	7	Fine-grained Alluvium
Bent 4	4	Exterior: 6.5’ x 6.5’ x 3’ Interior: 7.5’ x 7.5’ x 3’	22	7	Fine-grained Alluvium
Bent 5	4	Exterior: 6.5’ x 6.5’ x 3’ Interior: 7.5’ x 7.5’ x 3’	22	7	Fine-grained Alluvium
Bent 6	4	Exterior: 6.5’ x 6.5’ x 3’ Interior: 7.5’ x 7.5’ x 3’	22	7	Fine-grained Alluvium
Bent 7	4	Exterior: 6.5’ x 6.5’ x 3’ Interior: 7.5’ x 7.5’ x 3’	22	7	Fine-grained Alluvium
Bent 8	4	Exterior: 6.5’ x 6.5’ x 3’ Interior: 7.5’ x 7.5’ x 3’	22	7	Fine-grained Alluvium
Bent 9	4	Exterior: 6.5’ x 6.5’ x 3’ Interior: 7.5’ x 7.5’ x 3’	22	7	Fine-grained Alluvium
Bent 10	4	Exterior: 6.5’ x 6.5’ x 3’ Interior: 7.5’ x 7.5’ x 3’	22	7	Fine-grained Alluvium
Bent 11	4	Exterior: 6.5’ x 6.5’ x 3’ Interior: 7.5’ x 7.5’ x 3’	22	7	Fine-grained Alluvium
Bent 12	4	Exterior: 6.5’ x 6.5’ x 3’ Interior: 7.5’ x 7.5’ x 3’	22	7	Fine-grained Alluvium
Bent 13	4	Exterior: 6.5’ x 6.5’ x 3’ Interior: 7.5’ x 7.5’ x 3’	22	7	Fine-grained Alluvium
Bent 14	4	Exterior: 8’ x 8’ x 3’ Interior: 11.5’ x 11.5’ x 4.5’	22	9	Fine-grained Alluvium
Bent 15	4	Exterior: 8’ x 8’ x 3’ Interior: 11.5’ x 11.5’ x 4.5’	22	9	Fine-grained Alluvium
Bent 16	4	Exterior: 8’ x 8’ x 3’ Interior: 11.5’ x 11.5’ x 4.5’	22	9	Fill
Bent 17	4	Exterior: 14’x 14’ x 5’ Interior: 16.5’ x 16.5’ x 5’	Exterior: 12 Interior North: 14 Interior South: 12	18	Sand/Silt Alluvium
Bent 28	3	16’ x 16’ x 4’	22	27	Gravel Alluvium
Bent 29	4	Exterior: 6.5’ x 6.5’ x 3’ Interior: 7.5’ x 7.5’ x 3’	40	10	Fill
Bent 30	4	Exterior: 6.5’ x 6.5’ x 3’ Interior: 7.5’ x 7.5’ x 3’	40	10	Fill
Bent 31	4	Exterior: 6.5’ x 6.5’ x 3’ Interior: 7.5’ x 7.5’ x 3’	40	10	Fill
Bent 32	4	Exterior: 6.5’ x 6.5’ x 3’ Interior: 7.5’ x 7.5’ x 3’	40	10	Fill
Bent 33	4	Exterior: 8’ x 8’ x 3’ Interior: 11.5’ x 11.5’ x 4.5’	37	12	Fill
Bent 34	4	Exterior: 8’ x 8’ x 3’ Interior: 11.5’ x 11.5’ x 4.5’	37	12	Fill
Bent 35	1	9.25’ x 110’	41	9	CFD – Channel Facies

NOTES:

1 Elevations have been converted from City of Portland (COP) Datum to NAVD88 by adding 2.1 feet to the elevations shown on the plan set.

2 Bearing material is interpreted from the information in the plan set, existing borings, and current borings.

Exhibit 3-2: As-Constructed Foundation Summary for Driven Piles

Location	Number of Piles	[a]Pile Cap Dimensions (W x L x H) (ft)	[b]Pile Type and Section	[c]Approximate Bottom Pile Cap Elevation (ft)	[c]Approximate Pile Tip Elevation (ft)	Approximate Pile Length (ft)	[d]Pile Cap Bearing Material
Bent 18N	68	19' x 28' x 6'	16-inch dia. Timber	9	-2.8	11.8	Sand/Silt Alluvium
Bent 18S	71	19' x 28' x 6'	16-inch dia. Timber	9	-1.7	10.7	Sand/Silt Alluvium
Bent 19N	59	19' x 28' x 6'	16-inch dia. Timber	7	-35.5	42.5	Sand/Silt Alluvium
Bent 19S	50	19' x 28' x 6'	16-inch dia. Timber	7	-22.6	29.6	Sand/Silt Alluvium
Pier 1	276	33' x 71' x 21.7'	16-inch dia. Timber	-41.6	-72.4	30.8	Sand & Gravel Alluvium
Pier 2	382	68' x 78' x 37'	16-inch dia. Timber	-70	-94.2	24.2	Sand/Silt & Sand Alluvium
Pier 3	392	68' x 78' x 37'	16-inch dia. Timber	-68.6	-92.6	24	Sand Alluvium
Pier 4	277	36' x 68' x 21.5'	16-inch dia. Timber	-40.3	-70.7	30.4	Sand Alluvium
Bent 21N	63	24' x 24' x 10.5'	16-inch dia. Timber	2	-67.2	69.2	Sand/Silt Alluvium
Bent 21S	63	24' x 24' x 10.5'	16-inch dia. Timber	2	-76.4	78.4	Sand/Silt Alluvium
Bent 22N	61	24' x 24' x 10.5'	16-inch dia. Timber	2	-58.8	60.8	Sand/Silt Alluvium
Bent 22S	63	24' x 24' x 10.5'	16-inch dia. Timber	2	-59.2	61.2	Sand/Silt Alluvium
Bent 23N	62	24' x 24' x 10.5'	16-inch dia. Timber	2	-54.5	56.5	Sand/Silt Alluvium
Bent 23S	64	24' x 24' x 10.5'	16-inch dia. Timber	2	-58.7	60.7	Sand/Silt Alluvium
Bent 24N	72	24' x 27' x 10.5'	16-inch dia. Timber	7	-53.2	60.2	Fine-grained Alluvium
Bent 24S	72	24' x 27' x 10.5'	16-inch dia. Timber	7	-51.7	58.7	Fine-grained Alluvium
Bent 25N	77	27' x 27' x 10.5'	16-inch dia. Timber	10	-57.7	67.7	Fine-grained Alluvium
Bent 25S	79	27' x 27' x 10.5'	16-inch dia. Timber	10	-54.7	64.7	Fine-grained Alluvium
Bent 26N	70	24' x 27' x 10.5'	16-inch dia. Timber	10	-59	69	Fine-grained Alluvium
Bent 26S	68	24' x 27' x 10.5'	16-inch dia. Timber	10	-54.3	64.3	Fine-grained Alluvium
Bent 27N	63	24' x 24' x 10.5'	16-inch dia. Timber	10	-49.5	59.5	Fine-grained Alluvium
Bent 27C	25	15' x 15' x 8'	16-inch dia. Timber	12.6	-47.4	60	Fine-grained Alluvium
Bent 27S	64	24' x 24' x 10.5'	16-inch dia. Timber	10	-50.9	60.9	Fine-grained Alluvium

NOTES:
W = Pile cap dimension in longitudinal direction (perpendicular to bent/pier centerline), L = Pile cap dimension in transverse direction (parallel to bent/pier centerline)
Pile type and section are not shown in the plans, therefore pile type and section are assumed.
Elevations have been converted from City of Portland (COP) Datum to NAVD88 by adding 2.1 feet to the elevations shown on the plan set.
Bearing material is interpreted from the information in the plan set, existing borings, and current borings.

3.2 Existing Geotechnical Data

Numerous geotechnical borings were previously drilled at and around the project site by other geotechnical firms or agencies, both for the Burnside Bridge and for various unrelated projects including the Banfield Access Ramp, Ankeny Pump Station, West and East Side Combined Sewer Overflow (CSO) Projects, and borings for the Portland Development Commission. Approximate locations of the relevant historic borings are shown on the Site and Exploration Plan and Interpretive Subsurface Profile A-A', Figure 2-2. Site plans and logs of relevant historic borings are provided in Appendix A, Existing Information. While the borings performed by Shannon & Wilson for this project were logged in accordance with the ODOT Soil and Rock Classification Manual (ODOT, 1987), the borings presented in Appendix A, which were logged by others, may use other descriptive methodologies.

4 GEOLOGIC SETTING

4.1 Regional Geology

The greater Portland metropolitan area lies within the Portland Basin, a structural depression created by complex folding and faulting of the basement rocks. The Portland Basin is approximately 40 miles long and 20 miles wide, with the long axis trending to the northwest. The most prevalent basement rock of the Portland Basin is a sequence of lava flows of the Columbia River Basalt Group (CRBG), which flowed into the area between about 17 million and 6 million years ago (Beeson and others, 1991).

The Columbia and Willamette Rivers converge within the Portland Basin, and with their tributaries, have contributed to extensive sedimentary deposits which overly the basement rock formations. The Burnside Bridge lies within the Portland Quadrangle, where Beeson and others (1991) have mapped the Portland Basin sediments as Sandy River Mudstone (SRM), overlain by Troutdale Formation. According to Beeson and others (1991), the SRM locally consists of between 200 to 300 feet of claystone, siltstone, and sandstone beds deposited in the Miocene to Pliocene epochs (about 10 million to 3.5 million years ago), and the Troutdale Formation locally consists of about 100 to 400 feet of well-consolidated, friable to moderately well-cemented conglomerate and sandstone, also deposited in the Miocene to Pliocene epochs (about 12.5 million to 1.6 million years ago).

The SRM and Troutdale Formation are locally overlain in places by a sequence of catastrophic flood deposits. During the late stages of the last great ice age, between about 18,000 and 15,000 years ago, a lobe of the continental ice sheet repeatedly blocked and dammed the Clark Fork River in western Montana, which then formed an immense glacial

lake called Lake Missoula. The lake grew until its depth was sufficient to buoyantly lift and rupture the ice dam, which allowed the entire massive lake to empty catastrophically. Once the lake had emptied, the ice sheet again gradually dammed the Clark Fork Valley and the lake refilled, leading to 40 or more repetitive outburst floods at intervals of decades (Allen and others, 2009). These repeated floods are collectively referred to as the Missoula Floods.

Each short-lived Missoula Flood episode sent floodwaters that washed across the Idaho panhandle, through eastern Washington's scablands, and through the Columbia River Gorge. When the floodwater emerged from the western end of the gorge, it spread out over the Portland Basin and pooled to elevations of about 400 feet, depositing a tremendous load of sediment. Boulders, cobbles, and gravel were deposited nearest the mouth of the gorge and along the main channel of the Columbia River. Cobble-gravel bars reached westward across the basin, grading to thick blankets of micaceous sand and silt (Allen and others, 2009). Beeson and others (1991) divided the flood deposits into three facies: Fine-grained facies, Coarse-grained facies, and Channel facies. The Fine-grained facies consists of coarse sand to silt. The Coarse-grained facies consists of gravel, cobbles, and boulders in a sand and silt matrix. The Channel facies consists of complexly interlayered fine and coarse-grained material formed by channeling of flood deposits into earlier and/or contemporaneous deposits.

Irregular post-flood surfaces were filled in locally by pond or bog deposits and overbank alluvium. In historic times, many areas have been altered by anthropogenic grading, cuts, and fills. Generalized surficial geology near the bridge site, as compiled from multiple sources by the Oregon Department of Geology and Mineral Industries (DOGAMI), is shown in Published Geologic Mapping, Figure 2-1.

4.2 Local Geology

Based on geologic mapping (Beeson and others, 1991) and project geotechnical borings, the majority of the Burnside Bridge is underlain by Willamette River alluvial deposits over Troutdale Formation and at depth by Sandy River Mudstone. The thickness of the Willamette River alluvial deposits generally increases from west to east along the bridge. Just east of SE 2nd Avenue, the Troutdale Formation grades abruptly upward in elevation and becomes shallower, corresponding with a thinning of Willamette River alluvial deposits. SE 3rd Avenue is located near the eastern limits of the Willamette River alluvial deposits, where catastrophic flood deposits generally overlie the Troutdale Formation.

Geologic mapping by Beeson and others (1991), groups the alluvium into one unit composed of silt, sand, organic-rich clay, and gravel. Bridge geotechnical borings describe fine-grained sand and silt over gravel as the alluvial materials on the west bank of the

Willamette River. Within the current river channel, the alluvium generally consists of sand over gravel with some interbeds of fine-grained and coarse-grained material. The thickest alluvial deposits underlie the east bank of the current river channel, from the east bank to about SE 2nd Avenue, and consist of a thick stratum of fine-grained sand, silt, clay, and organic soil over a relatively thinner layer of gravel with sand. From around SE 2nd Avenue to just east of SE 3rd Avenue, the fine-grained alluvial material pinches out, leaving only gravel. Borings east of SE 3rd Avenue encountered the Fine-grained and Channel facies of the catastrophic flood deposits over Troutdale Formation.

Anthropogenic fill has been placed on top of the alluvial and catastrophic flood deposits in most locations along the length of the bridge for development.

5 EXPLORATION PROGRAM

5.1 Field Explorations

To date, the field exploration program for the Project included 33 geotechnical borings and eight (8) cone penetration tests (CPTs). Approximate locations of the explorations are shown on the Site and Exploration Plan and Interpretive Subsurface Profile, Figure 2-2.

The geotechnical borings were drilled by multiple drilling subcontractors with various drill rigs over the course of multiple mobilizations between September 2016 and November 2021. Details of drilling, sampling procedures, and our logs of the materials encountered in the explorations are presented in Appendix B, Drilling Explorations.

Several borings included in situ geophysical testing (P-S Suspension Logging) and pressuremeter testing (PMT), which are discussed and presented in Appendix C, In Situ Testing. CPT methods and results are discussed and presented in Appendix D, Cone Penetration Test Results.

5.2 Laboratory Testing

The soil samples obtained during the field explorations were reviewed in the laboratory, and some samples were selected for laboratory testing. The laboratory testing program for soil samples included both conventional soil index tests and more advanced laboratory tests to help evaluate the static and cyclic engineering properties of the soils. The soil index testing included moisture content tests, unit weight analyses, Atterberg limits tests, and particle size analyses. Soil index tests were used to characterize the subsurface conditions, develop our geotechnical soil units, and to evaluate engineering properties of the soils, where applicable.

As shown in Figure 2-2 and described in Section 6, the subsurface conditions at the site include thick deposits of fine-grained sands, silts, and clays. The engineering behavior of silty transitional soils are not well documented in literature. To enhance the subsurface characterization and to reduce the uncertainty in the static, seismic, and post-seismic response of these soils, our laboratory testing program also incorporated advanced laboratory testing of these transitional soils, including consolidation tests, monotonic direct simple shear tests, cyclic direct simple shear tests, post-cyclic monotonic direct simple shear tests, post-cyclic reconsolidation tests, and bender element tests. The development of site-specific engineering characterization based on the advanced laboratory testing is presented in Section 8.

In addition, corrosivity testing was also performed on select soil samples to evaluate the potential for corrosive soils at the site. Discussion on the results of the corrosivity testing is provided in Section 6.3.

Results of the laboratory tests and brief descriptions of the test procedures are presented in Appendix E, Laboratory Testing. All test procedures were performed in accordance with applicable ASTM International test standards, except as noted in Appendix E. We note that additional cyclic direct simple shear and post-cyclic laboratory tests have been performed and are currently in the review process. The results will be included in the subsequent NLTH geotechnical report.

6 SUMMARY OF SUBSURFACE CONDITIONS

6.1 Geotechnical Soil Units

We grouped the materials encountered in our field explorations and in the historic borings into 10 geotechnical units. Our interpretation of the subsurface conditions is based on the explorations and regional geologic information from published sources. The geotechnical units are as follows:

- Fill: highly variable mixtures of boulders, cobbles, gravel, sand, silt, and clay that may include wood debris, concrete debris, brick, glass, and other human-derived materials;
- Fine-grained Alluvium: very soft to medium stiff (less commonly stiff to very stiff) Silt and Clay with varying amounts of sand, typically less than 30 percent sand constituent (ML and CL); lesser amounts of Organic Clay and Organic Silt (OH and OL);
- Sand/Silt Alluvium: very loose grading with depth to dense or very soft grading with depth to stiff, Silty Sand (SM) and Sandy Silt (ML); trace gravel, trace silt/clay interbeds, and trace organics;

- Sand Alluvium: very loose to medium dense, occasionally dense to very dense, Sand to Gravelly Sand with varying amounts of silt (SP, SP-SM); lesser amounts of Silty Sand (SM); trace gravel interbeds; some zones contain organics and wood debris;
- Gravel Alluvium: medium dense to very dense Gravel with varying amounts of sand and fines (GP, GW, GP-GM, GW-GM, and GM); includes zones with cobbles and possible boulders; trace lenses of sand and silt;
- Catastrophic Flood Deposits - Fine-grained Facies: medium stiff to very stiff Silt (ML);
- Catastrophic Flood Deposits - Channel Facies: medium dense to very dense interbedded Sand and Gravel with varying amounts of fines (GW, GW-GM, GP-GM, SW-SM, SP, SP-SM, and SM); lesser layers of stiff Sandy Silt (ML); includes zones with cobbles and possible boulders;
- Upper Troutdale Formation: dense to very dense Sand and Gravel with varying amounts of fines, interbedded with hard Silt and Clay containing varying amounts of sand (GP, GW, GP-GC, SP, SP-SM, SM, SC, ML, MH, CL, and CH); some zones of cementation;
- Lower Troutdale Formation: very dense Gravel with varying amounts of sand and fines (GP, GW, GP-GM, GW-GM, GP-GC, GW-GC, GM, and GC); occasional sand and fine-grained layers were also encountered (SP, SP-SM, SM, MH, ML, CL, CH); some zones of cementation; includes zones with cobbles and possible boulders;
- Sandy River Mudstone: very stiff to hard Clay and Clayey Silt with varying amounts of sand interbedded with very dense Sand containing varying amounts of fines (CL, CH, MH, CL-ML, SM, SC, and, to a lesser extent, ML, SP-SM, and SP).

These geotechnical units were grouped based on their engineering properties, geologic origins, and distribution in the subsurface. Our interpretation of the unit distributions within the subsurface is presented on the Site and Exploration Plan and Interpretive Subsurface Profile A-A', Figure 2-2, and Interpretive Subsurface Cross Sections, Figures 6-1 through 6-11. Our interpretation emphasized some data points more than others, considering factors such as relative distance to the alignment and quality of the data source. Contacts between the units may be more gradational than shown in the profile, cross sections, and boring logs, and subsurface conditions may vary between explorations differently from what is shown on Figures 2-2 and 6-1 through 6-11.

Standard Penetration Test (SPT) N-values presented on the Shannon & Wilson drill logs in Appendix B and on Figures 2-2 and 6-1 through 6-11 are in blows per foot (bpf) as counted in the field (i.e., no corrections have been applied). The historic borings contain some logs where the SPT N-values are similarly presented "as counted in the field" and some where it is not specified if the N-values are corrected or not. Discussions of SPT N-values that follow in this report are based on SPT N-values as reported on the logs (current and historic). We

note that the subsurface conditions encountered at the site include deposits with coarse gravels and cobbles. Penetration tests in soils with large particle sizes may be unreliable due to sampler size effects and the actual soil density may be lower than that estimated by SPT N-value if the test was performed on a gravel or cobble. In addition to the SPT N-value, we also considered the available shear-wave velocity and PMT data to evaluate the density of the geotechnical soil units.

The sections below describe the geotechnical unit characteristics in greater detail and are predominantly based on the current Shannon & Wilson explorations and the in-situ and laboratory testing programs performed for the project. Appendix E includes plots of the soil index tests (Atterberg limits and grain size analyses) individually for each of the soil units described below.

6.1.1 Fill

Based on the available subsurface information, it appears varying thicknesses of Fill are present at the ground surface on both the west and east banks of the Willamette River in the project area. Some Fill was also encountered around the existing in-water piers. Fill thickness is highly variable and up to 25 feet or more. Fill composition varies across the site and includes mixtures of boulder and cobble riprap, gravel, sand, silt, and clay. Many of the borings encountered wood debris, concrete debris, asphalt fragments, brick fragments, metal, glass, and other human-derived materials in the Fill. Refer to the boring logs in Appendix A and Appendix B for greater details of Fill composition in specific areas. SPT N-values ranged from 1 to 67 bpf. Natural moisture contents of tested specimens ranged from 7 to 73 percent. Sieve analyses indicated fines contents that ranged from 5 to 41 percent by dry weight. Atterberg limits tests plasticity indices ranged from 7 to 13.

6.1.2 Fine-grained Alluvium

Fine-grained Alluvium was encountered in explorations on both sides of the river. The unit is intermittently present below the Fill and as interbeds within and between other alluvial units. The thickest accumulations were encountered on the east side of the river, between existing Burnside Bridge Bents 25 through 27, where thickness of the Fine-grained Alluvium is almost 50 feet. The Fine-grained Alluvium generally consists of very soft to medium stiff (less commonly stiff to very stiff) Silt and Clay with varying amounts of sand, with a sand constituent of typically less than 30 percent. Several samples from the unit were reported to contain organic material, and layers of Organic Clay and Organic Silt were encountered in borings B-11, B-18, and B-32. The unit includes Unified Soil Classification System (USCS) group designations ML, MH, CL, OH, and OL. SPT N-values in the unit ranged from 0 to 17 bpf and averaged 3 bpf. Natural moisture contents of tested specimens ranged from 26 to 110 percent and averaged 51 percent. Dry unit weights of tested specimens ranged from 40

to 80 pounds per cubic foot (pcf) and averaged 64 pcf. Sieve analyses indicated fines contents that ranged from 55 to 99 percent by dry weight and averaged 87 percent. Atterberg limits tests plasticity indices ranged from 0 to 55 and averaged 15.

6.1.3 Sand/Silt Alluvium

Sand/Silt Alluvium was encountered in explorations below Fill and below Fine-grained Alluvium, and also as interbeds within and between other alluvial units. The unit is most prevalent on the east side of the Willamette River, where thickness in the vicinity of Shannon & Wilson boring B-16 is up to approximately 125 feet. In the western and central portions of the site, thicknesses range from about 2 to 30 feet. The Sand/Silt Alluvium generally consists of Sandy Silt (ML) and Silty Sand (SM). Some samples contain trace interbeds of silt or clay, organics, or trace gravel. Two of the 145 SPTs in the Sand/Silt Alluvium met refusal, where more than 50 blows were required to drive the sampler through a six-inch interval. One of the SPTs which met refusal, occurred in boring B-32 where a possible large gravel or cobble was encountered within the Sand/Silt Alluvium at a depth of 120.4 feet. The other SPT which met refusal was also in boring B-32 and was performed at the contact between the Sand/Silt Alluvium and the underlying Gravel Alluvium. Non-refusal SPT N-values in the unit ranged from 0 to 40 bpf, averaged 10 bpf, and typically increased with depth. Natural moisture contents of tested specimens ranged from 28 to 56 percent and averaged 41 percent. Sieve analyses indicated fines contents that ranged from 9 to 77 percent by dry weight and averaged 47 percent. Atterberg limits tests plasticity indices ranged from 0 to 19 and averaged 5.

6.1.4 Sand Alluvium

Sand Alluvium typically makes up the bottom of the current Willamette River channel and was also encountered underlying the Sand/Silt Alluvium on the east riverbank, and as interbeds within the Gravel Alluvium. The Sand Alluvium unit typically thickens from about 12 feet near the west riverbank to about 70 feet near existing Pier 4 on the east bank of the river. The Sand Alluvium generally consists of very loose to medium dense, and occasionally dense to very dense, Sand to Gravelly Sand with varying amounts of silt including USCS group designations SP, SP-SM, and, to a lesser extent, SM. Some samples from within the unit contained organics and wood debris. SPT N-values in the unit ranged from 0 to 73 bpf and averaged 17 bpf. Natural moisture contents of tested specimens ranged from 13 to 48 percent and averaged 32 percent. Sieve analyses indicated fines contents ranged from 1 to 46 percent by dry weight and averaged 11 percent.

6.1.5 Gravel Alluvium

A layer of Gravel Alluvium, ranging from about 10 to 40 feet thick, was encountered underlying the Sand Alluvium below the Willamette River, and underlying and occasionally interbedded with other alluvial deposits on the adjacent banks. The Gravel Alluvium consists of loose to very dense Gravel with varying amounts of sand and fines including USCS group designations GP, GW, GP-GM, GW-GM, GP-GC, GM, and GC. The unit often contain cobbles and possible boulders, and trace lenses of sand and silt are also present. For the purposes of our interpretation, the Gravel Alluvium may include both coarse-grained Willamette River alluvium and coarse-grained Catastrophic (Missoula) Flood Deposits. The Gravel Alluvium is differentiated from the Catastrophic Flood Deposits – Channel Facies because it has a more consistent composition and contains fewer interbeds of silt and sand. During drilling in the Gravel Alluvium, drilling mud loss and hole-caving were frequently noted which is often indicative of open-matrix gravel containing limited matrix material. Forty-two out of 121 SPTs attempted in the Gravel Alluvium met refusal. Non-refusal SPT N-values ranged from 7 to 95 bpf and averaged 45 bpf. Natural moisture contents of tested specimens ranged from 10 to 35 percent and averaged 15 percent. Sieve analyses indicated fines contents ranged from 2 to 18 percent by dry weight and averaged 9 percent.

6.1.6 Catastrophic Flood Deposits – Fine-grained Facies

Catastrophic Flood Deposits - Fine-grained Facies sediments were encountered near the east end of the Burnside Bridge in borings made by GeoEngineers for the Portland Development Commission and in Shannon & Wilson Boring B-20. In boring B-20, the unit was encountered below the Fill and was approximately 13 feet thick. The Fine-grained Facies sediments generally consisted of loose/medium stiff, brown Silt with trace to some sand (ML). Due to the origin of the Catastrophic Flood Deposits, occasional cobbles and boulders encased in glacial ice and "rafted" down during the floods can be randomly found within the unit. Two SPT N-values in the unit were 6 and 4 bpf. Natural moisture contents of the two SPT specimens were 39 and 41 percent. Atterberg limits tests of the two SPT specimens had plasticity indices of nonplastic and 10. Dry unit weights of tested specimens by GeoEngineers ranged from 72 to 87 pcf.

6.1.7 Catastrophic Flood Deposits – Channel Facies

Catastrophic Flood Deposits - Channel Facies sediments were encountered below the Catastrophic Flood Deposits - Fine-grained Facies on the east side of the Burnside Bridge in borings made by GeoEngineers for the Portland Development Commission and in the Shannon & Wilson boring B-20. Shannon & Wilson's boring B-20 was terminated approximately 20 feet into the unit and never fully penetrated the bottom of the unit. The

encountered portions of the unit generally consist of medium dense to very dense interbedded sand and gravel deposits with varying amounts of fines, including USCS group designations GW, GW-GM, GP-GM, GM, SW-SM, SP, SP-SM, and SM. Lesser layers of stiff Sandy Silt (ML) were also reported in the unit. Portions of the unit contain cobbles and possible boulders. In boring B-20, the four SPT N-values in the unit ranged from 19 to 69 bpf and averaged 36 bpf. Natural moisture contents of three SPT specimens ranged from 11 to 23 percent and averaged 18 percent. Sieve analyses of the three specimens indicated fines contents that ranged from 14 to 27 percent by dry weight and averaged 18 percent.

6.1.8 Upper Troutdale Formation

The Troutdale Formation underlies the entire project site, beneath the overlying alluvial and fill units. Based on our explorations, we split the Troutdale Formation into an Upper Troutdale Formation unit and Lower Troutdale Formation unit. The Upper Troutdale formation is generally around 2 to 25 feet thick except in boring B-21 where 45 feet of the unit was encountered. Upper Troutdale Formation was encountered in the western half of the project area. The unit includes dense to very dense Sand and Gravel deposits with varying fines content interbedded with hard Silt and Clay deposits containing varying amounts of sand. The unit includes USCS group designations GP, GW, GP-GC, SP, SP-SM, SM, SC, ML, MH, CL, and CH. Some cementation was noted in portions of the unit and cobbles and boulders may be present within the unit.

The Upper Troutdale Formation contains more prevalent, lower-strength sand and fine-grained layers, compared to the underlying Lower Troutdale Formation. It also has relatively lower shear wave velocities. The upper unit may reflect Troutdale Formation that has weathered in place or that has been reworked to include Pleistocene alluvium. Fourteen out of 31 SPTs attempted in the Upper Troutdale Formation met refusal. Non-refusal SPT N-values ranged from 33 to 89 bpf, averaged 62 bpf, and were typically associated with layers with greater sand and fines content. Natural moisture contents of tested specimens ranged from 19 to 40 percent and averaged 19 percent. Sieve analyses indicated fines contents that ranged from 5 to 76 percent and averaged 15 percent. Atterberg limits tests from samples in fine-grained layers had plasticity indices that ranged from 8 to 33 and averaged 19.

6.1.9 Lower Troutdale Formation

Lower Troutdale Formation was encountered below the Upper Troutdale Formation on the west side of the project site, and directly below the Gravel Alluvium or Catastrophic Flood Deposits - Channel Facies on the east side of the project site. Thickness of the unit is on the order of 80 to 90 feet on the west side of the river and about 20 to 70 feet beneath the current river channel. On the east side of the river, none of the borings fully penetrated the Lower

Troutdale Formation and it appears to be over 100 feet thick. The unit typically consists of very dense Gravel with varying amounts of sand and fines, including USCS group designations GP, GW, GP-GM, GW-GM, GP-GC, GW-GC, GM, and GC. Zones of cementation are noted throughout the unit, and cobbles and boulders may be present within the unit. Some sand and fine-grained layers were also encountered (SP, SP-SM, SM, MH, ML, CL, CH). All but five of the 166 SPTs attempted in the Lower Troutdale Formation met refusal, most within the first 6 inches of penetration. The non-refusal SPT N-values ranged from 42 to 79 bpf, averaged 70 bpf, and were generally in the sand and fine-grained layers within the unit. Natural moisture contents of tested specimens ranged from 21 to 36 percent and averaged 27 percent. Sieve analyses indicated fines contents that ranged from 3 to 96 percent and averaged 18 percent. Atterberg limits tests of three samples from finer-grained layers had plasticity indices of 11, 15, and 28.

6.1.10 Sandy River Mudstone

Sandy River Mudstone was encountered below the Lower Troutdale Formation in borings along the western portion of the project from around existing Burnside Bridge Bent 18 to just east of existing Pier 3. Encountered portions of the unit include hard Clay and Clayey Silt with varying amounts of sand interbedded with very dense Sand that contains varying amounts of fines. The unit includes USCS group designations CL, CH, MH, CL-ML, SM, SC, and, to a lesser extent, ML, SP-SM, and SP. Trace gravel was observed in some samples, and in some areas the sand constituent could be remolded to clay under finger pressure. Seven out of 32 SPTs attempted in the Sandy River Mudstone met refusal. Non-refusal SPT N-values ranged from 21 to 98 bpf and averaged 63 bpf. Natural moisture contents of tested specimens ranged from 24 to 45 percent and averaged 32 percent. Sieve analyses indicated fines contents that ranged from 5 to 70 percent by dry weight and averaged 20 percent. Atterberg limits tests had plasticity indices that ranged from 0 to 43 and averaged 24.

6.2 Groundwater

The geotechnical borings performed by Shannon & Wilson for this study were drilled using mud rotary and rotosonic techniques. Mud rotary drilling techniques typically make it difficult to discern the depth to groundwater, if it is encountered, due to the use of artificial drilling fluids in the boreholes. Sonic rotary drilling generally allows observation of groundwater depths assuming no artificial fluids or water is added to the drill casing, and the drilling action does not heat up the rods enough to alter the moisture content of the samples. Logs of historic borings on the west side of the Willamette River, performed for the Ankeny Pump Station and the West Side CSO, report groundwater elevations ranging from approximately 6 to 10 feet (NAVD88). The log of ES-2005C, a historic boring performed for the East Side CSO on the east side of the Willamette River near the

intersection of SE Ankeny Street and SE 3rd Avenue, reports a groundwater elevation of approximately 14.8 feet. Subsurface profiles associated with the GeoEngineers borings performed for the Portland Development Commission indicate a groundwater elevation of 25 feet. One of the GeoEngineers borings, GEI-7, located near the intersection of NE Martin Luther King Boulevard and NE Couch Street, noted a layer of perched water at an elevation of approximately 50 feet during drilling.

Vibrating wire pressure transducers were installed in four borings (B-07, B-08, B-16, and B-32) to allow ongoing measurements of groundwater levels. Instrument installation details and all available data from the vibrating wire pressure transducers are included in Appendix B. The highest and lowest recorded groundwater levels from these four instruments are shown on Figure 2-2, Site and Exploration Plan and Interpretive Subsurface Profile A-A'.

Over the course of a year, water levels in the Willamette River typically fluctuate between elevations of approximately 6 and 20 feet. Based on information provided by HDR, the Ordinary High Water level is at elevation 20.1 feet and the average high stage water level is at elevation 11.43 feet. This is comparable to the groundwater elevations reported in the historic on-land borings, with the exception of the perched groundwater reported in GEI-7. Based on the materials present in the subsurface at the site, it is reasonable to assume that there is hydraulic connectivity between the Willamette River and groundwater in the adjacent banks. The annual average high-water level was used for geotechnical seismic hazard evaluations.

Groundwater levels throughout the site should be expected to vary seasonally and with changes in topography, precipitation, and the level of the Willamette River. Perched water zones are likely to be encountered above fine-grained layers. Locally, groundwater highs typically occur in the late fall to spring and groundwater lows typically occur in the late summer and early fall.

6.3 Soil Corrosivity

Analytical testing was performed to evaluate the corrosivity potential of the soil at the project site. The corrosivity testing suite included soil resistivity, pH, chloride content, sulfate content, sulfide content, and oxidation-reduction potential. Analytical testing was performed by GeoTesting Express of Acton, Massachusetts and subcontracted to TEi-Testing Services of Salt Lake City, Utah by GeoTesting Express. The test results are included in Appendix E. Soil corrosivity potential was evaluated based on the guidelines in Section 10.7.5 of the AASHTO LRFD (AASHTO, 2020).

Soil pH is a measurement of the hydrogen ion activity of the soil. Soil pH is reported in Standard Units (S.U.) on a scale ranging from 0 to 14, with 7 being neutral. Soils with a pH less than 7 are considered acidic, and soils with a pH greater than 7 are considered alkaline. According to the AASHTO specifications, soils with a pH less than 5.5 and soils with a pH between 5.5 and 8.5 that also have high organic content are considered potentially corrosive.

Resistivity (expressed as ohms-centimeter or ohms-cm) is the numerical expression of the ability of a soil to impede the transmission of an electrical current. Resistivity is the inverse of conductivity and is dependent on the presence of ions, their concentrations, mobility, and valence, as well as soil moisture and temperature. The AASHTO specifications state that effects of corrosion and deterioration shall be considered if resistivity values are less than 2,000 ohms-cm.

Sulfate and chloride concentrations were also measured. Sulfates can be converted to sulfides by naturally occurring bacteria. Sulfides, when allowed to oxidize, will produce sulfuric acid, which is highly corrosive. Chlorides will also chemically react and facilitate dissolution reactions with metals and concrete. AASHTO specifications classify the soil as corrosive if the concentration of sulfate or chloride is greater than 1,000 parts per million (ppm).

Soils in and around landfills and cinder fills, and soils subject to mine or industrial drainage conditions may also result in potential pile deterioration or be potentially corrosive.

6.3.1 West Riverbank

The corrosivity testing suite on the west bank of the Willamette River included samples from borings B-05, B-06, B-07, and B-08 between the depths of 11 and 16.5 feet. The results of the corrosivity testing are presented Exhibit 6-1.

Exhibit 6-1: Corrosivity Test Results West Riverbank

Boring	Sample ID	Sample Depth (ft)	pH (S.U.)	Resistivity (ohm-cm)	Sulfate (ppm)	Chloride (ppm)
B-05	N-3	15	6.4	3,926	< 10	20
B-06	N-1	11	6.4	2,479	< 10	21
B-07	N-1	11	6.5	2,169	< 10	23
B-08	N-1	15	5.7	4,442	< 10	17

NOTES:
ft = feet; S.U. = Standard Units; ohm-cm = ohms centimeter; ppm = parts per million (mg/kg).

In the tested samples from borings performed on the west riverbank, soil pH ranged from 5.7 to 6.5 and averaged 6.3. Tested resistivity values ranged from 2,169 to 4,442 ohm-cm and

averaged 3,254 ohm-cm. Sulfate content was less than 10 ppm in all samples and Chloride content of tested specimens ranged from 17 to 23 ppm and averaged 20 ppm. Based on these results, the soil has a low corrosivity potential.

6.3.2 Willamette River

The corrosivity testing suite within the Willamette River included samples from borings B-12 and B-27 between the depths of 7.9 and 22.3 feet. The results of the corrosivity testing are presented in Exhibit 6-2.

Exhibit 6-2: Corrosivity Test Results Willamette River

Boring	Sample ID	Sample Depth (ft)	pH (S.U.)	Resistivity (ohm-cm)	Sulfate (ppm)	Chloride (ppm)
B-12	N-2 & N-3	15 & 20.8	5.6	8,574	< 10	10
B-27	N-2	7.9	4.8	5,578	< 10	10

NOTES:
ft = feet; S.U. = Standard Units; ohm-cm = ohms centimeter; ppm = parts per million (mg/kg).

In the tested samples from borings performed within the Willamette River, soil pH ranged from 4.8 to 5.6 and averaged 5.2. Tested resistivity values ranged from 5,578 to 8,574 ohm-cm and averaged 7,076 ohm-cm. Sulfate content was less than 10 ppm in all samples and Chloride content of tested specimens was 10 ppm. Based on these results, the pH may indicate the soil is potentially corrosive.

6.3.3 East Riverbank

The corrosivity testing suite on the east bank of the Willamette River included samples from borings B-16, B-19, B-32, and B-33 between the depths of 10 and 24 feet. The results of the corrosivity testing are presented in Exhibit 6-3.

Exhibit 6-3: Corrosivity Test Results East Riverbank

Boring	Sample ID	Sample Depth (ft)	pH (S.U.)	Resistivity (ohm-cm)	Sulfate (ppm)	Chloride (ppm)
B-16	N-4	10	6.8	1,240	< 10	21
B-19	N-4	17.5	6.9	19,628	< 10	10
B-32	N-4	20	7.0	3,306	< 10	20
B-33	N-7	22.5	6.8	3,822	12	17

NOTES:
ft = feet; S.U. = Standard Units; ohm-cm = ohms centimeter; ppm = parts per million (mg/kg).

In the tested samples from borings performed on the west riverbank, soil pH ranged from 6.8 to 7.0 and averaged 6.9. Tested resistivity values ranged from 1,240 to 19,628ohm-cm and averaged 6,999 ohm-cm. Sulfate content was less than 10 ppm in three samples and 12 ppm in one and Chloride content of tested specimens ranged from 10 to 21 ppm and averaged 17 ppm. Based on these results, the soil has a low corrosivity potential.

7 SEISMIC GROUND MOTIONS

7.1 Design Ground Motions and Performance Requirements

Seismic evaluation for the Burnside Bridge was performed following guidelines presented in the AASHTO LRFD Bridge Design Specifications and the project specific seismic design criteria (HDR, 2021b). The project seismic design criteria identify two earthquake ground motion design / performance levels for the bridge:

- Limited Operation Design Earthquake (LODE) level – The ground motions for this earthquake performance level are defined as probabilistic 1,000-year return period ground motions. In the ODOT BDM and GDM, this performance level is referred to as "Life Safety."
- Full Operation Design Earthquake (FODE) level – The ground motions for this earthquake performance level are defined as deterministic mean motions for a CSZ full rupture event. This performance level is roughly equivalent to the "Operational" performance level in the ODOT BDM and GDM.

To develop ground motion time histories for use in 2-dimensional (2D) FLAC site-specific response and permanent ground displacement analyses for the LODE and FODE ground motion levels, we first developed the design and target spectra at the rock conditions consistent with the boundary conditions to be used in the FLAC model. We then developed earthquake time histories that are consistent with those target spectra. This section describes the details and the methodologies we used to develop the LODE (using a Probabilistic Seismic Hazard Analysis [PSHA]) and FODE (using a Deterministic Seismic Hazard Analysis [DSHA]) for input into the site-specific ground response analysis.

7.2 Probabilistic Seismic Hazard Analysis

7.2.1 Methodology

We included in the PSHA model local and regional faults considered to be significant contributors to the ground shaking hazard at the project site based on an examination of peer-reviewed literature. As described below, fault parameters of these seismic sources provided constraints for the PSHA model. For each fault, the use of logic trees provided a

means to incorporate into the model a range of evolving research-supported interpretations of fault characteristics and quantitatively evaluate uncertainties associated with these parameters.

We used our in-house version of the program code HAZ for this PSHA calculation. We significantly modified and updated the code, as needed, for the recent development of the seismic models or the calculation methods.

In this section, we define the PSHA seismic source model, summarize the seismic parameters, and describe how epistemic uncertainties were modeled.

7.2.1.1 Approach and Key Input Parameters

The Portland area is subject to ground shaking from seismogenic sources that can be grouped into three broad zones (Figure 7-1, Inset B):

- The CSZ Plate Interface Zone (i.e., the locked portion of the CSZ fault interface) that produces great mega-thrust earthquakes;
- The Intraslab Zone, (i.e., the deep subducted portion of the Juan de Fuca Plate in the CSZ), the source of Wadati-Benioff zone earthquakes; and
- The Crustal Fault Zone in the overriding North American Plate, where shallow crustal faults rupture.

These seismogenic sources were modeled in the PSHA as either discrete fault sources or areal source zones. Discrete fault sources were modeled as individual three-dimensional fault surfaces. Details of their geometry and fault behavior were incorporated into the source characterization. Areal source zones account for background crustal seismicity that cannot be attributed to recognized structures explicitly included in the seismic source model. In the PSHA, the CSZ was modeled both as a discrete, albeit large, fault at the interface and as an areal source in the deep subducted plate (intraslab) part of the subduction zone. Mapped, shallow crustal sources that are capable of generating greater than moment magnitude (M_W) 6.5 earthquakes were modeled as discrete faults generating the earthquakes within a wide magnitude range. Short shallow crustal sources that are capable of generating less than M_W 6.5 earthquakes were modeled as discrete faults generating the characteristic earthquakes.

Peer-reviewed studies provided the bases for source parameters incorporated in the PSHA, including:

- Fault model, which accounts for the presence of multiple fault strands or varying fault lengths;
- Geometry, including dip, rupture length, and seismogenic depth;

- Slip rate and/or recurrence interval;
- Maximum/minimum magnitude;
- Segmentation; and
- Recurrence model.

For discrete sources where the fault geometry adequately describes the rupture area, the earthquake magnitude was determined from the Wells and Coppersmith (1994) magnitude-rupture area relationship. In the PSHA analyses, we limited the rupture areas (and therefore magnitudes) between length to width ratios of 0.5 and 6.4 based on the range of ratios from observed earthquakes in the Wells and Coppersmith (1994) and Stirling and others (2002) databases. About two-thirds of all historical ruptures in these databases have an aspect ratio within this range. For discrete faults, we used slip rate and/or recurrence interval, slope of the recurrence curve (b-value), and maximum magnitude to describe earthquake recurrence. For areal source zones, the input earthquake recurrence parameters included the area geometries, maximum magnitude, and the Gutenberg-Richter a and b recurrence parameters derived from the historical earthquake record.

We used the recent National Seismic Hazard Model (NSHM; Petersen and others, 2014 and 2020, respectively) as a basis for our PSHA, but we modified it where new data became available since 2018, or if using local and site-specific data are appropriate for the project. The key differences between our PSHA model and 2018 NSHM are that we used:

- Next Generation Attenuation-Subduction project (NGA-Sub) Ground Motion Models (GMMs);
- Crustal faults not available in 2018 NSHM (e.g., East Bank fault) or updated faults where more recently published data was available (e.g., Gales Creek fault zone);
- Goldfinger and others (2017) model for CSZ interface;
- McCrory and other (2012) geometry model for CSZ intraslab; and
- Basin depth parameters to include basin effects.

7.2.1.2 Uncertainties and Logic Trees

Fault studies do not offer a complete view of fault characteristics and earthquake histories. They can be limited by the preservation of earthquake data, the identification of earthquake features, varying availability, quality, and magnitude of field data, etc. Consequently, we constructed logic trees to organize, quantify, and represent the epistemic uncertainty for each model parameter. Each node is a model parameter (e.g., dip, slip rate, or length) that may separate into multiple branches, which are then populated with the parameter values and their alternatives. Probability weights are assigned to each branch with the intention of

representing both the best estimates of the fault characteristics and the potential range of alternatives supported by the available data. If a source parameter has highly defensible evidence for a single particular value, a weight of 1.0 is assigned (single branch on the logic tree), otherwise uncertainty is weighted as a distribution of values summing to 1.0. Keefer and Bodily (1983) suggest that a three-point distribution of the 5th, 50th, and 95th percentiles (weighted 0.2, 0.6, and 0.2, respectively) best approximates parameters with a continuous distribution (e.g., slip rate, fault dip, and fault length). Typically, these three weights are assigned to parameter values and alternative branches, unless the available data suggest otherwise.

The full logic tree incorporates the seismic source characteristics considered and their alternatives. The product of the probability weights signifies a measure of the degree of confidence in the fault characteristics. In other words, branches containing characteristics with the highest degree of confidence are most heavily weighted and, consequently, impart the greatest influence in the model calculations. For a seismogenic source, the first weighted parameter on the logic tree is the probability of producing an earthquake in the current tectonic conditions. All faults in this study's PSHA have a non-zero probability; faults with well-documented activity have a 1.0 probability. Logic trees have been constructed for the CSZ interface, CSZ intraslab, and crustal areal background sources. Logic trees for discrete crustal faults are presented in Section 7.2.3.3.

7.2.1.3 Earthquake Recurrence Models

Earthquake recurrences for the seismic sources used three models:

- Truncated exponential (truncated Gutenberg-Richter model);
- Characteristic; and
- Maximum magnitude.

The recurrence model defines the earthquake magnitude-frequency distribution for a seismic source. The truncated exponential model is based on a truncated Gutenberg and Richter (1944) magnitude-frequency distribution. For the truncated exponential model, the annual frequency of the earthquake occurrence exceeding a magnitude m is defined by the following equation:

$$N(m) = N(m_{min}) \frac{10^{-b(m-m_{min})} - 10^{-b(m_{max}-m_{min})}}{1 - 10^{-b(m_{max}-m_{min})}}$$

where $N(m_{min})$ is the annual number of the earthquakes larger than minimum magnitude of m_{min}, b is the slope of the magnitude distribution in the Gutenberg-Richter model, and m_{max} is the maximum magnitude for the earthquake's distribution. The above equation is a

truncated form of the Gutenberg-Richter model (which originally defines a linear relationship between magnitude and $N(m)$ in log scale) with a magnitude limited to a lower bound value of m_{min} and an upper bound value of m_{max}. Magnitudes less than 5 are usually not considered important for engineering projects (Petersen and others, 2014), and we use larger than or equal to magnitude 5 as m_{min} for the truncated exponential model.

In the characteristic model, the characteristic earthquakes are distributed uniformly around the characteristic magnitude, m_{max} (over ±0.25 magnitude unit), and the remainder of the moment rate is distributed using the above equation with a maximum magnitude 0.25 unit lower than the characteristic magnitude (Youngs and Coppersmith, 1985).

For the maximum magnitude model, it is assumed that all of the seismic energy is released in characteristic earthquakes. In this model, the magnitudes are usually distributed around the characteristic magnitude, m_{max}, with a normal distribution truncated 0.24 unit higher than the characteristic magnitude.

The truncated exponential model is more consistent with seismicity observation in large areal sources, and the characteristic model is more appropriate for discrete faults (Aki, 1983; Youngs and Coppersmith, 1985). The maximum magnitude model is used for discrete faults that only produce large-magnitude earthquakes.

7.2.2 Regional Tectonics and Seismicity

The contemporary tectonics and seismicity of the region are the result of oblique, northeastward subduction at a rate of about 37 millimeters per year (mm/yr) (DeMets and others, 2010) of the Juan de Fuca oceanic plate beneath the North American continental plate (e.g., Wells and others, 1998; Wells and Simpson, 2001) (Figure 7-1, Inset A). This complex tectonic setting produces east-west compressive strain along the CSZ, as well as northward translation and rotation of the mobile, crustal, Cascadia fore-arc blocks that span the leading edge of the North America plate (Wells and Weaver, 1998; McCaffrey and others, 2007, 2013). Depicted in Figure 7-1 (Inset A), rotation of the Sierra-Nevada block and expansion of the Basin and Range drive the northward migration and clockwise rotation of the Cascadia fore-arc blocks (e.g., Pezzopane and Weldon, 1993; Wells and Weaver, 1998; Wells and Simpson, 2001). As a result, the southern portion of the fore arc, the Oregon Coast block, is impinging on western Washington at a rate of about 8 to 12 mm/yr, causing crustal shortening in northwest Oregon and western Washington (Wells and others, 1998; Wells and Simpson, 2001; Mazzotti and others, 2002).

The combined effect of margin-normal subduction and margin-parallel shortening produces complex and diverse deformation within the northern edge of the Cascadia fore arc and

triggers large (greater than M_W 6), damaging earthquakes from three seismogenic source zones (Figure 7-1, Inset B):

- The CSZ Plate Interface Zone (i.e., the locked portion of the CSZ fault interface) that produces great mega-thrust earthquakes;
- The Intraslab Zone, (i.e., the deep subducted portion of the Juan de Fuca Plate in the CSZ), the source of Wadati-Benioff zone earthquakes; and
- The Crustal Fault Zone in the overriding North American Plate, where shallow crustal faults rupture.

All three sources potentially produce earthquakes that impact the ground motion hazards at the bridge site. Offshore, elastic release of strain accumulated in the CSZ locked plate interface produces great megathrust earthquakes) that rupture the entire interface (magnitude [M] 9) about every 500 years (Atwater and Hemphill-Haley, 1997; Clague, 1997; Goldfinger and others, 2003 and 2012); the most recent rupture occurred in A.D. 1700 (Satake and others, 1996; Atwater and Hemphill-Haley, 1997; Clague, 1997; Yamaguchi and others, 1997; Goldfinger and others, 2003 and 2012). Onshore, migration and rotation of tectonic blocks produce deformation along shallow faults within the upper part of the crust. At depth, rupture within the subducting slab, referred to as the intraslab, has produced some of the largest recorded earthquakes (M_W 6.5 to 7) to strike the Pacific Northwest, in the northern California Coast and western Washington. However, over the past century intraslab earthquakes have been markedly infrequent in Oregon.

Compared to western Washington and northern California, Oregon has experienced relatively few large earthquakes since they have been instrumentally recorded (Figure 7-2) (Ludwin, 1991; Geomatrix Consultants Inc. [Geomatrix], 1995; Wong and Bott, 1995). Significant historical earthquakes in Oregon are listed in Table 7-1 (Wong and Bott, 1995). With respect to the bridge site, most notable are the following shallow earthquakes:

- 1877 M_L 5.75 Portland
- 1962 M_w 5.2 Portland
- 1993 M_L 5.6 Scotts Mills

where M_L is local magnitude. We note that although these earthquakes were shallow, they did not rupture the ground surface. Thus, they could not be conclusively attributed to specific mapped faults, although the 1993 Scotts Mills earthquake was inferred to originate along the Mount Angel fault (Thomas, 1996).

Because recorded seismicity offers a restricted window into earthquake histories along regional faults, ground motion studies in part rely upon paleoseismic studies to extend earthquake histories from about 150 years, the timeframe of historical records, to thousands

of years into the Holocene Epoch[1] and tens of thousands of years or more into the Quaternary Period. Ideally, the deepening of these earthquake histories can provide important parameters to assess the potential hazards each fault poses, such as earthquake recurrence, slip rate, estimated earthquake size, and when the fault was last active. While useful, paleoseismic-based earthquake histories tend to be incomplete. Figure 7-2 could be viewed as a generalized progress report of the current understanding of regional fault activity[2]. These mapped faults are broadly categorized into: 1) faults with substantial geologic evidence of Holocene rupture (red) and 2) faults with limited characterizations and/or uncertain earthquake timing (brown), but sufficient evidence to support suspected Quaternary deformation.

While paleoseismic evidence for Holocene-age large earthquakes along the CSZ Interface is compelling and has provided detailed fault parameters that are included in this PSHA, there have been very few studies that have confirmed Holocene activity along crustal faults located within 150 kilometers (km) of the bridge site. Recent studies that have produced significant geological evidence for Holocene rupture along two fault zones within the region: the Gales Creek fault zone and the Mount Hood fault zone. Relative to the bridge site, these fault zones are located approximately 38 km to the west and 75 km to the southeast, respectively. Based on current geological and geophysical evidence, the latest ruptures along the other 18 faults included in this PSHA may have occurred much earlier in the Quaternary (> 100 ka). For these faults, estimated slip rates are thus very low (< 0.2 mm/yr) and are about one order of magnitude less than faults in the Puget Sound area that are also responding to north-south contraction within the deforming forearc. There may be tectonic reasons for these low slip rates, or they might reflect a poor earthquake record due to lack of fault exposures, large uncertainties in age-dating deformed strata, lack of preservation, or possible removal of faulted material by erosion, among other complications. Because possible Quaternary activity along faults within 150 km of the bridge site can at least be suspected, they are inferred to be seismogenic and possible contributors to ground motions hazards and are therefore included in this PSHA.

[1] The Quaternary Period spans from approximately 2.6 million years ago to the present and is formed by two epochs: the Pleistocene Epoch and the Holocene Epoch. The latter is the most recent epoch and spans from approximately 11.6 thousand years ago (end of the last glacial period) to the present.
[2] Note information for some of the faults presented in this report post-dates the USGS Quaternary Fault and Fold Database (QFFD) displayed in Figure 7-2 (e.g., Gales Creek fault zone, Mount Hood fault zone, etc.).

7.2.3 Seismic Source Characterization

7.2.3.1 Cascadia Subduction Zone Interface Megathrust Source

At the subduction plate interface, the subducting oceanic slab and the overriding North American continental plates are locked together by friction. The strain stored in these locked plates is released in great, megathrust M_W 8 to M_W 9 earthquakes that rupture when the frictional strength of the fault is exceeded and the fault slips (Atwater and Hemphill-Haley, 1997; Goldfinger and others, 2003 and 2012; Wang and others, 2003). Along the coast, this fault slip can trigger sudden land subsidence, strong ground shaking, tsunami inundation, and submarine landsliding. Paleoseismic coastal studies have uncovered over a 5,000-year paleoseismic record of rapid land level changes and tsunamis associated with megathrust earthquakes along the 1,000-km length of the CSZ from northern California to Vancouver Island (e.g., Atwater, 1987 and 1992; Grant, 1989; Darienzo and Peterson, 1990 and 1994; Clarke and Carver, 1992; Obermeier, 1995; Meyers and others, 1996; Nelson and others, 1996; Peterson and Darienzo, 1996; Shennan and others, 1996; Atwater and Hemphill-Haley, 1997; Williams and others, 2005).

Offshore, evidence from paleoseismic studies provides temporal correlation of shaking-induced submarine landsliding deposits (turbidites) found in deep-sea channels along the entire length of the CSZ (Adams, 1990 and 1996; Goldfinger and others, 2003 and 2012). Based on the 10,000-year turbidite record, Goldfinger and others (2012) determined that the CSZ has ruptured not only along its entire length but also along fault segments for a total of 41 great earthquakes. With the latest update of the rupture model, Goldfinger and others (2017) developed seven models of full and partial rupture along the CSZ fault segments during the Holocene. Goldfinger and others (2017) identified seven rupture areas (shown in Figure 7-3) that have generated great CSZ earthquakes during the Holocene. The seven rupture areas and recurrence intervals are:

- Twenty (20) full or nearly full-length ruptures (Model A, Figure 7-3);
- Three nearly full-length ruptures involving coastal Washington, Oregon, and northern California (Model B, Figure 7-3);
- Rupture model C is subdivided into seven ruptures involving the southern three-quarters of the margin, between Astoria and northern California (Model C, Figure 7-3) and two ruptures along the southern Oregon and northern California margin (Model C', Figure 7-3);
- At least nine smaller ruptures between the mouths of the Rogue River in southern Oregon and the Eel River in northern California (Model D, Figure 7-3);
- Four smaller ruptures in northern California, between the mouths of the Smith River and the Eel River (Model E, Figure 7-3); and

- One rupture along the northern margin, between Astoria and southern Vancouver Island (Barkley) (Model F, Figure 7-3).

According to Goldfinger and others' (2017) (Figure 7-3) and Goldfinger and others' (2012) (Figure 7-4) interpretation of the turbidite data, the northern portion of the CSZ, which includes western Washington, mainly ruptures when the entire length of the zone ruptures, and this area has a recurrence interval of approximately 500 years, or twice that of the southern end of the CSZ. In their interpretation, smaller earthquakes, such as those off the coast of Oregon and California (i.e., models B through E in Figure 7-3 and models B through D in Figure 7-4), do not occur or rarely occur off the coast of Washington and British Columbia. Instead, the northern section of the CSZ likely experiences full-rupture megathrust earthquakes.

The onshore and offshore paleoseismic studies provide compelling evidence for dozens of earthquakes along the CSZ during the Holocene, including one megathrust as recent as AD 1700. However, researchers disagree about using the turbidites as proxy records for CSZ earthquakes and using the recurrence rates and aspects of fault segmentation derived from the turbidite records (Atwater and others, 2014). Atwater and others (2014) re-evaluated existing turbidite data and samples and concluded that differences in submarine canyon sedimentation histories along the CSZ might impose along-strike variation in the turbidite stratigraphy. This would complicate correlating turbidite or earthquake stratigraphy from site to site along the length of the CSZ.

Atwater and others (2014) also emphasize the importance of including onshore paleoseismic data to constrain CSZ rupture parameters. Consequently, in contrast to the Goldfinger and others' (2012, 2017) model that is inconsistent with partial rupture in the northern portion of the CSZ, Atwater and Griggs (2012) have suggested that:

- M_W 8.0 partial ruptures have occurred along the northern CSZ interface, based on onshore tsunami evidence at Discovery Bay, Washington; and
- These smaller ruptures might result in shorter overall recurrence intervals in the northern CSZ than previously suggested by Goldfinger and others (2012).

Accordingly, we account for the differing interpretations of the CSZ in our PSHA and model both full rupture and partial rupture along the CSZ (Figure 7-5). First, based on our review of peer-reviewed literature and following the 2014 and 2018 NSHM, we model rupture along the entire CSZ interface zone (full rupture) and assign it a weight of 1.0. Next, for partial rupture we modified the recurrence and segmentation portion of the 2014 and 2018 NSHM model based on our review of literature published since its development. The 2014 and 2018 NSHM models included the possibility that the CSZ can rupture segmentally and included two alternate models for partial rupture. The first partial rupture model follows

Goldfinger and others (2012), which identifies four segments with recurrence intervals that differ among the four rupture segments (Figure 7-4). This model has the shortest recurrence intervals in the south and no partial rupture in the north. The NSHM assigned a weighting factor of 0.75 to this branch of their logic tree. The second NSHM partial rupture model was included to accommodate the findings of Atwater and Griggs (2012) that questioned the recurrence model of Goldfinger and others (2012). This alternative branch included M_W 8.0 to 8.7 floating partial ruptures that can occur anywhere along the entire length of the CSZ, including the northern CSZ. The floating rupture has an area-proportional recurrence rate consistent with Goldfinger and others (2012) rate for the southern segments (combination of rupture Models B, C, and D in Figure 7-4), and this rate was applied to the entire CSZ. NSHM assigned this floating earthquake branch a weight of 0.25.

The 2014 and 2018 NSHM model results showed that the segmented rupture model of Goldfinger and others (2012) and the floating M_W 8.0 to 8.7 partial rupture model produce very similar hazard maps for onshore locations. In fact, Petersen and others (2014) determined that the mean rate of recurrence is the controlling factor for onshore locations rather than the segmentation details (see page 97 of Petersen and others, 2014). Following the publication of the 2014 NSHM map, Atwater and others (2014) continued their earlier 2012 work by examining the entire dataset from Goldfinger and others (2012) (Atwater and others [2012] examined only part of the Goldfinger dataset) and analyzing other existing deep sea cores not analyzed by Goldfinger and others (2012). This work bolstered their dispute with the Goldfinger and others (2012) segmentation model.

Considering the CSZ rupture model review of Atwater and Griggs (2012), work by Atwater and others (2014), and observations by Petersen and others (2014), we assigned a weight of 1.0 to the floating M_W 8.0 to 8.7 partial rupture model (Figure 7-5) and did not include the Goldfinger and others (2012 and 2017) segmentation model. The floating partial rupture model assigns an area-proportional recurrence rate consistent with Goldfinger and others (2017) rate for the southern and northern segments (combination of rupture Models B through F in Figure 7-3), and this rate is applied to the entire CSZ. This produces a higher hazard from the CSZ interface compared to the 2014 and 2018 NSHM model because it increases the rate of partial ruptures and hazard in the northern zone nearest the site and does not reduce the recurrence interval of larger events that rupture the entire subduction zone.

We based our updip and downdip extents of the seismogenic portion of the CSZ interface rupture on the work used in developing the 2014 and 2018 NSHM seismic hazard maps (Petersen and others, 2014; Petersen and others, 2020), including Flück and others (1997), Wang and others (2003), and Gomberg and others (2010). The seismogenic downdip boundaries used in the current study are shown in Figure 7-6. The updip extent of the

model is based on Flück and others (1997) and is the only updip boundary considered in the 2014 and 2018 NSHM models and, therefore, assigned a weight of 1.0. Three downdip rupture extents considered are: (a) the 1 centimeter per year (cm/yr) locking contour between the subducting and overriding slabs, (b) the midpoint between the 1 cm/yr and the fully locked zone, and (c) the top of the episodic non-volcanic tremor slip zone. The downdip model weights are provided in Figure 7-5.

The 2014 and 2018 NSHM uses three equally weighted magnitude-area relationships to calculate magnitude. The three magnitude area relationships, Papazachos and others (2004), Murotani and others (2008), and Strasser and others (2010), were developed from global subduction earthquakes. We used these relationships and rupture areas corresponding to the three downdip extents to calculate magnitudes for a full rupture of the CSZ interface in the PSHA model ranging from 8.6 to 9.3 and are the same as those used in the 2014 and 2018 NSHM (Figure 7-5).

7.2.3.2 Cascadia Subduction Zone Intraslab Earthquake Source

Despite the extensive paleoseismic history of M_W 8 to M_W 9 earthquakes rupturing at the CSZ plate interface, very few intraslab earthquakes have been identified in the paleoseismic record or instrumentally recorded in western Oregon. Possible reasons for a lack of intraslab earthquakes include crustal thickness and physical properties of the subducting slab, outlined below. Deep intraslab earthquakes likely occur as a result of the following physical changes within the subducting slab:

- Rock embrittlement from dehydration of hydrous minerals in the slab (Preston and others, 2003); and
- Internal deformation where the down-going slab flexes and produces extension (Weaver and Baker, 1988; McCrory and others, 2012).

The physical changes and tensional stresses in the subducting plate produce high-angle normal faulting earthquakes. Intraslab earthquakes are most common where the subducting slab is warped into arches beneath western Washington and northern California. This geometry contributes toward generating large, damaging earthquakes such as the 2001 M_W 6.8 Nisqually event near Olympia, Washington. Figure 7-7 shows estimated slab depth contours beneath these regions and locations of the associated intraslab earthquakes (McCrory and others, 2012). McCrory and others (2012) inferred that, in addition to dehydration processes, buckling of the slab in these locations may concentrate stress and strain, increase slab flexure, and thus promote earthquake occurrence. Conversely, the lack of intraslab earthquakes beneath Oregon is consistent with an anhydrous portion of the slab and a zone of undeformed slab geometry (Figure 7-7) (McCrory and others, 2012).

We used McCrory and others' (2012) plate geometry (Figure 7-7) within approximately 150 km of the site. BC Hydro (2012) used a similar, earlier version of this plate geometry by McCrory and others (2006). We did not use the 2014 NSHM geometry. The 2014 NSHM implements a simplified model that defines the western and eastern extents of the zones at longitude 124°W and 120°W, respectively, with three eastward descending slab depths of 42, 50, and 60 km between these longitudes. By comparison, the McCrory and others (2012) geometry provides a finer resolution of the plate location and depth, imaging the arch and change in slab orientation in the northern portion. The project location is located within the intraslab source zone, and the vertical distance (i.e., depth) to the top of the slab is approximately 45 to 48 km at the site, based on the McCrory and others (2012) model.

Spatially variable seismicity rates were obtained from the 2014 NSHM, and the grid rates were divided in the east-west direction by McCrory and others (2012) 10-km depth contours to obtain the seismicity at each contour depth. The m_{min} and b-values were found directly from the 2014 NSHM for the grid points. The 2014 NSHM uses a b-value of 0.4 for magnitudes less than 7.2 and 0.8 for magnitudes greater than 7.2.

We used a uniform distribution of hypocentral depths (point sources) below the top of the slab over a slab thickness of 12, 17, and 22 km, with weight factors of 0.2, 0.7, and 0.1, respectively (see Figure 7-8). The slab thicknesses and weighting are consistent with the BC Hydro (2012) model. A total 17-km intraslab thickness is estimated by Kao and others (2008) based on typical 7-km-thick oceanic crust and 10-km-thick zone in the uppermost oceanic mantle. While the distance metric in the GMMs is the closest distance to rupture, we modeled the earthquakes as point sources. Because of the relatively large depth beneath the site, the point-source simplification used in the model is reasonable in our opinion. The hypocentral depth was only used to evaluate the depth parameter in the GMMs.

Because intraslab events involve high-angle normal faulting, the area of the rupture surface and magnitude is strongly dependent on the thickness of the subducting slab. Young subduction zones, such as the CSZ, generally have relatively thin subducting slabs. Thermal modeling of the CSZ (Hyndman and Wang, 1993) and the observed geometry of the Wadati-Benioff Zone (Jarrard, 1986) confirm the likelihood that the subducting slab is relatively thin. Worldwide observations indicate that the largest intraslab earthquakes are on the order of M_W 8, with the largest of these occurring in older subducting slabs. The largest recorded intraslab earthquake beneath the Puget Lowland, the 1949 Olympia earthquake, was a surface wave magnitude M_W 7.1 event. Based on these observations, the 2014 NSHM uses two equally weighted maximum intraslab earthquake magnitudes of 7.5 and 8. For this project, we used the same maximum magnitude and weighting factors corresponding to the respective 2014 NSHM (see Figure 7-8).

7.2.3.3 Crustal Fault Sources

7.2.3.3.1 Tectonic History of Portland-Area Forearc Structural Basins

Geologic and geophysical studies of crustal faults in northwestern Oregon narrate long and complex tectonic histories that are driven by an evolving subduction zone-related stress field (e.g., Blakely and others, 1995; 2000; 2004; Yeats and others, 1996; McPhee and others, 2014; Wells and others, 2020b). As shown in Figure 7-9, two general orientations dominate the structural fabric of northwestern Oregon: northwest- and east-striking faults. The largest fault systems generally trend northwest, such as the Gales Creek fault zone, the Portland Hills faults, and the Canby-Molalla fault. These faults, and other sub-parallel faults shown in Figures 7-9 and 7-10, define the boundaries of the deep, synclinal Tualatin Basin, its neighboring parallel structure, the Portland Basin, and the intervening anticlinal Portland Hills (Tualatin Mountains). The shorter east- to northeast-trending faults, such as the Beaverton fault and the Grant Butte fault zone, mark the edges of uplifted buttes and hills that interrupt the generally low-lying basin floors near the southern boundaries of the Tualatin and Portland Basins, respectively (Yeats and others, 1996; Blakely and others, 2000; Anderson and others, 2013; McPhee and others, 2014; Wells and others, 2020b). Together, these two basins, along with the northern Willamette Basin, are formed by or are traversed by the majority of the faults included in this PSHA (Figures 7-9 and 7-10). In the text below, we focus on the structural basins nearest to the bridge site, the Tualatin and Portland Basins.

Basin geometry and recent geophysical studies suggest that the Tualatin and Portland Basins formed during a multi-stage tectonic history: first extensional faulting followed by the development of the present-day transpressional fold and thrust belt. Before the 15 Ma Columbia River Basalt Group (CRBG) flows inundated the area, the Tualatin and Portland Basins were originated as trans-tensional pull-apart structures within a larger subsiding marine basin in the fore arc outboard of the Cascade Magmatic Arc (Popowski, 1996; McPhee and others, 2014; Wells and others, 2020b). Based on gravity studies of the deep rocks beneath the Portland Hills, Scanlon and others (2021) inferred that the incipient Sylvan-Oatfield and Portland Hills faults were two normal faults bounding a small graben that later developed into the Tualatin Mountains-Portland Hills. Since CRBG emplacement, a developing dextral transpressional tectonic setting (Wells and others, 1998; 2001) reactivated and reorganized former normal faults, zones of crustal weakness, into the present-day fold and thrust geometry (Yeats and others, 1996; McPhee and others, 2014; Wells and others, 2020a). Transpression across the CSZ fore arc inverted the Sylvan-Oatfield and Portland Hills faults from normal faults to high-angle dextral-reverse faults, creating the Portland Hills anticline and separating the Portland and Tualatin Basins. The deepening of these basins and the uplift of the surrounding highlands along the northwest-trending faults shown in Figure 7-10 have produced a 6-km-deep structure below Tualatin

and a 2-km-deep structure below Portland (McPhee and others, 2014; Scanlon and others, 2021). Both basins are floored by CRBG that had been warped into the synclines that form the basins and the anticlines that border them (e.g., Beeson and others, 1989; McPhee and others, 2014; Scanlon and others, 2021). These rocks are overlain by basin infill that generally includes the Plio-Pleistocene, non-marine alluvial, fluvial, and volcanic deposits (including the Sandy River Mudstone and Troutdale Formation in both basins, and the Rhododendron Formation, Low-Potassium Tholeiitic flows, and Springwater Formation within the Portland Basin), Pliocene-Pleistocene Boring Lava, and the typically thick deposits of the late Pleistocene Missoula Flood deposits (e.g., Popowski, 1996; Yeats and others, 1996; Wilson, 1996; 1998; O'Connor and others, 2001; Evarts and others, 2009; Ma and others, 2012; Wells and others, 2020b).

7.2.3.3.2 Quaternary Faults Near the Bridge Site

The bridge site is located within 150 km of at least 20 crustal faults that are suspected of rupture during the Quaternary. Ten of these faults are mapped within 50 km of the project, including three faults located within 10 km of the bridge: the Portland Hills fault, the East Bank fault, and the Sylvan-Oatfield fault. This seismic source model includes faults with sufficient documented geologic evidence to infer Quaternary tectonic deformation attributed to these faults, and they are capable of producing at least a M_W 6.5 earthquake. All faults included in this seismic source model have also been included in the USGS QFFD and/or NSHM. Since there have been several iterations of the NSHM (e.g., 2002, 2008, and 2014), faults included in the 2014 NSHM and the preliminary 2023 NSHM are considered here. Although Petersen and others (2014) and Hatem and others (2021) do not explicitly describe which criteria individual faults met to be included in the 2014 NSHM and 2023 NSHM, based on available research, we infer that the faults with the best supporting evidence for Quaternary deformation are included in their model. There are other possible Quaternary-active faults within 150 km, but either they are not considered capable of generating a M_W 6.5 earthquake and would thus be included in the seismic background, and/or evidence for Quaternary activity is highly uncertain and thus are not considered a Class A fault (USGS, 2006).

A summary of the evaluated faults is provided in Table 7-2, the locations of their surface traces relative to bridge site are show in Figures 7-9 and 7-10, and the source parameters used in the PSHA are shown in Table 7-3. In Table 7-3, the first column summarizes possible Quaternary tectonic activity that has been documented by geologic and/or geophysical studies along these faults. Only faults with definitive studies that have conclusively identified Holocene deformation along these faults are assigned a seismic activity weighted value of 1.0. These faults include: the Gales Creek fault zone, the Mt Hood fault zone, and the White Branch fault. Other faults are inferred to be Quaternary

active, but likely older than late Pleistocene to Holocene, and are assigned seismic activity values of less than 1.0. Given the poor constraints of earthquake timing, very low (generally <0.2 mm/yr) slip rates are inferred for nearly all faults listed in Table 7-3. One exception is the Gales Creek fault zone, which has an inferred slip rate of up to 0.6 mm/yr (Horst and others, 2020; Wells and others, 2020a). Some of the confounding geologic factors noted by the sources cited in Table 7-2 include the following:

- Inability to date stratigraphic deposits in field exposures, or age estimates are inconclusive
- Seismic or other geophysically-identified deformed strata cannot be confidently correlated to strata of known ages
- Potential fault-deformed geomorphic features (e.g., stream channels or terraces and topographic scarps and escarpments) cannot be conclusively dated and/or attributed to a specific fault; or they are absent entirely
- Faulted surfaces have been eroded away and/or covered by thick Missoula Flood deposits or obscured by human development

The last factor has been particularly pernicious throughout the region due to the Late Pleistocene Missoula Floods scouring away tens of meters or more of sediment and rock from the paleo-ground surface and leaving behind a thick blanket of fluvial deposits (e.g., Liberty and others, 2003; O'Connor and others, 2001; Waitt, 1985) that mantles valleys and hillsides up to around elevation 400 feet (Benito and O'Connor, 2003; Burns and Coe, 2012). As a result, shallow Pleistocene deformation may have been erased from the stratigraphic record. Two exceptions are the Gales Creek fault zone and the Mt Hood fault zone (Table 7-2). Paleoseismic trenches excavated across multiple LiDAR-identified topographic lineaments within the Gales Creek fault zone have indicated that the fault zone was last active during the late Holocene (Horst and others, 2020; Wells and others, 2020). Work by Horst and others (2020) along the Parsons Creek fault strand documented three Holocene ground surface ruptures. They determined an average recurrence interval of 4 ka, which generally agrees with the long-term slip rate of 0.6 mm/yr from Wells and others (2020a). Madin and others (2017) and Bennett and others (2021) determined that multiple en echelon scarps that span between the edifice of Mount Hood and the Hood Canal were generated during Holocene earthquakes that ruptured glacial deposits and young lava flows. For most other faults in this model, evidence for post-Pleistocene deformation is lacking, which suggests that the faults have not been active during Holocene, the Missoula Flood deposits are poor stratigraphic recorders of earthquakes, and/or surface-deformation features are subdued to the point of being indistinct from the rest of the landscape. Liberty and others (2003) propose a possible alternative explanation: because many of the faults may have strong strike-slip components, such as the Portland Hills faults, geomorphic expression of faulting, such as fault scarps, might not be expected to develop at the ground surface.

Lateral motion combined with low slip rates might generate subtle deformation features such as disrupted drainages (e.g., Givler and others, 2009; Bemis and Wells, 2012). Other faults that could potentially fall into this category include the Canby-Molalla, Gales Creek, Mount Angel, Lacamas Lake, and Sandy River faults (Table 7-2).

Given the rarity of fault exposures and geomorphic expressions of surface deformation, researchers have augmented field studies with subsurface exploration methods to image potential shallow fault deformation, to identify the deeper extents of the faults, and to map fault lateral extents using well data, seismic reflection, gravity, and other geophysical exploratory methods (Table 7-2) (e.g., Popowski, 1996; Yeats and others, 1996; Wilson, 1998; Blakely and others, 1996; 2000; 2004; Pratt and others, 2001; Liberty and others, 2003; McPhee and others, 2014). The faults listed in Table 7-2 are relatively well-expressed in seismic reflection data and as gravity and magnetic anomalies. In general, these anomalies mark offset CRBG or underlying Eocene Siletz oceanic rocks, which have strong magnetic and gravity signatures when juxtaposed against the younger valley fill and they yield long-term slip rates (e.g., Beaverton fault, the Portland Hills fault zone, the Canby-Molalla fault, the Mount Angel fault, the Gales Creek faults, the Grant Butte fault, and the Sandy River fault) (e.g., Blakely and others, 2000; Wells and others, 2020a, 2020b). Possible offsets of the younger mid-Pleistocene Hillsboro Formation and the early-mid Pleistocene Boring Lava have been imaged in borehole mapping and high-resolution seismic surveys across the following faults (Table 7-2): the Beaverton fault, the Helvetia fault, the Sylvan-Oatfield fault, the Grant Butte fault, and the Lacamas Lake fault (e.g., Popowski and others, 1996; Yeats and others, 1996; Wilson, 1997). Because overlying Missoula Flood deposits do not appear to be deformed, it can be inferred that these faults likely have not been active since the early-mid Pleistocene. Several studies have attempted to use high-resolution seismic surveys to identify deformed Missoula Flood deposits across the Portland Hills fault, the East Bank fault, the Canby-Molalla fault, and the Mount Angel fault (Table 7-2) (Pratt and others, 2001; Blakely and others, 2002; Givler and others, 2009). However, positively attributing these features to fault deformation (as opposed to fluvial depositional structures) and verifying the deposit ages by field studies remain unsettled.

Given that there is a paucity of conclusive evidence for recent (< late Pleistocene) rupture along nearly all of the faults located near the project site, slip rates are generally low (< 0.2 mm/yr), some one to two orders of magnitude lower for faults where the last rupture, largely based on geophysical subsurface data, is highly uncertain or inferred to be early-mid Quaternary (e.g., Newberg fault, Helvetia fault, Bolton fault, Beaverton fault). We generally used the same slip rates used in the QFFD or the 2014/2023 NSHM (Table 7-3), except for the faults that had additional data that indicated other rates, either higher (e.g., Gales Creek fault zone, White Branch fault, Willapa Bay fault zone), or lower (many, including the Portland Hills fault, Beaverton fault, Mount Angel fault, etc.). The Beaverton fault slip rates

of 0.01-0.2 mm/yr are based on estimates of 200-350 m of offset of the Hillsboro Formation across the fault (Popowski, 1996; Wilson, 1997; McPhee and others, 2014). Slip rates of 0.05-0.2 mm/yr for the Canby-Molalla fault reflect a range of possible lateral and vertical slip of the CRBG along and across the fault. We inferred possible slip estimates of around 0.05-0.2 mm/yr for the Sylvan-Oatfield fault based on mapping of the fault while exposed in a tunnel excavation and high-resolution gravity studies (Blakely and others, 2004; Walsh and others, 2011; McPhee and others, 2014; Wells and others, 2020a). Because the Sylvan-Oatfield fault is inferred to be structural linked and/or kinematically related to the Portland Hills fault and possibly the East Bank fault (e.g., Blakely and others, 1995; McPhee and others, 2014; Wells and others, 2020b), we distributed these the slip rates across the three faults. Sources for parameters for these faults are listed in Table 7-2; source parameters used in the PSHA are listed in Table 7-3.

7.2.3.4 Regional Shallow Crustal Background Sources

Areal source zones account for background (floating or random) earthquakes that are not attributed to known faults specifically included in this seismic source model. We adapted the 2014 NSHM spatially varying background seismicity grids with two separate modeling algorithms, fixed-smoothing and adaptive-smoothing, with weighting factors of 0.6 and 0.4, respectively. The seismicity rates were spatially smoothed to account for uncertainties in the locations of earthquakes with two-dimensional Gaussian function. For the fixed-smoothing grid, the smoothing was performed within a fixed 50-km distance, but for the adaptive-smoothing grid, the smoothing was performed with a variable distance depending on the spatial density of the seismicity in the earthquake data.

For the crustal background model, we used the 2014 NSHM spatially varying rate model, including a maximum magnitude, a single seismogenic thickness of 14 km, and m_{min} and b-value. These crustal background source parameters were obtained from the 2014 NSHM within 150 km of the bridge site.

Figure 7-11 shows the crustal background logic tree, mainly consistent with the 2014 NSHM, used in our PSHA.

7.2.4 Ground Motion Model

The GMMs describe the distribution of ground motion amplitude parameters (typically pseudo-spectral acceleration) as a function of seismological parameters (such as magnitude and source-to-site distance) and site subsurface condition, typically expressed as the time averaged shear wave velocity in the upper 30 m of the soil/rock profile, or V_{S30}. We used a V_{S30} of 760 meters per second (m/sec) (approximately, 2,500 feet per second [fps]), which

corresponds to AASHTO Site Class B/C boundary conditions. This V_{S30} / Site Class were used to be consistent with the 2D FLAC model boundary conditions (see Section 8.1.1.1).

The standard deviation function for each GMM provides the aleatory variability of the dataset used to develop the equation. While there are some inherent epistemic uncertainties associated with a given GMM, we used multiple GMMs to better capture these uncertainties.

7.2.4.1 Cascadia Subduction Zone Ground Motion Models

Three GMMs were recently developed and published as part of the Pacific Earthquake Engineering Research Center (PEER) NGA-Sub zones based on global subduction seismic database with region-specific features applicable to several subduction regions in the world, including the CSZ (Kuehn and others, 2020; Parker and others, 2020; Abrahamson and Gülerce, 2020). Because of the significance of the subduction GMMs in assessing the seismic hazard in the Pacific Northwest, Shannon & Wilson worked with WSDOT and its designated peer reviewer (Kenneth Campbell) to evaluate the suitability of these GMMs and developed a computer code for NGA-Sub GMMs to be used in regional PSHAs. A few revisions confirmed by the modelers were made to the NGA-Sub GMMs since the PEER reports were published. The revisions were validated by running and comparing the performance of the revised models used in this study with those provided by Ken Campbell. The NGA-Sub review process included evaluation of the estimated median spectral acceleration values, and within- and between-event variabilities for various scenario events in the Pacific Northwest. These peer-reviewed NGA-Sub implementations were used for the project site.

The three GMMs used in this study for both subduction interface and subduction intraslab include:

- Kuehn and others (2020) (KBCG20)
- Parker and others (2020) (PSBAH20)
- Abrahamson and Gülerce (2020) (AG20)

A fourth NGA-Sub GMM was also recently developed under the PEER NGA-Sub program (Si and others, 2020 [SMK20]) based solely on the Japanese ground motion database. Therefore, we believe the applicability of SMK20 is limited to subduction zone earthquakes in Japan; the SMK20 was not considered in our seismic hazard study. We anticipate the suite of three GMMs used in this PSHA will be also adopted by the USGS for the future edition of the NSHM.

We understand that the ground motion database used for developing the above GMMs includes only a few small ($M_W < 5$) subduction interface earthquakes from CSZ and Cascadia. Each of the three NGA-Sub GMMs selected for this PSHA uses its own unique procedure and assumptions to predict the ground options for the larger magnitude earthquakes in Cascadia region. Since there is no strong evidence to prefer one model over the others at this time, we equally weighted all three NGA-Sub models in our analysis.

An approach similar to the method proposed by Al Atik and Youngs (2014) was used to incorporate within-model epistemic uncertainty (σ_ε) of the NGA-Sub GMMs in our analyses. However, there are three main issues in using the NGA-Sub σ_ε in the PSHA:

- Only KBCG20 offers within-model σ_ε,
- The KBCG20's within-model σ_ε varies with earthquake scenario, and
- The within- and between-model σ_ε are not independent.

The epistemic model included in PSBAH20 PEER report is a between-regional-model variation and is based on distribution of the application region (Cascadia region in our case) constant term estimated from other PSBAH20's regional model's constant term. The PSBAH20's regional models include: Global, Aleutian Islands, Alaska, Cascadia, Central America (North), Central America (South), Japan-Pacific, Japan-Philippine Sea, South America (North), South America (South), and Taiwan regions. The PSBAH20's between-regional-model variation is limited to constant term variation and does not include variation for other regional coefficients. While the PSBAH20's between-regional-model σ_ε partially contains the PSBAH20's within-model σ_ε, the variation for all the constants, regional or non-regional coefficients, is needed for a complete within-model σ_ε estimate.

Also, we understand that the AG20 offers no σ_ε for Cascadia sites. To this end, the KBCG20's period-dependent within-model σ_ε was estimated deterministically (i.e., using characteristic magnitude, source-to-site distance, and Pacific Northwest basin term appropriate for the site), and the median ground motion estimates from all three NGA-Sub GMMs were adjusted by the KBCG20's within-model σ_ε. We understand that using this type of within-model σ_ε is an approximate solution for applying within-model σ_ε to each of the thousands of probabilistic scenarios within the PSHA. We used M_W 8.9, source-to-site distance of 129 km, depth to top of the rupture of 5 km, and depth to 2.5 kilometers per second (km/sec) shear wave velocity of 2.1 km (0.7 weight) and 0.5 km (0.3 weight) for interface earthquakes, and M_W 7.0, source-to-site distance of 59 km, depth to top of the rupture of 50 km, and depth to 2.5 km/sec shear wave velocity of 2.1 km (0.7 weight) and 0.5 km (0.3 weight) for intraslab earthquakes to estimate the within-model σ_ε at the site. In the PSHA, we assigned a weight factor of 0.63 to the median ground motion (i.e., corresponding to 50th percentile ground motion) and median ± 1.645σ_ε (corresponding to 5th and 95th

percentile ground motions) with a weight factor of 0.185 for both the 5th and 95th percentile ground motions. This method is based on a conservative assumption of independent within-model and between-model σ_ε variables.

The GMM logic tree for the CSZ (both interface and intraslab) is shown in Figure 7-12.

7.2.4.2 Shallow Crustal Ground Motion Models

A larger number of GMMs are available for shallow crustal earthquakes. Selection of appropriate GMMs for the PSHA involves consideration of the similarity between the database used in the development of a given GMM and the shallow crustal sources in the Pacific Northwest, and range of the periods over which the GMM provides predictions.

Consistent with the 2018 NSHM, we used the following four empirical GMM models developed by the PEER Next Generation Attenuation Relationships for Western US (NGA-West2) project to model the shallow crustal earthquake horizontal ground motion attenuation:

- Abrahamson and others (2014) (ASK14)
- Boore and others (2014) (BSSA14)
- Campbell and Bozorgnia (2014) (CB14)
- Chiou and Youngs (2014) (CY14)

The NGA-West2 GMMs are the latest update to the 2008 NGA-West GMMs. Among the key changes in the NGA models are that the strong ground motion dataset was expanded significantly, and regional site and path effects were incorporated in the models. Each of the NGA-West2 GMMs incorporates V_{S30} as a shallow site-response parameter. These models were weighted equally and are consistent with those used in the 2018 NSHM.

Similar to subduction GMMs, the approach proposed by Al Atik and Youngs (2014) to incorporate epistemic uncertainties for the NGA-West2 crustal shallow GMMs was used in our analyses. The median ground motion estimates from the GMMs were adjusted for within-model σ_ε values provided by Al Atik and Youngs (2014) for NGA-West2 models. In the PSHA, we assigned a weight factor of 0.63 to the median ground motion (i.e., corresponding to 50th percentile ground motion) and median ± $1.645\sigma_\varepsilon$ (corresponding to 5th and 95th percentile ground motions) with a weight factor of 0.185 for both the 5th and 95th percentile ground motions, consistent with the Al Atik and Youngs (2014) uncertainty model.

The GMM logic tree for crustal sources is shown in Figure 7-13.

7.2.4.3 Intensity Measure of Ground Motion Models

The NGA-West2 GMMs' predicted ground motion values used in this study are 5% damped RotD50 pseudo-spectral acceleration (PSA). RotD50 is 50th percentile (median) of the rotated orientation-independent, period-dependent, combined horizontal components as defined by Boore (2010). Among the NGA-Sub GMMs, the AG20's predicted median ground motion is 5% damped RotD50 PSAs. Two other NGA-Sub GMMs (KBCG20 and PSBAH20) also predict the 5% damped PSAs, but the intensity measure for their provided ground motions is not clear from their PEER reports. However, we could confirm with one of the authors of the KBCG20 model (Ken Campbell) that the RotD50 is the ground motion that is provided by all the NGA-Sub GMMs used for this study.

7.2.4.4 Portland Basin Effects

Ground motions may be amplified within a geologic sedimentary basin, such as the Portland Basin, due to a number of complicated mechanisms (e.g., waves trapped within the basin when post-critical incidence angles develop and the focusing of seismic energy in spatially restricted areas on the surface). The three NGA-Sub GMMs and four NGA-West2 GMMs used in this study include basin response terms, and the basin effects were incorporated in our PSHA by assigning appropriate values to the basin terms. Specifically, the GMMs use one of two sediment depth parameters to model basin effects:

- $Z_{1.0}$, depth to subsurface material with a shear wave velocity of 1 km/sec, and
- $Z_{2.5}$, depth to subsurface material shear wave velocity of 2.5 km/sec.

The basin term for three of the NGA-West2 GMMs (ASK14, BSSA14, and CY14) uses the $Z_{1.0}$ basin depth parameter. However, the CB14 and three NGA-Sub GMMs (Cascadia model) use the $Z_{2.5}$ basin depth parameter. Among the NGA-Sub GMMs, the PSBAH20 developed Pacific Northwest (PNW)-specific basin term for sites within the Everett, Portland, Tacoma, Tualatin, Georgia, and North Willamette basin boundaries. We used the PNW-specific basin term of the PSBAH20 in our PSHA. The KBCG20 and AG20 do not include a basin term for the Portland Basin; however, they include Cascadia specific basin response, which we applied in our analysis.

We performed a parametric study and evaluated the sensitivity of the NGA-Sub GMMs spectral acceleration values given V_{S30} value of between 200 and 760 m/sec and $Z_{2.5}$ value of between 0.1 and 2.1 km and discussed the results in a check-in meeting with the HDR and the review team. Based on our discussion, we agreed to obtain the basin depth parameters for our analyses from two independent sources:

- Stephenson and others (2017) 3D community velocity model (CVM) developed for the PNW ($Z_{1.0}$ = 0.12 km, $Z_{2.5}$ = 2.1 km); and

- Shear wave velocity at the soil profile along the project alignment with the top of the CRBG estimated at 500 feet below ground surface ($Z_{1.0}$ = 0.15 km, $Z_{2.5}$ = 0.5 km).

Given that the Stephenson and others (2017) CVM has been used as a basis for the basin amplification of PNW sites in the NGA-Sub GMMs database, the NGA-Sub GMMs are expected to be mainly calibrated with the $Z_{2.5}$ values estimated from Stephenson and others' (2017) CVM. For this reason, we gave a weight factor of 0.7 for the basin depths estimated from Stephenson and others (2017) CVM and slightly less than half of that (0.3 weight factor) for the basin depths consistent with the typical shear wave velocity and estimated depth to Columbia River Basalt at the site. The logic tree for basin term parameters used in our analyses is shown in Figure 7-14.

7.2.5 Probabilistic Seismic Hazard Analysis Results

From the PSHA, we calculated hazard curves for the individual seismic sources, mean Uniform Hazard Spectrum (UHS) derived from the hazard curves, and developed ground motion hazard deaggregation by source, magnitude, and source-to-site distance. For some mean annual rates of exceedance (or ground motion return periods) and spectral periods, the ground motion hazard may come predominantly from a single, specific seismic source; at other exceedance rates/return periods and structural periods, the predominant source may change, or multiple sources may be significant contributors to the ground motion hazard. The contribution to ground motion hazard by various sources informs the selection and development of earthquake time histories and is therefore presented below.

7.2.5.1 Mean Uniform Hazard Spectrum

The horizontal mean UHS from the site-specific PSHA analysis for 1,000-year return period ground motion is plotted in Figures 7-15 and 7-27. The UHS is the sum of the hazards from various seismic sources included in the seismic source characterization model. The ordinates of the UHS are the pseudo spectral acceleration values from the various seismic sources with a specific probability of exceedance in a given time span corresponding to a return period. We obtained the mean UHS for the 5% damping pseudo-spectral acceleration values for RotD50 component.

For comparison, the mean UHS for 1,000-year return period from the 2014 and 2018 NSHM is also shown in Figure 7-15 for the same site condition (i.e., AASHTO Site Class B/C boundary, or V_{S30} of 760 m/sec). The spectral acceleration ratios between our ground motions and those from the NSHMs are also plotted in Figure 7-16. As observed from these figures, our calculated 1,000-year ground motions for long periods (i.e., periods > ~1.0 second) are lower than the 2014 and 2018 NSHM. However, for short periods (i.e., periods < ~1.0 second), our calculated 1,000-year ground motions are greater than the 2014 and 2018

NSHM. As shown in Figure 7-16, within the 0.25- to 2-second period range of interest (see Section 7.5.1.1), our mean UHS value is 14% higher at 0.25 second and 7% lower at 2.0 seconds than the 2018 NSHM. Our mean UHS is also 7% higher and 7% lower than the 2014 NSHM at the same periods. The main factors that account for the differences between the spectra include:

- Inclusion of additional nearby crustal faults in our seismic source model, and updating existing faults geometries, slip rates, and probability of activities;
- Using the recently published NGA-Sub GMMs that were not available for 2014 and 2018 NSHM;
- Including the site-specific basin depth parameters in our PSHA calculations; and
- Differences in implementation of sources and GMMs between the computer codes used to perform the PSHA calculations.

7.2.5.2 Hazard Curves

The hazard curves for horizontal ground motion versus mean annual rate of exceedance or return periods from the PSHA are presented in Figures 7-17 through 7-26 for peak ground acceleration (PGA), 0.25-, 0.5-, 1.0-, and 2.0-second periods.

The hazard curve plots are provided first for discretely modeled crustal faults in Figures 7-17 through 7-21 and then shown for combined crustal faults, crustal background, CSZ interface, and CSZ intraslab in Figures 7-22 through 7-26. The sum of the hazard curves from all the sources was included in each plot (black curves). For comparison, the total hazard curve is also included in discretely modeled crustal faults plots (gray curve). In these figures, the difference between the total hazard curve and the total crustal faults is the hazard contribution from other seismic sources. For instance, in Figure 7-18, the difference between total hazard curve and total crustal fault is the combined contribution from crustal background, CSZ interface, and CSZ intraslab sources at 0.25-second period.

The hazard curves for the discrete crustal faults show that the Sylvan-Oatfield fault zone (SOFZ) is the dominant individual fault contributor to the ground motion hazard for a return period of 1,000 years (mean annual exceedance of approximately 0.0004) with a slightly lesser but still significant contribution from the Portland Hills fault (PHF) and East Bank fault (EBF). The hazard contribution of the Bolton fault (BF) is about equal to the PHF and EBF at periods 0.25 and 0.5 second (Figures 7-18 and 7-19), but it decreases quickly at longer periods of 1.0 and 2.0 second (Figures 7-20 and 7-21).

Figures 7-22 through 7-26 show that the contribution of the CSZ interface source increases with increasing period and becomes the dominant contributor for a period of 1.0 second and greater. However, the CSZ interface contribution for short periods (e.g., 0.25-second) is less

than the hazard contribution from the combined crustal sources. Also, Figures 7-22 through 7-26 show that while the CSZ intraslab hazard contribution is lower than the crustal and CSZ interface for periods between 0.25 and 2.0 seconds, it is nevertheless a significant contributor to the ground motion hazard towards the lower bound of the period range of interest and should be considered in selecting the input ground motion time histories.

7.2.5.3 Hazard Deaggregations

Deaggregation results for the mean 1,000-year return period are shown in Appendix F, Figures F-1 through F-5. These figures show the hazard contribution for different combinations of magnitude and source-to-site distance. The deaggregation results are presented in terms of magnitude and source-to-site distance versus ground motion hazard for PGA and periods 0.25, 0.5, 1.0, and 2.0 seconds. Tabulated in each of these figures are the mean magnitude, mean distance, and mean ground motion epsilon. For a given set of fault parameters (e.g., fault type, magnitude, and source-to-site distance) and GMM, the ground motion epsilon is the number of standard deviations a particular ground motion is above the mean ground motion. Also, tabulated in these figures is relative hazard contribution by source. In these figures, the height of the vertical columns corresponds to the proportion of the total ground motion hazard contributed by various combinations of earthquake magnitude and distance. For instance, in Figure F-5, earthquake sources with M_W ranging from 9.2 to 9.4 and rupture distance from the site ranging from 75 to 100 km (i.e., the tallest bars) contribute the most to the 1,000-year 2.0-second ground motion hazard at the site. The significant contribution from the CSZ interface can be seen from this figure by the relatively tall bars between magnitudes ranging from 8.6 to 9.4 and distances ranging between 75 and 150 km.

For the 1,000-year horizontal ground motion hazard and over the range of periods between 0.25 and 2.0 seconds (Figures F-2 through F-5), the mean magnitude ranges from 7.0 to 8.1, mean source-to-site rupture distance ranges from 40 to 80 km, and epsilon ranges from about 0.61 to 0.65. A positive epsilon value indicates that the spectral acceleration that is consistent with the return period, on average, is higher than the GMM predicted median ground motion. The mean epsilon value of 0.65, for instance, corresponds to an average of median plus 0.65 standard deviation for GMMs used in the PSHA.

7.2.6 Near-Fault Effects

For sites within 6 miles (10 km) of an active surface or a shallow fault, as identified by the USGS, AASHTO requires studies be considered to quantify near-fault effects on ground motions to determine if these could significantly influence the bridge response. ASCE 7-16 has similar requirements, but notes that if a fault has an estimated slip rate of less than 1 mm/yr, consideration of near-fault effects is not required, presumably because the

contribution of these faults to the overall ground motion is limited. Among the faults in our source model, the PHF, EBF, and SOFZ are located within approximately 10 km of the site and are capable of creating characteristic earthquakes of up to M_W 7 (see Table 7-3). The estimated "best value" slip rate in our model is in the order of 0.1 mm/yr for these faults. As can be seen from the hazard and deaggregation plots, the relative hazard contribution from any one of these faults is relatively low. Therefore, we did not consider additional near-fault effects for the ground motions to be used in the 2D FLAC analyses.

7.3 Deterministic Seismic Hazard Analysis for CSZ Interface

For the FODE level ground motion hazard, we calculated a deterministic spectrum for the CSZ interface mega-thrust event. We developed the 5% damping 50th percentile response spectrum (i.e., median) for the CSZ interface generating a characteristic type of the event with a full rupture along the source.

Epistemic uncertainties in seismic source characterization are reflected in the logic tree weights of the PSHA. However, in the deterministic approach, a characteristic earthquake can be identified by selecting the most likely or "best estimate" for each source parameter (i.e., fault type, location, geometry, maximum magnitude, and source-to-site distance). The source parameters that are given the highest weight in PSHA are considered the most likely in defining the characteristic earthquake for the deterministic analysis. Based on our CSZ interface logic tree PSHA, we identified CSZ interface characteristic earthquake as M_W 8.9 with the rupture-to-site distance of 129 km. These parameters correspond to the values given the highest weighting or "best estimate" in the PSHA CSZ interface logic tree.

Consistent with our PSHA, we used the same set of the GMMs to calculate the 50th percentile deterministic spectra. We also used the same $Z_{1.0}$ and $Z_{2.5}$ basin parameters and V_{S30} values. The 50th percentile deterministic CSZ interface spectrum is plotted in Figure 7-27.

7.4 Seismic Hazard Level Spectra

Response spectra for AASHTO Site Class B/C boundary conditions for both LODE and FODE levels are shown in Figure 7-27. The spectra were developed for Site Class B/C boundary to be consistent with the 2D FLAC model boundary conditions (see Section 8.1.1.1). The spectral acceleration values for Site Class B/C boundary LODE and FODE ground motion levels are tabulated in Exhibit 7-1.

Exhibit 7-1: Spectral Acceleration Values (in g's) for Site Class B/C Boundary LODE and FODE Ground Motion Levels

Period (seconds)	LODE	FODE
0.01	0.282	0.073
0.02	0.290	0.075
0.03	0.322	0.080
0.05	0.410	0.095
0.075	0.526	0.109
0.1	0.596	0.119
0.15	0.654	0.135
0.2	0.630	0.143
0.25	0.579	0.145
0.3	0.524	0.144
0.4	0.434	0.140
0.5	0.375	0.133
0.75	0.270	0.114
1	0.204	0.093
1.5	0.130	0.068
2	0.100	0.054
3	0.058	0.0339
4	0.0408	0.0247
5	0.0311	0.0201
7.5	0.0199	0.0126
10	0.0130	0.0087

7.5 Input Bedrock Ground Motions

Two suites of ground motion time histories were selected and scaled for LODE and FODE levels following the AASHTO LRFD Bridge Design Specifications and project specific seismic criteria (HDR, 2021b). Each suite consists of nine (for LODE level) or seven (for FODE level), single horizontal component time histories for a total of 16 time histories.

The following subsections describe the method that we utilized to select and develop the time histories for LODE and FODE levels.

7.5.1 Limited Operation Design Earthquake Level - Probabilistic 1,000-Year Spectrum

We developed the target spectra to select the time histories for LODE level based on the probabilistic 1,000-year mean UHS. A separate target spectrum was calculated for each of the crustal, CSZ interface, and CSZ intraslab sources contributing to the hazard. The LODE target spectra were calculated using Conditional Mean Spectrum developed for each of these sources.

7.5.1.1 Period Range of Interest

Because the time histories will be used in the 2D FLAC analyses to evaluate the stability and displacements of the riverbanks, the period range of interest is based on the fundamental period of the soil profiles that underlie the banks. Based on the shear wave velocities of the soils that underlie the riverbanks (see Section 8.1.2.1) the period range of interest ranges from 0.25 to 2.0 seconds.

7.5.1.2 Conditional Mean Spectra

Baker and Cornell (2006) suggest that a UHS may not be suitable for selection and development of spectrum-compatible time histories to be used in dynamic response analysis. Using a UHS as a target spectrum requires that large amplitude spectral values for all periods occur in one individual time history. This requirement may be unrealistic with regard to actual recorded ground motions and time histories generated by real earthquake sources that contribute to the UHS, particularly when significant contributions come from more than one earthquake source. Consequently, spectral matching or scaling to a UHS may result in unrealistic time histories for a given site. The Conditional Mean Spectrum (CMS) provides a rational method to develop a target spectrum that matches the UHS at the period range of interest (i.e., a spectrum conditioned on the occurrence of the spectral value at the period of interest) that is more representative of ground motions from an actual earthquake source.

We used method 4 from Lin and others (2013) to develop probabilistic CMS considering associated aleatory and epistemic uncertainties included in the PSHA model. Selection of the seismic source parameters (e.g., magnitude, distance, focal depth, hanging wall effect, rupture style) for CMS calculation can be subjective when there is a wide range of sources or alternative source parameters. Unlike a deterministic CMS that uses a single set of seismic parameters (i.e., a scenario event), the probabilistic CMS is an aggregate of the seismic parameters used in the PSHA model. A CMS was calculated for each branch of the PSHA logic tree. Then, the probabilistic CMS was taken as the aggregate of the CMS from each

logic tree branch using the weighting factor for each branch. The probabilistic CMS can be provided for a specific source or a group of sources with some common characteristics.

We developed the CMS for the LODE level ground motion hazard conditioned at spectral periods 0.3, 0.5, 0.75, 1.0, and 1.5 seconds using the procedure outlined in Baker (2011). The CMS are typically developed for seismic sources with significant contribution to the ground motion hazard. Evaluation of the deaggregation plots (Appendix F, Figures F-1 through F-5) shows that the seismic hazard at the site is the result of hazards from crustal faults, crustal background, CSZ interface, and CSZ intraslab sources. Therefore, the CMS were calculated separately for each of these sources. However, because the crustal time histories will be developed as representative of both crustal faults and crustal background sources, we probabilistically combined the crustal faults and crustal background CMS to create the crustal CMS, which are applicable for both types of crustal sources.

Figures 7-28 through 7-30 present the calculated CMS for crustal, CSZ interface, and CSZ intraslab sources, respectively.

7.5.1.3 Target Spectra

Following the completion of the PSHA, CMS, and conditioned periods required for target spectra development were reviewed at a check-in meeting with HDR and the review team. In the meeting, we agreed that the required ground motion for time history development will be designated as probabilistic CMS conditioned at 0.5 and 1.0 second periods (i.e., the range of fundamental periods for horizontal direction response of the bridge site riverbanks) for each of the crustal, CSZ interface, and CSZ intraslab sources. In assessing the suitability of the target spectrum, we applied the criterion that within the period range of interest (i.e., 0.25 to 2.0 seconds) the target spectrum should be at a minimum 75% of the horizontal mean UHS. These target spectrum criteria were loosely adopted from American Society of Civil Engineers (ASCE) 7-16 (2017).

We developed the target spectra for 1,000-year return period using the following method:

The target spectrum is equal to (T denotes spectral period in seconds):

- CMS conditioned at 0.5 second for $T<0.25$
- Maximum of 75% of mean UHS and CMS conditioned at 0.5 second for $0.25 \leq T<0.5$
- Mean UHS for $0.5 \leq T \leq 1.0$ second
- Maximum of 75% of mean UHS and CMS conditioned at 1.0 second for $1.0<T \leq 2.0$
- CMS conditioned at 1.0 second for $2.0<T$

As needed, we smoothed the target spectrum between the UHS to 75% of UHS, and 75% of UHS to the CMS. The smoothing included linear interpolation (in log-log space) of the ratio between starting period spectral value over end period spectral value.

The target spectra developed based on the above method are shown in Figures 7-28 through 7-30 and tabulated in Exhibit 7-2.

Exhibit 7-2: Spectral Acceleration Values (in g's) for LODE Level Source-Specific Target Spectra

Period (seconds)	Crustal	CSZ Interface	CSZ Intraslab
0.01	0.271	0.170	0.200
0.02	0.277	0.175	0.207
0.03	0.303	0.187	0.221
0.05	0.373	0.217	0.266
0.075	0.465	0.240	0.308
0.1	0.525	0.266	0.337
0.15	0.610	0.342	0.416
0.2	0.611	0.399	0.463
0.25	0.574	0.434	0.472
0.3	0.527	0.424	0.455
0.5	0.375	0.375	0.375
0.75	0.270	0.270	0.270
1	0.204	0.204	0.204
1.5	0.113	0.133	0.110
2	0.075	0.098	0.075
3	0.0379	0.055	0.0286
5	0.0158	0.0294	0.0101
7.5	0.0073	0.0171	0.00416
10	0.00418	0.0112	0.00214

7.5.1.4 Distribution of Time Histories in Suite of Ground Motions

We used deaggregation data from the PSHA to determine the number of time histories in the suite of ground motions for each of the significant contributors to the seismic hazard over the period range of interest. A summary of the seismic hazard contribution for LODE level (i.e., 1,000-year return period) is tabulated in Exhibit 7-3.

Exhibit 7-3: Hazard Contribution (in Percent) for Seismic Sources

Period (seconds)	Crustal	CSZ Interface	CSZ Intraslab
0.25	63	25	12
0.3	61	27	12
0.5	52	37	11
0.75	45	46	9
1	41	51	8
1.5	35	59	6
2	29	66	5

As can be seen from Exhibit 7-3, the hazard contribution from seismic sources varies with the period. The number of time histories needed for each of source type was discussed in our check-in meeting with HDR and the review team. In the meeting, it was agreed that the required number of time histories for each of the sources would be three and that the results of the analyses with these time histories would be "averaged" by the relative contribution of a given source to the total hazard within the period range of interest. Based on the hazard contributions in Exhibit 7-3, the weighting given to each set of source-specific time histories is shown in Exhibit 7-4.

Exhibit 7-4: Time History Weighting by Seismic Source

Period Range of Interest (seconds)	Crustal	CSZ Interface	CSZ Intraslab
0.25 - 2.0	0.45	0.45	0.10

7.5.2 Full Operation Design Earthquake Level - Deterministic CSZ Interface Full Rupture Spectrum

The target spectrum for the FODE level is the 50th percentile deterministic CSZ interface full rupture event. This spectrum is shown in Figure 7-27.

7.5.3 Time History Selection

Candidate reference time histories (i.e., seed motions) were selected for consistency with the magnitude, distance, site conditions, acceleration response spectrum shape, and tectonic regime of the seismic sources that were identified by the deaggregation data for period 0.5 to 1.0 second.

We reviewed the PEER NGA-West2 project dataset for candidate crustal earthquake time histories. A significant number of previously processed (filtered and/or baseline corrected)

records are available for crustal events through the PEER center and in most of the cases, no additional processing is needed for these records.

There are relatively few recorded large-magnitude subduction interface or medium-magnitude subduction intraslab earthquakes. There are no recorded CSZ interface earthquakes in modern history, and our time history selection was limited to areas with similar active subduction zone (e.g., South America, Japan). For CSZ interface and CSZ intraslab events, we reviewed South American, Center for Engineering Strong Motion Data, National Strong Motion project, K-NET (Kyoshin network), and KiK-net (Kiban Kyoshin network) datasets to select the appropriate time histories. We also considered M9 Project dataset for the CSZ interface time histories simulated at the location of the Burnside Bridge. Some of the time histories in these datasets are either uncorrected (raw data) or often corrected such that it might affect the time histories in the period range of interest. Thus, we processed (filtered and/or baseline corrected) each selected seed time history from these datasets when needed.

For the LODE level, the selected ground motion sets of the time histories for crustal sources, the CSZ interface, and CSZ intraslab sources are tabulated in Exhibits 7-5, 7-6, and 7-7, respectively. For the FODE level, all the time histories are for CSZ interface and are tabulated in Exhibit 7-8.

Exhibit 7-5: Selected LODE Level Crustal Time Histories

Mechanism	Reverse	Reverse Oblique	Reverse
Earthquake	Northridge	Christchurch, New Zealand	Niigata, Japan
Date	1994	2011	2004
Station	Burbank-Howard Rd.	MQZ	NIGH12
M_W	6.7	6.2	6.6
R_{epi} (km)	-	-	-
R_{hyp} (km)	-	-	-
R_{jb} (km)	16	14	10
R_{rup} (km)	17	16	11
V_{S30} (m/sec)	582	650	564
I_a (m/sec)	0.219	0.157	1.347
Lowest Useable Frequency (Hz)	0.125	0.025	0.05
Scale Factor	2.043	2.143	0.851
Component	NORTHR-HOW-060	CCHURCH-MQZ-E	NIIGATA-NIGH12-EW

NOTES:

Hz = Hertz; Ia = Arias intensity; R_{epi} = distance to epicenter; R_{hyp} = hypocentral distance R_{jb} = Joyner-Boore distance; R_{rup} = source-to-site rupture distance

Exhibit 7-6: Selected LODE Level Subduction Interface Time Histories

Mechanism	Subduction Interface	Subduction Interface	Subduction Interface
Earthquake	Maule, Chile	Maule, Chile	Tohoku, Japan
Date	2010	2010	2011
Station	ANTU	SLUC	TAIWA
M_W	8.8	8.8	9
R_{epi} (km)	362	373	173
R_{hyp} (km)	363	375	174
R_{jb} (km)	106	113	72
R_{rup} (km)	117	124	86
V_{S30} (m/sec)	622	1411	579
I_a (m/sec)	2.096	2.796	4.974
Lowest Useable Frequency (Hz)	0.025	0.025	0.0125
Scale Factor	0.684	0.606	0.497
Component	Maule-ANTU-90	Maule-STL-90	Tohoku-MYG009-NS

Exhibit 7-7: Selected LODE Level Subduction Intraslab Time Histories

Mechanism	Subduction Intraslab	Subduction Intraslab	Subduction Intraslab
Earthquake	Olympia, WA	Nisqually, WA	Nisqually, WA
Date	1965	2001	2001
Station	OLY0	EARN	BEVT
M_W	6.7	6.8	6.8
R_{epi} (km)	59	81	91
R_{hyp} (km)	84	97	105
R_{jb} (km)	53	70	79
R_{rup} (km)	76	89	95
V_{S30} (m/sec)	399	506	632
I_a (m/sec)	0.359	0.074	0.033
Lowest Useable Frequency (Hz)	0.1	-	-
Scale Factor	1.534	3.214	4.015
Component	Olympia-OLY-176	Nisqually-EARN-ENE	Nisqually-BEVT-ENE

Exhibit 7-8: Selected FODE Level Subduction Interface Time Histories

Mechanism	Subduction Interface	Subduction Interface	Subduction Interface	Subduction Interface	Subduction Interface	Subduction Interface	Subduction Interface
Earthquake	Tohoku, Japan	Tohoku, Japan	Maule, Chile	Maule, Chile	M9 Project	M9 Project	M9 Project
Date	2011	2011	2010	2010	2019	2019	2019
Station	OGUNI	YOKOTE	SLUC	VICH	Burnside Bridge 005	Burnside Bridge 018	Burnside Bridge 024
M_W	9	9	8.8	8.8	9	9	9
R_{epi} (km)	268	236	373	461	-	-	-
R_{hyp} (km)	269	237	375	-	-	-	-
R_{jb} (km)	152	130	113	-	-	-	-
R_{rup} (km)	159	138	124	178	-	-	-
V_{S30} (m/sec)	444	571	1411	-	600	600	600
I_a (m/sec)	0.069	0.216	2.796	0.039	1.836	1.252	1.206
Lowest Useable Frequency (Hz)	0.0125	0.0125	0.025	0.025	0.025	0.0125	0.0125
Scale Factor	2.368	1.185	0.244	2.204	0.388	0.437	0.553
Component	Tohoku-YMTH05-NS2	Tohoku-AKT017-EW	Maule-STL-90	Maule-VICH-360	M9-CSZ005-EW	M9-CSZ018-EW	M9-CSZ024-EW

In our selection process, the overall shape of the response spectra of the candidate ground motions and their relative closeness to the target spectrum in the period range of interest were given priority. We also considered secondary intensity measures including conditional Arias intensity, conditional cumulative absolute velocity, and significant duration of the time histories in the screening process. The conditional intensity measures were used to identify the candidate time histories that are consistent with the target response spectra. For this purpose, the intensity measures of the scaled time histories were compared to an estimated conditional intensity measure range of 16th to 84th percentile for the target spectrum. The time histories selected for CSZ interface were limited to two large-magnitude events, M_W 9.0 Tohoku (2011) and M_W 8.8 Maule (2010), and also a M9 Project simulated dataset due to unavailability of data for similar types of events.

7.5.4 Time History Scaling

The selected time histories in Exhibits 7-5 through 7-8 were scaled to their respective target spectra. We used an optimization procedure to calculate a scale factor by minimizing the

difference between the acceleration response spectrum and target acceleration spectrum in equally spaced (in log scale) period intervals.

Figures 7-31 through 7-33 show the response spectra of the selected LODE level time histories scaled to the crustal, CSZ interface, and CSZ intraslab target spectra, respectively. Figure 7-34 shows the same figure for FODE level. As observed from these figures, the geometric mean of the scaled response spectra for the selected time histories approximately follows the target spectra. The scale factors were obtained for a period range of 0.01 to 10 seconds using a limited number of equally spaced periods (in log scale). In calculating scale factors, more importance was given to periods closer to period range of interest. Calculated scale factors for each of the ground motion sets are provided in Exhibits 7-5 through 7-8.

The electronic files of the acceleration time histories in ASCII format and in standard gravitational acceleration (g's) are attached to the electronic copy of this report (portable document format, PDF, file of this report). These files include nine reference (i.e., unscaled) acceleration time histories for the LODE level and seven reference time histories for the FODE level (a total of 16 time histories).

Appendix G provides plots of the scaled acceleration, velocity, and displacement time histories. The time history response spectra (acceleration, velocity, and displacement) and normalized Arias Intensity (the normalized sum of squared ground acceleration values over time, i.e., a Husid plot) variation are also plotted in these figures. The name of each ground motion in each time history set provided in the title of the figures includes the orientation of the motion. The direction of the horizontal component is identified by azimuth in degrees (e.g., 270 or 360 degrees), east-west and north-south directions, or longitudinal and transverse directions.

8 SEISMIC SITE RESPONSE ANALYSES AND HAZARD EVALUATION

Seismic evaluations for the project were performed in accordance with the guidance provided in the AASHTO LRFD Bridge Design Specifications and project specific seismic criteria (HDR, 2021b) for both LODE (1,000-year probabilistic) and FODE (deterministic CSZ) ground motion hazard levels. Site response analyses were performed to evaluate site-specific seismic hazards and inform our geotechnical design recommendations provided in Sections 9 and 10. The following sections present our site-specific response analysis and site-specific seismic hazard evaluations, respectively.

8.1 Site Response Analysis

2D site response analyses were performed to evaluate the seismic hazards at the site, including liquefaction, cyclic softening, and post-seismic strength; permanent lateral ground deformations; and seismically induced settlement. 2D site response analyses were also performed to develop site-specific design spectra. The site response analyses used to inform our seismic hazard evaluation and design recommendations were conducted using the finite difference program Fast Lagrangian Analysis of Continua (FLAC; Itasca, 2019). The 2D site response analysis modeled a soil profile that varied both vertically and laterally along the bridge alignment and considered the topographic features along the primary portion of the bridge alignment, including the Waterfront Seawall (Seawall) located east of the proposed Bent 5 location on the west riverbank. Given the proximity of the existing Burnside Bridge Pier 1 foundations to the Seawall, the Pier 1 foundations were also considered in our analysis. Other portions of the model only considered free-field soil response.

Based on conversations with the design team, we understand that ground improvement is being considered to support the foundations at Bent 8 for the cable-stayed bridge option. We performed analyses both with and without ground improvement to facilitate the ongoing design efforts. Our analyses that considered ground improvement evaluated a single, conceptual, ground improvement option to inform the bridge type selection process. Additional modeling and analyses will be required to develop final design recommendations if ground improvement will be used for the project.

We performed our site response analysis by propagating the horizontal input motions described in Section 7 as vertically propagating shear waves at the bottom boundary of the 2D model, and the wave propagation throughout the profile was computed based on models that approximate the soil's response to cyclic loading. As such, the inputs for our site response analysis included the model geometry and boundary conditions, soil constitutive model parameters, ground improvement model parameters, and existing Seawall and Pier 1 foundation model parameters. The following sections present the site response inputs, a description of the analysis execution process, and the analysis results. Figures associated with our site response analysis are provided in Appendix H.

8.1.1 Model Geometry and Boundary Conditions

The 2D model surface geometry was developed based on the available site survey data and field observations as shown in Figure 2-2. The model considered the portion of the bridge alignment provided in Figure 2-2 (distance along the profile line from 0 to 2,600 as shown in Figure 2-2). Groundwater was assumed to be located at elevation 10 feet. The model included the river bottom, the landward slopes on the east and west side of the river channel, and the Seawall located east of the proposed Bent 5 location. The model did not

include bridge abutments at the extreme edges of the alignment. The horizontal model boundaries were extended 200 feet in both lateral directions to reduce the potential for boundary effects to influence the model behavior at the proposed bridge bent locations. The bottom of the model was set at elevation -150 feet. The model and mesh geometry, including soil layering, are provided in Figure H-1. Figure H-1 also includes the locations of the existing structures that were included in our model, which are discussed in more detail in later sections.

The boundary conditions were set to approximate free-field conditions along the model sides and a non-reflecting (i.e., compliant) boundary at the base. The bottom boundary was modeled as a compliant boundary in the horizontal direction and a rigid boundary in the vertical direction. Because the primary earthquake loading was in the form of horizontal shear waves and the impedance contrast between the Lower Troutdale Formation at the base of the model and the overlying soil layers (generally Gravel Alluvium or Upper Troutdale Formation), p-wave reflections from a rigid vertical boundary were assumed to be relatively small.

We note that the soils encountered in our subsurface exploration program at and below the bottom model boundary included both Lower Troutdale Formation and Sandy River Mudstone units. In 2D site response analysis, it is desirable to have a consistent and sufficiently stiff boundary at the model base to allow for uniform application of the input time histories and to reduce the potential for excessive mesh deformation or bending along the bottom boundary. Therefore, the lowest layer in our 2D model corresponded to the Lower Troutdale Formation. Subsequent model diagnostic evaluations were performed and found that the deformations along the bottom model boundary were less than 0.6 inches across the entire 3,000-foot-long model base for each of the applied motions indicating the Lower Troutdale Formation provides a sufficiently stiff base boundary condition for the 2D model. However, the input motions for the model need to be selected so that they are representative of the site conditions below the base of the model, expressed as a time averaged shear wave velocity over 100 feet, V_{S30}, value or a Site Classification. Due to the variability in the soils observed at depth, we performed preliminary analyses to evaluate a single, representative, site condition below the base of our model. This evaluation is described in the following section.

8.1.1.1 Evaluation of Base Conditions for Evaluation of Input Ground Motions

The bottom of our site response model is at elevation -150 feet. The soils encountered below this elevation in our subsurface exploration program included Lower Troutdale Formation and Sandy River Mudstone. Sandy River Mudstone was encountered in Shannon & Wilson borings drilled between approximately 600 to 1,400 feet along the profile line provided in

Figure 2-2. Geologic cross sections provided by Beeson and others (1991) estimate that the deep geology of the site includes Troutdale Formation overlying Sandy River Mudstone in turn overlying Columbia River Basalt. Beeson and others (1991) estimate the Sandy River Mudstone at the project site is approximately 200 feet thick, and the upper contact elevation dips to the east. This geologic interpretation is consistent with the conditions encountered in our subsurface explorations and our understanding of the local and regional geology.

Based on the available measured shear wave velocity data, we estimated the V_{S30} for the depth interval between elevation -150 feet and -250 feet across the site. This estimate included extrapolation based on our geologic interpretation and site-specific shear wave velocity correlations developed for the project as described in Section 8.1.2.1. The average V_{S30} between elevations -150 and -250 feet across the site was approximately 2,500 fps, which corresponds to AASHTO Site Class B/C Boundary conditions.

To evaluate the effect of the deep geologic structure at the site on the base input motions for our 2D site response model and the response between elevation -150 feet and the ground surface, we performed one-dimensional (1D) nonlinear total stress site response analysis using DEEPSOIL (Hashash and others, 2020). 1D site response was performed on three generalized soil profiles, corresponding to the conditions encountered in Borings B-1, B-3, and B-2, that were selected to be representative of the conditions encountered at the west and east riverbanks and within the river channel, respectively. At each generalized soil profile, three 1D models were evaluated, with the differences between each model being the depth to and compliant half-space velocity of the bottom model boundary. Each generalized soil profile considered model base boundaries as follows:

- Elevation -150 feet with a half-space velocity of 4,500 fps, representative of Lower Troutdale Formation;
- Within the Sandy River Mudstone with a half-space velocity of approximately 1,750 fps; and
- Columbia River Basalt contact with a half-space velocity of 5,000 fps.

The Sandy River Mudstone (where not encountered in our explorations) and Columbia River Basalt upper contact elevations were selected based on Beeson and others (1991). The half-space velocities for the Lower Troutdale Formation, Sandy River Mudstone, and Columbia River Basalt were determined based on the available shear wave velocity measurements, shear wave velocity models developed for the region (Roe and Madin, 2012), and our experience with these units. An illustration of the three generalized soil profiles is provided in Exhibit 8-1.

Exhibit 8-1: 1D Generalized Soil Profiles Used In Base Input Motion Evaluations

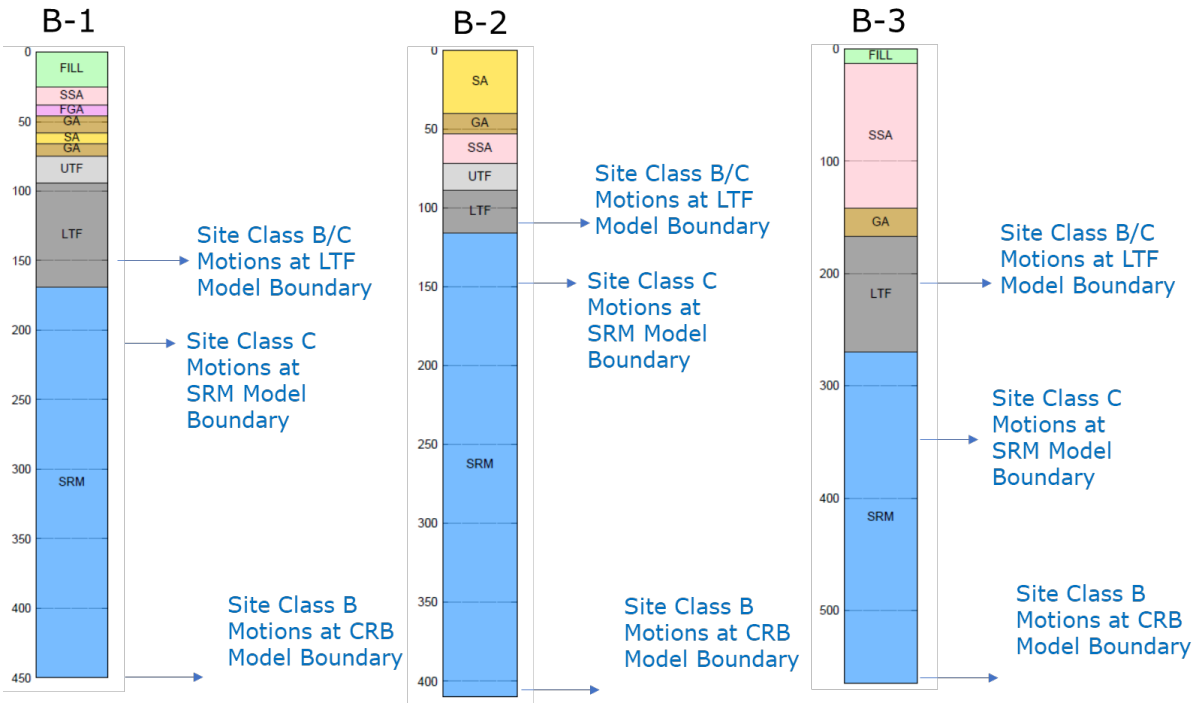

We developed three suites of base input motions for our study by scaling a subset of seven input base motions developed for the site response analysis performed as part of our Geotechnical Report: Burnside Bridge Environmental Impact Study, dated February 2021 (Shannon & Wilson, 2021). The motions in each suite were scaled to be consistent with a target design response spectrum developed using the existing, publicly available, USGS Probabilistic Seismic Hazard Analysis Data (Petersen and others, 2014). The motions for each base condition were evaluated based on the site location and the following Site Classifications:

- For motions applied at elevation -150 feet, the target design spectrum was developed for Site Class B/C boundary conditions, consistent with the site-averaged V_{S30} evaluation described previously;
- For motions applied within the Sandy River Mudstone, the target design spectrum was developed for Site Class C conditions; and
- For motions applied at the Columbia River Basalt contact, the target spectrum was developed using Site Class B conditions.

The input base motions for each generalized soil profile and base boundary model were applied and the response was computed. At each generalized soil profile, the average results for each base boundary model were compared for parameters that are known to be important for nonlinear deformation analysis and supplementary analysis procedures (e.g.,

liquefaction triggering, Newmark-type slope displacement estimates, etc.) including site response, cyclic shear stresses, and mobilized cyclic shear strains. A summary of the results of the 1D site response analysis are provided in Exhibits 8-2, 8-3, and 8-4 for the Boring B-1, B-2, and B-3 profiles, respectively. These plots show profiles of the geometric mean of the peak acceleration, peak shear strain, and average cyclic stress ratio, defined as 0.65 times the peak cyclic shear stress divided by the vertical effective stress, for all of the applied motions for each of the three base boundary conditions considered at each generalized profile. The analysis showed that all three base boundary models generally produced a similar response over the depth range considered in our 2D site response analysis. Based on these results the input ground motions were developed, as described in Section 7, for a V_{S30} of 2,500 fps.

Exhibit 8-2: Boring B-1 1D Site Response Analysis Results

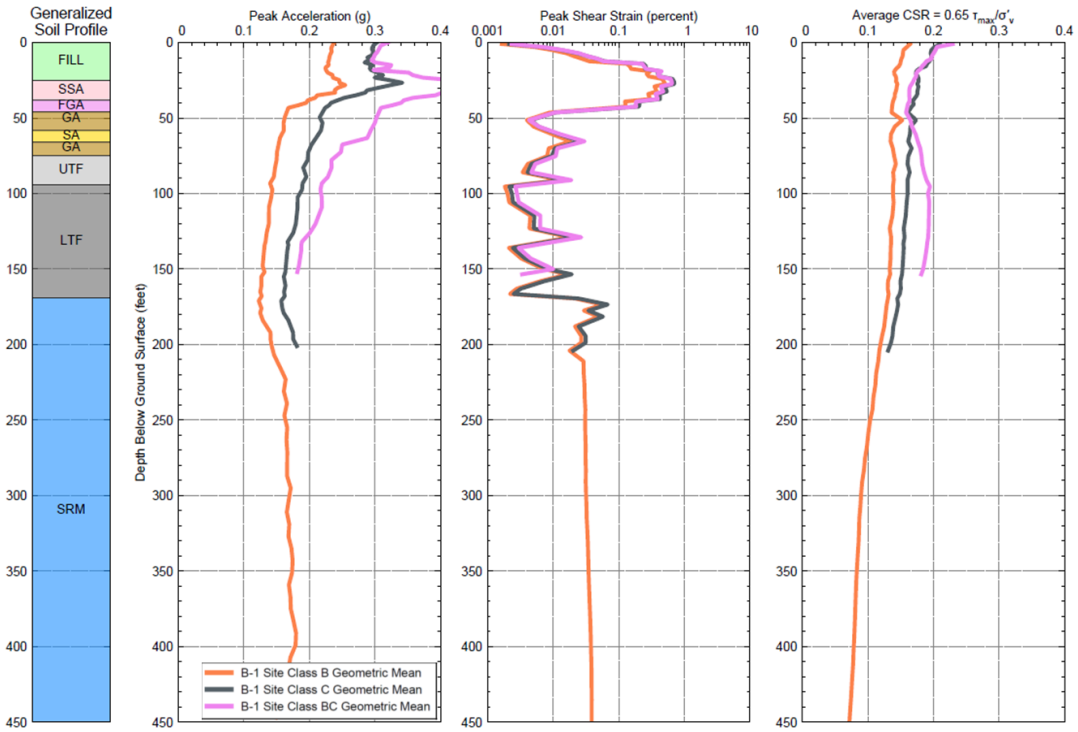

Exhibit 8-3: Boring B-2 1D Site Response Analysis Results

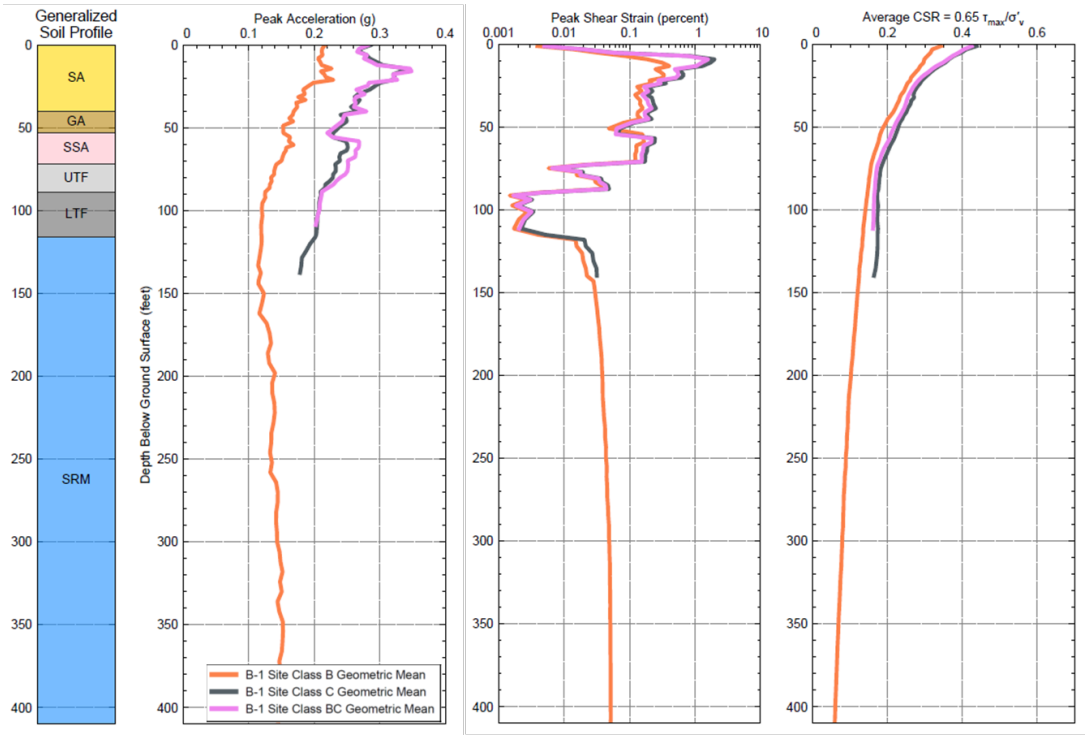

Exhibit 8-4: Boring B-3 1D Site Response Analysis Results

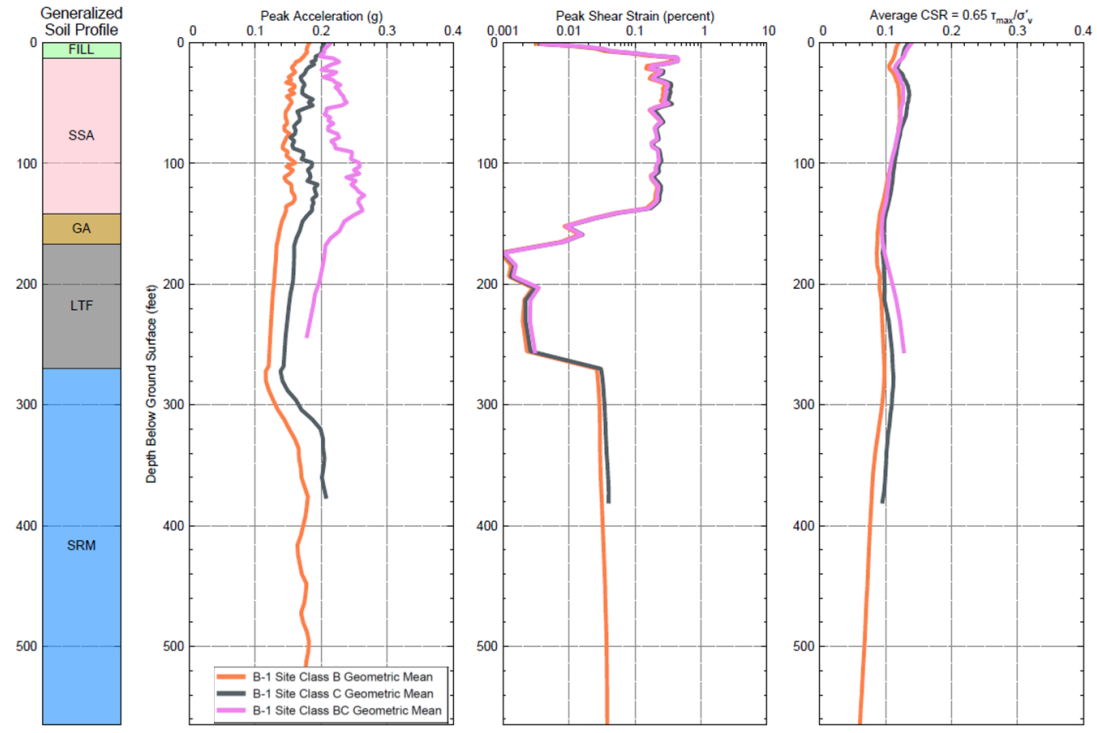

8.1.2 Soil Constitutive Model Parameters

The soil conditions modeled in our site response analyses were developed using the subsurface investigation and laboratory test programs documented in Sections 5 and 6. Soils with similar dynamic characteristics (i.e., shear strength, stiffness, modulus reduction and damping behavior, and liquefaction / cyclic strength degradation susceptibility) were grouped together into dynamic soil units. The dynamic soil units considered in our site response analysis are shown in Figure H-1 and correspond to the geotechnical soil units provided in Section 6, with the following exceptions:

- The Catastrophic Flood Deposits (both Fine-grained and Channel Facies), that were only encountered above the water table on the far east side of the alignment, typically consisted of silts, sands, and gravels of variable composition and consistency. These soils were considered to have similar dynamic characteristics as Fill, and these units were combined in our analysis. Both units are referred to as Fill for the purposes of the site response analysis presented in this section.
- The saturated soils located above the Gravel Alluvium on the east side of the bridge alignment between Shannon & Wilson borings B-13 and B-18 were typically silts and sands with variable composition and consistency and were classified as Sand Alluvium, Sand/Silt Alluvium, and Fine-grained Alluvium. As shown on Figure H-1, the soils in this portion of the alignment were divided into two general groups based on their anticipated behavior with respect to cyclic loading:
  - Sandy Sand-Silt Alluvium: Soils that were evaluated as predominantly sand-like and were considered susceptible to liquefaction and significant strength loss (i.e., residual strength conditions) due to excess pore pressure generation (e.g., Boulanger and Idriss, 2014).
  - Silty Sand-Silt Alluvium: Soils that were evaluated as predominantly fine-grained and were considered susceptible to pore pressure-induced cyclic strength degradation (e.g., Boulanger and Idriss, 2007).
- The groundwater level considered in our model was near the lower contact of the Fill. In the site response analysis, Fill soils located below the groundwater table were grouped with the underlying alluvial dynamic soil unit (Fine-grained, Sand, or Sand-Silt Alluvium).

In addition, per AASHTO Section 10.5.4.2 and GDM Section 6.5.1.3, we performed two analysis types:

- **Total Stress Analyses:** Analysis that assumes the soil does not undergo liquefaction and/or pore pressure-induced cyclic degradation and excess pore pressures are not allowed to develop during the dynamic analysis. Total stress analyses correspond to the "non-liquefied" conditions as defined in the codes listed above.

- **Effective Stress Analyses:** Analyses that considers the generation of excess pore pressure and the potential for liquefaction and/or pore pressure-induced cyclic strength degradation. The effective stress analyses correspond to the "liquefied" conditions as defined in the codes listed above.

Both the total and effective stress analyses were performed assuming undrained conditions and undrained strengths. All the soil constitutive models used in our site response analyses, including both total and effective stress conditions, require an estimate of the initial, or small strain, shear modulus, G_{max}. The following section describes our procedure to estimate G_{max} for each of the dynamic soil units considered in our analysis. Subsequent sections detail the soil input parameters unique to the total and effective stress analyses, respectively.

8.1.2.1 Initial Shear Modulus Profiles

We evaluated G_{max} for each dynamic soil unit using an estimate of the shear wave velocity (V_S). The V_S for each dynamic soil unit was evaluated based on the V_S measurements performed as part of our subsurface investigation program. To extrapolate V_S values throughout the soil profile, we developed site-specific relationships for V_S for each dynamic soil unit as a function of vertical effective stress using an equation of the form:

$$V_S = V_{S1} (\sigma'_V / P_a)^{\alpha}$$

where V_{S1} is the vertical effective stress normalized V_S, σ'_V is the vertical effective stress, P_a is atmospheric pressure (in the same units as σ'_V), and α is a curve fitting exponent. Note that setting the exponent α equal to zero represents a constant V_S. The site-specific V_S relationship parameters V_{S1} and α were evaluated for each dynamic soil unit using regression analysis based on the measured V_S data and an estimate of the vertical effective stress profiles at the locations the measurements were performed.

To evaluate G_{max} for input into our FLAC model, the vertical effective stress was evaluated at FLAC zone (see FLAC mesh provided in Figure H-1) and the corresponding V_S was computed based on the site-specific V_S relationship parameters for the dynamic soil unit of the given zone. With an estimate of V_S at each zone, G_{max} was computed as:

$$G_{max} = \rho V_S^2$$

where ρ is the soil density. Additional modulus input parameters (i.e., bulk and elastic modulus), were computed based on an estimate of the Poisson's ratio and elasticity equations. The values of density, Poisson's ratio, and the site-specific V_S model parameters V_{S1} and α used to develop the soil model input parameters for our 2D site response analysis are summarized in Exhibit 8-5.

Exhibit 8-5: Density, Poisson's Ratio, and Site-specific Shear Wave Velocity Relationship Parameters

Dynamic Soil Unit	Density, ρ (slugs/cubic foot)	Poisson's Ratio	V_{S1} (feet per second)	α
Fill	3.57	0.35	520	0
Fine-grained Alluvium	3.43	0.35	420	0.44
Silty Sand-Silt Alluvium	3.43	0.35	420	0.44
Sandy Sand-Silt Alluvium	3.43	0.35	420	0.44
Sand Alluvium	3.7	0.35	420	0.44
Gravel Alluvium	3.85	0.3	1,200	0.3
Upper Troutdale Formation	3.95	0.3	525	1.5
Lower Troutdale Formation	4.3	0.25	4,250	0

Note that for the Alluvial and Upper Troutdale Formation dynamic soil units, the V_S values are dependent on the vertical effective stress and as such are not constant and vary throughout the soil profile. A summary of the V_S values estimated using the methodology described in this section and implemented in our site response analysis is provided in Figure H-2. The discontinuity in Figure H-2 below the existing structure locations represent zones that include pile elements. The strength and stiffness properties in these zones were modified to account for the presence of the piles as discussed in later sections.

8.1.2.2 Total Stress Analysis Model Parameters

For the total stress analyses, all the geotechnical soil units were modeled using either Mohr-Coulomb or elastic material models provided in FLAC. The Mohr-Coulomb model treats the soil as a purely-elastic-purely-plastic material. The model behaves as a linear elastic material at shear stresses less than the shear strength of the soil; if the shear strength of the soil is reached or exceeded, the model behaves as a purely plastic material. The elastic material model is identical to the Mohr-Coulomb model but without a strength limit. Because it requires less computational power than the Mohr-Coulomb model, the elastic material model can dramatically improve analysis run times. The elastic model was used to model the Lower Troutdale Formation dynamic soil unit. Based on the results of the dynamic analysis, the peak applied shear stresses in this unit were between approximately 20 and 50 percent of the shear strength limit of the material, and in our opinion, the use of an elastic soil model was considered appropriate.

The input properties for the Mohr-Coulomb model, as implemented in FLAC, include the mass density, cohesion, friction angle, tension limit, dilation angle, bulk modulus, and shear

modulus. The mass density accounts for the mass of the soil; the cohesion, friction angle, tension limit, and dilation angle describe the shear strength limit of the soil; and the bulk and shear modulus describe the elastic behavior of the soil. The elastic material model requires inputs for the mass density, shear modulus, and bulk modulus.

The elastic behaviors of the Mohr-Coulomb (when the shear stress is below the strength limit) and elastic material models alone do not account for the strain-dependent modulus reduction and damping behavior that is observed in actual soils (e.g., Vucetic and Dobry, 1991). We used FLAC's hysteretic model in conjunction with the Mohr-Coulomb and elastic models to provide a more accurate representation of the dynamic soil response. The hysteretic model allows the user to provide a modulus reduction curve, expressed as a closed-form equation, which is used by FLAC to modify the elastic response to be consistent with the cyclic behavior of soils as observed in cyclic laboratory experiments. Our analysis utilized the three-parameter sigmoidal hysteretic formulation as implemented in FLAC. The damping ratio is not specified in FLAC and was evaluated based on the results of single-element cyclic direct simple shear (CDSS) test simulations. We calibrated the hysteretic input parameters to obtain a reasonable match to the target modulus reduction and damping ratio relationships for each dynamic soil unit using relationships presented in literature based on the subsurface investigation and laboratory testing program and our experience with dynamic analyses in similar soils.

Exhibit 8-6 summarizes the hysteretic Mohr-Coulomb and elastic model-specific input parameters. Note that the input parameters for mass density, Poisson's ratio, and the site-specific V_S relationship parameters used to evaluate the moduli were presented previously. The soil strength parameters and modulus reduction and damping relationships were evaluated based on the subsurface investigation and laboratory testing program and our experience with dynamic analysis in similar soil types. The Fine-grained Alluvium and Silty Sand-Silt Alluvium were observed to have strength parameters that varied with depth, and the strength was characterized using a site-specific relationship. The strength characterization for these materials is described in the following section. The tension limit was not defined and was computed internally by FLAC based on the provided cohesion and friction angle values (tension limit is 0 for materials that do not have both cohesion and frictional components). The dilation angle was set to 0 for all soil units considered in the analysis. For numerical stability and to prevent excess deformations at the ground surface, a cohesion of 100 psf was added to the top two rows of elements across the entire model.

Exhibit 8-6: Input Parameters for Hysteretic Mohr-Coulomb and Elastic Models

Dynamic Soil Unit	Cohesion (pounds / square foot)	Friction Angle (degrees)	Modulus Reduction and Damping Relationship [1]
Fill	0	32	Electrical Power Research Institute (1993) [C0=0.963, C1=-0.658, and C1=-1.440]
Fine-grained Alluvium	Site-specific strength relationship [2]		Electrical Power Research Institute (1993) [C0=0.938, C1=-0.633, and C1=-1.090]
Silty Sand-Silt Alluvium	Site-specific strength relationship [2]		Electrical Power Research Institute (1993) [C0=0.938, C1=-0.633, and C1=-1.090]
Sandy Sand-Silt Alluvium	0	32	Electrical Power Research Institute (1993) [C0=0.938, C1=-0.633, and C1=-1.090]
Sand Alluvium	0	32	Electrical Power Research Institute (1993) [C0=0.938, C1=-0.633, and C1=-1.090]
Gravel Alluvium	0	38	Rollins and others (2020) [C0=0.965, C1=-0.796, and C1=-1.619]
Upper Troutdale Formation	0	40	Vucetic and Dobry (1991) [C0=0.963, C1=-0.658, and C1=-1.262]
Lower Troutdale Formation	Modeled as elastic		Silva and others (1997) [C0=0.981, C1=-0.597, and C1=-0.862]

NOTES:

1 The three-parameter sigmoidal function inputs, C0, C1, and C2 for implementation in FLAC are provided in brackets.

2 Strength parameters were developed based on a site-specific, depth-dependent, relationship described in the following section.

8.1.2.2.1 Site-specific Strength Characterization for Fine-grained Alluvium and Silty Sand-Silt Alluvium

We developed a site-specific relationship to characterize the strength of the fine-grained dynamic soil units (Fine-grained Alluvium and Silty Sand-Silt Alluvium) based on the subsurface investigation and laboratory test program, which included consolidation and static direct simple shear tests. The shear strength of the fine-grained dynamic soil units was evaluated using the stress history and normalized soil engineering properties (SHANSEP) methodology as described by Ladd and Foott (1974), which estimates the undrained shear strength, S_U, as a ratio of the vertical effective stress, σ'_v. The shear strength ratio, S_U/σ'_v is typically evaluated as a function of the overconsolidation ratio, OCR, as follows:

$$S_U/\sigma'_v = S \cdot OCR^m$$

where S and m are fitting parameters that describe the shear strength ratio at an OCR of 1.0 (normally consolidated) and the curvature of the power function relationship, respectively.

We evaluated an estimate of the OCR for the fine-grained dynamic soil units based on the results of consolidation tests performed on select samples from within the fine-grained dynamic soil units and the measured CPT data. Both work-energy (Becker and others, 1987) and Casagrande's method (Casagrande, 1936) were used to evaluate the OCR for each consolidation test. The results of these evaluations were plotted as a function of depth below the ground surface, Z, as shown in Exhibit 8-7.

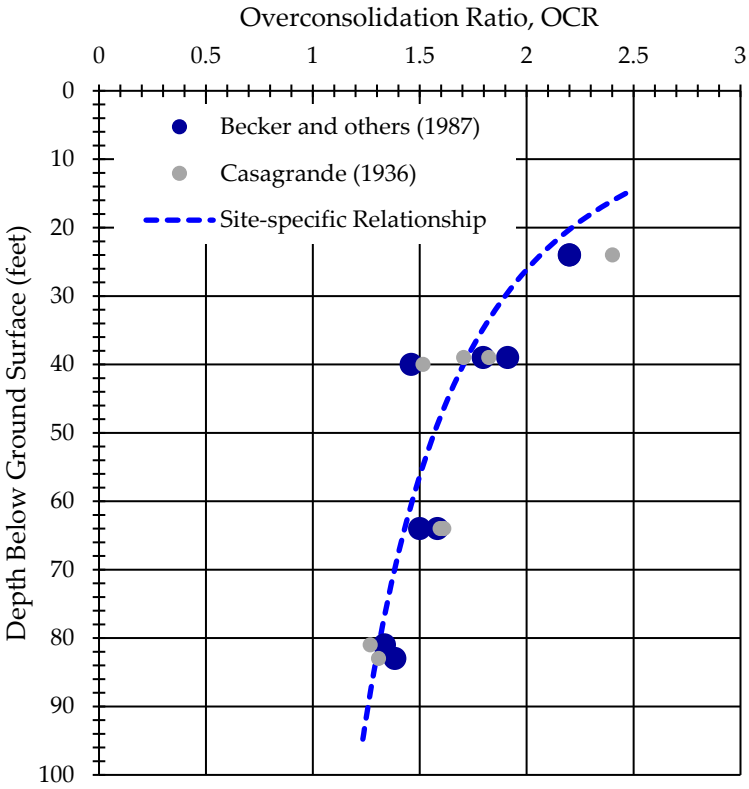

Exhibit 8-7: OCR Interpretation from Laboratory Data

Based on the laboratory test results, with consideration for the results of the CPT data and empirical relationships (Mayne, 2005; Agaiby and Mayne, 2019), we evaluated a site-specific relationship between the OCR of the fine-grained dynamic soil units and Z as:

$$OCR = 6.8\ Z^{-0.375}$$

A plot of the site-specific relationship is included in Exhibit 8-7. To evaluate the consistency of the lab-based OCR profile across the site, we calibrated a site-specific CPT-based OCR relationship based on the functional form of Agaiby and Mayne (2019) as follows:

$$OCR = 0.33\ (q_t - \sigma_v)^m\ (P_a / 100)^{1-m} / \sigma'_v$$

where q_t is the total cone tip resistance, σ_v is the total vertical stress, P_a is atmospheric pressure, and m is a fitting coefficient based on the CPT material index, I_c. Based on CPT's performed near borings where consolidation test data was available, we evaluated a site-specific relationship for the fitting exponent m based on the laboratory evaluation of OCR, the CPT data measured at the depth of the sample and estimates of σ_v and σ'_v. We evaluated the site-specific relationship for m using the same functional form for the m-I_c relationship as Agaiby and Mayne (2019) as,

$$m = 1.15 - 0.33 / [1 + (I_c / 3{,}1)^{25}]$$

Exhibit 8-8 shows a comparison of the calibrated CPT-based OCR estimates, provided for soils with an I_c greater than 2.4, with the site-specific OCR relationship. The calibrated CPT-based estimate is in good agreement with the site-specific relationship adopted for the project.

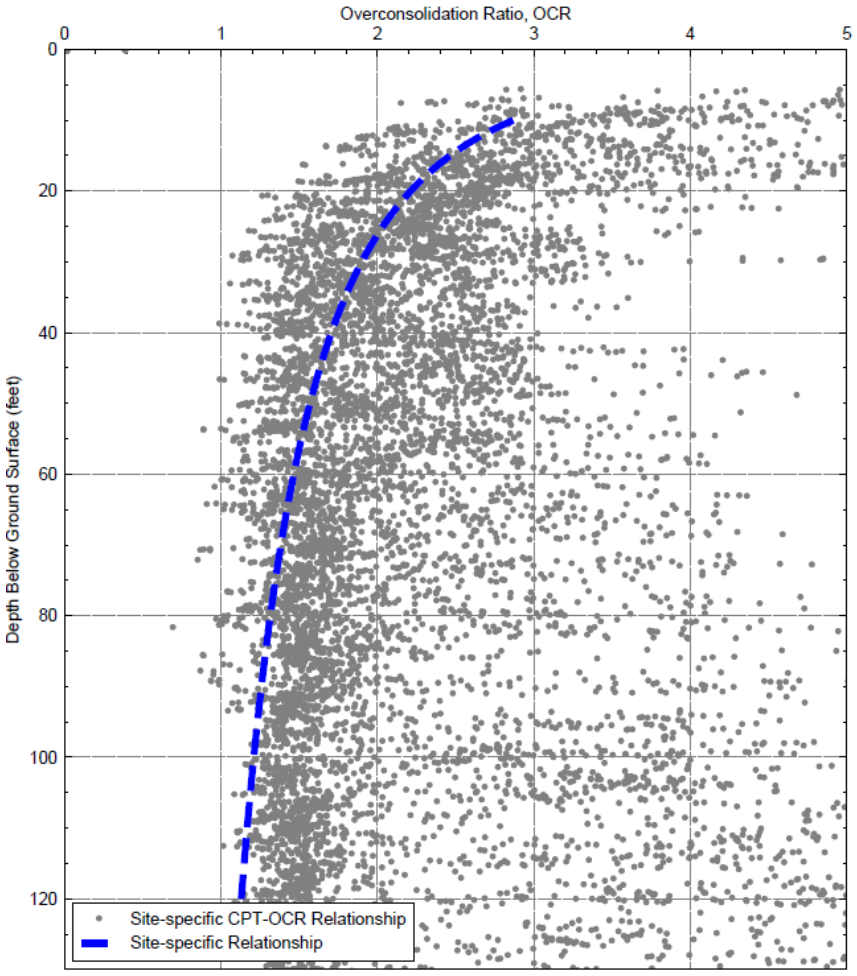

Exhibit 8-8: Site-specific OCR Profile Comparison to CPT Data

Next, we evaluated the parameters S and m used to define the shear strength ratio as a function of OCR. We evaluated the parameters S and m based on the results of our laboratory testing program, relationships between undrained shear strength and the measured CPT data, and existing empirical relationships relating the undrained shear strength and OCR for similar soils from literature (e.g., Beaty and others, 2014; Loehr and others, 2016; Jana and Stuedlein, 2021). The parameters S and m used in our site-specific strength characterization for the fine-grained dynamic soil units were evaluated as 0.25 and 0.85, respectively. By combining the shear strength ratio and OCR relationships, we can define a site-specific relationship for the shear strength ratio as a function of depth as:

$$S_U/\sigma'_V = 1.28 \cdot Z^{-0.32}$$

To implement the site-specific shear strength relationship for the fine-grained dynamic soil units in our 2D site response model, the depth below the ground surface was computed for each FLAC zone. For zones that were modeled as Fine-grained Alluvium or Silty Sand-Silt Alluvium, the shear strength ratio was then computed. Contours of the shear strength ratio are provided in Figure H-2. Next the vertical effective stress in each zone was obtained from FLAC and multiplied by the shear strength ratio to generate an estimate of the static shear strength for each zone. The shear strengths used in our seismic analysis included a 20 percent increase to account for loading rate effects per Idriss and Boulanger (2008) and our experience with similar soils. For the total stress analysis, the computed shear strength in each zone was input as a cohesion value in the Mohr-Coulomb material model.

We note that the evaluations of the site-specific OCR and strength profiles will be revisited and potentially refined during the NLTH phase of the project as more laboratory data becomes available. All additional data and any refinements to our evaluations will be documented in the subsequent NLTH geotechnical report.

8.1.2.3 Effective Stress Analysis Model Parameters

The Mohr-Coulomb and elastic material models described previously do not model the generation of excess pore water pressures. Based on the results of our subsurface investigation and laboratory test program, our geologic interpretation, and the liquefaction screening evaluations described in the GDM, we considered the Sand Alluvium, Sandy Sand-Silt Alluvium, and Silty Sand-Silt Alluvium to be susceptible to pore-pressure induced strength loss during a seismic event. All other dynamic soil units were not considered susceptible pore-pressure induced strength loss and the hysteretic Mohr-Coulomb and elastic material models described previously are applicable to both total and effective stress analyses.

To account for the generation of excess pore water pressures, we used two user-defined constitutive models, PM4SAND (Boulanger and Ziotopoulou, 2017) and PM4SILT (Boulanger and Ziotopoulou, 2018). Both the PM4SAND and PM4SILT constitutive models follow the basic framework of the bounding surface plasticity model presented by Manzari and Dafalias (1997) and Defalias and Manzari (2004) with modifications to provide better approximations of the cyclic behavior of clean sands and low to medium plasticity fine-grained soils, respectively. Specifically, the PM4SAND model is well suited to model soils that are susceptible to liquefaction and the potential for a relatively sudden loss of strength when the excess pore pressures become large. The PM4SILT, on the other hand, is best suited to model soils that are susceptible to gradual cyclic strength degradation during seismic loading. The following two sections present the input parameters used for the PM4SAND and PM4SILT constitutive models, respectively. The PM4SAND and PM4SILT material models were used to model the soil response during seismic loading. Figure H-1 shows the various model assignments used in our effective stress analysis. A discussion on our post-seismic strength evaluations is provided in Section 8.2.

8.1.2.3.1 PM4SAND

PM4SAND was used to model the Sand Alluvium and Sandy Sand-Silt Alluvium in our effective stress analyses. The PM4SAND model consists of 23 potential input parameters. Of the 23 potential input parameters, there are three primary inputs:

- **Relative density, Dr:** which primarily controls the stress-strain response and dilatancy characteristics of the soil. Per Boulanger and Ziotopoulou (2017), the corrected SPT blow count, $(N_1)_{60,cs}$ can be related to relative density using the expression $Dr = [(N_1)_{60,cs} / 46]^{1/2}$;
- **Shear modulus coefficient, Go:** which is used to evaluate the small strain modulus, G_{max}; and
- **Contraction rate parameter, hpo:** which adjusts the rate at which excess pore pressure is developed and, therefore, when liquefaction is triggered for a given cyclic loading history.

Using single element tests under constant amplitude harmonic loading, we calibrated the PM4SAND input parameter hpo so the model response approximated the SPT-based liquefaction triggering charts of Boulanger and Idriss (2014) for given values of Dr, Go, and vertical effective stress. The parameter Go was evaluated so that the G_{max} value computed internally by PM4SAND matched the G_{max} value computed with our site-specific relationship described previously. All secondary input parameters for PM4SAND were left at their default values.

An example of a PM4SAND calibration test is provided in Exhibit 8-9, which shows the response of a single element to a constant amplitude stress-controlled load analogous to a

cyclic direct simple shear test performed in the laboratory. The results are summarized in terms of the cyclic stress ratio (CSR; defined as the ratio of the applied shear stress to the initial vertical effective stress), shear strain, number of applied harmonic loading cycles, and the excess pore pressure ratio (defined as the ratio of the excess pore pressure to the initial vertical effective stress) response of the element. The provided example calibration shows the response for a soil element with an $(N_1)_{60,cs}$ of 15 (corresponding to a Dr of approximately 0.57), at an initial overburden effective stress of 1 atmosphere with no static shear stress (i.e., level ground conditions). The input parameter Go was computed as 415 to match the site-specific relationship for both the Sand Alluvium and Sandy Sand-Silt Alluvium dynamic soil units. The applied CSR was selected to be 0.16 based on the Boulanger and Idriss (2014) liquefaction triggering charts. The parameter hpo was calibrated to produce liquefaction, defined for purposes of our model calibrations as the instance that excess pore pressure ratio exceeds 0.98 or a single amplitude shear strain exceeded 3 percent, was initiated after approximately 15 harmonic loading cycles. The initiation of liquefaction and 15 loading cycles criteria was selected based on guidance in Idriss and Boulanger (2014) and Boulanger and Ziotopoulou (2017), which assume 15 loading cycles is representative of a magnitude 7.5 earthquake. The results show that the calibrated PM4SAND model is able to produce the intended excess pore pressure and corresponding cyclic strength and stiffness degradation response consistent with the liquefiable soil behavior presented in literature.

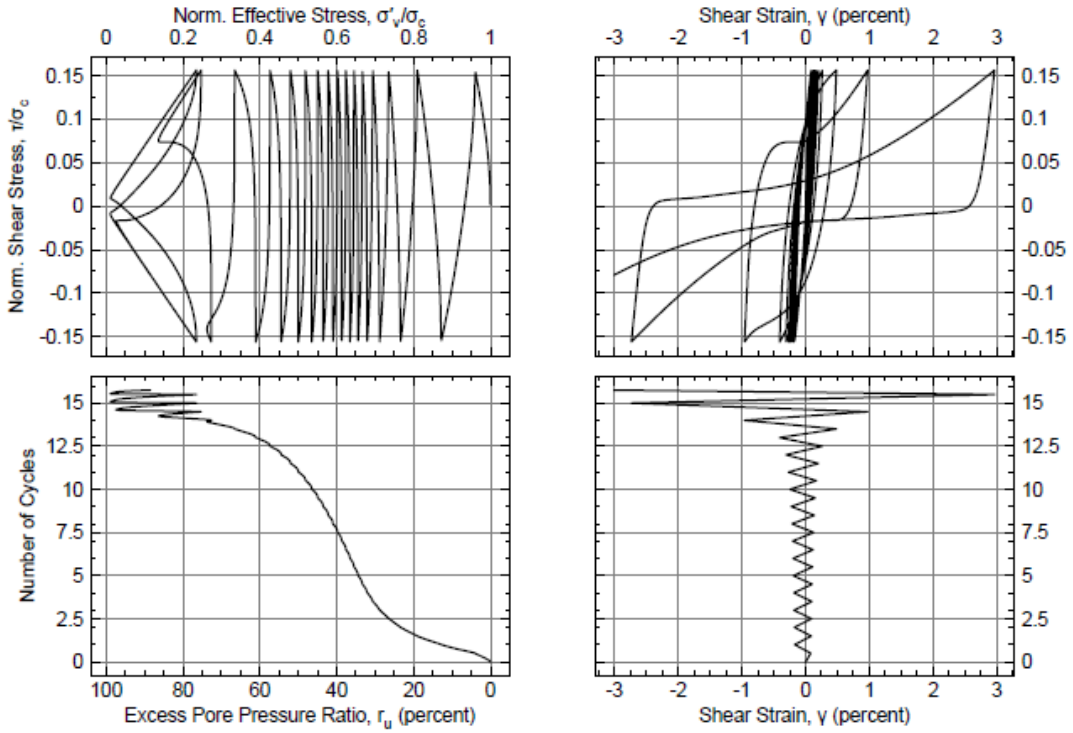

Exhibit 8-9: Example Single-element PM4SAND Calibration for Liquefaction Triggering

The calibration process was repeated over a range of $(N_1)_{60,cs}$ values and initial vertical effective stresses. The ranges of input parameters were selected to incorporate the ranges of blow counts and stress conditions assumed in our model. Given the presence of deep liquefiable layers encountered at the site, the calibrations prioritized capturing the effects of initial vertical effective stress on liquefiable soil behavior. Calibrations were performed to evaluate the parameter hpo that produced a response that was representative of the liquefaction triggering behavior of Boulanger and Idriss (2014) under level ground conditions assuming an at rest lateral earth pressure coefficient, K_0, of 0.5. The parameter hpo was evaluated for $(N_1)_{60,cs}$ values of 5, 10, 15, 20, and 25 at initial vertical effective stresses of 0.5, 1, 1.5, 2.5, 3.5, 4.5, and 5 atmospheres. Exhibit 8-10 tabulates the results of our calibrations for hpo at each of the considered combinations of $(N_1)_{60,cs}$ and vertical effective stress. Because both the Sand Alluvium and Sandy Sand-Silt Alluvium were modeled using the same overburden stress-dependent shear wave velocity parameters, the provided PM4SAND calibrations are applicable to both dynamic soil units.

Exhibit 8-10: Calibration Results for hpo for Each Considered Combination of $(N_1)_{60,cs}$ and σ'_V

σ'_V \ $(N_1)_{60,cs}$	5	10	15	20	25
0.5 atm	0.65	0.58	0.56	0.66	1.39
1.0 atm	0.69	0.61	0.59	0.65	1.19
1.5 atm	0.69	0.62	0.59	0.61	1.05
2.5 atm	0.69	0.63	0.59	0.60	0.91
3.5 atm	0.69	0.64	0.60	0.59	0.84
4.5 atm	0.70	0.67	0.61	0.59	0.80
5.0 atm	0.70	0.67	0.62	0.60	0.78

Exhibit 8-11 shows the results of the calibrations in terms of the cyclic resistance ratio (CRR; defined as the cyclic stress ratio required to initiate liquefaction after 15 loading cycles), as a function of $(N_1)_{60,cs}$. The calibrations were able to closely approximate the Boulanger and Idriss (2014) relationship for level ground conditions at an initial vertical effective stress of 1 atmosphere.

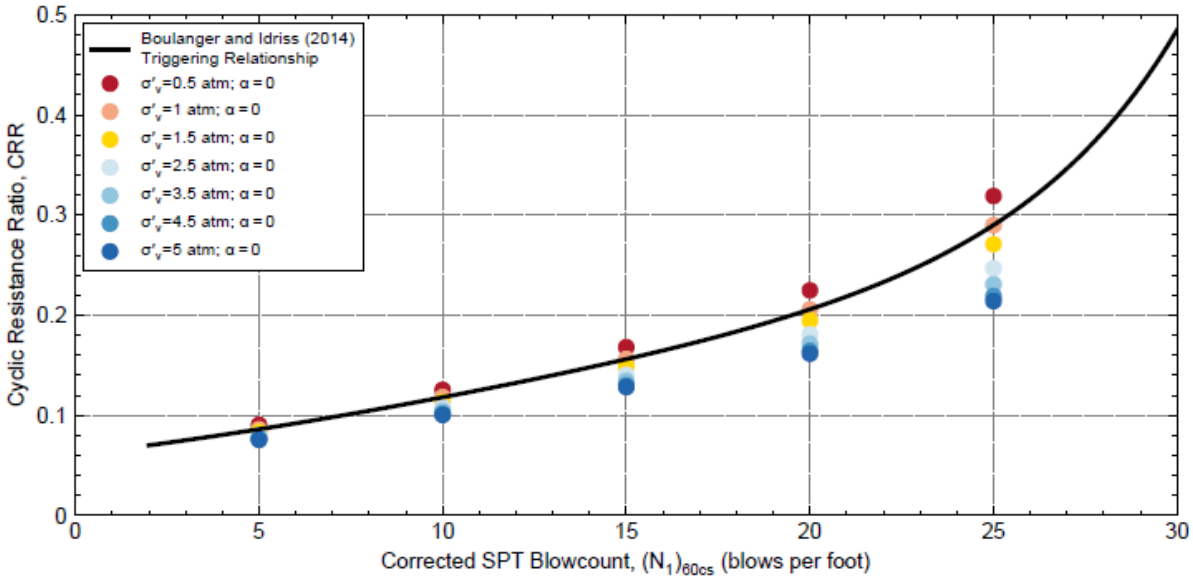

Exhibit 8-11: PM4SAND Level Ground Liquefaction Triggering Calibration Summary

The effect of initial effective stress levels other than 1 atmosphere was evaluated using the overburden correction factor, K_σ, defined as the ratio of the CRR at a given initial vertical effective stress to the CRR at a vertical effective stress of 1 atmosphere. Exhibit 8-12 compares the K_σ evaluated based on the calibration results with the K_σ relationships proposed by Boulanger and Idriss (2014).

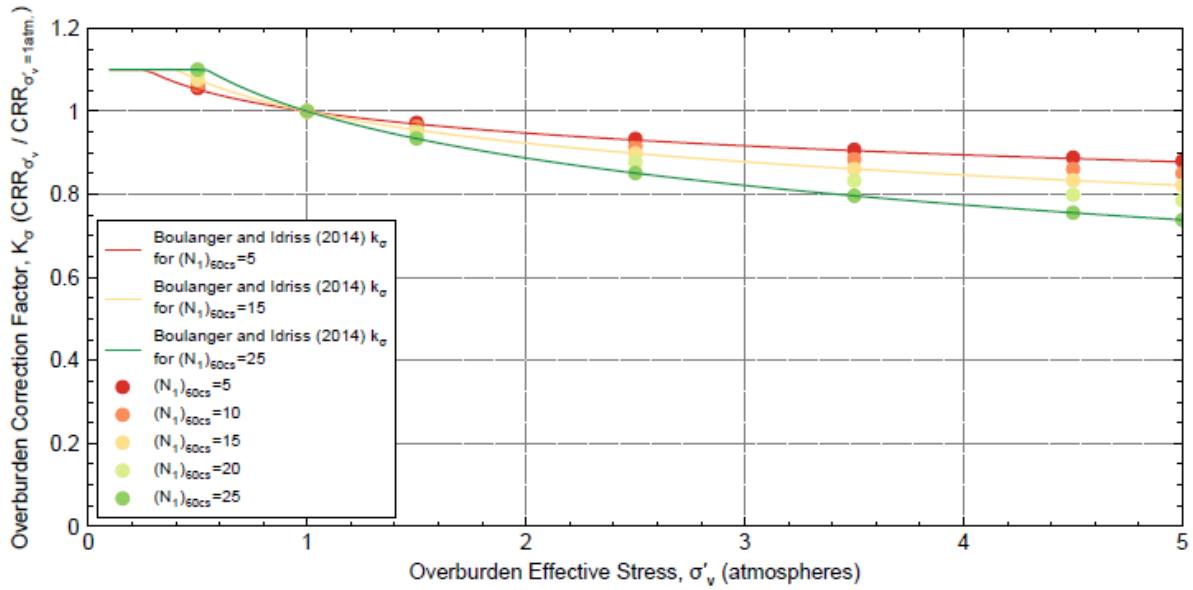

Exhibit 8-12: PM4SAND Initial Vertical Effective Stress Effects Calibration Summary

In addition to initial vertical effective stress, static shear stresses are also known to influence the behavior of liquefiable soils. The effects of static shear stress are commonly expressed in terms of a static shear stress correction factor, K_α, defined as the ratio of the CRR at a given

static shear stress to the CRR assuming level ground conditions. Exhibit 8-13 shows the K_α computed from the results of our calibrations as a function of the static shear stress ratio, defined as the ratio of the static shear stress to the initial vertical effective stress. While the calibrations prioritized the effects of vertical effective stress, the behavior of PM4SAND with respect to static shear stress effects is in general agreement with the behavior of liquefiable soils as observed in the field and in the laboratory.

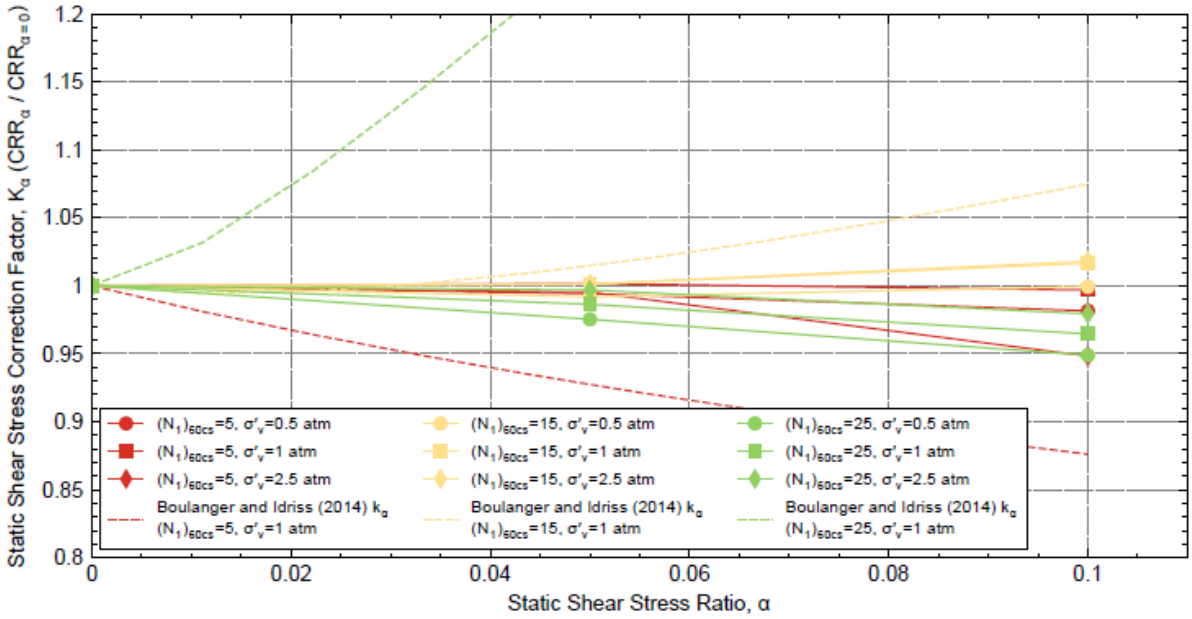

Exhibit 8-13: PM4SAND Static Shear Stress Effects Calibration Summary

Our calibrations also considered the modulus reduction and damping behavior of similar granular soils based on Electrical Power Research Institute (EPRI; EPRI, 1993). We evaluated the modulus reduction and damping behavior of the calibrated PM4SAND model by performing strain-controlled single element direct simple shear tests where the strain amplitudes were varied, and the modulus reduction and damping behavior was evaluated and summarized for each of the considered strain amplitudes.

A representative example of the summarized modulus reduction and damping evaluations is provided in Exhibit 8-14 for an $(N_1)_{60,cs}$ of 15 and initial vertical effective stresses of 0.5, 1, and 1.5 atmospheres. Because PM4SAND was only used to model saturated soils susceptible to liquefaction, the modulus reduction and damping evaluations were performed assuming undrained conditions. The results show the calibrated PM4SAND model can approximate the intended modulus reduction behavior over the range of strain amplitudes considered. The damping ratio is in general agreement with the EPRI relationships at cyclic strains between approximately 0.001 and 0.05. At strains below 0.001, the damping ratio evaluated by model is below the EPRI relationships. To compensate for

this, our site response analyses incorporated a small amount of Rayleigh damping, as described in Section 8.1.4. We note that at strains above approximately 0.05, the damping ratio evaluated by the model is larger than the EPRI relationships. However, PM4SAND was only used to model liquefiable soils that develop excess pore pressures, while the EPRI relationships were based on tests performed on unsaturated soil samples. At large strain magnitudes the effects of excess pore pressure-induced strength degradation dominate the soil response (Dobry and others, 1982; National Research Council, 1985). This effect is not accounted for in the EPRI relationships. Therefore, in our opinion the deviation of the calibrated PM4SAND model and the EPRI relationships at large strains is expected and the PM4SAND response provides a reasonable approximation of the cyclic behavior of liquefiable soils encountered at the site.

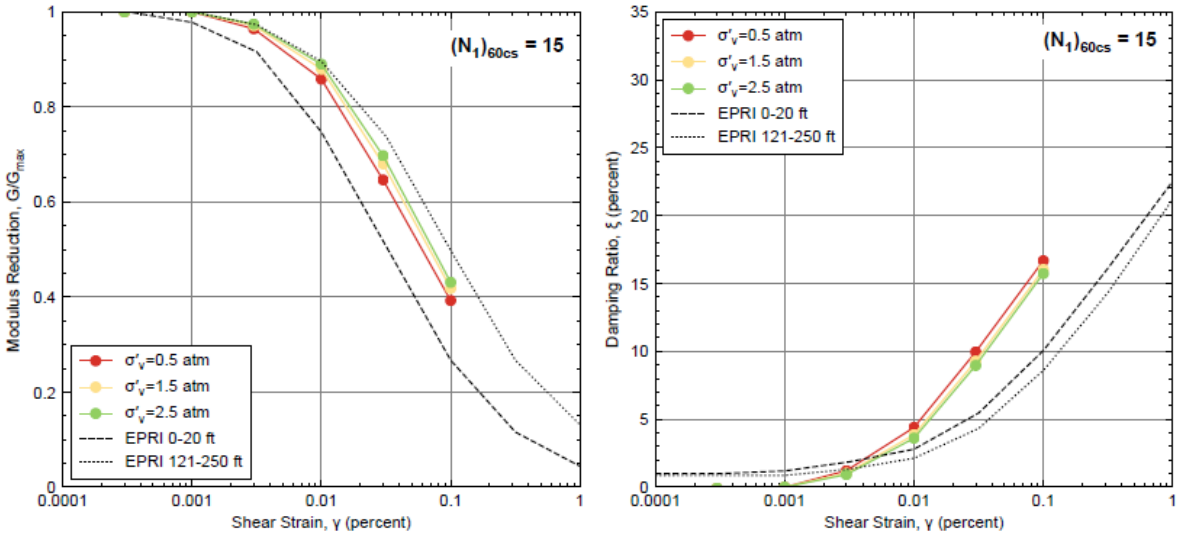

Exhibit 8-14: Example PM4SAND Modulus Reduction and Damping Behavior Summary

The input parameter for Dr was evaluated using the observed blow counts from our subsurface investigation program and the Dr-$(N_1)_{60,cs}$ relationship provided previously. We evaluated the values for $(N_1)_{60,cs}$ based on the available Shannon & Wilson subsurface explorations and the correction procedures of Idriss and Boulanger (2014). The fines content for each SPT blow count was evaluated from the laboratory test data. When fines content data was available for a given sample, that measured value was used directly. When the fines content data was not available, the representative fines content was evaluated by averaging the fines content data from adjacent samples with similar soil descriptions within the same boring. For reference the average fines contents for all tests performed in the Sand Alluvium and Sandy Sand-Silt Alluvium dynamic soil units were approximately 11 and 30 percent, respectively. Then the available blow count data was grouped based on the dynamic soil unit (Sand Alluvium and Sandy Sand-Silt Alluvium) and evaluated to identify

the potential for spatial trends. Based on our evaluations, a depth-dependent relationship for $(N_1)_{60,cs}$ was identified for both the Sand Alluvium and Sandy Sand-Silt Alluvium.

Exhibit 8-15 shows plots of $(N_1)_{60,cs}$ as a function of depth below the ground surface, Z, based on the SPT and CPT data obtained within the Sand Alluvium (left plot) and Sandy Silt-Sand Alluvium (right plot) dynamic soil units. The in-situ test data for the Sand Alluvium only included SPT blow counts. The Sandy Sand-Silt Alluvium included both SPT and CPT estimates of soil density. To convert the CPT data to equivalent $(N_1)_{60,cs}$ values, the CPT data was converted to corrected CPT resistance, $q_{C1N,cs}$, and subsequently to CRR based on the CPT-based relationships from Boulanger and Idriss (2014). Then, $(N_1)_{60,cs}$ values were obtained by inverting the $(N_1)_{60,cs}$ – CRR relationship to obtain $(N_1)_{60,cs}$ values that were consistent with the CRR evaluated using $q_{C1N,cs}$.

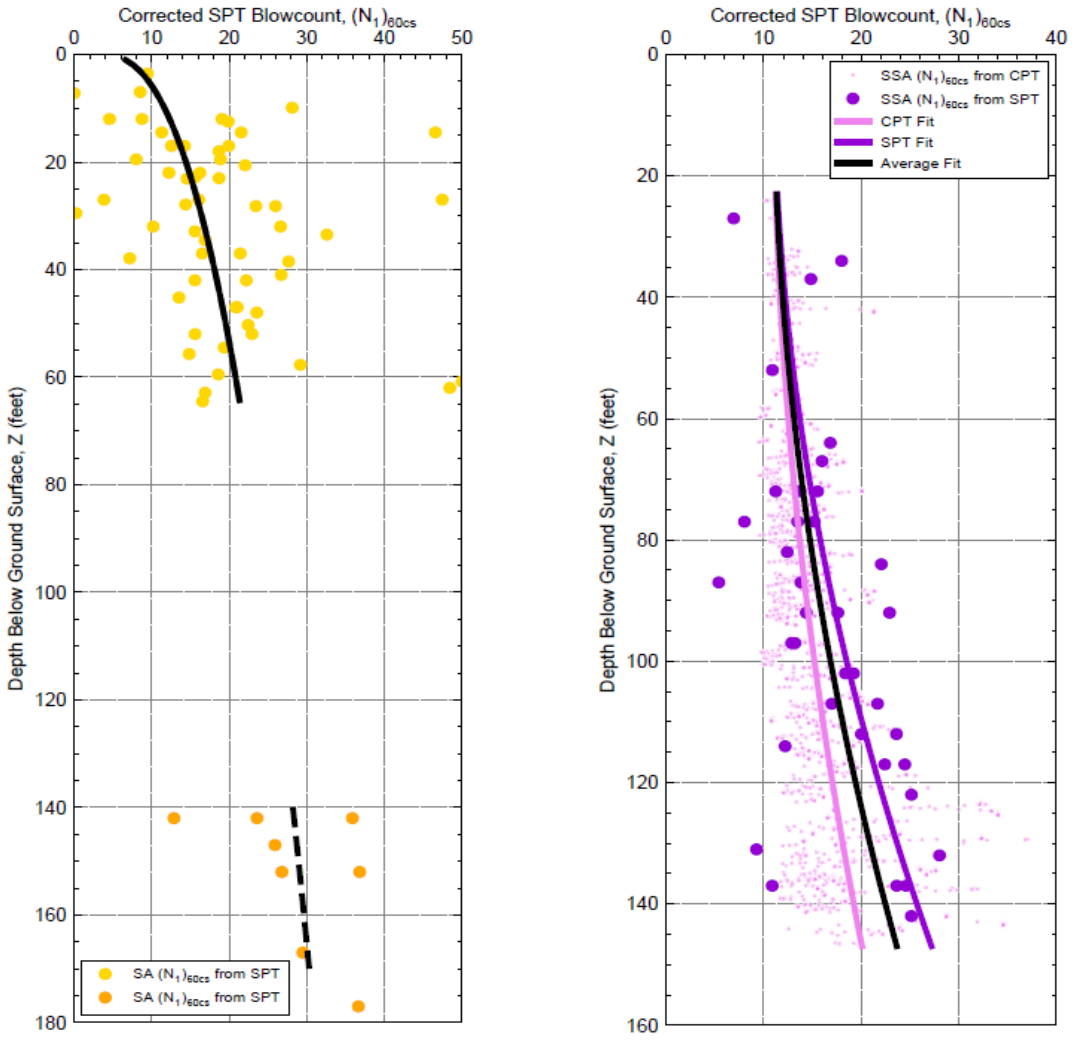

Exhibit 8-15: Corrected SPT Blow Count $(N_1)_{60,cs}$ for Sand Alluvium (Left Plot) and Sandy Sand-Silt Alluvium (Right Plot)

The $(N_1)_{60,cs}$ value for the Sand Alluvium and Sandy Sand-Silt Alluvium dynamic soil units was evaluated using a site-specific relationship for each unit individually, plotted as the black trend lines in Exhibit 8-15. The relationships were developed in order to capture the general trend of increasing $(N_1)_{60,cs}$ with depth and were constructed to generally capture the 25th to 50th percentile range of the measured data. Histograms and empirical cumulative density functions for the measured data and the fitted values are provided in Exhibit 8-16. We note that further evaluations and refinement of the distribution of $(N_1)_{60,cs}$ for the Sand Alluvium and Sandy Sand-Silt Alluvium may be performed and documented during the NLTH phase of the analysis.

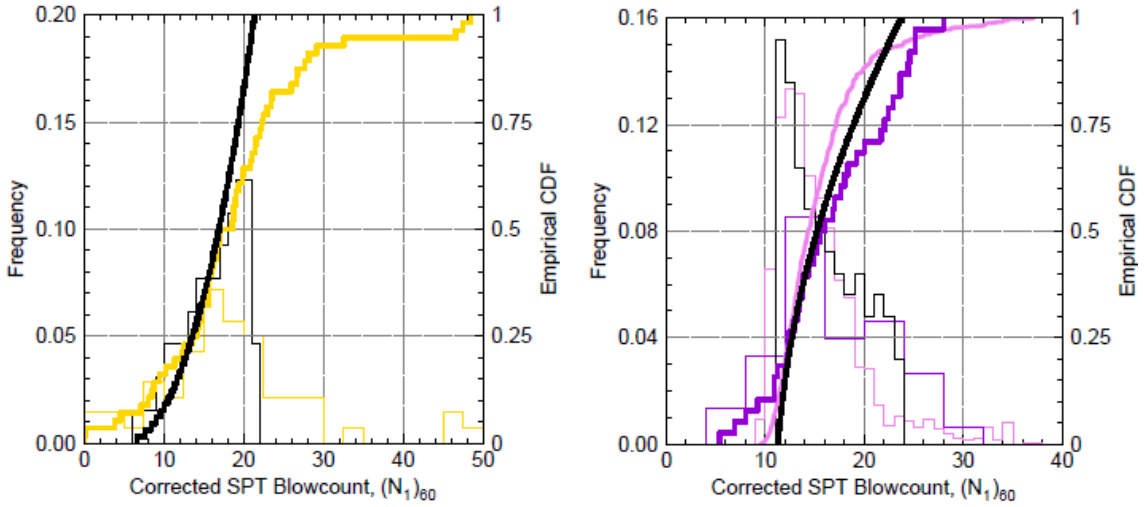

Exhibit 8-16: Histograms and Cumulative Density Functions of Corrected SPT Blow Count $(N_1)_{60,cs}$ for Sand Alluvium (Left Plot) and Sandy Sand-Silt Alluvium (Right Plot)

To implement the $(N_1)_{60,cs}$ relationships in our 2D site response model, the depth below the ground surface was computed for each FLAC zone. For zones that were modeled using PM4SAND, the representative $(N_1)_{60,cs}$ was evaluated using the site-specific relationship for the given dynamic soil unit and the equivalent Dr value was computed and assigned. Contours of the $(N_1)_{60,cs}$ values used to develop the PM4SAND input parameters for the effective stress site response analysis are provided in Figure H-2. The parameter hpo was assigned to each zone based on the project-specific calibrations as a function of the assigned $(N_1)_{60,cs}$ and the vertical effective stress in the given element. Interpolation was used to evaluate the parameter hpo for combinations of $(N_1)_{60,cs}$ and initial vertical effective stress not explicitly considered in our calibrations.

8.1.2.3.2 PM4SILT

PM4SILT was used to model the fine-grained dynamic soil units in our effective stress site response analysis. The PM4SILT model consists of 26 potential input parameters, three of which are considered primary input parameters. The primary input parameters include the

parameters Go and hpo described previously for PM4SAND. The parameter Go was assigned using the same methodology as described in Section 8.1.2.3.1. However, as opposed to Dr, PM4SILT utilizes the shear strength ratio. The shear strength ratio used for the dynamic soil units modeled as PM4SILT in the effective stress analysis was based on the site-specific strength relationship, with consideration for loading rate effects, and was evaluated and assigned in the same manner as described in Section 8.1.2.2.1.

Using single element tests with constant amplitude harmonic loading, we calibrated the PM4SILT input parameter hpo to approximate the results of our project specific CDSS testing program for a given value of shear strength ratio, Go, and initial vertical effective stress. To obtain reasonable approximations of the cyclic behavior of the fine-grained dynamic soil units as observed in the CDSS testing program, the secondary input parameters $n^{b,wet}$, e_0, λ, c_z, and c_e were modified from their default values as follows:

- $n^{b,wet}$, which represents the ratio that the peak shear strength can exceed the critical state shear strength, was set to 1.0.
- e_0, the initial void ratio, which affects how volumetric strains translate to changes in the state parameter, was set to 1.1.
- λ, the slope of the critical state line, was set to 0.145.
- c_z, which controls the strain levels at which soil fabric effects become influential on the model behavior under cyclic loading was set to 50.
- c_e, which effects the rate of strain accumulation in undrained cyclic loading conditions was set to 0.25.

All other secondary input parameters were left at their default values. We note that additional CDSS test results are currently being reviewed. The additional CDSS test data will be presented and incorporated in future project reports and analyses.

To facilitate the PM4SILT calibrations, the cyclic strength ratio, defined as the ratio of the applied peak cyclic stress to the undrained shear strength, and the number of uniform loading cycles to reach a single peak amplitude shear strain of 3 percent was evaluated for each available CDSS test in the dataset that reached 3 percent shear strain during cyclic loading. The 3 percent shear strain criterium was selected based on guidance in the PM4SILT manual (Boulanger and Ziotopoulou, 2018) and is a value commonly cited in literature (e.g., Idriss and Boulanger, 2008; Jana and Stuedlein, 2021). The parameter hpo was then calibrated over combinations of undrained shear strength ratio and initial vertical effective stress conditions consistent with those assumed in our site response model. A summary of the CDSS test data and the PM4SILT calibrations expressed as the cyclic stress ratio versus the number of cycles to 3 percent shear strain is provided in Exhibit 8-17. Based on the site-specific shear strength ratio relationship described previously, calibrations were

performed for dynamic shear strength ratios between 0.6 and 0.32 and initial vertical effective stresses between 1 and 4 atmospheres. Tabulated values of the calibrated parameter hpo for each considered combination of shear strength ratio and vertical effective stress is provided in Exhibit 8-18.

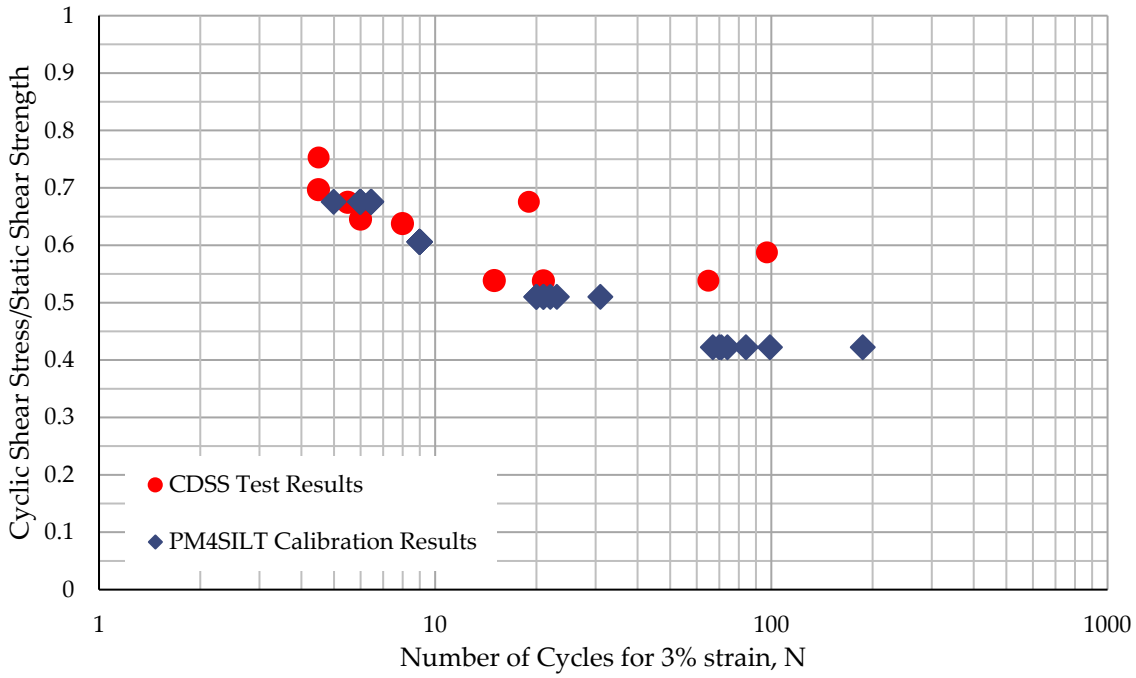

Exhibit 8-17: Summary of PM4SILT Calibrations to Approximate Laboratory Data

Exhibit 8-18: Calibration Results for hpo for Each Considered Combination of S_U/σ'_V and σ'_V

Dynamic Shear Strength Ratio[1], S_U/σ'_V	Vertical Effective Stress, σ'_V	hpo
0.6	4.0 atm	1.0
0.48	3.5 atm	1.2
0.42	3.0 atm	1.5
0.38	2.5 atm	1.8
0.36	2.0 atm	2.3
0.34	1.5 atm	3.2
0.32	1.0 atm	5.6

1 Dynamic shear strength ratio was computed using the site-specific strength relationship with adjustment for loading rate effects.

An example of a PM4SILT calibration test is provided in Exhibit 8-19, which shows the response of a single element to a constant amplitude stress-controlled load analogous to the cyclic direct simple shear tests performed in the laboratory. The results are summarized in the same manner as PM4SAND calibrations described previously. The provided example calibration shows the response for a soil element with a shear strength ratio of 0.3, an initial

vertical effective stress of 3 atmospheres, and zero static shear stress. The input parameter Go was computed as 530 to match the site-specific relationship for both the Fine-grained Alluvium and Silty Sand-Silt Alluvium dynamic soil units. The applied CSR was selected to be 0.18. The parameter hpo was calibrated to produce a single amplitude shear strain that exceeded 3 percent at a number of cycles that was representative of the response observed in the CDSS test program. The secondary parameters described previously were iteratively evaluated so that the cyclic shear strain accumulation for the model adequately captured the relatively gradual accumulation of cyclic strains as observed in the laboratory.

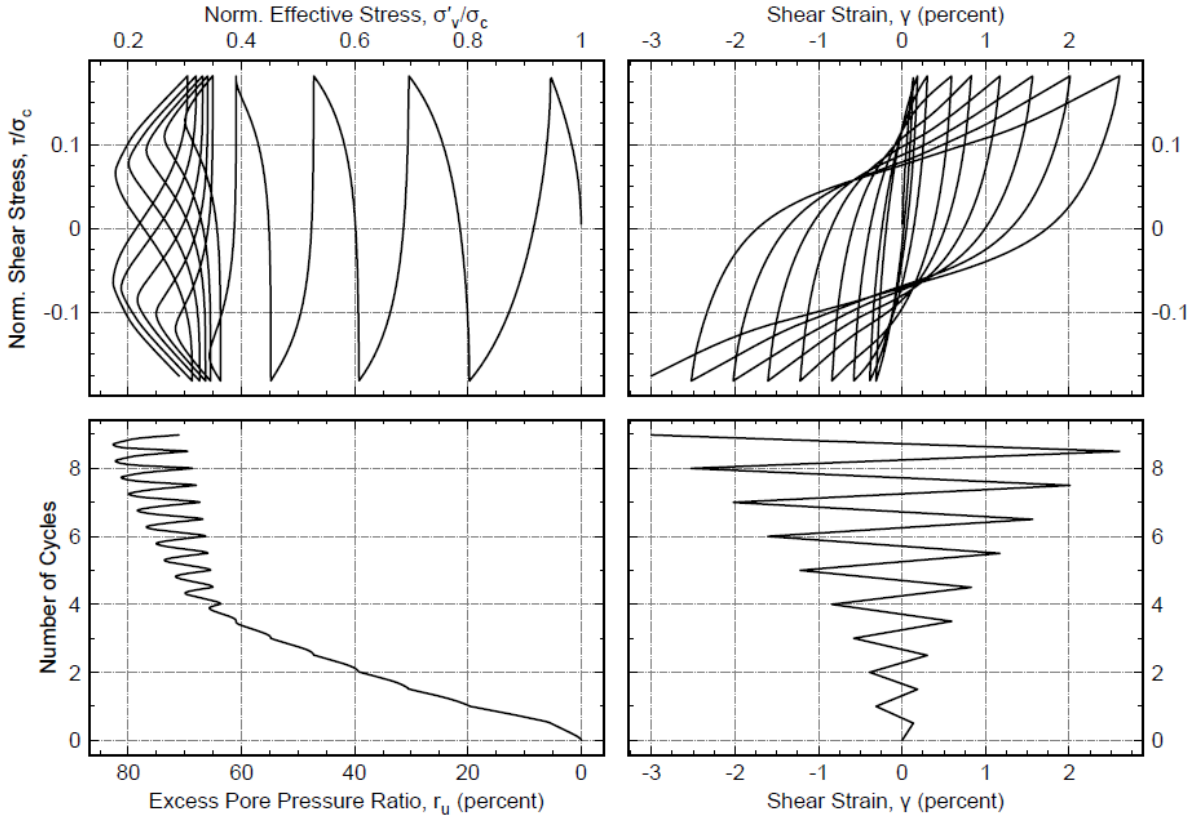

Exhibit 8-19: Example Single-element PM4SILT Calibration to Approximate Laboratory Data

Exhibit 8-20 provides a comparison of the calibrated PM4SILT model to one of the CDSS tests performed in the laboratory. The laboratory test corresponds to Boring B-17 Sample U2 with the test conducted at a vertical effective stress of 2,900 psf with an applied CSR of 0.25. The PM4SILT model assumed the same vertical effective stress and loading conditions, a dynamic shear strength ratio of 0.48, and all other input parameters defined as presented previously. Both the test result and the PM4SILT simulation reached 3 percent shear strain between 7 and 9 cycles of loading, produced a similar amount of pore pressure, and showed comparable rates of strain accumulation.

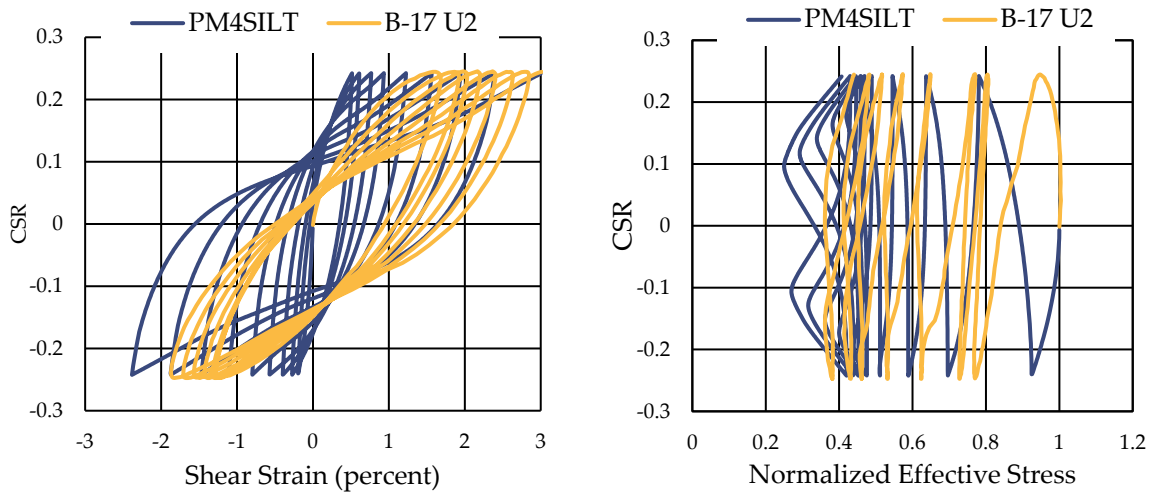

Exhibit 8-20: Comparison of a CDSS test from Boring B-17 Sample U2 and PM4SILT Simulation

Our calibrations also considered the modulus reduction and damping behavior of similar fine-grained soils based on the relationships proposed by Vucetic and Dobry (1991). We evaluated the modulus reduction and damping behavior of the calibrated PM4SILT model by performing strain-controlled single element direct simple shear tests where the strain amplitudes were varied, and the modulus reduction and damping behavior was evaluated and summarized for each of the considered strain amplitudes.

A summary of the modulus reduction and damping evaluations for PM4SILT is provided in Exhibit 8-21 for the considered range of shear strength ratios and initial vertical effective stress conditions. Because PM4SILT was only used to model saturated soils susceptible to cyclic strength degradation, the modulus reduction and damping evaluations were performed assuming undrained conditions. The results show the calibrated PM4SILT model closely approximates the modulus reduction behavior for the Vucetic and Dobry PI equal to 15 relationship over the range of strain amplitudes considered. The damping ratio is in general agreement with the Vucetic and Dobry relationships at cyclic strains between approximately 0.001 and 0.1. At strains below 0.001, the damping ratio evaluated by model is below the Vucetic and Dobry relationships. To compensate for this, our site response analyses incorporated a small amount of Rayleigh damping, as described in Section 8.1.4. We note that at strains above approximately 0.1, the damping ratio evaluated by the model is slightly larger than the Vucetic and Dobry relationships. The deviation from the Vucetic and Dobry relationships at strain amplitudes greater than 0.1 percent was due to the cyclic degradation behavior of the model that was considered representative of the soil behavior as observed from the CDSS testing program and was considered reasonable.

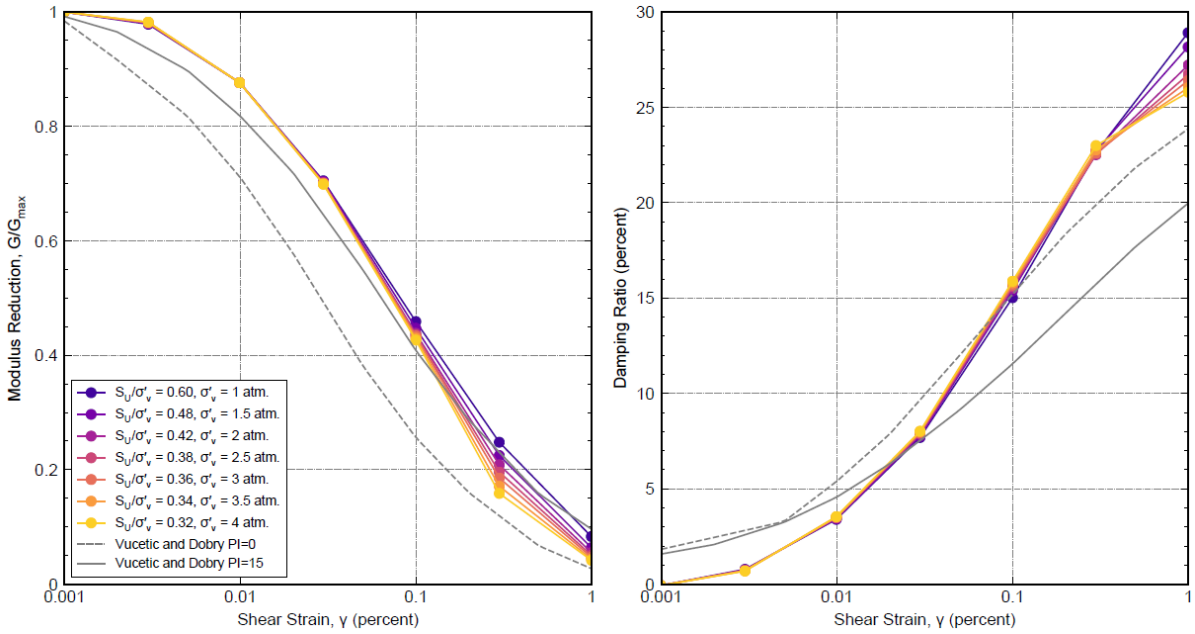

Exhibit 8-21: PM4SILT Modulus Reduction and Damping Behavior Summary

In addition to cyclic response, the monotonic response of PM4SILT was performed to evaluate the peak strength behavior of the model. Exhibit 8-22 shows the results of the monotonic direct shear test simulations for the range of shear strength ratios and effective vertical stresses considered in our calibrations. The results show that the PM4SILT model simulates the intended peak strength response with reasonable stress-strain behavior under monotonic loading conditions.

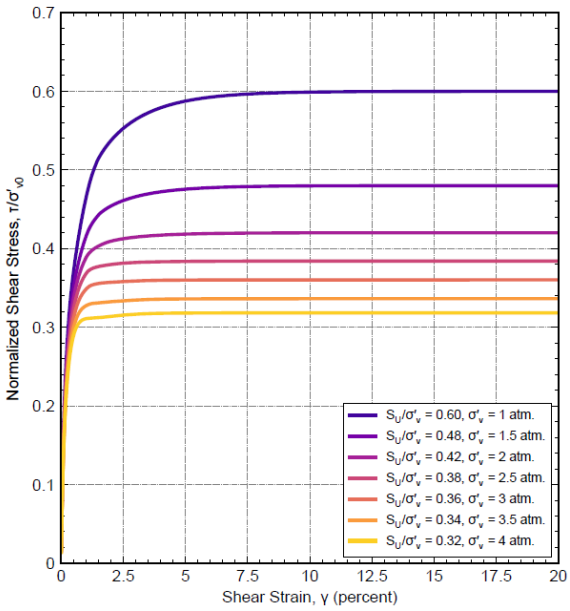

Exhibit 8-22: PM4SILT Monotonic Loading Behavior Summary

To implement the results of the PM4SILT calibrations in our 2D site response model, the shear strength ratio was evaluated as described in Section 8.1.2.2.1 and assigned directly to the constitutive model. The parameter hpo was assigned to each zone based on the project-specific calibrations as a function of the assigned shear strength ratio and the vertical effective stress in the given element. Interpolation was used to evaluate the parameter hpo for combinations of shear strength ratio and initial vertical effective stress not explicitly considered in our calibrations.

8.1.3 Ground Improvement Model Parameters

We understand the design team is considering a ground improvement mitigation option at Bent 8 for the cable-stayed bridge alternative. Our 2D site response included analyses both with and without ground improvement. For our preliminary ground improvement evaluations, the ground improvement zone was modeled as a 100-foot-wide zone centered around Bent 8 for the cable-stayed bridge alternative and extended from the ground surface down to the Gravel Alluvium as shown in Figure H-3. At this stage of design, the ground improvement was assumed to penetrate approximately 5 feet into the Gravel Alluvium. Additional discussion on the ground improvement considered for the project is provided in Section 9.

The soils within the ground improvement zone were modeled using the hysteretic Mohr-Coulomb material model described previously. Our preliminary analyses assumed a cementitious ground improvement option (e.g., jet grouting or deep soil mixing) would be required. The input properties for the ground improvement model, listed below, were developed based on the recommendations of Axtel and Stark (2008), the results of our subsurface exploration program, and our experience.

- Mass density of 3.6 slugs per cubic foot
- Cohesion of 21,600 pounds per square foot (150 pounds per square inch)
- Shear modulus of 5,800,000 pounds per square foot
- Bulk modulus of 7,700,000 pounds per square foot
- Modulus reduction and damping behavior based on Axtel and Stark (2008) using the FLAC three-point sigmoidal hysteretic damping model with parameters C0, C1, and C2 of 1.1, -0.7, and -1.3, respectively.

As noted previously, additional analysis will be required to refine the assumed properties, geometry, and modeling methodology listed above if ground improvement is required for the bridge option selected for final design. If required, additional studies and documentation will be provided in the NLTH phase of the project.

8.1.4 Existing Structure Model Parameters

The existing Seawall structure was considered in our FLAC model because it is located approximately 40 feet from the proposed Bent 5 location, is laterally continuous, and creates a vertical discontinuity in the topography along the centerline of the bridge profile. The existing Pier 1 foundation was also considered in our model. Based on the available as-built drawings, we understand the existing Pier 1 foundation consists of a massive concrete structure located approximately 25 feet in front of the Seawall. We understand following demolition of the bridge, the Pier 1 foundations located 5 feet below the mudline will remain in place. In our opinion the presence of the existing Pier 1 foundations will impact the extent and magnitude of seismically induced ground displacements adjacent to the Pier 1 foundations and influence the performance of the Seawall and were also considered in our model. All other existing foundation elements along the bridge alignment were not considered in our 2D site response analysis. Based on review of available as-built plans, additional existing foundation elements were not included because:

- Significant uncertainty in the geometry, installation depth, and condition of the foundation elements over the life cycle of the proposed bridge;
- The dimensions of the foundation elements were not sufficient to provide resistance to the entire area of the foundations for the proposed bridge and the potential ground improvement zone; and
- We understand the existing bridge and I-5 foundations on the east side of the alignment are generally founded on timber or steel piles that were not designed to meet the same criteria as the proposed bridge structure and are relatively flexible. The differences in seismic design criteria and foundation flexibility between the existing and proposed foundations present a strain-incompatibility, the existing foundations would require significant displacements to mobilize any potential resistance, and significant loads would still be transferred to the proposed shaft foundations. In our opinion, the performance of the existing foundations during the design seismic event is expected to be poor and would not provide a reliable resistance to lateral soil deformations and the associated loads on the proposed drilled shaft foundations.

As noted above, the existing timber piles in the area considered for ground improvement were not included in our model. These timber pile foundations are not continuous across the width of the ground improvement zone, are slender flexible elements relative to the mass of the ground improvement zone, and are not founded in a competent bearing layer. In our opinion, the performance of these foundations during a seismic event is expected to be poor and they would not provide any reliable benefit to the ground improvement zone; therefore, the existing foundation elements were not considered in our ground improvement evaluations.

Based on the as-built drawings provided in Appendix A, we understand the Seawall consists of an L-shaped concrete structure that is approximately 21 feet wide at the base and steps to 3 feet wide at the top, supported on timber piles installed both vertically and with a batter inclined toward the river channel. We understand the existing Pier 1 foundation includes an approximately 33-foot-wide, 20-foot-tall concrete block with an approximately 19-foot-wide stem that extends above the mudline. The bottom of the concrete is at approximately elevation -45 and is supported on vertical timber piles. Our analysis assumed the existing Pier 1 foundation stem will be demolished to 5 feet below the existing mudline.

The following sections describe the modeling methods used to evaluate the concrete and pile portions of the Seawall and existing Pier 1 foundations, respectively. Our model only approximated the global behavior of the Seawall and existing Pier 1 foundations in order to develop reasonable estimates of site response and ground deformation at the proposed bridge bent locations. Our site response model did not consider internal failure mechanisms of the Seawall such as concrete cracking or shear failures at the concrete-timber pile interface. A full evaluation of the seismic performance of the Seawall would require structural analysis and additional dynamic soil structure interaction modeling which is not included in our scope of services for this project.

8.1.4.1 Concrete Foundation Model Properties

The concrete portions of the Seawall and the existing Pier 1 foundations were modeled using the elastic material model in FLAC using properties consistent with concrete. Internal failure or cracking of the concrete was not evaluated and the concrete was assumed to behave perfectly elastically during a seismic event. Therefore, hysteretic damping was not applied. The mass density and modulus parameters were evaluated assuming normal-weight, normal-density concrete with a compressive strength of 4,000 pounds per square foot and a Poisson's ratio of 0.2. The elastic model properties used to evaluate the concrete foundation elements were as follows:

- Mass density of 4.6 slugs per cubic foot
- Shear modulus of 216,000,000 pounds per square foot
- Bulk modulus of 288,000,000 pounds per square foot

The dimensions of the concrete foundation elements included in FLAC were evaluated as rectangular with a uniform width. The uniform width was evaluated by computing a rectangular area that was equivalent to the cross-sectional area of the irregularly shaped foundation elements. The locations of the concrete foundation elements in our FLAC model are shown in Figures H-1 to H-3.

8.1.4.2 Pile Foundation Model Properties

Due to uncertainties in the installation depth, geometry, and condition of the timber pile , individual pile elements were not explicitly modeled in our 2D site response analysis. Instead, the pile and soil mass below the concrete elements were modeled using the Mohr-Coulomb material model in FLAC using input properties that were evaluated to be representative of the lateral response of the soil-pile system that supports the existing structures. To develop the input properties for the pile-soil zone, we modeled the lateral pile-soil reaction in LPILE.

Based on the as-built drawings and our understanding of the state of practice for design and construction at the time the original bridge was built, we assumed the timber piles supporting the concrete elements were Douglas Fir timber piles that tapered from 16 inches at the top of the pile to 12 inches at the tip. The timber piles were modeled as an elastic section in LPILE with material properties consistent with ASTM Standard D 25 (ASTM, 2017). Our analysis assumed a fixed-head connection at the pile-cap interface based on the as-built drawings and the strength and stiffness contrast between the timber piles and the concrete pile cap.

The soil properties used in our LPILE analysis were evaluated based on the as-built drawings and the results of our subsurface investigation and laboratory program. We assumed that the piles were installed through Sand and Silt-Sand Alluvium and terminated within the Gravel Alluvium. The LPILE input properties for the Sand and Silt-Sand Alluvium were evaluated with consideration for potential densification due to pile driving. We assumed an improvement factor (defined as the ratio of the densified soil SPT blowcount to the SPT blowcount prior to pile driving) of 2.3 based on the pile installation geometry and guidance provided in Stuedlein and others (2016) and Rhyner (2018). A lateral resistance reduction factor, or p-multiplier, of 0.3 was included to account for the shadowing effect of adjacent piles based on the general pile spacing provided in the as-built drawings and AASHTO Table 10.7.2.4-1.

We evaluated the equivalent strength and stiffness of the pile-soil zone by modeling the timber pile and soil system as described above and applying a distributed load with depth along the pile. Based on preliminary analysis without consideration of the pile foundations, the global behavior of the Seawall and existing Pier 1 foundation system is controlled by global stability for a failure surface that passes around the wall and through the underlying Sand and Sand-Silt Alluvium. Therefore, the distributed load was applied over the depth of the Sand and Sand-Silt Alluvium. A schematic of the methodology is provided in Exhibit 8-23, where P_A and P_B are the loads at the top and bottom of a linearly distributed loading profile, respectively.

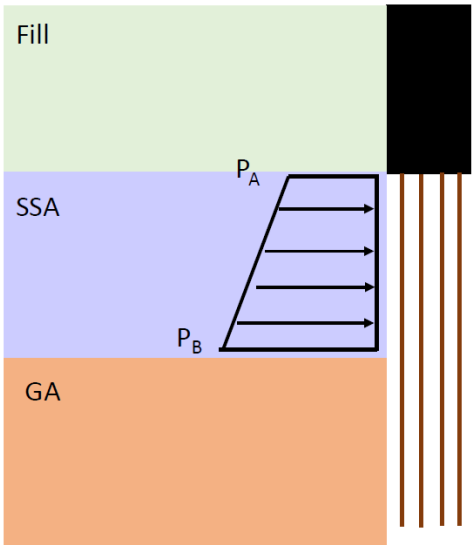

Exhibit 8-23: Analysis Methodology for Evaluation of Pile-Soil Zone Properties

To determine the strength and stiffness properties for the pile-soil zones we performed the following steps:

1. Model the pile and soil system in LPILE.
2. Compute the loads P_A and P_B based on the vertical effective stress at the top and bottom of the Sand and Sand-Silt Alluvium and an assumed friction angle. The friction angle in this step is representative of the friction angle of the pile-soil zone.
3. Evaluate the lateral response to the distributed load.
4. Compare the maximum shears and bending moments in the pile and compare them to the assumed allowable shear and moment for the timber pile based on ASTM D25.
5. Repeat Steps 2 through 4 using a new estimate of the friction angle until pile failure in shear or bending is reached. The friction angle that corresponds to the precipice of pile failure was considered the composite strength of the pile-soil zone.
6. For the analysis that corresponds to the precipice of pile failure, evaluate the shear modulus of the pile-soil zone as the applied stress from the distributed load divided by the strain evaluated from the pile deflection over the depth of the Sand and Sand-Silt Alluvium.

Based on our LPILE analyses, we evaluated the strength and shear stiffness of the pile-soil zone using the Mohr-Coulomb elastic-perfectly plastic model with a friction angle of 40 degrees and a shear stiffness of 23,000,000 psf. Other Mohr-Coulomb input properties such as damping and hysteretic behavior were modeled using the properties presented previously for Sand Alluvium during total stress analysis. To account for the pile batter for the Seawall foundations, pile-soil zones were included between the Seawall and existing Pier 1 foundation. Sensitivity analyses were performed and found that the estimated

deformations generally increased as the shear stiffness is decreased. Given the uncertainty in the condition, geometry, and installation depth of the foundation elements, additional studies and refinements may be performed during the NLTH phase of the project. Any additional studies and refinements will be documented in the subsequent NLTH geotechnical report.

8.1.5 Analysis Execution Process

Based on the model geometry, boundary conditions, and soil model constitutive parameters described previously, we performed 2D dynamic simulations using FLAC to evaluate the seismic hazards at the site. The model simulations were conducted in the following stages:

1. Define initial model geometry to approximate the ground conditions prior to construction of the existing Burnside Bridge and Seawall structure.
2. Initialize soil total stresses based on the assumed soil densities and an assumed horizontal stress coefficient of 0.5.
3. Set initial pore pressures and mechanical pressures applied at river mudline by the weight of the river water.
4. Assign elastic properties based on the site-specific shear wave velocity relationships.
5. Solve for static equilibrium assuming elastic conditions for all units.
6. Assign Mohr-Coulomb constitutive model to the appropriate soil units and resolve for static equilibrium.
7. Update the properties of the Seawall and existing Pier 1 foundations located below the ground surface, including the pile-soil zones, and resolve for static equilibrium.
8. Incrementally construct the Seawall structure located above the original ground surface until the existing top-of-wall elevation is achieved.
9. Place fill behind Seawall in one-element-high horizontal lifts, resolve for static equilibrium after each lift is placed.
10. For analysis that considered ground improvement, add the ground improvement zone and update the soil properties, resolve for static.
11. Assign the hysteretic constitutive model to the soil units. For the effective stress analysis, assign PM4SAND and PM4SILT constitutive model to the appropriate soil units and assign model parameters as described previously.
12. Assign the input ground motion at the base of the model as an upward propagating shear stress history. In our experience, the hysteretic, PM4SAND, and PM4SILT constitutive models tend to underdamp high frequency waves associated with small shear strains. Therefore, we applied 1 percent of stiffness-proportional Rayleigh damping at 10 Hz to the model. A water bulk modulus of 20 times the soil stiffness was assigned to the model so that shear strain-induced pore pressure increase (i.e., potential

liquefaction and pore pressure-induced cyclic softening) could occur in the appropriate soil units for the effective stress analysis.

13. Solve for the time dependent response of the model due to loading by the input earthquake ground motions.

Plots of the static stress conditions, summarized in terms of the vertical effective stress, at rest lateral earth pressure coefficient (defined as the ratio of the lateral stress to the vertical effective stress), K_0, and static shear stress ratio (defined as the ratio of the static shear stress to the vertical effective stress), α, evaluated just prior to the dynamic start of dynamic analysis (Stage 12) are provided in Figure H-4. The vertical stress conditions vary smoothly with depth across the model and reach maximum values of about 15,000 psf at the deepest model locations. The K_0 values are generally between 0.4 and 0.6 except in the vicinity of slopes where they are less than 0.4, and in the region of the concrete Seawall and Pier 1 foundations where they approach unity. In our opinion these values are considered reasonable because soils behind a fill wall, and between rigid concrete structures K_0 estimates are expected to be higher. The α values are generally below 0.1 for most of the alignment and are around 0.2 or larger near the ground surface in the vicinity of slopes and the concrete Seawall and Pier 1 foundations. These results are considered a reasonable estimate of the stress conditions at the site prior to dynamic loading.

8.1.6 Site Response Analyses Results

We performed our 2D site response analyses with the suite of base input motions described in Section 7 using the soil profiles, soil models, and implementation procedure described previously. Analyses were performed for both total and effective stress conditions per AASHTO requirements. The input motions were applied at the base of the 2D profile and the response to cyclic loading was computed. Our site response analyses for the model that did not consider ground improvement included both total and effective analyses using both 1,000-year probabilistic and deterministic CSZ input motion suites. Based on discussions with the design team, we understand that ground improvement at Bent 8 for the cable-stayed option may be required to mitigate the estimated displacements for the effective stress analysis at the 1,000-year probabilistic hazard level. We understand that based on the current preliminary design evaluations, it is not anticipated that ground improvement mitigation will be required for the tied-arch bridge option. Therefore, the model that considered ground improvement was evaluated for effective stress conditions using the 1,000-year probabilistic motion suite. The provided results represent free-field conditions at each of the proposed bridge bent locations. Plots summarizing the results of these analyses are presented in Appendix H and include:

- Contour plots showing the displacement, peak excess pore pressure ratio, and the maximum shear strain at the end of dynamic loading from the 2D analysis for the

proposed bridge alignment. As discussed in Section 8.2.3, post-seismic stability analyses were performed to evaluate the potential for deformation after the end of shaking and found that the post-seismic deformations were minimal and the models were stable at the end of dynamic loading. The provided contour plots include:

- Figures H-5 to H-13: Contours of total stress site response without ground improvement for the 1,000-year probabilistic hazard level,
- Figures H-14 to H-20: Contours of total stress site response without ground improvement for the deterministic CSZ hazard level,
- Figures H-21 to H-29: Contours of effective stress site response without ground improvement for the 1,000-year probabilistic hazard level,
- Figures H-30 to H-36: Contours of effective stress site response without ground improvement for the deterministic CSZ hazard level, and
- Figures H-37 to H-45: Contours of effective stress site response with ground improvement for the 1,000-year probabilistic hazard level.

- At each proposed bent location, we generated a summary figure that includes the generalized soil profile and plots of permanent, end of shaking, displacement, peak acceleration, peak shear strain, and peak pore pressure ratio as a function of depth for each of the analyses. The profile plots also include the average response of the applied motion suite. For the 1,000-year probabilistic hazard level the average was computed based on the seismic hazard deaggregation used to evaluate the seismic sources in the motion suite, as described in Section 7. The average response was computed by applying full weights to the three CSZ interface and crustal motions and using a weighting factor of one-third for the three applied CSZ intraslab motions. The displacement profiles for the 1,000-year probabilistic hazard level also shows the average response computed for each source individually. The deterministic CSZ hazard level only includes motions from a CSZ interface event; therefore, the direct arithmetic average is provided. These plots are provided in the following figures:
  - Figures H-46 to H-56: Profile plots of total stress site response without ground improvement for the 1,000-year probabilistic hazard level,
  - Figures H-57 to H-67: Profile plots of total stress site response without ground improvement for the deterministic CSZ hazard level,
  - Figures H-68 to H-78: Profile plots of effective stress site response without ground improvement for the 1,000-year probabilistic hazard level,
  - Figures H-79 to H-89: Profile plots of effective stress site response without ground improvement for the deterministic CSZ hazard level, and
  - Figure H-90: Profile plots of effective stress site response with ground improvement for the 1,000-year probabilistic hazard level response at Bent 8 for the cable-stayed option. Based on review of the results, the response at Bents 1 through 7 and Bents 9 and 10 were not significantly impacted by the presence of ground improvement at Bent 8 for the cable-stayed option.

Our seismic hazard evaluation based on the results of our site response analyses is presented in the following section. Interpretation and geotechnical design recommendations based on the results of our site response analyses and seismic hazard evaluations are presented in Sections 9 and 10.

8.2 Seismic Hazards Evaluation

The seismic hazards considered in our evaluations include ground shaking, liquefaction and cyclic strength degradation, permanent ground deformation, settlement, ground surface fault rupture, tsunami, and seiche. In our opinion, the potential for surface fault rupture is low. While it is estimated that there are portions of the Portland Hills and East Bank Faults within 1 mile of the bridge alignment, the estimated slip rates for both faults are low. In addition, the total length of the Portland Hills and East Bank faults are approximately 30.4 and 18 miles long, respectively. In our opinion, the likelihood of a ground surface fault rupture generated by these faults at the project site is low.

The risk of seismically induced tsunami and seiche is very low at the site given the project locations is over 60 miles inland from the Pacific Ocean (where a tsunami wave would initially reach landfall), and the Willamette River is not a closed water body (typically required for the occurrence of seismic seiche). Therefore, the primary seismic hazards at the site are ground shaking, liquefaction and cyclic strength degradation, permanent ground deformation, and settlement. Each of these hazards are discussed individually in the following sections.

8.2.1 Recommended Design Response Spectrum

We understand that for the current design phase, the ground shaking hazard for the proposed bridge will be evaluated using response spectra. We evaluated our recommended design response spectra for the proposed bridge based on AASHTO and the GDM. We developed the design response spectrum for both 1,000-year probabilistic and deterministic CSZ hazard levels based on the ground surface response at each of the proposed bent locations from our total and effective stress 2D site response analysis. For each hazard level and analysis method, we computed the surface response spectrum as well as the response spectral ratio, defined as the ratio of the surface response spectrum to the base input response spectrum, individually at each proposed bent location. Response spectra summary figures, showing the surface response spectra and the response spectral ratio evaluated at each proposed bridge bent location are provided in Appendix H as follows:

- Figures H-91 to H-101: surface response spectra summary for total stress analysis at the 1,000-year probabilistic hazard level,

- Figures H-102 to H-112: surface response spectra summary for effective stress analysis at the 1,000-year probabilistic hazard level,
- Figures H-113 to H-123: surface response spectra summary for total stress analysis at the deterministic CSZ hazard level, and
- Figures H-124 to H-134: surface response spectra summary for effective stress analysis at the deterministic CSZ hazard level.

The average surface response spectrum and response spectral ratio were evaluated for each hazard level. Summaries showing the average surface response spectrum and response spectral ratio at all proposed bent locations are provided in Figures H-135 and H-136 for the 1,000-year probabilistic hazard level total and effective stress analysis and Figures H-137 and H-138 for deterministic CSZ hazard level total and effective stress analysis, respectively.

Per AASHTO and the GDM, we evaluated our recommended ground surface design response spectrum based on the amplified surface response spectrum, computed as the design spectrum of the base input motions multiplied by the average response spectral ratio computed from our site response analysis. In addition, AASHTO and the GDM specify that the recommended design response spectrum developed from site response analysis cannot be less than two-thirds of the specification-based spectrum evaluated using site soil conditions without any modifications for liquefaction. We note that the subsurface conditions vary across the alignment. To account for this variability, we grouped the proposed bridge bent locations based on their AASHTO site classification evaluated based on our subsurface exploration and laboratory testing program and geologic interpretation. Based on our evaluations, the proposed bridge bent locations can be placed in two generalized groups corresponding to Site Class D and Site Class E conditions as follows:

- **Site Class D Bents:** Bents 1 through 5, Bent 9, and Bent 10.
- **Site Class E Bents:** Bents 6 and 7, Bent 8 cable-stayed, and Bent 8 tied-arch.

We developed our recommended ground surface design response spectrum for each bent group at each hazard level by plotting the amplified surface response spectra from both total and effective stress analysis for each individual bent in the given group. The target spectrum was developed by generating a smoothed envelope of the response from each bent while adhering to the code-based minimum requirements using specification-based spectrum evaluated per the GDM. The enveloping was performed in tripartite space and considered the spectral velocity and displacement in addition to spectral acceleration.

Figure H-139 shows our design response spectra development for the Site Class D bents at the 1,000-year probabilistic hazard level. The figure includes the amplified surface spectrum at each bent in the group for both total and effective stress analysis, as well as the

specification-based Site Class D spectrum and two-thirds of the specification-based spectrum. Our recommended ground surface design response spectrum corresponds to the approximate envelope of the individual pier response for periods below about 1 second. Beyond 1 second, the results of the site response analysis fall below the code-specified minimum and our recommended design spectrum followed two-thirds of the specification-based spectrum out to the maximum of the period range provided by the GDM. To evaluate our recommended design spectrum at periods beyond the maximum range provided by the GDM, we assumed a constant spectral displacement out to a period of 10 seconds. As shown in Figure H-139, this assumption effectively envelopes the results of our site response analysis at a period of 10 seconds.

The general process described above was repeated for the Site Class E bents at the 1,000-year probabilistic hazard level, as shown in Figure H-140, and for the Site Class D and E bents at the deterministic CSZ hazard level, as shown in Figures H-141 and H-142, respectively. Linear-linear plots of our recommended design response spectrum for the 1,000-year probabilistic and deterministic CSZ are shown in Figures 8-1 and 8-2, respectively. Tabulated values of our recommended ground surface response spectra are provided for the 1,000-year probabilistic and deterministic CSZ in Tables 8-1 and 8-2, respectively.

8.2.2 Seismically Induced Excess Pore Pressure Development and Post-seismic Soil Strength

Our subsurface investigation and laboratory testing program identified soils that are susceptible to strength loss due to the generation of excess pore pressures during seismic loading. These included loose to medium dense, predominantly sandy soils, that are susceptible to liquefaction, and low to medium plasticity predominantly fine-grained soils that are susceptible to cyclic strength degradation. We evaluated the post-seismic strength of these soils based on the results our effective stress site response analysis, the subsurface exploration and laboratory testing program, and available literature. Post-seismic strengths were used to evaluate the potential for post-seismic deformations as described in Section 8.2.3 and to support lateral drilled shaft analyses as described in Section 10.2.

For soils that were susceptible to liquefaction, liquefaction was considered to occur when the excess pore pressure ratio exceeds 0.9. The relationship between the excess pore pressure ratio and the factor of safety (FS) against liquefaction is nonlinear and depends on the characteristics of the given soil deposit (i.e., gradation, particle shape, etc.). Based on the excess pore pressure ratio versus FS against liquefaction chart provided by Tokimatsu and Yoshimi (1983), an excess pore pressure ratio of 0.9 generally corresponds to an FS against liquefaction of approximately 1.1 for typical clean sands. The FS against liquefaction criteria of 1.1 is based on guidance provided in GDM Section 6.5.2.1.

As shown in the contour plots presented previously, in general our effective stress analyses estimate that liquefaction will occur in the portions of the Sand Alluvium near the ground surface located in the river channel and near the toe of the east riverbank. High excess pore pressures in these areas were observed for both the 1,000-year probabilistic and deterministic CSZ hazard levels but were more pronounced at the 1,000-year probabilistic hazard level. Our analysis also indicated areas where significant excess pore pressures were developed but were less than the established criteria for liquefaction.

For soils considered susceptible to excess pore pressure generation during cyclic loading, the post-seismic shear strength was reduced as a function of the excess pore pressure ratio. When the criteria for liquefaction was reached, the soil shear strength was reduced to the residual strength value. Residual strength values were established based on the procedures provided in GDM Section 6.4.1 which express the residual strength as a function of in-situ test data and initial stress conditions. For pore pressure ratios below the liquefaction criteria, the post-cyclic strength was reduced using a linear relationship between the soil's static and residual strength estimates.

Most of the soils located west of the existing Seawall and on the east riverbank were evaluated as predominantly fine-grained soils that are susceptible to cyclic strength degradation. The post-seismic strengths for these soils were evaluated based on the results of our laboratory test program, which included post-cyclic direct simple shear data. The results of these tests are summarized in Exhibit 8-24 which plot the ratio of the post-cyclic strength mobilized at 5 percent shear strain to the static shear strength (estimated using the site-specific relationship defined previously and static strength tests where available) as a function of the peak excess pore pressure ratio developed during the cyclic portion of the test. The available laboratory data shows there is relatively little strength reduction when the peak excess pore pressure ratio is less than approximately 0.5. These results are consistent with the behavior observed in similar tests performed on Willamette and Columbia River silts (e.g., Beaty and others, 2014). We note that review of additional post-cyclic testing is underway and will be included in the evaluations performed as part of future NLTH design efforts.

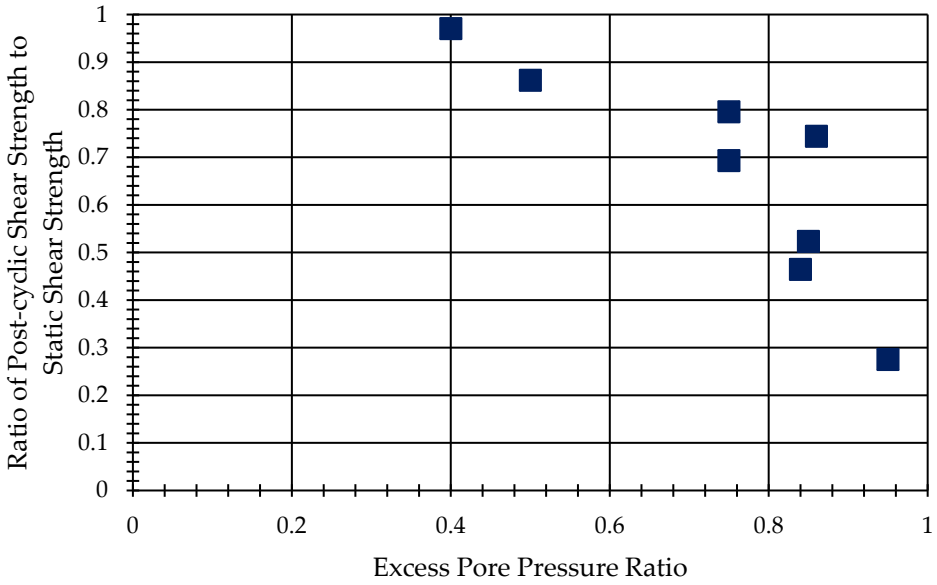

Exhibit 8-24: Post-cyclic Strength as a Function of Excess Pore Pressure Ratio

The post-seismic strengths in the soils susceptible to cyclic strength degradation were evaluated based on the pore pressure response estimated in our effective stress site response analysis and the results of the post-cyclic strength testing. As observed in our effective stress analysis summary plots, the excess pore pressure ratios estimated from our analysis in the predominantly fine-grained soils were generally less than 0.4 and the post-cyclic strength reduction was generally modest.

8.2.3 Seismically Induced Permanent Ground Deformation

The contour plots presented previously show the distribution of permanent ground deformation across the alignment. The profile plots presented previously provide the estimated permanent deformation response as a function of elevation at each of the proposed bent locations. Note that the displacements at the proposed bent locations represent free-field conditions and do not consider the effect of the proposed bridge foundations on the predicted displacements. Our analysis indicated that the permanent deformations at the site were primarily controlled by inertial effects combined with a strength reduction in soils susceptible to excess pore pressure generation and/or cyclic strength degradation. We considered the potential for post-seismic deformations under static conditions assuming residual soil strengths. For select analyses, the post-seismic deformation was evaluated as follows:

1. The peak excess pore pressure in each element modeled as PM4SAND or PM4SILT (see Section 8.1.2.3) was obtained, and the post-seismic strength was evaluated per Section 8.2.2.

2. All elements modeled as PM4SAND or PM4SILT during the dynamic analysis were switched to Mohr-Coulomb model and assigned strengths developed in Step 1.
3. Using the post-cyclic strengths and model geometry from the end of shaking, the model was brought to equilibrium by continuing the simulation for an additional 30 seconds under gravity loading only. Review of the displacement and velocity response of the model was performed to confirm that 30 seconds was sufficient to bring the model to static equilibrium.

An example of the post-seismic strength assignments is shown in Figure H-143, which provides contours of the peak excess pore pressure ratio and the corresponding post-seismic strengths, expressed as the ratio of the initial vertical effective stress, for the pore pressure conditions estimated following the 1,000-year probabilistic Northridge motion. The estimated residual strength ratios are on the order of 0.08 to 0.12 in areas of the Sand Alluvium and Sandy Sand-Silt Alluvium that experienced large excess pore pressure ratios. The Fine-grained Alluvium and Silty Sand-Silt Alluvium showed post-seismic strengths generally in the range of 0.2 to 0.35 that varied both with depth and with the distribution of excess pore pressure ratio across the profile. Typical results of the post-seismic deformation analysis are shown in Figure H-144, which provides contours of the permanent displacement at the end of shaking and following post-seismic static equilibrium as well as a contour of the difference between the end of shaking and post-seismic displacements based on the end of shaking conditions summarized in Figure H-143. Our post-seismic analyses showed that the difference between the post-seismic and end of shaking displacements were generally less than 1 percent throughout the profile and less than 0.5 percent at the proposed bridge bent locations, indicating the model was stable after shaking and the end of shaking and post-seismic displacements were considered equivalent.

In general, our effective stress analysis predicts that significant permanent ground deformations will occur within approximately 100 feet of the existing Seawall, within the river channel, and along the slope east of the river channel. The maximum deformations predicted in our analysis occur within the slope east of the river channel, with a maximum estimated displacement of 15.9 feet during the 1,000-year probabilistic hazard level. We note that the 2D site response analyses presented in this report assumed existing conditions for the mudline within the river channel. We understand that the design team is planning on regrading the mudline elevations within the channel as part of the construction of the proposed bridge. Final mudline elevations were not available for the analyses presented in this report. We understand that the mudline elevation in the channel will be graded to be relatively flat, with mudline elevations generally ranging between -55 and -60 feet, and will remove the steep topographic features in the vicinity of the in-water pier locations. In our opinion, the regrading activities will significantly reduce the magnitude and depth of the displacements currently estimated at the in-water bents. Estimates of the displacement at

the in-water bent locations based on the updated future mudline elevations will be developed and documented in the subsequent NLTH design efforts.

At the proposed bridge bent locations, our analyses estimate that seismically induced permanent ground deformations will develop at Bents 5, 6, 7, and both of the considered Bent 8 options. The average permanent deformations estimated from our effective stress site response analyses at these Bents varied between 1 inch and 4 feet depending on the Bent location and seismic hazard level considered. During the total stress analysis, which did not consider the generation of excess pore pressures, the permanent displacements were significantly lower. Our analyses that considered ground improvement at the proposed Bent 8 for the cable-stayed option indicated that ground improvement could significantly reduce the estimated permanent ground deformations. Including ground improvement reduced average estimated permanent displacement from approximately 10.5 inches to approximately 1.5 inches at cable-stayed Bent 8 for the 1,000-year probabilistic hazard level. A summary of the average permanent ground deformations from the effective stress analysis at Bents 5, 6, 7, and 8 are summarized in Exhibit 8-25.

Exhibit 8-25: Average Permanent Ground Displacement from Effective Stress Analysis

Bent	Average Permanent Displacement (inches)	
	1000-year Probabilistic Hazard Level	Deterministic CSZ Hazard Level
5	5	1
6	26	8.5
7	48	22
8 Cable-stayed Tower (No Ground Improvement)	10.5	7
8 Cable-stayed Tower (With Ground Improvement)	1.5	NA
8 Tied-arch	4	3

At Bents 1 through 4, 9, and 10, the permanent ground deformations were observed to be small, generally less than 0.5 inches, and the displacement trends across individual ground motions were inconsistent (see Appendix H). The small permanent displacements estimated at these piers are considered a minor artifact of the numerical modeling and are likely due to the polarity of the ground motion. We note that the bridge abutments at Bents 1 and 10 were not included in our model. Considerations for the seismic performance of the bridge abutments will be evaluated using conventional methods as part of future design efforts.

Ground improvement recommendations to mitigate permanent ground deformations are presented in Section 9. The effects of permanent ground deformations on the proposed new foundations are presented in Section 10 of this report.

8.2.4 Seismically Induced Settlement

Soils that generate excess pore pressures during cyclic loading are also susceptible to seismically induced densification and settlement after the pore pressures dissipate following earthquake loading. For the predominantly sandy soils that were susceptible to liquefaction, we estimated the seismically induced settlement using the method of Ishihara and Yoshimine (1992), which relates the peak shear strain observed during cyclic loading to post-cyclic volumetric strain. We estimated the cyclic shear strain using the average of the maximum shear strains that developed during shaking at each seismic hazard level as evaluated from our effective stress site response analysis. For the predominantly fine-grained soils, seismically induced settlement was estimated using the results of the laboratory test program, which included post-cyclic consolidation testing, summarized in Exhibit 8-26 as the post-cyclic volumetric strain as a function of the peak excess pore pressure developed during the cyclic portion of the test. These results are consistent with the behavior observed in similar tests performed on Willamette and Columbia River silts (e.g., Beaty and others, 2014).

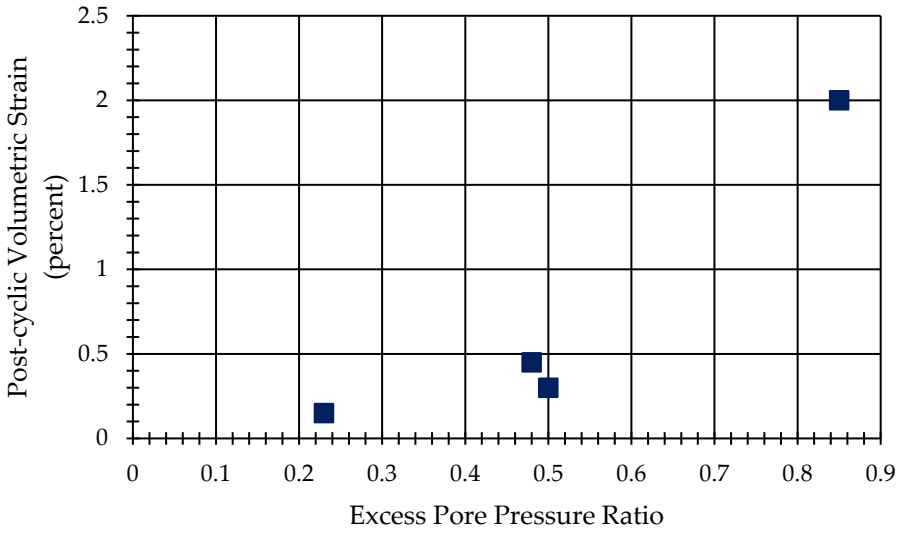

Exhibit 8-26: Post-cyclic Volumetric Strain as a Function of Excess Pore Pressure Ratio

We estimated the seismically induced settlement for the predominantly fine-grained soils based on the excess pore pressure ratio using the average pore pressure ratio that developed during shaking at each seismic hazard level as evaluated from our effective stress site

response analysis and the volumetric strain-excess pore pressure relationship developed from the available laboratory test data.

Once estimates of volumetric strain were obtained, the estimated settlement response was computed by integrating the volumetric strains with depths. Plots summarizing our settlement evaluations are provided at each proposed bent location in Figures H-145 to H-155 and H-156 to H-166 for the 1,000-year probabilistic and deterministic CSZ hazard levels, respectively. Tabulated values of the ground surface settlement evaluated at each Bent is provided in Exhibit 8-27.

Exhibit 8-27: Average Seismic Settlement Based on Effective Stress Analysis

Bent	Average Seismic Settlement (inches)	
	1,000-year Probabilistic Hazard Level	Deterministic CSZ Hazard Level
1 through 5	< 0.5	< 0.5
6	2.5	2
7	7.5	7.5
8 Cable-stayed Tower	1.5	1
8 Tied-arch	1.5	1
9 and 10	< 0.5	< 0.5

9 SEISMIC MITIGATION GROUND IMPROVEMENT RECOMMENDATIONS

We understand that based on the results of the seismic hazard evaluation, ground improvement mitigation at the east riverbank may be needed to achieve the required performance criteria of the large diameter drilled shafts located at Bent 8 cable-stay option tower due to seismically induced permanent ground deformation. To facilitate the bridge type selection process, we performed preliminary ground improvement evaluations. Our evaluations considered a variety of ground improvement alternatives such as jet grouting, stone columns, cement deep soil mixing, densification, and drainage. If ground improvement is required for final design, the recommendations provided in this section will need to be revisited as more information such as final bridge geometry and seismic performance criteria for the ground improvement becomes known.

Based on our nonlinear site response analyses for the 1,000-year probabilistic hazard level, seismically induced permanent ground deformations on the order of 1 foot were estimated for the east side of the river along the bridge alignment. The primary zone of permanent deformation at the east riverbank is within the Sand/Silt Alluvium layer between approximate Elevation 0 and -105 feet, as shown on Figure 9-1. Based on conversations with

the design team and their preliminary analysis, we understand the proposed bridge may not be able to accommodate the estimated deformations at cable-stay option Bent 8 location on the east side of the river. To reduce these deformations, we considered ground improvement at the Bent 8 cable-stay tower area. We have considered three ground improvement alternatives that are practical to implement at this site: stone columns, jet grouting, and cement deep soil mixing. These ground improvement methods contribute to improving performance of the soil by densifying (stone columns) or "reinforcing" (jet grouting and deep soil mixing) the zones susceptible to seismic deformation to improve the soil strength and reduce permanent ground deformation during the design seismic events.

9.1 Seismic Mitigation Ground Improvement Alternatives

Ground improvement methods that are typically used for liquefaction and seismic deformation mitigation include excavation and replacement, soil densification (e.g., vibro-compaction, deep dynamic compaction), drainage (e.g., EQ Drain), soil reinforcement (e.g., jet grouting, deep soil mixing), or a combination of methods such as soil densification and drainage (e.g., stone columns) or soil densification and reinforcement (e.g., compaction grouting). The selection of appropriate mitigation method(s) for a particular site depends on factors such as soil type (fines content, organic content, pH, etc.), site access, right-of-way constraints, cost, environmental concerns, and vibration impacts on existing facilities, among others.

Based on our understanding of the site conditions, stone columns, jet grouting, and cement deep soil mixing will be the most feasible and economical ground improvement methods. The following table discusses the advantages and disadvantages of each method.

Exhibit 9-1: Comparison of Ground Improvement Alternatives

Alternative	Description	Advantages	Disadvantages
Stone Columns	Install stone columns in the Fine-grained Alluvium and the Sand/Silt Alluvium to densify or reinforce the native soils, in a square or triangular pattern. The typical area replacement ratio is at least 25 percent.	▪ Lower up front construction costs. ▪ Relatively simple construction quality control. ▪ Relatively conventional ground improvement construction.	▪ Densification is not feasible due to the relatively high percentage of fines in the soils. ▪ Larger ground improvement area is required which is not available due to constrained site conditions. ▪ Potential for vibration impacts on existing railroad and buildings.

Alternative	Description	Advantages	Disadvantages
Improved Soil Mass (Jet Grouting)	Construct continuous jet grout columns in the Fine-grained Alluvium and the Sand/Silt Alluvium in a grid pattern. The typical area replacement ratio is at least 50 percent.	▪ Improves soil shear strength much more effectively than stone columns; therefore, provides much more resistance within relatively a small area compared to stone columns. ▪ Can penetrate dense gravel layers. ▪ Better precision for grouting near existing foundations compared to deep soil mixing.	▪ Construction generates significant surface spoils. ▪ Potentially difficult environmental permitting. ▪ Relatively difficult construction quality control. ▪ Most expensive alternative. ▪ Potential negative impact on the existing railroad, such as heaving concerns. Careful design and construction approach is required.
Improved Soil Mass (Deep Soil Mixing)	Construct continuous soil mixing columns in the Fine-grained Alluvium and the Sand/Silt Alluvium in a grid pattern. The typical area replacement ratio is at least 50 percent.	▪ Improves soil shear strength much more effectively than stone columns; therefore, provides much more resistance within relatively a small area compared to stone columns. ▪ Relatively low construction cost compared to jet grouting.	▪ Construction generates significant surface spoils. ▪ Potentially difficult environmental permitting. ▪ Relatively difficult construction quality control. ▪ Existing timber pile foundations will be obstructions for the deep soil mixing equipment.

Stone column ground improvement is not the preferred seismic mitigation alternative due to the high fines content of the soil, which will make it not feasible to sufficiently densify the soil.

Deep soil mixing or jet grouting, or a combination of both, are the preferred ground improvement alternatives at the cable-stay option Bent 8 location. The existing bridge Bent 25 is supported on timber piles, and timber piles or other buried obstructions may be present near the railroad. Deep soil mixing is not feasible within the existing timber pile areas unless the piles are removed completely. The remainder of this section presents our geotechnical design recommendations and construction considerations for construction of Improved Soil Mass (ISM), including ISM-jet grouting and ISM-deep soil mixing, ground improvements at the site.

9.2 Design Recommendations for ISM at Bent 8 (Cable-Stay Tower)

The jet-grouting method of soil improvement uses a modified rotary drill to inject water, cement, and air into the soil under pressure, simultaneously mixing and replacing the soils with cement grout to create a concrete-like soil column. The jet -grouting method uses a small-diameter drill to penetrate the soil to the desired depth. The injection of water, cement, and air begins at the bottom of the hole and continues upward to the desired elevation. It is the small initial diameter of the jet -grouting method that allows this method to be used where dense gravel layers need to be penetrated. Jet grouting ground improvement will construct a series of overlapping soil-cement cylindrical columns to form a grid of soil-cement panels surrounding unimproved soil, which will improve the strength

and stiffness of the existing soil. This method can be used to construct soil-cement columns that typically range from 2 to 10 feet in diameter, dependent on jet grouting methods.

Jet grouting typically produces spoil volumes equal to about 80 to 100 percent of the volume of soil treated (i.e., area replacement ratio multiplied by the total soil volume in the ISM). This spoil material will consist of a blend of eroded soil and cement grout with a pH value greater than 10 (considered a hazardous material) that is flushed to the ground surface during jet grouting. Based on the information provided by HDR (Hazmat subconsultant), the upper 25 feet of soils in borings B-17 and B-33 (which were drilled within the proposed ground improvement footprint) are contaminated. Therefore, the jet grouting spoils may need to be disposed of at a landfill site.

Deep soil mixing (DSM) ground improvement consists of constructing a grid of soil-cement panels surrounding unimproved soil, similar to jet grouting. This method can be used to construct soil-cement columns that typically range from 2 to 8 feet in diameter. A series of overlapping columns would be used to construct the soil-cement panels in a cellular configuration. The interior cells of the improved soil mass would consist of unimproved soil.

DSM is accomplished by advancing a drill (mixing tool) into the soil while pumping a cement slurry through the connecting drill steel and mixing the soil to the target depth. Additional mixing of the soil is completed as the tool is withdrawn to the surface. This process constructs individual soilcrete columns that are typically constructed to overlap, forming a row of soilcrete that improves the strength and stiffness of the existing soil.

The ease of mixing depends on the soil type, strength, water content, plasticity, stratigraphy, and texture. With wet soil mixing, treatment is possible to depths up to 100 feet. Excess soilcrete generated may range from 30 to 50 percent of the treated volume (i.e., area replacement ratio multiplied by the total soil volume in the ISM). This spoil material will consist of a blend of soil and cement grout with pH value greater than 10 (considered to be hazardous material) that is returned to the ground surface during mixing. Based on the information provided by HDR (Hazmat subconsultant), the upper 25 feet of soils in borings B-17 and B-33 (which were drilled within the proposed ground improvement footprint) are contaminated. Therefore, the DSM spoils may need to be disposed of at a landfill site.

A single or multiple column test program is often performed at the beginning of jet grouting or DSM construction to determine the injection or mixing energy, penetration rate, batching, and pumping operations. Many specialty contractors who perform this work use proprietary equipment and software for real-time monitoring of all injection parameters during the jet grouting or soil mixing process.

9.2.1 ISM Configuration and Seismic Deformation

The main purpose of the ISM ground improvement at Bent 8 of the cable-stay option is to reduce the additional lateral load on the proposed drilled shaft foundations at Bent 8 (cable-stay tower) resulting from seismically induced permanent ground deformations. The proposed ISM zone, as shown in both plan and profile in Figure 9-1, would reduce the seismically induced permanent ground deformation, which would reduce the additional lateral load on the Bent 8 cable-stay tower foundation.

We understand the required ISM configuration is controlled by the estimated permanent ground deformation at Bent 8 cable-stay tower location during the 1,000-year probabilistic seismic hazard level. Therefore, the 1,000-year probabilistic seismic ground motions were used in the ISM configuration evaluations. The depth and longitudinal extents of the ISM were developed based on an iterative process utilizing the nonlinear site response model to generate the estimated maximum tolerable soil lateral displacement at Bent 8 cable-stay tower, which was set by the structural engineer, that can be accommodated by the cable-stay bridge option. The preliminary extents of the ISM zone are developed based on the requirement to cover the proposed drilled shaft locations and the site constraints for the railroad (to the west), including potential negative impacts on the railroad. The estimated average soil lateral displacements for the 1,000-year probabilistic hazard level at the Bent 8 cable-stay tower location for pre-ISM and post-ISM conditions are shown in Exhibit 9-2.

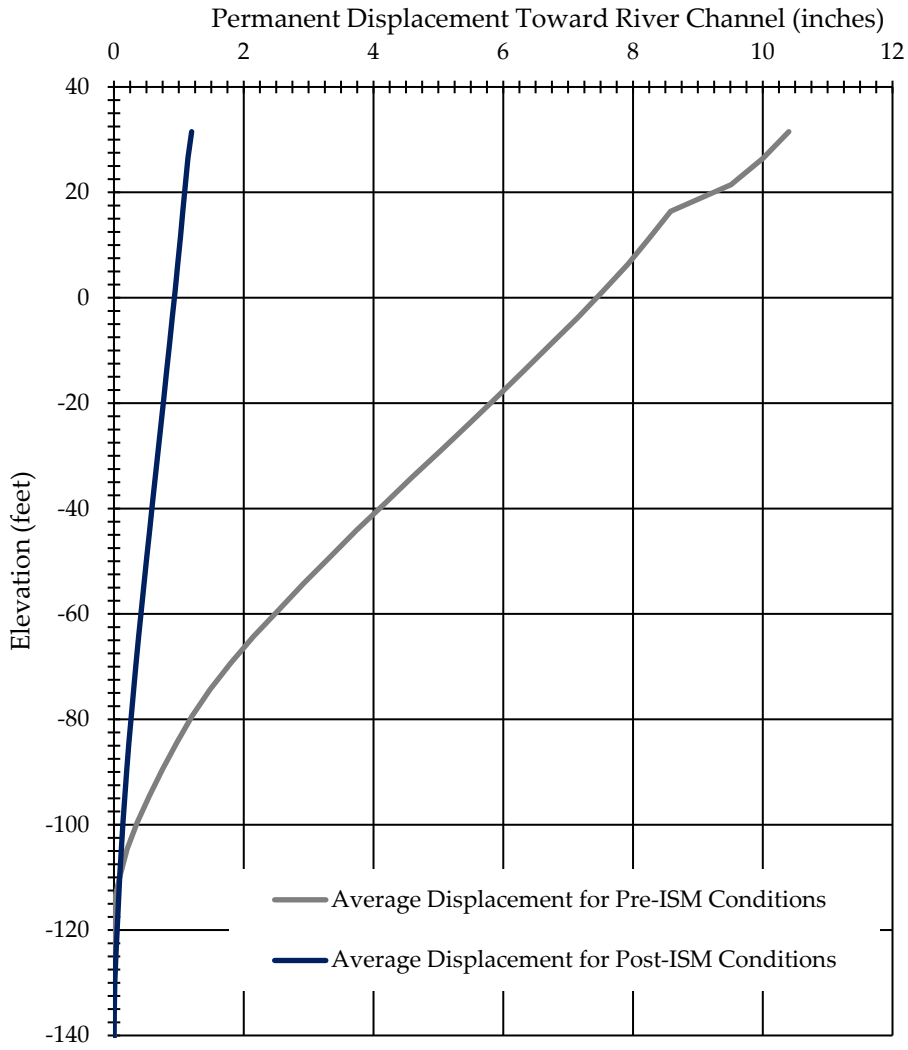

Exhibit 9-2: Comparison of Estimated Average Soil Lateral Displacement During the 1,000-year Probabilistic Seismic Hazard Level at Bent 8 Cable-Stay Tower for Pre- and Post-ISM Conditions

Based on the results of the nonlinear site response modeling analysis, the preliminary ISM configuration required to develop the tolerable lateral displacement at the Bent 8 location of the cable-stay option is approximately 100 feet wide, 105 feet long, and approximately 145 to 155 feet below ground surface (bottom elevation of approximately -114 feet), as shown on Figure 9-1. This includes an embedment of 5 feet into the Gravel Alluvium. Due to the difficulty of performing jet grouting and DSM within the dense Gravel Alluvium, subsequent nonlinear site response analyses performed during the NLTH design phase will consider modelling the ISM zone without any penetration into the Gravel Alluvium. We anticipate jet grouting or DSM will be performed to the top of the dense to very dense Gravel Alluvium as confirmed by drill action and/or refusal. Additionally, the proposed

ISM requires an average composite shear strength of 150 pounds per square inch (psi) (see Section 8.1.3).

9.2.2 Improved Soil Properties and Required Area Replacement Ratio

As described in Section 9.2.1, the proposed ISM requires an average composite shear strength of 150 psi. We designed the ISM with a minimum area replacement ratio (improved soil volume as a percentage of total soil volume in the ISM) of 55 percent to limit liquefaction potential of unimproved soil within the ISM and limit the required average soil-cement unconfined compressive strength to less than 500 psi. In our opinion, 500 psi average soil-cement unconfined compressive strength is near the upper limit of achievable soil-cement strength at this site based on the subsurface conditions and using jet grouting or DSM methods. To determine the required average shear strength of the soil-cement, the ISM composite shear strength was proportioned to account for the lesser shear strength of the unimproved soil between the soil-cement grids as follows:

- Soil-cement shear strength: $S_{sc} = [S_{comp} - S_{soil} * (1 - A_r)] / A_r$
- where A_r = area replacement ratio = $Volume_{ism} / Volume_{total}$, S_{soil} = shear strength (peak or residual) of unimproved soil, S_{comp} = ISM composite shear strength, and S_{sc} = soil-cement column shear strength

Due to the low shear strength contribution from the unimproved soil between the soil-cement grids relative to the required composite shear strength of 150 psi, the required average soil-cement shear strength is 272 psi for a 55 percent area replacement ratio.

The required average value for the unconfined compressive strength (UCS) of the soil-cement (q_{sc}) is determined based on the recommended procedure in the Federal Highway Administration (FHWA) Design Manual: Deep Mixing for Embankment and Foundation Support (FHWA, 2013). This method uses factors to account for the effect of soil-cement curing time between soil mixing and application of design loads on the ISM, in this case lateral spreading at the riverbank from a design seismic event, and the effect of strain softening on the unconfined compressive strength of the soil-cement (f_r). For the geotechnical design analyses presented in this report, we assumed 365 days between ground improvement and application of design loads on the ISM. This means that the required design unconfined compressive strength of the ISM will be achieved one year after completion of ISM construction.

- Soil-cement UCS (28-day): $q_{sc} = 2 * [S_{sc} / (f_r * f_c)]$

The UCS of soil-cement by jet grouting or deep soil mixing is reported to be in the range of 20 to 1,250 psi depending on soil type, subsurface conditions, and method of installation (FHWA, 2017). Adverse subsurface conditions (such as organic content greater than 10

percent, or poor construction practice) could result in lower UCS values. For the analyses presented in this report, except where noted, an average soil-cement UCS value of 460 psi was used for the ISM at Bent 8 cable-stay option tower location. Note that, based on the distribution of test results that are commonly obtained in jet grouting and deep soil mixing projects, the specifications indicate that the 28-day UCS that must be achieved in the field will consist of the following:

- A minimum of 90 percent of the UCS 28-day Test Specimens must be equal to or greater than 150 psi.
- A minimum of 50 percent of the UCS 28-day Test Specimens must be equal to or greater than 460 psi.

The soil-cement properties used in the design analyses presented in this report are summarized in Exhibit 9-3.

Exhibit 9-3: Summary of Soil-Cement Properties Used for ISM Design at Bent 8 Cable-Stay Tower

Design Parameter	Design Value
Average Soil-Cement 28-day UCS, q_{sc}	460 psi
Residual Compressive Strength Factor, f_r	0.8
Soil-Cement Curing Factor, f_c	1.48
Average Shear Strength of Soil-Cement Columns, S_{sc}	272 psi
Required Area Replacement Ratio, A_r	55%
Average ISM Composite Shear Strength, S_{comp}	150 psi

9.2.3 ISM Stability Analyses

After development of the ISM configuration and the minimum required ISM shear strength and area replacement ratio, we evaluated stability of the ISM block in accordance with the recommendations presented in the FHWA Deep Mixing Manual (FHWA, 2013) for the following failure modes: combined overturning and bearing capacity, crushing of soil-cement columns at the ISM toe, sliding, and shearing between soil-cement columns. The evaluations were performed for post-seismic conditions and did not account for any embedment into dense Gravel Alluvium.

In accordance with the recommendations presented in the FHWA Deep Mixing Manual (FHWA, 2013), a factor of safety (FS) of 1.1 was used for post-seismic conditions for each failure mode. For each failure mode, in accordance with the FHWA recommendations, the appropriate FS was applied to the shear strength of the soil to determine a mobilized shear strength (i.e., strength reduction technique).

The base width of the ISM is considered to be sufficient to resist combined overturning and bearing capacity failure if the horizontal distance (x_n) from a point "O" at the toe of the ISM to the resultant of the total normal force acting upwards on the base of the ISM is greater than zero. According to the FHWA recommendations, if x_n is greater than one-half of the ISM base width (B/2) then evaluation of crushing of soil-cement columns at the ISM toe and shearing between soil-cement columns is not required. A definition sketch for the combined overturning and bearing calculations is shown in Exhibit 9-4, below.

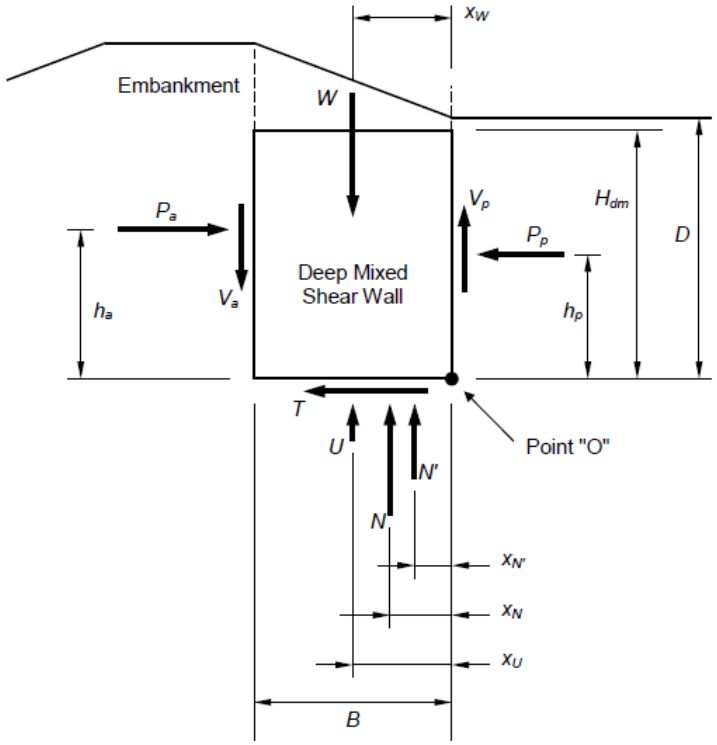

Exhibit 9-4: Definition Sketch for Combined Overturning and Bearing Calculations (FHWA, 2013)

For the sliding evaluation, we compared the horizontal driving force on the ISM to the interface friction resistance between the base of the ISM and Gravel Alluvium. The friction resistance was calculated as the total normal force acting upwards on the base of the ISM multiplied by a coefficient of friction. To determine the composite coefficient of friction (μ_{comp}) for sliding evaluation, the soil-cement coefficient of friction (μ_{sc}) was proportioned to account for the lesser coefficient of friction of the unimproved soil between the soil-cement grids (μ_{soil}). Coefficient of friction was proportioned by the volume of improved soil and volume of unimproved soil as:

- $\mu_{comp} = \mu_{sc} * A_r + \mu_{soil} * (1 - A_r)$
- where A_r = area replacement ratio = $Volume_{ism}$ / $Volume_{total}$, $\mu_{soil} = 0.7$, and $\mu_{sc} = 0.6$.

We used an ultimate composite coefficient of friction of equal to 0.65 to calculate sliding resistance. The appropriate FS was applied to the ultimate coefficient of friction.

Based on our stability evaluation, the required depth and longitudinal extents of the ISM that were developed based on the nonlinear site response modeling are sufficient to resist combined overturning and bearing capacity, crushing of soil-cement columns at the ISM toe, and sliding. The required overlap of the soil-cement columns is governed by the shearing evaluation.

9.2.4 Recommended ISM Design Dimensions and Parameters

The minimum recommended ISM footprint and location at the cable-stay option Bent 8 is shown on Figure 9-1. Exhibit 9-5 provides preliminary ISM design dimensions and parameters based on the results of our analyses. We recommend the ground improvement contractor be responsible for selecting a soil-cement column layout and diameter that meets the recommended parameters and dimensions in Exhibit 9-5 and provides a closed cellular grid configuration. A definition sketch for the soil-cement column dimensions referenced in Exhibit 9-5 is shown in Exhibit 9-6, below.

Exhibit 9-5: Recommended Design Dimensions and Parameters for ISM at Bent 8 Cable-Stay Tower

Design Parameter	Design Value
Minimum Average (50th Percentile) 28-day Soil-Cement UCS	460 psi
Minimum 90th Percentile 28-day Soil-Cement UCS	150 psi
Minimum Top Elevation of ISM	29 feet
Minimum Bottom Elevation of ISM	-110 feet
Minimum Soil-Cement Column Diameter, d	3 feet
Maximum Soil-Cement Column Diameter, d	10 feet
Minimum Soil-Cement Column Overlap to Diameter Ratio, e/d	0.2
Minimum Area Replacement Ratio	55%

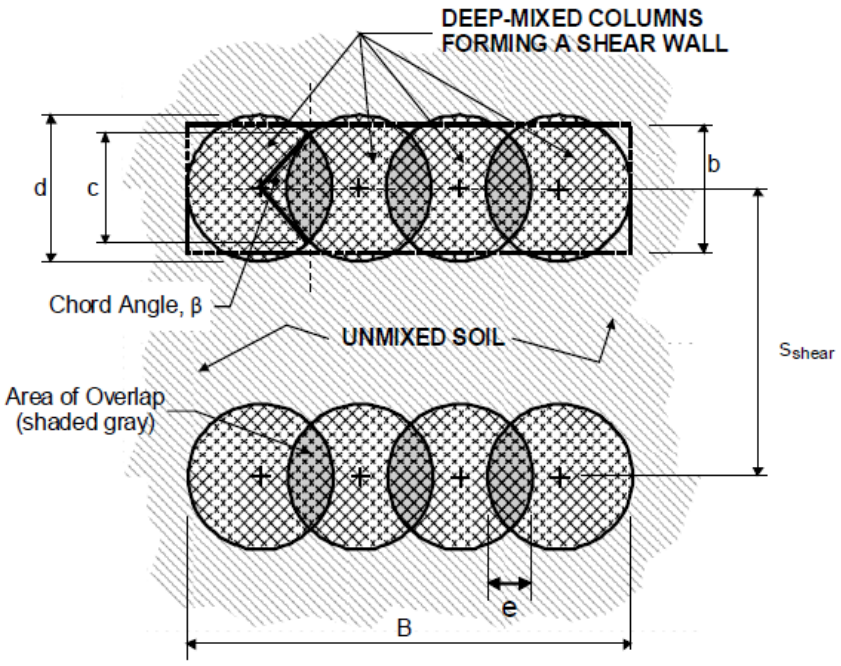

Exhibit 9-6: Definition Sketch for Soil-Cement Column Dimensions (FHWA, 2013)

9.3 Geotechnical Risks and Mitigation Solutions

There are a number of geotechnical risks related to the ground improvement construction for this project. Due to the complexity of the ground improvement construction for this project, we recommend contractor selection be qualification-based. The following sections summarize the risks related to the proposed ground improvement construction and state the general approach at the final design stage to address respective risks, when feasible.

- **Risk:** Borings show a high level of subsurface variability which can lead to a wide range of achieved soil-cement strengths. If the required soil-cement strength cannot be met, the area replacement ratio will need to be increased.
  - *Mitigation:* The project-specific special provision section for Improved Soil Mass construction will require the contractor to perform a Pre-Construction Mix Design Testing Program (bench-scale testing) by obtaining samples of the soils to be improved and mixing with grout in the laboratory to determine the optimum grout mix that will meet the specified strength. The specifications will also allow the contractor to propose changing the specified soil-cement strength by changing the minimum area replacement ratio. However, while the project specifications and a bench-scale testing program can help reduce this risk, we recommend additional contingency funds be set aside for ground improvement related claims as a result of highly variable subsurface conditions.
- **Risk:** The deep soil mixing and jet grouting processes generate soil-cement waste, which must be properly disposed of. With Agency approval, this material can be re-

used for general on-site fill above the ordinary high water/groundwater level, such as backfill of temporary excavations for the ISM construction, but is not recommended for roadway embankments or backfill around structures that may be sensitive to high pH soils (such as metal culverts). This material can only be left on site if environmental regulations permit, as it is typically found to have a high pH value.

  - *Mitigation:* If the spoils cannot be re-used on site, they must be transported and disposed of off-site at a facility qualified to handle the spoils, which is a significant cost depending on the quantity of spoils. These costs may be significantly less if the Agency has a nearby disposal site capable of accepting the ISM spoils. We understand that the current construction cost estimate assumes off-site disposal of all spoils by the contractor. Therefore, if the spoils are re-used on-site or disposed of at an Agency site, the Agency may need to negotiate a reduction in cost with the contractor.

- **Risk:** Deep soil mixing and jet grouting generate significant surface spoils, which if not managed properly, may migrate into storm drains or nearby bodies of water. The ground improvement contractor will need to work closely with the general contractor to manage and dispose of the spoils properly and coordinate the ground improvement construction with other operations at the site.
  - *Mitigation:* Specifications will require the contractor to submit detailed equipment set up and construction site layout including storage areas, staging areas, mixing plant locations, haul routes, work platform areas, and description of coordination of the ground improvement construction activities with other construction activities at the site. Specifications will also require the contractor to submit and comply with a Spoils Management Plan which will include containment measures to keep grout and spoils from migrating off-site, including into regulated work zones, no work zones, storm drains, or railroad right-of-way.

- **Risk:** We understand an existing Bureau of Environmental Services (BES) 30-inch diameter, corrugated metal pipe (CMP) storm drain is running through the proposed ground improvement zone. We understand the storm drain is located at a depth of approximately 13 feet and is running in an east-west orientation. The existing pipe would likely be significantly impacted during ground improvement construction. Additionally, there is a risk of grout migrating into the existing pipe backfill on either side of the ground improvement zone. The existing pipe also appears to conflict with the proposed pile cap.
  - *Mitigation:* We recommend that the project includes permanent relocation of the existing CMP storm drain outside the footprint of the proposed pile cap and ground improvement zone. Additionally, the ends of the existing pipe and backfill on either side of the ground improvement zone should be properly sealed during pipe relocation to prevent grout spoils from infiltrating the existing pipe and backfill.

- **Risk:** Potential obstructions such as existing timber piles at Bent 25 and near the railroad may be encountered during jet grouting and deep soil mixing and result in

change orders due to relocation and/or addition of soil-cement columns to maintain continuity of the closed cellular ISM.

  - *Mitigation:* The ground improvement sheets will show the typical existing piles at Bent 25 with reference to the as-built drawings for the existing pile layouts. In addition, specifications will require the contractor to provide a soil-cement column layout such that known obstructions within the ISM, such as existing piles at Bent 25, are encapsulated within the soil-cement cellular structure. Therefore, the specification will limit previously unidentified obstructions to those that are not identified in the contract documents and encountered during deep soil mixing or jet grouting activities that would cause a significant decrease in the rate of advancement if removed using the techniques and equipment used to perform the deep soil mixing and jet grouting. Obstructions may include manmade or man-placed objects such as old railroad ties or cobbles and boulders that are not identified in the contract documents with a boulder advisory. Existing piles may be considered obstructions, but only if their location was not disclosed by the as-built drawings. Specifications will require the engineer to be the sole judge of the classification of any previously unidentified obstructions. Relocation or addition of soil-cement columns due to previously unidentified obstructions will be paid as extra work.

- **Risk:** The existing Bent 25 is supported by timber pile groups. The existing piles could be potential obstructions for DSM ground improvement. In addition, existing piles may cause shadowing effects for the jet grout soil-cement columns.
  - *Mitigation:* If the existing piles at Bent 25 are not removed completely, we recommend more expensive jet grouting be performed for the ISM surrounding the existing pile caps and extending a minimum of 5 feet outside the extents of the existing piles within the ISM. Specifications will require the contractor to provide a soil-cement column layout such that known obstructions within the ISM, such as existing piles at Bent 25, are encapsulated within the soil-cement cellular structure. However, if the as-built plan locations and lengths of the piles are not accurate or if the soil-cement columns are not located or aligned properly, piles still may be encountered during jet grouting or potentially even DSM, and shadowing effects may occur. Specifications will require downhole verticality measurements for all jet grout soil-cement columns around the existing Bent 25 pile caps. If the downhole verticality measurements and/or coring indicate potential for shadowing effects, additional soil-cement columns may be required. If the shadowing effects are due to alignment or location of soil-cement columns that exceed the tolerances provided in the specifications, cost for additional soil-cement columns will be the responsibility of the contractor. If the shadowing effects are due to existing piles whose location was not disclosed by the as-built drawings, addition of soil-cement columns may be paid as extra work.

10 BRIDGE REPLACEMENT FOUNDATION DESIGN RECOMMENDATIONS

10.1 Foundation Alternatives

Foundation evaluation and selection for the proposed replacement bridge is dependent upon several factors, including foundation demands, performance criteria, site constraints, and construction considerations. Foundations for the proposed replacement bridge will need to support significant static and seismic axial and lateral loads. Foundation design will need to address liquefaction and associated effects, including liquefaction-induced settlement, downdrag loads, and/or lateral forces from permanent ground deformation. The proposed construction sequencing includes demolition of the existing bridge prior to foundation construction. However, foundation installation needs to address risks to adjacent existing infrastructure and buildings.

The following sections describe the foundations alternatives considered and the recommended foundation types for the bridge abutments (Bents 1 and 10), interior land bents (Bents 2 through 5 and Bents 8 and 9), and in-water bents (Bents 6 and 7). The proposed bent locations are included in Figure 2-2. Foundation alternatives were evaluated and reviewed in conjunction with HDR and the Design Team.

10.1.1 Bridge Abutments

Based on the subsurface conditions encountered and the anticipated range of design loads, small-diameter drilled shafts are considered to be a suitable foundation solution for the proposed abutment locations. Driven piles are not preferred due to potential vibration impacts to adjacent existing structures and utilities during pile installation. Spread footings are not feasible due to the subsurface conditions, the seismic hazards present at the site, and the risks associated with performing large excavations in a dense urban environment.

10.1.2 Interior Land Bents

Large-diameter drilled shafts bearing in the Lower Troutdale Formation are considered the most economical and feasible foundation alternative at the proposed interior on-land bent locations. Spread footings are not a suitable foundation alternative for the interior land bents due to the large design loads, subsurface conditions, and the seismic hazards present at the site. Groups of small- or large-diameter driven piles are not preferable due to potential vibration impacts to existing structures and utilities during pile installation. Additionally, driven pile groups may not be feasible due to the anticipated range of loads and bent footprint limitations.

10.1.3 In-Water Bents

Foundation selection for in-water Bents 6 and 7 considered large-diameter drilled shafts, large-diameter driven pile groups, and caisson foundation alternatives. Large-diameter driven pile groups are considered not feasible due to anticipated foundation demands, particularly uplift considerations, in light of bent footprint limitations. Furthermore, hard driving conditions are anticipated in the Gravel Alluvium and Lower Troutdale Formation that would require extended driving with an impact hammer that could be subject to environmental permitting limitations. Sunken caisson foundations were considered for the in-water bents. Sunken caissons are constructed by stacking a series of precast or cast-in-place concrete sections at the bent location. The caisson is sunk to the planned tip elevation by the self-weight of the concrete sections as additional sections are added and the interior cells of the caisson are dredged. Exhibit 10-1 summarizes advantages and disadvantages of large-diameter drilled shafts and caisson foundation alternatives at Bents 6 and 7.

Exhibit 10-1: Comparison of Foundation Alternatives at In-Water Bents 6 and 7

Foundation Type	Advantages	Disadvantages
Sunken Caisson	• Sections may be precast on land in a controlled environment • Pile cap is not required • Large cross-sectional area is beneficial in resisting scour effects	• Installation may be challenging due to variable subsurface conditions • Very sensitive to differential settlement • Requires complete removal of existing bascule piers • Requires removal of all existing timber pile foundations within caisson footprint
Drilled Shaft Group	• Shafts can be designed for variable subsurface conditions • Existing pile removal limited to proposed drilled shaft locations • Does not require complete removal of existing pile caps	• Drilled shaft quality control will be both challenging and critical to foundation performance • Difficult to construct large diameter drilled shafts on a temporary work bridge in the river, especially using an oscillator for shaft construction • Requires construction of a pile cap

In our opinion, caisson foundations carry a high degree of risk due to the variable subsurface conditions underlying Bent 6. The variable conditions could impact caisson construction by causing tilting of the caisson during the installation process if one side of the caisson encounters denser material while the other side is located within a relatively soft layer. Similarly, achieving uniform embedment may be challenging due to variability in the contact elevation of the Lower Troutdale Formation. For example, if one side of the caisson encounters refusal in Lower Troutdale Formation and the other side is located within Upper Troutdale Formation clay, there is a risk of long-term differential settlement. Caissons are

very sensitive to differential settlements since they are rigid, monolithic structures. Therefore, the Design Team concluded that a large-diameter drilled shaft group is the most feasible, lower risk, and economical foundation alternative for Bents 6 and 7.

10.2 Drilled Shaft Design Recommendations

Proposed bridge foundations will consist of 3-foot to 10-foot diameter drilled shafts bearing in the Lower Troutdale Formation. Twelve-foot diameter drilled shafts were considered at the in-water bents but are currently not preferred during preliminary design. Drilled shafts will be designed to resist axial and lateral loads in accordance with AASHTO and ODOT GDM and BDM requirements. Foundation design will incorporate excess pore pressure induced strength loss, including liquefaction, and its associated effects including loss of resistance, seismically induced-downdrag loads, and lateral forces from permanent ground deformation.

Our analyses and recommendations are intended to support three design cases:

- Strength Limit
- Extreme Event: Full/Non-liquefied Strength
- Extreme Event: Liquefied/Reduced Strength.

Strength Limit recommendations reflect full strength, static soil resistances. The Extreme Event: Full/Non-liquefied Strength case considers the full soil strength and foundation resistance for consideration with peak ground accelerations during a seismic event. The Extreme Event: Liquefied/Reduced Strength case reflects the reduction in soil strength and foundation resistance due to liquefaction and pore pressure development during ground shaking. Our recommended liquefied/reduced strength parameters are based on our interpretation of laboratory test results and the results of the seismic hazards evaluation for the 1,000-year return period event discussed in Section 8.2.

Drilled shaft recommendations are provided for each pier considering generalized conditions within the pier footprint for the current NEPA-phase evaluation. In general, conservative soil contacts are assumed considering upper bound thicknesses of lower strength layers and deeper contacts of higher strength layers. The recommendations will be updated and refined in subsequent design stages to better incorporate subsurface variation at pier locations.

The following sections provide our recommendations for axial and lateral resistance, estimated downdrag loads, and foundation loads due to permanent ground deformation. We have also included a discussion of potential geotechnical risks and mitigation solutions pertaining to drilled shaft installation at the project site. Drilled shaft recommendations

assume that temporary casing may be used for shaft installation and that partial-depth permanent casing will only be used at Bents 6 and 7. We understand that the permanent casing at Bents 6 and 7 will be extended a nominal distance (15 feet is currently assumed) into the Gravel Alluvium.

10.2.1 Drilled Shaft Axial Compression and Uplift Resistance

We performed axial compressive and uplift resistance evaluations for drilled shafts in general accordance with the AASHTO LRFD (AASHTO, 2020). Our evaluations were based on the subsurface conditions encountered in the project borings. We estimated unit side and base resistance values based on the average SPT N-values within each unit, shear wave velocity measurements, laboratory test results, load tests in similar soil conditions from other projects, and our experience. Results of pressuremeter tests were reviewed and will be incorporated into future design efforts. Our evaluations do not consider scour effects since flood scour elevations were not provided during this phase of the project.

Axial compressive and uplift resistances are shown on the figures presented in Appendix I. The figures include plots of nominal and factored axial compressive resistance versus depth for Strength and Extreme Event limit states. Recommended resistance factors for each limit state are provided in the notes section of each figure. Uplift resistance is equal to the nominal side resistance multiplied by the respective resistance factor.

We understand that HDR is using the computer program FB-MultiPier to model the soil-structure interaction of the bridge foundations. We have provided soil model recommendations for side resistance (t-z, referred to as "axial" in the program), torsional, and base resistance (Q-z, referred to as "tip" in the program) springs for the interpretive subsurface profiles at each bent. The recommended soil models and associated input parameters for each bent are included in Table I1 in Appendix I. The recommended axial and torsional FB-MultiPier soil models were selected to facilitate model input and approximate the anticipated, simplified foundation response. We note that the recommended curve for the axial t-z response is the Driven Pile Sand (API) curve. In our opinion, this simple curve provides a reasonable approximation of drilled shaft side resistance that is more suitable than other models available in FB-MultiPier. Our recommendations in Table I1 also include a custom base resistance (Q-z) spring for Lower Troutdale Formation. The recommended custom base resistance spring is described in more detail in the following section. Additionally, we note that the recommended soil models and parameters are intended only to support NEPA-level design. We anticipate developing custom t-z, torsional, and Q-z springs during final design.

As shown in the Appendix I axial resistance plots and Table I1, drilled shaft base resistance is only considered in the Lower Troutdale Formation and below. Some base resistance may

be present in overlying layers; however, the amount is considered insufficient to support shaft loads and is not included.

10.2.1.1 Lower Troutdale Resistance

The Lower Troutdale Formation is a unique geologic unit that warrants additional consideration in foundation design. As described in Section 6.1.9, the unit typically consists of very dense gravel with varying amounts of sand and fines. SPT sampling typically encounters refusal blow counts similar to other gravel deposits. However, shear wave velocity measurements in the Lower Troutdale Formation are typically in the range of 4,000 to 6,000 feet per second (fps). For reference purposes, shear wave velocities in rock are typically in the range of 2,500 to 5,000 fps and hard rock is typically classified as greater than 5,000 fps. In our experience, the Lower Troutdale Formation has significant strength and can develop high foundation resistances.

We evaluated the Lower Troutdale Formation resistance and load deformation properties based on axial load test data from nearby projects, including the Willamette River Transit Bridge (Tilikum Crossing Bridge) located approximately 1 mile south of the project site and the I-5 Columbia River Crossing (CRC) project, located approximately 7 miles to the north. The drilled shaft load testing at the Tilikum Crossing Bridge was performed on two, 118-inch diameter shafts founded in the Lower Troutdale Formation. The load test data considered from the CRC project was performed on a 98.4-inch diameter shaft founded in the Troutdale Formation. We reviewed the characteristics of the Tilikum and CRC Troutdale formations in comparison with those along the Burnside Bridge alignment. Based on our review and comparison of SPT resistance, shear wave velocity measurements, and material descriptions including composition and degree of cementation, it is our opinion that the Lower Troutdale Formation encountered for the Burnside Bridge project has equal or greater strength compared to that of the Tilikum and CRC test sites.

The Tilikum and CRC load tests were performed using bi-directional testing methods. The Tilikum load tests were performed on production shafts and thereby mobilized project design loads but limited the amount of shaft displacement. The total upward and downward movements of the Tilikum shafts was less than 0.5 and 0.75 inches, respectively, for both tests. The CRC load test was performed on a sacrificial test shaft. The shaft was loaded with the goal of achieving shaft "failure" with upward and downward shaft movements in the range of 1 and 4 inches, respectively.

Based on our review of the load test data, we recommend drilled shafts at Bents 1 through 8 be designed considering nominal unit side and base resistance values of 20 kips per square foot (ksf) and 165 ksf, respectively. These values are generally representative of those achieved in the Tilikum production shaft load tests. For Bents 9 and 10, we recommend

nominal unit side and base resistance values of 10 ksf and 80 ksf, respectively. The recommended resistance values were reduced to account for uncertainty related to the shallower depth of Troutdale Formation encountered at Bents 9 and 10 compared to that of reference load test shafts. Exhibit 10-2 presents a summary of the normalized shaft movements measured in the load tests to achieve the typical nominal side and tip resistances recommended in this report. The shaft movements are normalized as a percentage of the shaft diameter to reflect the different diameters used in the load test program. Given that nominal side and base resistances are typically mobilized around 0.5% and 5% of the shaft diameter, respectively, the nominal side and base resistance values are likely greater than the recommended values provided herein. Higher values could likely be developed in a project-specific load test program performed on sacrificial test shafts loaded to failure. However, we anticipate the recommended values could be achieved on a production shaft load test program, where displacements are limited to the range presented in Exhibit 10-2.

Exhibit 10-2: Summary of Load-Displacement Data Considered for Lower Troutdale Formation

Load Test Location	Normalized Shaft Displacement at 20 ksf Unit Side Resistance	Normalized Tip Displacement at 165 ksf Unit Base Resistance
Tilikum Crossing, Pier 3	0.26%	0.62%
Tilikum Crossing, Pier 4	0.32%	0.45% (extrapolated)
I-5 CRC, CS-1	0.26%	0.99%

As described in Section 10.2.1, t-z and Q-z model inputs are required for foundation evaluation using the program FB-MultiPier. In our opinion, the Driven Pile Sand (API) axial model included in FB-MultiPier provides a simplified representation of t-z behavior of the drilled shafts in Troutdale Formation suitable for NEPA-phase evaluation. The recommended soil parameters for the axial model are included in Table I1. However, the available FB-MultiPier Q-z models do not adequately characterize the Troutdale base resistance load deformation response. Based on the data described above, we recommend a simple, bilinear custom Q-z spring for input in the FB-MultiPier program. The origin of the spring is located at z = 0 and Q = 0. The spring reaches a maximum value at the nominal unit base resistance (q_{nom}) times the shaft cross-sectional area (A) with a shaft displacement equal to 1.25% of the shaft diameter. The third point of the spring should be set at a displacement equal to 10% of the shaft diameter, a displacement at which a bearing capacity failure is typically considered to have occurred. The spring is presented graphically in Exhibit 10-3.

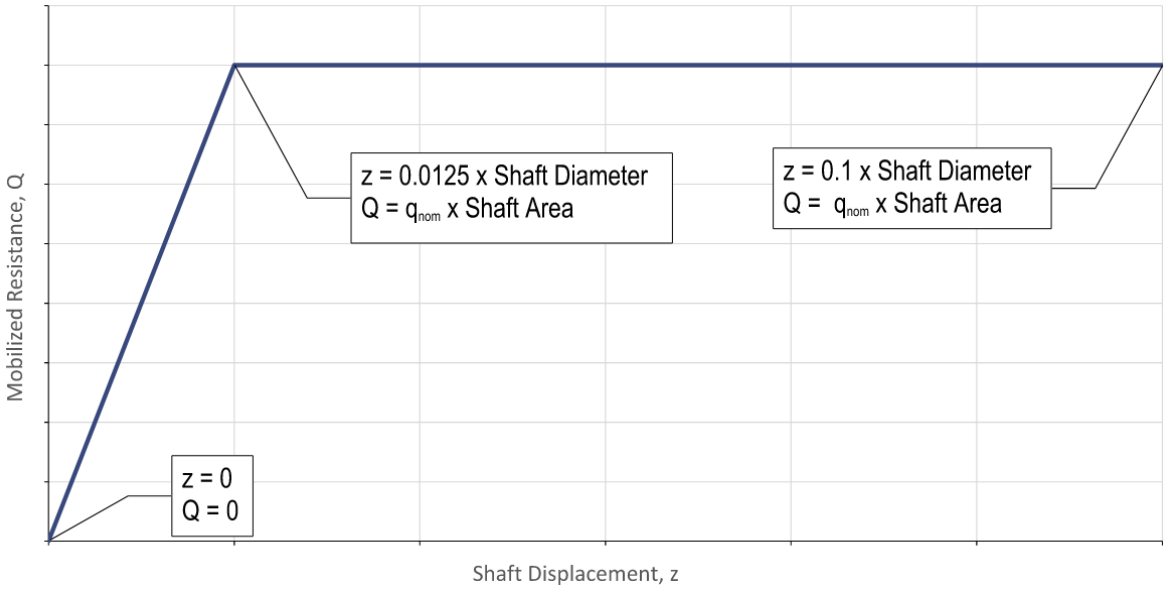

Exhibit 10-3: Generalized Plot of the Recommended Q-z Spring for Lower Troutdale Formation

The unit base resistance (q_{nom}) values included in Table I1 are valid for drilled shaft tip elevations located at least 1.5 times the shaft diameter (1.5D) above the Lower Troutdale Formation-Sandy River Mudstone contact. If the shaft tip elevation is located within 1.5D of the top of the Sandy River Mudstone, the unit base resistance should be linearly interpolated between the full unit base resistance (e.g., 165 ksf) at a distance of 1.5D from the Sandy River Mudstone and 80 ksf at the Sandy River Mudstone contact. We recommend evaluating differential settlement at Bent 6 drilled shafts due to the varying thickness of Lower Troutdale Formation and varying contact for Sandy River Mudstone. For the current design, the required nominal shaft resistance at Bent 6 is in the range of approximately 15,000 kips. In such case, the majority of the load is carried in Lower Troutdale side resistance, thereby mitigating differential settlement concerns.

10.2.1.2 Group Efficiency Factors

The axial resistances indicated on the figures in Appendix I are valid for drilled shafts in a single row with a center-to-center spacing of at least three times the shaft diameter (3D), or multiple rows of shafts with a minimum center-to-center spacing equal to four times the shaft diameter (4D). If drilled shafts are designed with a center-to-center spacing less than described above, a reduction factor for group effects should be applied in accordance with AASHTO LRFD Table 10.8.3.6.3-1.

10.2.1.3 Load Testing

A load test program is required to confirm the design properties and high axial resistances currently recommended for the Lower Troutdale Formation. As described in Section

10.2.1.2, the design properties are based on results of load tests from other nearby projects. The values are substantially higher than those provided in AASHTO and FHWA guidance and require confirmation for our project site conditions and construction means and methods. Additionally, a project-specific load test program enables the potential use of increased resistance factors in design. If a load test program is not performed, the design resistance parameters will need to be reviewed and substantially reduced due to the lack of project-specific load testing.

Load tests should be performed using the bi-directional load testing method on production shafts, constructed using production shaft means and methods. A bi-directional load cell is a sacrificial hydraulic jack installed between two steel plates that are embedded in the drilled shaft. As the cell is loaded, it exerts equal force in the upward and downward directions. In this process, the self-weight and side resistance of the shaft above the bi-directional load cell provides reaction to mobilize base resistance and side resistance below. Simultaneously, side resistance and base resistance below the bi-directional load cell provide reaction to mobilize side resistance above.

A load test program would be designed to represent the sizes, depths, and geologic conditions for drilled shaft foundations along the bridge alignment. For planning purposes, we recommend tests be performed at in-water Bents 6 and 7, along with a minimum of one interior land bent. Instrumentation will be incorporated into the load test program to enable evaluation of side and base resistance at each shaft. Results will be compared between the tested shafts for evaluation of side resistance properties by layer, mobilized base resistance, and potential shaft scaling effects. Test results may be used to revise shaft lengths and/or resistances if unit side and base resistances are significantly different than considered in design. If a load testing program is incorporated into the project design, the Strength Limit load resistance factors of 0.55 and 0.5 used for side and base resistance, respectively, may be increased to 0.7 per AASHTO LRFD.

We anticipate that unit side and base resistances recommended in Section 10.2.1.1 could be achieved in a production shaft load test program, where displacements are limited to less than 1 inch. Higher resistance values could be achieved in a load test program on sacrificial test shafts, where the shaft is loaded to failure and displacements are not limited. However, this would result in significant extra cost to the project. The use of sacrificial or production shafts for load testing will be explored during final design.

10.2.2 Drilled Shaft Downdrag Loads

Liquefiable soil and soil that experiences elevated pore pressures during a seismic event may undergo seismic settlement following ground shaking. Downdrag loads may develop on foundations when the settlement of the soil exceeds the downward movement of the

shaft. We evaluated the potential for downdrag loads to occur based on the results of the seismic hazard evaluation for 1,000-year return period ground motions, discussed in Section 8.2. According to AASHTO LRFD, drilled shafts are expected to experience downdrag loads from surrounding soils if the soils settle 0.4 inches or more relative to shaft displacement. Anticipated downdrag loads are summarized in Exhibit 10-4 and provided in Note 6 of the axial resistance figures in Appendix I.

Exhibit 10-4: Estimated Post-Seismic Downdrag Loads for 1,000-year Return Period Ground Motions

Location	Single Shaft Downdrag Load (kips)
Bent 1	0
Bent 2	0
Bent 3	0
Bent 4	0
Bent 5	0
Bent 6	86
Bent 7	490
Bent 8 (Cable-Stay Tower)	1,040
Bent 8 (Tied-Arch)	930
Bent 9	0
Bent 10	0

10.2.3 Drilled Shaft Lateral Resistance

We understand that the drilled shaft foundations will be subjected to lateral loads resulting from live, seismic, and permanent ground displacement loading. We understand that the laterally loaded shaft analyses will be performed using FB-MultiPier and LPILE software. Table I1 presents the recommended soil models and geotechnical input parameters to perform lateral load-displacement (p-y) analyses for the drilled shafts. Recommended parameters may be updated in future design stages to incorporate PMT results in select geologic units.

10.2.3.1 Group Effects

The lateral soil resistance parameters provided in Table I1 represent soil resistance for a single drilled shaft. At shaft spacings less than five shaft diameters, shaft efficiency is reduced, and reduction factors (p-multipliers) should be applied to the p-y curves. Based on design plans downloaded from ProjectWise on January 7, 2022, a majority of the bents will be supported on drilled shafts with a center-to-center spacing of less than five diameters.

Therefore, p-multipliers should be applied as described in AASHTO Section 10.7.2.4 - Horizontal Pile Foundation Movement.

10.2.3.2 Ground Improvement Interaction

As discussed in Section 9 of this report, ground improvement is being recommended at Bent 8 of the cable-stay bridge option. The ground improvement design is in progress and detailed evaluation will be performed in the next design phase. Depending on the ground improvement design, interaction effects may be present between the Bent 8 (cable-stay tower) drilled shafts and shaft cap and ground improvement that may result in changes to the permanent ground deformations, driving loads on the drilled shafts and shaft cap, and drilled shaft and shaft cap lateral p-y response. The interaction effects are dependent on the ground improvement layout, strength, and proximity to the drilled shafts and shaft cap.

The foundation recommendations provided herein do not incorporate ground improvement interaction effects at Bent 8 (cable-stay tower). The recommendations could be considered to reflect a sufficiently wide buffer zone such that the ground improvement does not affect lateral soil parameters. Ground improvement interaction effects will be evaluated in the next design phase and will include updated recommendations for Bent 8 (cable-stay tower).

10.2.4 Foundation Loads Due to Permanent Ground Deformations (No Ground Improvement)

Permanent lateral soil displacements are anticipated at Bents 5 through 8 during both the 1,000-year return period and deterministic CSZ level seismic events. We recommend the design team use a soil displacement-based approach in LPILE to assess the kinematic foundation loads imposed by these displacements. Recommended soil displacements and combinations of kinematic and inertial loading are described in the following sections. The lateral soil displacement analysis should consider the reduced strength soil inputs provided in Table I1.

10.2.4.1 Soil Displacement Profiles

The soil displacement profiles are based on the "All Motion Average" permanent displacements described in Section 8.2.3 and included on the site response profile figures in Appendix H. The recommended soil displacement profiles for the 1,000-year return period ground motions are provided in Exhibit 10-5.

We note that the displacement profiles at Bents 6 and 7 are based on results from the current FLAC model that considers the existing mudline bathymetry along the riverbed. The displacement profiles at Bents 6 and 7 were used in the current design in NEPA phase. We understand the post-construction grades around the in-water bents will be flattened and we

anticipate the estimated displacement profiles will be significantly reduced. The revised grades will be considered as part of future NLTH design efforts.

Exhibit 10-5: Permanent Ground Deformation Profiles for 1,000-year Return Period Ground Motions

Location	Elevation (feet)	Displacement (inches)
Bent 5	35	5.0
	9	5.0
	-9	1.2
	-40	0
Bent 6	-50 *(existing mudline)*	26
	-56	26
	-59	12
	-64	0
Bent 7	-43 *(existing mudline)*	48
	-55	48
	-60	15
	-100	0
Bent 8 (Cable-Stay Tower)	31	10.5
	-70	2.0
	-115	0
Bent 8 (Tied-Arch)	31	4.0
	11	3.5
	-55	0.6
	-100	0

10.2.4.2 Combination of Kinematic and Inertial Loading

The combination of seismic inertial loading with kinematic loading due to liquefaction/pore-pressure induced lateral ground deformation was determined by HDR in consideration of existing agency guidance from Caltrans and WSDOT. For the NEPA phase evaluation, the design considers:

- 100% seismic inertial forces with 0% kinematic loads
- 50% seismic inertial forces with 100% kinematic loads

This combination is consistent with Caltrans guidance. WSDOT guidance utilizes a lower combination of 100% seismic inertial forces with 25% kinematic loads. However, given the preliminary design development level, the HDR design team utilized the more conservative

Caltrans load combination with review and concurrence from Multnomah County and feedback from the external Bridge and Seismic Working Group.

10.2.5 Geotechnical-Related Risks and Mitigation Solutions

There are potential geotechnical related risks for the proposed drilled shaft foundation construction due to the spatial constraints, existing infrastructure, and subsurface conditions at the site.

- **Risk:** Several of the proposed Bent 6 and 7 shafts are located within the footprint of the existing bridge piers that are supported on timber piles. We understand the timber piles are installed on 3-foot center-to-center spacing. Demolition of the existing structure currently includes partial removal of the pile cap to elevation -55 feet; however, the timber piles are to remain in place and will pose a conflict with the proposed shaft layout. Based on the timber pile spacing, it is likely the proposed 10-foot-diameter Bent 6 and 7 shafts will overlay multiple existing piles. In our experience, the presence of timber piles can significantly impede casing advancement and drilling rates. With the presence of multiple piles, there is potential that an oscillator casing could bind up on the timbers.
  - *Mitigation:* We recommend a specialty drilled shaft contractor perform additional review of the conditions and presence of multiple timber piles at Bent 6 and 7 shaft locations. We recommend consideration of removal of the existing timber piles within the footprint of the drilled shaft. If the timber piles are not removed, the Project Team should evaluate schedule impacts, slowed progress, and delays associated with drilling through the timber piles in association with the duration of the Willamette River in-water work window.
- **Risk:** Time between completion of shaft clean-out and concrete placement will be longer than a typical shaft for deeper shaft depths that require reinforcement cage splices. This includes shafts at Bent 8 (Cable-Stay Tower), Bent 8 (Tied-Arch), and potentially Bent 5. The potential long duration of reinforcement cage placement could allow silt in the drilling slurry to fall out of suspension and accumulate at the base of the shaft following clean-out. Accumulation of sediment could affect the base resistance of the shaft. In addition, the time of concrete placement will also be longer than a typical shaft which increases the risk of concrete blockage in the pump and/or tremie and other issues which may lead to a stoppage in concrete placement and a cold joint in the shaft.
  - *Mitigation:* Full depth casing will stop additional silt and sand from entering the excavation after the shaft excavation and clean-out are complete. The use of flocculent will aid silt to fall out of suspension and water exchange may also facilitate cleaning of the slurry. We recommend a combination of these measures to reduce risk of sediment accumulation at the base of the shaft.

10.3 Bridge Abutments and Approach Retaining Walls

We understand that evaluation of proposed retaining walls at both bridge abutments and approach embankments has been limited to a conceptual-level geometric study for the current project phase. The current plan for the west abutment includes construction of a new concrete pier wall supported on a row of small diameter drilled shafts in front of the existing abutment wall. The area between the proposed and existing walls would be backfilled with reinforced soil or lightweight fill. We understand the top of the existing east abutment wall would have to be removed to accommodate the adjacent span superstructure. However, the remainder of the existing abutment wall would be left in place and the adjacent bridge span would be supported on a row of small diameter drilled shafts located behind the existing abutment wall.

We understand that new retaining walls are assumed at all four quadrants of the bridge approaches. The Design Team anticipates significant challenges with wall design and construction, particularly in the northwest, southwest, and southeast quadrants, due to existing retaining walls and buildings immediately adjacent to the wall alignments. Retaining wall types and configurations for proposed walls along both bridge approaches are currently under development. Additional geotechnical investigations and geotechnical retaining wall design evaluations will be performed during future design phases.

11 GEOTECHNICAL CONSTRUCTION CONSIDERATIONS

11.1 Drilled Shafts

Drilled shaft construction requires drilling a hole of a specified diameter and depth and then backfilling the hole with reinforced concrete. The selection of equipment and procedures for constructing drilled shafts is a function of the shaft dimensions, the subsurface conditions, and groundwater elevation. Consequently, the side and base resistance and long-term performance of drilled shafts can be significantly influenced by the equipment and construction procedures used to install the shafts. Construction procedures and methods are of paramount importance to the success of the drilled shaft installations at this project site.

11.1.1 Temporary Casing

We recommend that temporary casing be used at all shaft locations to stabilize drilled shaft side walls and reduce the risk for sediment build-up at the bottom of the shaft during clean-out and reinforcement cage placement. Additionally, the use of temporary casing at the land bents will reduce the risk of impacts to existing infrastructure within the project

vicinity. In addition, temporary casing should be installed by non-vibratory, non-impact methods (such as an oscillator or rotator) to mitigate the potential for negative impacts on adjacent existing structures and utilities resulting from casing installation vibrations.

11.1.2 Drilling Slurry

We recommend the use of drilling slurry in addition to temporary casing to counterbalance hydrostatic pressures and maintain base stability. In addition, polymer slurry may be used to "lubricate" the casing and aid in casing advancement/extraction. Selection of slurry type will be the responsibility of the contractor; however, we recommend mineral slurries not be used on the project to avoid unplanned reductions to the shaft side resistance. The slurry level in the excavation should be maintained a minimum of 10 feet above the hydrostatic or artesian water level at the shaft location for polymer and water slurries, and 5 feet above for mineral slurry. The sand content of polymer and water slurries prior to final clean out and immediately prior to concrete placement should be less than one percent.

11.1.3 Excavation in Lower Troutdale Formation

We understand that all drilled shafts will be founded in the Lower Troutdale Formation. The extent of embedment within the Lower Troutdale Formation has not yet been determined. As described in Section 6.1.9, we anticipate that the Lower Troutdale Formation typically consists of very dense Gravel with varying amounts of sand and fines. Zones of cementation are noted throughout the unit, and cobbles and boulders may be present in some areas. The contractor should anticipate that excavation within the Lower Troutdale Formation will require removal of cobbles and boulders and may be difficult and slow.

11.1.4 Potential Obstructions

As discussed in Section 6, cobbles and boulders were inferred by drill action in the Fill, Gravel Alluvium, Catastrophic Flood Deposits – Channel Facies, and Lower Troutdale Formation units during our subsurface explorations. The Contractor may encounter cobbles or boulders during drilling in the Fill, Gravel Alluvium, Catastrophic Flood Deposits – Channel Facies, and Lower Troutdale Formation units. Cobbles and boulders may also be "dragged" down by the drilling equipment from these soil layers into other units. Therefore, the Contractor's drilling equipment should be capable of breaking or cutting through and removing cobbles and boulders.

A layer of riprap is known to exist surrounding the existing pile caps at the bascule pier locations. Unless the riprap is removed prior to construction, the contractor should

anticipate encountering a surficial layer of riprap during drilled shaft excavation at proposed Bents 6 and 7.

We understand that some of the proposed drilled shafts at Bents 6 and 7 will be advanced through a portion of the existing pile cap that will be left in place. Additionally, we understand the existing timber pile foundations will be left in place and drilled through during drilled shaft installation. Appropriate tooling and methods should be selected by the contractor to facilitate drilled shaft excavation through the existing pile cap and timber piles where applicable.

11.1.5 Shaft Clean Out

Drilled shaft excavation bottom cleanout should be performed in accordance with Oregon Standard Specifications for Construction (OSSC) Section 00512, and its project-specific special provision. Use of an approved flocculant may be required to drop sediments out of suspension in the slurry. We recommend the base of the excavation be covered with no more than ½-inch of loose or disturbed material over 50 percent of the base area, with a maximum allowable thickness of 1.5 inches, prior to placing concrete. Final shaft cleanout should be verified with a downhole shaft inspection device (SID) that includes a video camera and one or more sediment measuring gages. We recommend the SID inspection be performed at a minimum of five locations around the base of each shaft for shaft diameters equal to or less than 8 feet, and at a minimum of 12 locations around the base of each shaft for shaft diameters greater than 8 feet. Final shaft cleanout and inspection should be observed by a qualified geotechnical engineer or representative.

11.1.6 Shaft Quality Control

We recommend that an experienced and qualified geotechnical engineer or representative familiar with the subsurface conditions of the project site observe drilled shaft construction. The construction of the drilled shafts by the casing and/or wet method will prevent downhole visual inspection. An experienced and qualified geotechnical engineer or representative familiar with the subsurface conditions at the site and with this project should visually evaluate soil mucked from the excavation or retrieved from the auger flights and cleanout buckets. These observations would assess whether the subsurface conditions assumed for design are actually present. The geotechnical engineer or representative should also observe and evaluate the base of the excavated shaft to determine that the base cleanout conforms to project special provisions, OSSC Section 00512, and our recommendations in Section 11.1.5.

After completing the installation of drilled shafts, cross-hole sonic logging (CSL) and thermal integrity profiling (TIP) should be performed on all shafts to evaluate concrete

integrity. The integrity tests should be performed and analyzed by experienced and qualified personnel. If voids, low-velocity (strength) zones, or other abnormalities/defects are detected in the CSL and/or TIP testing, the test findings should be analyzed to determine if the installed drilled shafts satisfy the design requirements or if mitigation and/or additional CSL/TIP tests are required on other shafts.

11.2 Ground Improvement

11.2.1 Site Preparation and Excavation

Site preparation for ground improvement will include: (1) clearing, grubbing, and roadside cleanup, (2) removal of existing structures and underground utilities, and (3) temporary excavation and construction of a working platform. These construction activities should generally be accomplished in accordance with OSSC, Section 00300.

Disturbance of subgrade soil due to construction equipment and activities could affect support of the ground improvement equipment, such as a DSM drill rig. The contractor should take necessary steps to protect the subgrade from becoming disturbed, such as construction of a crushed rock working platform for drill rig support. At a minimum, we recommend a 1-foot-thick working platform consisting of a layer of compacted sand and gravel be constructed at the ground surface in the ground improvement area.

11.2.2 Environmental Considerations

Deep soil mixing and jet grouting generate significant surface spoils, which if not managed properly, may migrate into storm drains or nearby bodies of water. The ground improvement contractor will need to work closely with the general contractor to manage and dispose of the spoils properly and coordinate the ground improvement construction with other operations at the site. We recommend the contractor be required to submit a spoils management plan prior to construction, which should include the containment means and methods to keep spoils and grout from entering regulated work zones and no work zones, including the railroad right-of-way.

11.2.3 Potential Re-Use of ISM Spoils On-Site

Excess soilcrete generated from ISM construction may range from 30 to 100 percent of the treated volume (i.e., area replacement ratio multiplied by the total soil volume in the ISM). Based on this estimate, the volume of excess soilcrete generated from the ISM construction may range from approximately 10,000 to 30,000 cubic yards. With Agency approval, this material could be reused to backfill the temporary excavations at Bent 8 cable-stay tower and other areas of the project site if environmental regulations do not prohibit this material from being reused, as it typically is found to have a high pH. We do not recommend use of

ISM spoils to backfill around structures that are sensitive to high pH soils (such as metal culverts), construct roadway embankments, or backfill below the ordinary high water (OHW) level. The current construction cost estimate assumes off-site disposal of the spoils by the contractor. If the spoils are re-used on-site, the County may need to negotiate a reduction in cost with the contractor.

All loose, disturbed, and otherwise unacceptable material, and any other excess material generated by the ISM construction, should be removed from the treatment area after completion of soil-cement column installation.

If they can be used, the spoils should be placed and compacted as soon as they set up enough to support construction equipment. We recommend a stockpile area for ISM spoil-curing be identified in the contract plans. The contractor should submit a spoils management plan prior to construction, which should include the containment means and methods used to keep spoils from entering nearby bodies of water and adjacent properties. Placement and compaction of the ISM spoils should follow the ODOT OSSC, Section 00330, and the project Special Provisions. The cured ISM spoils should be broken to a maximum particle size of 6 inches prior to placement and compaction.

11.2.4 Bench Scale Testing

Laboratory bench scale testing is typically performed on DSM and jet grouting projects by the Agency/Engineer during design, and/or the Contractor prior to production work, to identify a range of cement mix designs and installation procedures that are likely to produce treated soils in production that meet the specified design parameters for the project. The engineering properties of deep mixed and jet grouted soils are dependent on a variety of factors such as soil type, water content, organic contents, non-uniformity of the soil deposit, mix design, curing conditions, loading conditions, and mixing energy. Bench scale testing involves laboratory preparation and testing of treated soil (soil-cement) to study the influence of these various factors on the measured engineering properties.

A laboratory bench scale testing program performed by the Agency/Engineer during the design phase can be used to establish the reasonably attainable treated soil properties for use in design. If bench scale testing is performed by the Agency/Engineer during design, the results should be provided to all bidders. However, even if bench scale testing is performed by the Agency/Engineer during design, the Contractor will typically elect to perform additional bench scale testing to optimize binder quantities, mix designs, and use modified testing procedures that simulate the specific mixing conditions for a proprietary soil mixing/jet grouting system or that may be correlated to the field operation of the Contractor's soil mixing/jet grouting method. Therefore, for this project, the Contractor will be required to perform the bench scale testing. The results of the bench scale testing should

be submitted along with the proposed grout mix based on the testing, prior to beginning the field test program recommended in Section 11.2.5.

11.2.5 Full-Scale Field-Testing Program

The Contractor should perform a full-scale field-testing program, or demonstration program, prior to beginning production DSM or jet grouting, in accordance with the project Special Provisions. The demonstration program involves the installation of trial soil-cement columns using the means, methods, and materials proposed by the Contractor and defined based on information from bench scale testing, to demonstrate that the specified design parameters will be achieved. During the demonstration program, the Contractor may experiment with mixing parameters to identify suitable mix designs, installation procedures, and to develop and support an alternative cost-effective design that may be part of a value engineering proposal.

We recommend the Contractor be required to construct a minimum of three overlapping soil-cement columns that meet the specified design parameters. If both DSM and jet grouting are proposed, one demonstration section should be constructed for each ground improvement method. The soil-cement test columns should be the same dimensions as the production soil-cement columns. Coring, wet sampling, and unconfined compressive strength testing are among the methods that should be used to determine acceptability of the test columns. The test columns may be used as production columns if properties and configurations meet the specified requirements.

11.2.6 Production ISM Construction

Production ISM construction should be performed in accordance with Section 00345 – Improved Soil Mass, which is included in the project specifications by Special Provision, and using the accepted means, methods, and materials from the demonstration program.

11.2.6.1 Potential Obstructions

If the timber piles supporting the existing bridge at Bent 25 are not removed, these will be obstructions for DSM equipment and may prevent continuous placement of jet-grouted and DSM columns. In addition, timber piles or other buried obstructions may be present near the railroad. If the existing piles at Bent 25 are not removed completely, we recommend more expensive jet grouting be performed for the ISM surrounding the existing pile caps and extending a minimum of 5 feet outside the extents of the existing piles within the ISM.

In practice, surface and subsurface obstructions may prevent continuous placement of the jet-grouted and DSM columns. Boulders and other subsurface obstructions may also result in a non-uniform improved soil mass due to jet grout shadowing effects. "Shadows" of

unimproved soil can develop directly behind a subsurface obstruction (e.g., a boulder) because it will prevent the uniform distribution of the injected cement. Theoretically, no shadowing would occur if jet grouting occurs on all sides of an obstruction. Therefore, in order to maintain continuity of the closed cellular ISM, additional soil-cement columns may be required if a boulder or other subsurface obstruction is encountered during jet grouting or DSM, or during subsequent coring of a soil-cement column. Refer to Section 9.3 for our approach to mitigating change orders and other risks associated with encountering subsurface obstructions during ISM construction.

11.2.6.2 Soil-Cement Column Acceptance Criteria

Coring, wet sampling, downhole soil-cement column verticality measurements, and unconfined compressive strength testing are among the methods that should be used to determine acceptability of the production soil-cement columns in accordance with the project Special Provisions. We recommend full-depth continuous coring be performed in 3 percent of production soil-cement elements. An element refers to a DSM or jet grout element that is produced by a single stroke of the mixing or grouting tools at a single equipment location. Therefore, a column produced by a single-axis machine, a set of overlapping columns produced by a single stroke of a multiple-shaft mixing tool, and a rectangular barrette produced by a mixing tool with horizontal axis rotating cutter blades are each considered elements. Wet samples should be collected from at least two in-situ soil-cement columns per rig per shift that soil-cement columns are installed.

Each core run should have minimum 80 percent recovery and the full-depth core a minimum of 85 percent recovery to meet uniformity of mixing acceptance criteria. Obtaining good core recovery when gravel or cobbles are present in the treated ground may be difficult. In this case, downhole video logging of the core holes or alternate coring procedures may be used in lieu of core recovery to assess element uniformity.

The specifications for the ISM at the location of Bent 8 of the cable-stay option will indicate that the 28-day UCS that must be achieved in the field will consist of the following:

- A minimum of 90 percent of the 28-day UCS test population must be equal to or greater than 150 psi.
- A minimum of 50 percent of the 28-day UCS test population must be equal to or greater than 460 psi.

UCS test results from each UCS test sample location and depth interval should be grouped with UCS test results from the nearest nine UCS test sample locations in the same depth interval to create a UCS test result population of ten samples. The UCS test sample location

being evaluated should be considered to meet acceptance testing if the UCS test population meets the acceptance criteria.

11.3 General Earthwork Considerations

11.3.1 Site Preparation and Excavation

Site preparation will include: (1) clearing, grubbing, and roadside cleanup; (2) removal of existing structures and underground utilities; and (3) subgrade preparation and excavation. These construction activities should generally be accomplished in accordance with the OSSC. If temporary shoring is needed for these activities, the design of such shoring is traditionally the responsibility of the contractor.

After site stripping and preparation activities are completed, the exposed subgrade to receive fill should be proof-rolled with a fully loaded 10- to 12-yard dump truck or similar heavy rubber-tired construction equipment to identify soft, loose, or unsuitable areas. The proof-roll should be conducted prior to fill placement.

The site stripping and proof-roll should be observed by a qualified geotechnical engineer or representative, who should determine stripping depth, evaluate the suitability of subgrade, and identify areas of yielding. If loose and/or wet, soft soil zones are identified during proof-rolling, the soils should be removed and replaced with compacted structural fill.

Disturbance of subgrade soil due to construction equipment and activities could affect support of the proposed walls, embankment, and other construction equipment. The contractor should take necessary steps to protect subgrade from becoming disturbed.

11.3.2 Temporary Cut and Fill Slopes

Temporary cut and fill slopes are typically the responsibility of the contractor and should comply with applicable local, state, and federal safety regulations, including the current Occupational Safety and Health Administration (OSHA) Excavation and Trench Safety Standards. For general guidance, we suggest that temporary construction slopes be made at 1H:1V or flatter. In areas of loose fills, very soft soil, or groundwater seepage, flatter slopes are likely to be required.

11.3.3 Temporary Shoring

We understand that the contractor may install temporary shoring during construction. The ODOT GDM (ODOT, 2019), Section 15.3.26, provides a list of allowable retaining wall types for use as temporary shoring. The selection of the preferred temporary shoring system is the responsibility of the contractor and should comply with local, state, and federal safety

regulations, including the current OSHA Excavation and Trench Safety Standards. During the final design phase, the design team will evaluate the potential use of temporary shoring during construction and provide a guideline for the selection of temporary shoring types.

11.3.4 Excavation Groundwater Control

Where excavation will be performed within the active river channel or below the groundwater level, construction of a cofferdam and the use of temporary dewatering may be required during construction. Temporary shoring techniques and dewatering techniques should be evaluated together, because one temporary shoring technique may work well with certain dewatering techniques and not well with others.

The contractor shall be responsible for the actual means and methods to dewater the temporary excavation during construction. Typical dewatering techniques include well points, wells, educator pumps, and sump pumps.

Any water collected during dewatering, and any excavated soil, should be treated and disposed of in a manner meeting local, state, and federal environmental regulations and requirements.

11.3.5 Wet Weather Construction

Excavation and construction operations may expose the on-site soils to inclement weather conditions. The stability of exposed soils may rapidly deteriorate due to a change in moisture content (i.e., wetting or drying) or the action of heavy or repeated construction traffic. Accordingly, if construction occurs during periods of rain, foundation excavations should be adequately protected from the elements and from the action of repetitive or heavy construction loadings. We recommend access roadways be constructed with at least 12 inches of Stone Embankment Material (OSSC, Section 00330.16) overlying a non-woven subgrade separation geotextile meeting the requirements of the OSSC, Section 02320.

12 LIMITATIONS

The analyses, conclusions, and recommendations contained in this report are based on site conditions as they presently exist, and further assume that the explorations are representative of the subsurface conditions throughout the site; that is, the subsurface conditions everywhere are not significantly different from those disclosed by the explorations. If subsurface conditions different from those encountered in the explorations are encountered in future explorations or appear to be present during construction, we should be advised at once so that we can review these conditions and reconsider our

recommendations, where necessary. If there is a substantial lapse of time between the submission of this report and the start of construction at the site, or if conditions have changed because of natural forces or construction operations at or adjacent to the site, we recommend that we review our report to determine the applicability of the conclusions and recommendations.

Within the limitations of scope, schedule, and budget, the analyses, conclusions, and recommendations presented in this report were prepared in accordance with generally accepted professional geotechnical engineering principles and practice in this area at the time this report was prepared. We make no other warranty, either express or implied. These conclusions and recommendations were based on our understanding of the project as described in this report and the site conditions as observed at the time of our explorations.

Unanticipated soil conditions are commonly encountered and cannot be fully determined by merely taking soil samples from test borings. Such unexpected conditions frequently require that additional expenditures be made to attain a properly constructed project. Therefore, some contingency fund is recommended to accommodate such potential extra costs.

We developed our opinions of probable construction costs based on our experience with similar projects. The costs include several assumptions, including:

- The subsurface conditions that will be encountered,
- Decisions of other design professionals and government agency personnel,
- The means and methods of construction the Contractor will employ,
- The Contractor's techniques in determining price and market conditions at the time of construction, and
- Other factors over which we have no control.

Given the assumptions that must be made, Shannon & Wilson cannot guarantee the accuracy of the opinion of probable construction costs. Shannon & Wilson is not a construction cost estimator or construction contractor, nor should our rendering of an opinion of probable construction costs be considered equivalent to the nature and extent of services a construction cost estimator or contractor would provide.

This report was prepared for the exclusive use of HDR Engineering, Inc., and Multnomah County for use in the Earthquake Ready Burnside Bridge NEPA and Type Selection Phase. Our report, conclusions, and interpretations should not be construed as a warranty of subsurface conditions included in this report.

The scope of our present work did not include environmental assessments or evaluations regarding the presence or absence of wetlands, or hazardous or toxic substances in the soil, surface water, groundwater, or air, on or below or around this site, or for the evaluation or disposal of contaminated soils or groundwater should any be encountered.

Shannon & Wilson, Inc., has prepared and included the attached "Important Information About Your Geotechnical/Environmental Report," to assist you and others in understanding the use and limitations of our reports.

13 REFERENCES

Abrahamson, N. and Gülerce, Z., 2020, Regionalized ground-motion models for subduction earthquakes based on the NGA-SUB database: PEER Report 2020/25, Pacific Earthquake Engineering Research Center, University of California, Berkeley, p. 197.

Abrahamson, N.A., Silva, W.J., and Kamai, R., 2014, Summary of the ASK14 ground motion relation for active crustal regions: Earthquake Spectra, v. 30, no. 3, p. 1,025-1,055.

Adams, J., 1990, Paleoseismicity of the Cascadia Subduction Zone: Evidence from turbidities off the Oregon-Washington margin: Tectonics, v. 9, no. 4, p. 569-583.

Adams, J., 1996, Great earthquakes recorded by turbidities off the Oregon-Washington coast, in Rogers, A.M., Walsh, T.J., Kockelman, W.J., and Priest, G.R., eds., Assessing Earthquake Hazards and Reducing Risk in the Pacific Northwest, U.S. Geological Survey Professional Paper 1,560, p. 147-158.

Agaibe, S.S., and Mayne, P.W., 2019, CPT evaluation of yield stress profiles in soils, Journal of Geotechnical and Geoenvironmental Engineering, ASCE, 145(12), 04019104.

Aki, K., 1983, Seismological evidence in support of the existence of characteristic earthquakes: Earthquake Notes, v. 54, p. 60-61.

Al Atik, Linda, and Youngs, R.R., 2014, Epistemic uncertainty for NGA-West2 models: Earthquake Spectra, v. 30, no. 3, p. 1301-1318.

Alexander, K., 2020, Slip rates and kinematics of active crustal faults in the central Oregon Cascades: Western Washington University, M.S., Thesis, 66 p.

Allen, J.E., Burns, M., and Burns, S., 2009, Cataclysms on the Columbia: The Great Missoula Floods (2nd ed.): Portland, Oregon, Hooligan Press, 204 p.

American Association of State Highway and Transportation Officials (AASHTO), 2015, AASHTO guide specifications for LRFD seismic bridge design (2nd ed., with interim revisions): Washington, D. C., AASHTO.

American Association of State Highway and Transportation Officials (AASHTO), 2018, AASHTO LRFD movable highway bridge design specifications (2nd ed., with interim revisions): Washington, D. C., AASHTO.

American Association of State Highway and Transportation Officials (AASHTO), 2020, AASHTO LRFD bridge design specifications (9th ed., with 2021 Errata): Washington, D. C., AASHTO, 2 v.

Anderson, J.L., Tolan, T.L., and Wells, R.E., 2013, Strike-slip faults in the western Columbia River flood basalt province, Oregon and Washington, in Reidel, S.P., Camp, V.E., Martin, B., Ross, M.E., Tolan, T., Wells, R., and Wolf, J., eds., Evolution of the Columbia River Basalt Group, Geological Society of America Special Paper 497, p. 325-347.

Anderson, M., Steely, A., Horst, A., Dassow, W., Lau, T., Reedy, T., Amaral, C., and Stanton, K., 2021, The Doty Fault Zone: Centerpiece of a Long-Lived, Slow-Moving, Transpressive Fault System in Southwestern Washington, presented at GSA Connects 2021, Portland, Oreg.: Boulder, Colo., Geological Society of America, XX p.Atwater, B.F., 1987, Evidence for great Holocene earthquakes along the outer coast of Washington State: Science, v. 236, p. 942-944.

American Society of Civil Engineers, 2017, Minimum design loads and associated criteria for buildings and other structures: Reston, Va., American Society of Civil Engineers, ASCE Standard ASCE/SEI 7-16, 2 v.

ASTM D 25, 2017, Standard specifications for round timber piles, American Society for Testing and Materials, West Conshohocken, PA.

Atwater, B.F., and Hemphill-Haley, E., 1997, Recurrence intervals for great earthquakes of the past 3500 years at Northeastern Willapa Bay, Washington: U.S. Geological Survey Professional Paper 1576.

Atwater, B.F., Carson, B., Griggs, G.B., Johnson, H.P., and Salmi, M.S., 2014, Rethinking turbidite paleoseismology along the Cascadia subduction zone: Geology, v. 42:9, p. 827-830.

Atwater, B.F., and Griggs, G.B., 2012, Deep-sea turbidities as guides to Holocene earthquake history at the Cascadia subduction zone—Alternative views for a seismic-hazard workshop: U.S. Geological Survey Open-File Report 2012–1043, 58 p.

Axtel, P.J., and Stark, T.D., 2008, Increase in shear modulus by soil mix and jet grout methods, Deep Foundations Institute Journal, 2(1), p. 11-21.

BC Hydro, 2012, Probabilistic seismic hazard analysis (PSHA) model – Volume 2: Seismic source characterization (SSC) model, Report E658, September.

Baker, J. W. and Cornell, C. A., 2006, Spectral shape, epsilon and record selection: Earthquake Engineering and Structural Dynamics, v. 35, no. 9, p. 1077-1095.

Baker, J. W., 2011, Conditional mean spectrum: tool for ground-motion selection: Journal of Structural Engineering, v. 137, no. 3, p. 322-331.

Beaty, M., Schlechter, S., Greenfield, M., Bock, J., Dickenson, S., Kempner, L., and Cook, K., 2014, Seismic evaluation of transmission tower foundations at river crossings in the Portland-Columbia River region, In Proceedings of the 10th U.S. National Conference on Earthquake Engineering, Earthquake Engineering Research Institute, Anchorage, AK.

Becker, D. E.; Crooks, J. H. A.; Been, K.; and Jefferies, M .G., 1987, Work as a criterion for determining in situ and yield stresses in clays: Canadian Geotechnical Journal, v. 24, no. 4, p. 549-564.

Bemis, S.P., and Wells, R.E., 2012, Evidence for Quaternary faulting along the Gales Creek fault zone, northwest Oregon, Seismological Society of America Annual Meeting, April 17th-19th, San Diego, CA.

Beeson, M.H., Fecht, K.R., Reidel, S.P., and Tolan, T.L., 1985, Regional correlations within the Frenchman Springs Member of the Colum-bia River Basalt Group: New insights into the middle Miocene tec-tonics of northwestern Oregon: Oregon Geology, v. 47, p. 87–96.

Beeson, M.H., Tolan, T.L., and Anderson, J.L., 1989, The Columbia River Basalt Group in western Oregon: Geologic structures and other factors that controlled flow emplacement patterns, in Reidel, S.P., and Hooper, P.R., eds., Volcanism and Tectonism in the Columbia River Flood-Basalt Province: Geological Society of America Special Paper 239, p. 223–246, https:// doi.org /10 .1130 /SPE239 -p223.

Beeson, M.H., and Tolan, T.L., 1990, The Columbia River Basalt Group in the Cascade Range; a middle Miocene reference datum for structural analysis: Journal of Geophysical Research, v. 96, p. 19,547–19,559.

Beeson, M.H., Tolan, T.L., and Madin, I.P., 1991, Geologic Map of the Portland Quadrangle, Multnomah and Washington Counties, Oregon, and Clark County, Washington: Oregon Department of Geology and Mineral Industries, Geological Map Series GMS-75, scale 1:24,000.

Bennett, S. Streig, A., Levinson, R., Roberts, N., Dunning, A., Wells, R., Madin, I., O'Connor, J., Reynolds, N., Pringle, P., Grant, A., 2021, The Most Recent Earthquake on the Mount Hood Fault Zone, North-Central Oregon: Implications for Cascading Earthquake, Landslide, and Flood Multi-Hazards in the Columbia River Gorge, presented at GSA Connects 2021, Portland, Oreg.: Boulder, Colo., Geological Society of America, XX p.

Blakely, R.J., Wells, R.E., Yelin, T.S., Madin, I.P., and Beeson, M.H., 1995, Tectonic setting of the Portland-Vancouver area, Oregon and Washington: Constraints from low-altitude aeromagnetic data: Geological Society of America Bulletin, v. 107, p. 1051–1062."

Blakely, R.J., Wells, R.E., and Weaver, C.S., 1999, Puget Sound aeromagnetic maps and data: U.S. Geological Survey Open-File Report 99-514, http://pubs.usgs.gov/of/1999/of99-514/.

Blakely, R.J., Wells, R.E., Tolan, T.L., Beeson, M.H., Tréhu, A.M., and Liberty, L.M., 2000, New aeromagnetic data reveal large strike-slip (?) faults in the northern Willamette Valley, Oregon: Geological Society of America Bulletin, v. 112, p. 1225–1233.

Blakely, R.J., Stephenson, W.J., and Popowski, T., 2002, The Canby-Molalla fault, Oregon: Geological Society of America Abstracts with Programs, v. 34, no. 5, p. A-107.

Blakely, R.J., Beeson, M.H., Cruikshank, K., Wells, R.E., Johnson, A., and Walsh, K., 2004, Gravity study through the Tualatin Mountains, Oregon: Understanding crustal structure and earthquake hazards in the Portland urban area: Seismological Society of America Bulletin, v. 94, p. 1402–1409.

Boore, D.M., 2010, Orientation-independent, nongeometric-mean measures of seismic intensity from two horizontal components of motion: Bulletin of the Seismological Society of America, v. 100, no. 4, p. 1830-1835.

Boore, D.M., Stewart, J.P., Seyhan, E., and Atkinson, G.M., 2014, NGA-West2 equations for predicting PGA, PGV, and 5% damped PSA for shallow crustal earthquakes: Earthquake Spectra, v. 30, no. 3, p. 1057-1085.

Boulanger, R. W., and Idriss, I. M. (2007). "Evaluation of cyclic softening in silts and clays." Journal of Geotechnical and Geoenvironmental Engineering, ASCE, 133(6), 641-652.

Boulanger, R. W. and Idriss, I. M., 2014, CPT and SPT-based liquefaction triggering procedures: Davis, Calif., University of California Davis, Center for Geotechnical Modeling, report UCD/CGM-14/01, 134 p.

Boulanger, R.W., and Ziotopoulou, K., 2017, PM4SAND (version 3.1): A sand plasticity model for earthquake engineering applications, Report No. UCD/CGM-17/01, Center for Geotechnical Modeling, Department of Civil and Environmental Engineering, University of California, Davis, CA, October, 114 p.

Boulanger, R.W., and Ziotopoulou, K., PM4SILT (version 1): A silt plasticity model for earthquake engineering applications, Report No. UCD/CGM-18/01, Center for Geotechnical Modeling, Department of Civil and Environmental Engineering, University of California, Davis, CA, January, 109 p.

Campbell, K.W., and Bozorgnia, Y., 2014, NGA-West2 ground motion model for the average horizontal components of PGA, PGV, and 5% damped linear acceleration response spectra: Earthquake Spectra, v. 30, no. 3, p. 1087-1115.

Casagrande, A., 1936, The determination of the pre-consolidation load and its practical significance, In Proceedings of the 1st International Soil Mechanics and Foundation Engineering Conference, Cambridge, Mass., Casagrande (ed.), Harvard University, Cambridge, Mass., Vol. 3, p. 60-64.

Chiou, B.S.-J., and Youngs, R.R., 2014, Update of the Chiou and Youngs NGA model for the average horizontal component of peak ground motion and response spectra: Earthquake Spectra, v. 30, no. 3, p. 1117-1153.

Clague, J.J., 1997, Evidence for Large Earthquakes at the Cascadia Subduction Zone: Reviews of Geophysics, v. 35, no. 4, p. 439-460.

Clarke, S.H., Jr., and Carver, G.A., 1992, Late Holocene tectonics and paleoseismicity, southern Cascadia Subduction Zone: Science, v. 255, p. 188-192.

Dafalias, Y.F. and Manzari, M.T., 2004, Simple plasticity sand model accounting for fabric change effects, Journal of Engineering Mechanics, 130(6), p. 622-634.

Darienzo, M.E.; Peterson, C.D.; and Clough, Charles, 1994, Stratigraphic evidence for great subduction-zone earthquakes at four estuaries in northern Oregon, U.S.A.: Journal of Coastal Research, v. 10, no. 4, p. 850-876.

Darienzo, M., and Peterson, C., 1990, Investigation of coastal neotectonics and paleoseismicity of the southern Cascadia margin as recorded in coastal marsh systems," in Jacobson, M.L. ed., National Earthquake Hazards Reduction Program, Summaries of Technical Reports, Volume XXXI, U.S. Geological Survey Open File Report 90-680, p. 131-139.

DeMets, C., Gordon, R.G. and Argus, D.F., 2010, Geologically Current Plate Motions: Geophysical Journal International, v. 181, no. 1, p. 1–80.

Dobry, R., Ladd, R.S., Yokel, F.Y., Chung, R.M., and Powell, D., 1982, Prediction of pore water pressure buildup and liquefaction of sands during earthquakes by the cyclic strain method, NBS Building Science Series 138, Gaithersburg, MD: National Bureau of Standards.

Electrical Power Research Institute (EPRI), 1993, Guidelines for determining design basis ground motions: Palo Alto, Calif., Electrical Power Research Institute, Report no.TR 102293 5 v.

Evarts, R.C., and O'Connor, J.E., 2008, Geologic map of the Camas quadrangle, Clark County, Washington and Multnomah County, Oregon: U.S. Geological Survey Scientific Investigations Map 3017, scale: 1:24,000.

Evarts, R.C., O' Connor, J.E., Wells, R.E., and Madin, I P., 2009, The Portland Basin: A (big) river runs through it: GSA Today, v. 19, Is. 9, p. 4-10.

Flück, P., Hyndman, R.D., and Wang, Kelin, 1997, Three-dimensional dislocation model for great earthquakes of the Cascadia subduction zone: Journal of Geophysical Research, v. 102, no. 89, p. 20,539–20,550.

Geomatrix Consultants, Inc., 1995, Final report - seismic design mapping – state of Oregon: Report prepared by Geomatrix Consultants, Inc., project no. 2442, personal services contract 11688, for Oregon Department of Transportation, January.

Givler, R., Witter, R., Madin, I., and Amos, C., 2009, Paleoseismology of the Mount Angel fault in the Willamette Valley, Oregon— Collaborative research with William Lettis & Associates, Inc. and the Oregon Department of Geology and Mineral Industries: Technical report to the U.S. Geological Survey under contracts 06-HQ-GR0147 and 06-HQ-GR0148, 51 p.

Goldfinger, C., Nelson, C.H., and Johnson, J.E., 2003, Deep-Water Turbidites as Holocene Earthquake Proxies: The Cascadia Subduction Zone and Northern San Andreas Fault Systems: Annali Geofisica, v. 46, p. 1169-1194.

Goldfinger, C., Nelson, C.H., Morey, A., Johnson, J.E., Gutierrez-Pastor, J., Eriksson, A.T., Karabanov, E., Patton, J., Gracia, E., Enkin, R., Dallimore, A., Dunhill, G., and Vallier, T., 2012, Turbidite Event History: Methods and Implications for Holocene Paleoseismicity of the Cascadia Subduction Zone: USGS Professional Paper 1661-F, 184 p, 64 Figures.

Goldfinger, C., Galer, S., Beeson, J., and others, 2017, The importance of site selection, sediment supply, and hydrodynamics: a case study of submarine paleoseismology on the northern Cascadia margin, Washington USA: Marine Geology, v. 384, p. 4-46.

Gomberg, J., Bedrosian, P., Bodin, P., and others, 2010, Slow-slip phenomena in Cascadia from 2007 and beyond—A review: Geological Society of America Bulletin, v. 122, no. 7/8, p. 963-978.

Grant, W.C., 1989, More evidence from tidal-marsh stratigraphy for multiple late Holocene subduction earthquakes along the northern Oregon Coast: Geological Society of America Abstracts with Programs, v. 21, no. 4, p. 86.

Gutenberg, B., and Richter, C.F., 1944, Frequency of earthquakes in California: Bulletin of the Seismological Society of America, v. 34, no. 4, p. 185-188.

Hashash, Y.M.A., Musgrove, M.I., Harmon, J.A., and others, 2020, DEEPSOIL 7.0 user manual, Urbana, IL, Board of Trustees of University of Illinois at Urbana-Champaign.

Hatem, A.E., Collett, C.M., Gold, R.D., Briggs, R.W., Angster, S.A., Field, E.H., Anderson, M., Ben-Horin, J.Y., Dawson, T., DeLong, S., DuRoss, C., Thompson Jobe, J., Kleber, E., Knudsen, K.L., Koehler, R., Koning, D., Lifton, Z., Madin, I., Mauch, J., Morgan, M., Pearthree, P., Petersen, M., Pollitz, F., Scharer, K., Powers, P., Sherrod, B., Stickney, M., Wittke, S., and Zachariasen, J., 2021, Earthquake geology inputs for the National Seismic Hazard Model (NSHM) 2023, version 1.0: U.S. Geological Survey data release, https://doi.org/10.5066/P918XCUU.

HDR Engineering, Inc., 2021a, Earthquake Ready Burnside Bridge: Draft Environmental Impact Statement: Report prepared by HDR Engineering, Inc., Portland, Oreg., for Multnomah County, Oreg., February.

HDR Engineering, Inc., 2021b, Earthquake Ready Burnside Bridge: Revised Seismic Design Criteria Report: Report prepared by HDR Engineering, Inc., Portland, Oreg., for Multnomah County, Oreg., December.

Horst, A.E., Streig, A.R., Wells, R.E., and Bershaw, J., 2020, Multiple Holocene Earthquakes on the Gales Creek Fault, Northwest Oregon Fore-Arc: Bulletin of the Seismological Society of America, v. 111 (1), p. 476–489.

Hyndman, R.D., and Wang, K., 1993, Thermal constraints on the zone of major thrust earthquake failure: The Cascadia Subduction Zone: Journal of Geophysical Research, v. 98, p. 2,039 2,060.

Ishihara, K. and Yoshimine, M., 1992, Evaluation of settlements in sand deposits following liquefaction during earthquakes, Soils and Foundations, 32(1), p. 173-188.

Itasca Consulting Group, 2019, Fast lagrangian analysis of continua (FLAC), v. 8.1: Minneapolis, Minn., Itasca Consulting Group, Inc.

Jana, A. and Stuedlein, A.W., 2021, Monotonic, cyclic, and postcyclic responses of an alluvial plastic silt deposit, Journal of Geotechnical and Geoenvironmental Engineering, ASCE, 147(3), 04020174.

Jarrard, R.D., 1986, Relations among subduction parameters: Reviews of Geophysics, v. 24, no. 2, p. 217-284.

Kao, H., Wang, K., Chen, R-Y., Wada, I., He, J. and Malone, S.D., 2008, Identifying the rupture plane of the 2001 Nisqually, Washington, earthquake: Bulletin of the Seismological Society of America, vol. 98, no.3, p. 1546-1558.

Keefer, D.I., and Bodily, S.E., 1983, Three-point approximations for continuous random variables: Management Science, v. 26, p. 595-609.

Ladd, C.C. and Foott, R., 1974, "New design procedure for stability of soft clays." Journal of the Geotechnical Engineering Division, ASCE, 100(GT7), 763-786.

Lau, T., Anderson, M., Steely, A., Horst, A., Amaral, C., Reedy, T. Dassow, W., and Stanton, K, 2021, Geophysical Insight into the Doty Fault Zone: Potential Field Modeling and Constraints on Activity, presented at GSA Connects 2021, Portland, Oreg.: Boulder, Colo., Geological Society of America, XX p.

Liberty, L.M., Hemphill-Haley, M.A., and Madin, I.P., 2003, The Portland Hills Fault: uncovering a hidden fault in Portland, Oregon using high-resolution geophysical methods: Tectonophysics, v. 268, p. 89-103.

Lin, Ting; Harmsen, S. C.; Baker, J. W.; and Luco, Nicolas, 2013, Conditional spectrum computation incorporating multiple causal earthquakes and ground-motion prediction models: Bulletin of the Seismological Society of America, v. 103, no. 2A, p. 1103-1116.

Loehr, J.E., Lutenegger, A., Rosenblad, B., and Boeckmann, A., 2016, Geotechnical site characterization: U.S. Federal Highway Administration, Geotechnical Engineering Circular no. 5, Report No. FHWA-NHI-16-072, 688 p.

Ludwin, R.S., Weaver, C.S., and Crosson, R.S., 1991, Seismicity of Washington and Oregon in Slemmons, D.B., E.R. Engdahl, M.D. Zoback, and D.D. Blackwell (eds.), Neotectonics of North America, p. 77-98.

Ma, L., Madin, I., Duplantis, S., Williams, K., 2012, Lidar-based surficial geologic map and database of the greater Portland, Oregon, area, Clackamas, Columbia, Marion, Multnomah, Washington, and Yamhill Counties, Oregon, and Clark County, Washington: Oregon Department of Geology and Mineral Industries Open-File Report O-12-02.

Mabey, M.A., Madin,I.P., Youd, T.L., and Jones, C.F., 1993, Earthquake hazard maps of the Portland Quadrangle, Multnomah and Washington Counties, Oregon, and Clark County, Washington: Oregon Department of Geology and Mineral Industries Geologic Map Series GMS-79.

Madin, I.P., 1990, Earthquake-hazard geology maps of the Portland metropolitan area, Oregon—Text and map explanation: State of Oregon, Department of Geology and Mineral Industries Open-File Report 0-90-2, 21 p., 8 pls., scale 1:24,000.

Madin, I., 2009, Geologic map of the Oregon City 7.5' quadrangle, Clackamas County, Oregon: Oregon Department of Geology and Mineral Industries Geologic Map Series GMS–119, scale 1:24,000.

Madin, I., Streig, A., Burns, W., and Ma, L., 2017, The Mount Hood Fault Zone—Late Quaternary and Holocene Fault Features Newly Mapped with High resolution Lidar Imagery, *In* Scott, W.E., and Gardner, C.A., 2017, Field-trip guide to Mount Hood, Oregon, highlighting eruptive history and hazards: U.S. Geological Survey Scientific Investigations Report 2017–5022–G, 115 p., https://doi.org/10.3133/sir20175022g.

Manzari, M.T. and Dafalias, Y.F., 1997, A critical state two-surface plasticity model for sand, Geotechnique, 47(2), p. 255-272.

Mayne, P.W., 2005, Integrated ground behavior: In-situ and lab tests, In Vol. 2 of Deformation characteristics of geomaterials, p. 155-177, London: Taylor & Francis.

Mazzotti, S., Dragert, H., Hyndman, R.D., Miller, M.M., and Henton, J.A., 2002, GPS Deformation in a Region of High Crustal Seismicity, North Cascadia Forearc: Earth and Planetary Science Letters, v. 198, p. 41-48.

Meyers, R.A., Smith, D.G., Jol, H.M., and Peterson, C.D., 1996, Evidence for eight great earthquake-subsidence events detected with ground penetrating radar, Willapa Bay, Washington: Geology, v. 24, p. 99-102.

McCaffrey, R., King, R.W., Payne, S.J., and Lancaster, M., 2013, Active Tectonics of Northwestern U.S. Inferred from GPS-derived Surface Velocities: Journal of Geophysical Research, Solid Earth, v. 118, no. 2, p. 709–723.

McCaffrey, R., Qamar, A.I., King, R.W., Wells, R., Khazaradze, G., Williams, C.A., Stevens, C. W., Vollick, J.J., and Zwick, P. C., 2007, Fault Locking, Block Rotation and Crustal Deformation in the Pacific Northwest: Geophysical Journal International, v. 169, no. 3, p. 1315–1340.

McCrory, P.A., compiler, 2003, Fault number 592, Willapa Bay fault zone, in Quaternary fault and fold database of the United States: U.S. Geological Survey website, https://earthquakes.usgs.gov/hazards/qfaults, accessed 01/21/2022 12:26 PM.

McCrory, P.A., Blair, J.L., Oppenheimer, D.H., and Walter, S.R., 2006, Depth to the Juan de Fuca slab beneath the Cascadia subduction margin – A 3-D model for sorting earthquakes: U.S. Geological Survey Data Series 91, ver. 1.2, 13 p.

McCrory, P.A., Blair, J.L., Waldhauser, Felix, and Oppenheimer, D.H., 2012, Juan de Fuca slab geometry and its relation to Wadati-Benioff zone seismicity: Journal of Geophysical Research, v. 117, no. B9, paper B09306, 23 p.

McCrory, P.A., Foster, D.S., Danforth, W.W., and Hamer, M.R., 2002, Crustal deformation at the leading edge of the Oregon Coast Range block, offshore Washington (Columbia River to Hoh River): U.S. Geological Survey Professional Paper 1661-A, 47 p., 2 pls.

McPhee, D.K., Langenheim, V.E., Wells, R.E., and Blakely, R.J., 2014, Tectonic evolution of the Tualatin Basin, northwest Oregon, as revealed by inversion of gravity data: Geosphere: v.10 no. 2, p. 264-275.

Muratani, Satoko; Miyake, Hiroe; and Koketsu, Kazuki, 2008, Scaling of characterized slip models for plate – boundary earthquakes: Earth, Planets and Space, v. 60, no. 9, p. 987-991.

National Research Council, 1985, Liquefaction of soils during earthquakes, Committee on Earthquake Engineering, Commission on Engineering and Technical Systems, Washington DC: National Academy Press.

Nelson, A.R., Shennan, I., and Long, A.J., 1996, Identifying coseismic subsidence in tidal-wetland stratigraphic sequences at the Cascadia Subduction Zone of western North America: Journal of Geophysical Research, v. 101, p. 6115-6135.

Obermeier, S.F., 1995, Preliminary estimates of the strength of prehistoric shaking in the Columbia River Valley and the southern half of coastal Washington, with emphasis for a Cascadia Subduction Zone earthquake about 300 years ago: U.S. Geological Survey Open-File Report 94-589, 46 p.

O'Connor, J.E., Sarna-Wojcicki, A., Wozniak, K.C., Pollette, P.J., and Fleck, R.J., 2001, Origin, extent, and thickness of Quaternary geologic units in the Willamette Valley, Oregon: U.S. Geological Survey Professional Paper 1620, 52 p.

Oregon Department of Transportation (ODOT), 1987, Soil and Rock Classification Manual, Salem, Oregon, available: ftp://ftp.odot.state.or.us/techserv/Geo-Environmental/Geotech/Manuals/Soil_Rock_Classification_Manual.pdf.

Oregon Department of Transportation (ODOT), 2021, Bridge Design Manual (rev. May 2021): Salem, Oregon, available: https://www.oregon.gov/ODOT/Bridge/Pages/Bridge-Design-Manual.aspx.

Oregon Department of Transportation (ODOT), 2019, Geotechnical Design Manual: Salem, Oregon, available: https://www.oregon.gov/ODOT/GeoEnvironmental/Pages/Geotech-Manual.aspx.

Oregon Department of Transportation (ODOT), 2021, Standard Specifications for Construction: Salem, Oregon, available: https://www.oregon.gov/ODOT/Business/Pages/Standard_Specifications.aspx.

Papazachos, B.C., Scordilis, E.M., Panagiotopoulos, D.G., Papazachos, C.B., and Karakaisis, G.F., 2004, Global relations between seismic fault parameters and moment magnitudes of earthquakes: Bulletin of the Geological Society of Greece, v. v. 36, p. 1,482-1,489.Parker, G. A.; Stewart, J. P.; Boore, D. M., and others, 2020, NGA-subduction global ground-motion models with regional adjustment: PEER Report 2020/03, Pacific Earthquake Engineering Research Center, University of California, Berkeley, p. 96.

Personius, S.F., compiler, 2002, Fault number 714, Helvetia fault, in Quaternary fault and fold database of the United States: U.S. Geological Survey website, https://earthquakes.usgs.gov/hazards/qfaults, accessed 01/24/2017 12:24 PM.

Personius, S.F., compiler, 2002, Fault number 715, Beaverton fault zone, in Quaternary fault and fold database of the United States: U.S. Geological Survey website, https://earthquakes.usgs.gov/hazards/qfaults, accessed 01/24/2017 12:24 PM.

Personius, S.F., compiler, 2002, Fault number 716, Canby-Molalla fault, in Quaternary fault and fold database of the United States: U.S. Geological Survey website, https://earthquakes.usgs.gov/hazards/qfaults, accessed 01/24/2017 12:24 PM.

Personius, S.F., compiler, 2002, Fault number 717, Newberg fault, in Quaternary fault and fold database of the United States: U.S. Geological Survey website, https://earthquakes.usgs.gov/hazards/qfaults, accessed 01/24/2017 12:21 PM.

Personius, S.F., compiler, 2002, Fault number 853a, Metolius fault zone, Green Ridge section, in Quaternary fault and fold database of the United States: U.S. Geological Survey website, https://earthquakes.usgs.gov/hazards/qfaults, accessed 01/21/2022 12:23 PM.

Personius, S.F., compiler, 2002, Fault number 864, Clackamas River fault zone, in Quaternary fault and fold database of the United States: U.S. Geological Survey website, https://earthquakes.usgs.gov/hazards/qfaults, accessed 01/21/2022 12:14 PM.

Personius, S.F., compiler, 2002, Fault number 866, Hood River fault zone, in Quaternary fault and fold database of the United States: U.S. Geological Survey website, https://earthquakes.usgs.gov/hazards/qfaults, accessed 01/21/2022 12:16 PM.

Personius, S.F., compiler, 2002, Fault number 875, Oatfield fault, in Quaternary fault and fold database of the United States: U.S. Geological Survey website, https://earthquakes.usgs.gov/hazards/qfaults, accessed 01/24/2017 12:25 PM.

Personius, S.F., compiler, 2002, Fault number 876, East Bank fault, in Quaternary fault and fold database of the United States: U.S. Geological Survey website, https://earthquakes.usgs.gov/hazards/qfaults, accessed 01/24/2017 12:26 PM.

Personius, S.F., compiler, 2002, Fault number 878, Grant Butte fault, in Quaternary fault and fold database of the United States: U.S. Geological Survey website, https://earthquakes.usgs.gov/hazards/qfaults, accessed 01/24/2017 12:27 PM.

Personius, S.F., compiler, 2002, Fault number 879, Damascus-Tickle Creek fault zone, in Quaternary fault and fold database of the United States: U.S. Geological Survey website, https://earthquakes.usgs.gov/hazards/qfaults, accessed 01/24/2017 12:27 PM.

Personius, S.F., compiler, 2002, Fault number 880, Lacamas Lake fault, in Quaternary fault and fold database of the United States: U.S. Geological Survey website, https://earthquakes.usgs.gov/hazards/qfaults, accessed 01/24/2017 12:28 PM.

Personius, S.F., compiler, 2002, Fault number 882, Happy Camp fault, in Quaternary fault and fold database of the United States: U.S. Geological Survey website, https://earthquakes.usgs.gov/hazards/qfaults, accessed 01/21/2022 12:18 PM.

Personius, S.F., compiler, 2002, Fault number 1809, White Branch fault zone, in Quaternary fault and fold database of the United States: U.S. Geological Survey website, https://earthquakes.usgs.gov/hazards/qfaults, accessed 01/21/2022 12:24 PM.

Personius, S.F., and Lidke, D.J., compilers, 2003, Fault number 580, Faults near The Dalles, in Quaternary fault and fold database of the United States: U.S. Geological Survey website, https://earthquakes.usgs.gov/hazards/qfaults, accessed 01/21/2022 12:20 PM.

Personius, S.F., Lidke, D.J., and Haller, K.M., compilers, 2014, Fault number 873, Mount Angel fault, in Quaternary fault and fold database of the United States: U.S. Geological Survey website, https://earthquakes.usgs.gov/hazards/qfaults, accessed 01/21/2022 12:12 PM.

Personius, S.F., and Haller, K.M., compilers, 2017, Fault number 718, Gales Creek fault zone, in Quaternary fault and fold database of the United States: U.S. Geological Survey website, https://earthquakes.usgs.gov/hazards/qfaults, accessed 01/21/2022 12:10 PM.

Personius, S.F., and Haller, K.M., compilers, 2017, Fault number 877, Portland Hills fault, in Quaternary fault and fold database of the United States: U.S. Geological Survey website, https://earthquakes.usgs.gov/hazards/qfaults, accessed 01/21/2022 12:00 PM.

Peterson, C.D., and Darienzo, M.E., 1996, Discrimination of climatic, oceanic, and tectonic mechanisms of cyclic marsh burial, Alsea Bay, Oregon, in Rogers, A.M., Walsh, T.J., Kockelman, W.J., and Priest, G.R., eds., Assessing earthquake hazards and reducing risk in the Pacific Northwest: U.S. Geological Survey Professional Paper 1560, p. 115-146.

Petersen, M.D., Moschetti M.P., Powers, P.M., and others, 2014, Documentation for the 2014 update of the United States national seismic hazard maps: U.S. Geological Survey Open-File Report 2014-1091, 243 p.

Petersen, M.D.; Shumway, A.M.; Powers, P.M.; and others, 2020, The 2018 update of the US National Seismic Hazard Model: overview of model and implications: Earthquake Spectra, v. 36, no. 1, p. 5-41.

Pezzopane, S.K., and Weldon II, R.J., 1993, Tectonic Role of Active Faulting in Central Oregon: Tectonics, v. 12, no. 5, p. 1140–1169.

Popowski, T.A., 1996, Geology, structure, and tectonic history of the Tualatin Basin, northwestern Oregon: Corvallis, Oregon State University, M.S. Thesis, 126 p.

Pratt, T.L., Odum, J., Stephenson, W., Williams, R., Dadisman, S., Holmes, M., Haug, B., 2001. Late Pleistocene and Holocene tectonics of the Portland Basin, Oregon and Washington, from high-resolution seismic profiling: Bulletin of the Seismological Society of America 91 (4), 637– 650.

Preston, L.A., Creager, K.C., Crosson, R.S., and others, 2003, Intraslab earthquakes: dehydrating the Cascadia slab: Science, v. 302, p. 1197-1200.

Redwine, J., R. E. Klinger, L. A. Piety, R. E. Wells, B. L. Sherrod, J. C. Howe, R. Levinston, K. Hornsby, and A. Niem, 2017, Quaternary activity on the Gales Creek fault, Northwest Oregon: Geological Society of America Abstracts with Programs, v., 49, p. 281–287, doi: 10.1130/abs/2017AM-306019.

Rhyner, C.R., 2018, Densification of granular soils by pile driving and implications for evaluation of liquefaction, In Proceedings of IFCEE 2018, GSP 294, ASCE.

Roe, W.P., and Madin, I.P., 2012, 3D geology and shear-wave velocity models of the Portland, Oregon, metropolitan area, Oregon Department of Geology and Mineral Industries Open-file Report O-13-12, 52 p.

Rollins, K.M., Singh, M., and Roy, J., 2020, "Simplified equations for shear-modulus degradation and damping of gravels." Journal of Geotechnical and Geoenvironment Engineering, ASCE, 146(9), 04020076.

Satake, K., Shimazaki, K., Tsuji, Y., and Ueda, K., 1996, Time and size of a giant earthquake in Cascadia inferred from Japanese tsunami records of January 1700, Nature, 379, p. 246-249.

Scanlon, D.P., Bershaw, J., Wells, R.E., and Streig, A.R., 2021, The spatial and temporal evolution of the Portland and Tualatin forearc basins, Oregon, USA: Geosphere, v. 17, no. 3, p. 804– 823, https://doi.org /10.1130 /GES02298.1.

Shannon & Wilson, Inc., 2021, Geotechnical report, Burnside Bridge Environmental Impact Study: Report prepared by Shannon & Wilson, Inc., Lake Oswego, Oreg., 102636-001, for HDR Engineering, Inc., Portland, Oreg., February, 75 p.

Shennan, I., Long, A.J., Rutherford, M.M., Green, F.M., Innes, J.B., Lloyd, J.M., Zong, Y., and Walker, K.J., 1996, Tidal marsh stratigraphy, sea-level change and large earthquakes, I: a 5,000 year record in Washington, USA: Quaternary Science Reviews, v. 15, p. 1,023-1,059.

Si, H., Midorikawa, S., and Kishida, T., 2020, Development of NGA-Sub ground-motion model of 5%-damped pseudo-spectral acceleration based on database for subduction earthquakes in Japan: PEER Report 2020/06, Pacific Earthquake Engineering Research Center, University of California, Berkeley, p. 56.

Silva, W., Abrahamson, N., Toro, G., and Constantino, C., Description and validation of the stochastic ground motion model: Pacific Engineering and Analysis, El Cerrito, California, Report prepared for the Engineering Research and Applications Division, Department of Nuclear Energy, Brookhaven National Laboratory, Associated Universities, Inc., Upton, New York. 1176 p.

Steely, A., Anderson, M., von Dassow, W., and others, 2021, Geologic and geophysical assessment of tectonic uplift and fault activity in the Doty and Willapa Hills, southwest Washington : Final report: Report prepared by Washington Geological Survey for Washington State Department of Ecology, 279 p. ; 1 plate.

Stephenson W.J., Reitmann, N.G., and Angster S.J., 2017, P- and S-wave velocity models incorporating the Cascadia subduction zone for 3D earthquake ground motion simulations - Update for OFR 2007-1348. Open-File report no. 2017-1152. Reston, VA: US Geological Survey, 17 p.

Stirling, M.; Rhoades, D.; and Berryman, B., 2002, Comparison of earthquake scaling relations derived from data of the instrumental and preinstrumental era: Bulletin of the Seismological Society of America, vol. 92, no. 2, p. 812-830.

Strasser, F.O., Arango, M.C., and Bommer, J.J., 2010, Scaling of the source dimensions of interface and intraslab subduction-zone earthquakes with moment magnitude: Seismological Research Letters, v. 81, p. 941-950.

Stuedlein, A.W., Gianella, T.N., and Canivan, G., 2016, Densification of granular soils using conventional and drained timber displacement piles, Journal of Geotechnical and Geoenvironmental Engineer, ASCE, 142(12), 04016075.

Thomas, G.C., Crosson, R.S., Carver, D.L., and Yelin, T.S., 1996, The 25 March 1993 Scotts Mills, Oregon, earthquake and aftershock sequence—Spatial distribution, focal mechanisms, and the Mount Angel fault: Bulletin of the Seismological Society of America, v. 86, no. 4, p. 925-935.

Tokimatsu, K. and Yoshimi, Y., 1983, Empirical correlation of soil liquefaction based on SPT N-value and fines content, Soils and Foundations, 23(4), p. 56-74.

Unruh, J.R., Wong, I.G., Bott, J.D.J., Silva, W.J., and Lettis, W.R., 1994, Seismotectonic evaluation, Scoggins Dam, Tualatin Project, northwestern Oregon: Final Report prepared for U.S. Department of the Interior, Bureau of Reclamation, 206 p., 4 pls., scale 1:500,000.

U.S. Geological Survey (USGS), 2006, Quaternary fault and fold database for the United States, from USGS web site: http//earthquakes.usgs.gov/regional/qfaults/.

Vucetic, M. and Dobry, R., 1991, Effect of soil plasticity on cyclic response: Journal of Geotechnical Engineering, v. 117, no. 1, p. 89-107.

Waitt, R.B., 1985. Case for periodic, colossal jokulhloups from Pleistocene glacial Lake Missoula. Geological Society of America Bulletin 96, 1271–1286.

Walsh, K.P., Peterson, G.L., Beeson, M.H., Wells, R.E., Fleck, R.J., Evarts, R.C., Duvall, Alison, Blakely, R.J., and Burns, Scott, 2011, A tunnel runs through it--An inside view of the Tualatin Mountains, Oregon: U.S. Geological Survey Scientific Investigations Map 3144.

Wang, Kelin; Wells, R.E.; Mazzotti, Stephane; and others, 2003, A revised dislocation model of interseismic deformation of the Cascadia subduction zone: Journal of Geophysical Research, v. 108, no. B1, paper ETG 9, 13 p.

Weaver, C.S., and Baker, G.E., 1988, Geometry of the Juan de Fuca plate beneath Washington and northern Oregon from seismicity: Bulletin of the Seismological Society of America, v. 78, p. 264-275.

Wells, D.L., and Coppersmith, K.J., 1994, New empirical relationships among magnitude, rupture length, rupture width, rupture area, and surface displacement: Bulletin of the Seismological Society of America, v. 84, no. 4, p. 974-1002.Wells, R.E., Blakely, R.J., and Bemis, S.P., 2020, Northward migration of the Oregon forearc on the Gales Creek fault: Geosphere, v. 16, p. 660-684.

Wells, R.E., Blakely, R.J., and Bemis, S., 2020a, Northward migration of the Oregon forearc on the Gales Creek fault: Geosphere, v. 16, p. 660–684, https:// doi .org /10 .1130/GES02177 .1.

Wells, R.E., Haugerud, R.A., Niem, A.R., Niem, W.A., Ma, L., Evarts, R.C., O'Connor, J.E., Madin, I.P., Sherrod, D.R., Beeson, M.H., Tolan, T.L., Wheeler, K.L., Hanson, W.B., and Sawlan, M.G., 2020b, Geologic map of the greater Portland metropolitan area and surrounding region, Oregon and Washington: U.S. Geological Survey Scientific Investigations Map 3443, pamphlet 55 p., 2 sheets, scale 1:63,360, https://doi.org/10.3133/sim3443.Wells, R.E., and Simpson, R.W., 2001, Northward Migration of the Cascadia Forearc in the Northwestern U.S. and Implications for Subduction Deformation: Earth, Planets and Space, v. 53, no. 4, p. 275-283.

Wells, R.E., Weaver, C.S., and Blakeley, R.J., 1998, Fore-arc migration in Cascadia and its neotectonic significance: Geology, v. 26, p. 759-762.

Williams, H.F.L., Hitchinson, I., and Nelson, A.R., 2005, Multiple sources for late-Holocene tsunamis at Discovery Bay, Washington State, USA: The Holocene, v. 1, no. 1, 60 73 p.

Wilson, D.E., 1997, Post-middle Miocene geologic history of the Tualatin basin, Oregon, with hydrogeologic implications: Portland, Oreg., Portland State University doctoral dissertation, 321 p.

Wilson, D.E., 1998, Post-middle Miocene geologic evolution of the Tualatin basin, Oregon: Oregon Geology, v. 60, no. 5, p. 99–116.

Wong, I., Silva, W., Bott, J., Wright, D., Thomas, P., Gregor, N., Li, S., Mabey, M., Sojourner, A., and Wang, Y., 2000, Earthquake scenario and probabilistic ground shaking maps for the Portland, Oregon, metropolitan area: Oregon Department of Geology and Mineral Industries Interpretive Map Series IMS-16.

Woodring, D., 2020, Kinematics of the Columbia Hills Anticline and the Warwick Strike-Slip Fault, Yakima Fold and Thrust Belt, Washington, USA.: Oregon State University M.S. Thesis, 150 p.

Yamaguchi, D.K., Atwater, B.F., Bunker, D.E., Benson, B.E., Reid, M.S., 1997, Tree-ring Dating the 1700 Cascadia Earthquake: Nature, v.389, p. 922-923.

Yeats, R.S., Graven, E.P., Werner, K.S., Goldfinger, C., and Popowski, T.A., 1996, Tectonics of the Willamette Valley, Oregon, in Rogers, A.M., Walsh, T.J., Kockelman, W.J., and Priest, G.R., eds., Assessing earthquake hazards and reducing risk in the Pacific Northwest: U.S. Geological Survey Professional Paper 1560, v. 1, p. 183-222.

Youngs, R.R., and Coppersmith, K.J., 1985, Implications of fault slip rates and earthquake recurrence models to probabilistic seismic hazard estimates: Bulletin of the Seismological Society of America, v. 75, no. 4, p. 939-964.

TABLE 7-1 - Largest Historical Earthquakes Felt In Oregon

Date[1]	Time (GMT)	Magnitude[2]	Maximum MM Intensity	Location	Comments
Nov. 23, 1873	05:00	ML 6.75	VIII	Crescent City	Largest historic event
Oct. 12, 1877	17:00	ML 5.75	VII	Portland	Portland's second largest event
Feb. 4, 1892	04:30	ML 5	VI	Portland	"Severe shock"
Mar. 5. 1893	?		VI or VII	Umatilla	
Apr. 2, 1896	11:17	ML 4	VI	McMinnville	
Apr. 19, 1906	09:30		v	N of Lakeview	Three felt aftershocks
Oct. 14, 1913	23:00		VI	Hells Canyon	
May. 18, 1915	03:00		v	Portland	One of three shocks
Apr. 14, 1920	23:45		v	Crater Lake	One of three shocks
Feb. 25, 1921	20:00		v	E of Sweetwater	
Jan. 11, 1923	04:29		VI	Lakeview	
Jan. 6, 1924	23:10		v	Milton-Freewater	
Apr. 9, 1927	05:00		v	Pine Valley-Cuddy Mnt	
Jul. 19, 1930	02:38	ML 4	V-VI	20 km NW of Salem	Cracked plaster
Jul. 16, 1936	07:07	ML 6.1	VII+	Milton-Freewater	Eastern Oregon's largest event
Jul. 18, 1936	16:30		v	Milton-Freewater	Aftershock
Aug. 4, 1936	09:19		v	Milton-Freewater	Aftershock
Aug. 28, 1936	04:39		v	Milton-Freewater	Aftershock
Dec. 29, 1941	18:37	ML 4.5	VI	Portland	Minor damage
Jun. 12, 1942	09:30		v	Pine Valley-Cuddy Mountain	Minor damage
Nov. I, 1942	17:00		v	Portland	
Jan. 7, 1951	22:45		v	Hermiston	
Dec. 16, 1953	04:32	ML 4.5	VI	Portland	Minor damage in Portland
Nov. 17, 1957	06:00	ML 4.5	VI	S of Tillamook	Felt strongest near Salem
Mar. 12. 1958	12:09	ML 4.5		SE of Adel	
Jun. 2. 1959	18:49	ML 4.7		NW of Burns	
Aug. 19, 1961	04:56	ML 4.5	VI	SE of Salem	Minor damage in Albany
Nov. 7, 1961	01:29	ML 5	VI	NW of Portland	Minor damage in Portland
Nov. 6, 1962	03:36	Mw 5.2, ML 5.5	VII	Vancouver-Portland	Damage in Portland
Mar. 7, 1963	23:53	Mb 4.6	v	West of Salem	Minor damage in Salem

TABLE 7-1 - Largest Historical Earthquakes Felt In Oregon

Date[1]	Time (GMT)	Magnitude[2]	Maximum MM Intensity	Location	Comments
Nov. 23, 1873	05:00	ML 6.75	VIII	Crescent City	Largest historic event
Dec. 27, 1963	02:36	ML 4.5	VI	Vernonia	Minor damage
May. 30. 1968	00:35	ML 5.I	v	Adel	Swarm
Jun. 3, 1968	13:27	ML 5.0	v	Adel	Damage
Jun. 4, 1968	02:34	ML 4.7	VI	Adel	Swarm
Apr. 13, 1976	00:47	ML 4.8	V-VI	Deschutes Valley	Minor damage
Mar. 25, 1993	13:34	ML 5.6	VII	Scotts Mills	$28 million in damage
Sep. 21, 1993	03:28	ML 5.9	VII	Klamath Falls	Two deaths
Sep. 21, 1993	05:45	ML 6.0	VII-VIII	Klamath Falls	$7.5 million in damage
Dec. 4, 1993	22:15	ML 5.1	VII	Klamath Falls	Aftershock

Notes:

1 This table is adapted from Wong and Bott (1994).

2 ML = local magnitude; Mb = body-wave magnitude; Mw = moment magnitude

Table 7-2 - Potential Quaternary-Active Faults Located Within 150 Kilometers of Burnside Bridge site

Fault	Geologic Evidence for Tectonic Activity in Quaternary and Fault Characteristics[1]	Significant Paleoseismic Evidence for Earthquakes <12,000 Yr	Fault included in USGS Model/Database?[2]	Estimated Maximum Magnitude[3]	Approximate Distance from EQRB (km)	Sources
PORTLAND HILLS FAULT (PHF)	Considered part of the dextral-oblique Portland fault zone that, along with the East Bank and Oatfield/Sylvan faults, bound the Portland Hills anticlinal uplift (Beeson and others, 1990; Blakely and others, 1995). These faults may be structurally linked at depth (McPhee and others, 2014). Prominent escarpment of mapped faulted CRB along northeast face of Portland West Hills, but PHF trace buried by undeformed Quaternary surficial deposits (Madin, 1990). No mapped features that indicate Holocene surface deformation along PHF. However, indirect evidence of Quaternary depfrmation: (1) seismic reflection and ground-penetrating radar data imply possible offset Missoula Flood deposits (Pratt and others, 2001; Liberty and others, 2003); and, (2) deformed and liquefied Pleistocene Missoula flood deposits at North Clackamas Park (Wong and others, 2001). Given lack of surface expression of fault, QFFD cites a low slip rate (<0.2) (Personius and Haller, 2017, Fault 877). This is consistent with slip rates estimated for the Sylvan-Oatfield fault, based on fault exposure in tunnel excavation (Walsh and others, 2011).	No	QFFD (Fault 877) NSHM14 NSHM23v1	7	1	Madin, 1990; Beeson and others, 1991; Unruh and others, 1994; Blakely, 1995; Pratt and others, 2001; Liberty and others, 2003; McPhee and others, 2014; Personius and Haller, 2017 (Fault 877); Walsh and others 2011; Wong and others, 2001, Wells and others, 2020b
EAST BANK FAULT (EBF)	Considered part of the dextral-oblique Portland fault zone that, along with the Portland Hills and Oatfield/Sylvan faults, bound the Portland Hills anticlinal uplift (Beeson and others, 1990; Blakely and others, 1995). These faults may be structurally linked at depth (McPhee and others, 2014). Exposures of the EBF and subsurface exploration show fault offsets CRBG and Troutdale Fm (Pliocene) by 60-90 m (Beeson and others, 1990); but the EBF is largely concealed at the surface by undisplaced Missoula Flood deposits (Madin, 1990). Seismic reflection data suggest at depth paleochannels and deposits related to the Missoula Flood deposits are vertically offset by 2-5 m, suggesting possible late Quaternary activity and slip rate of ~0.2 mm/yr (Pratt and others, 2001). Due to the lack of geomorphic expression of the fault, Personius (2002, Fault 876) assumes low slip rates (<0.2).	No	QFFD (Fault 876)	6.8	1	Beeson and others, 1991; Madin and others, 1990; McPhee and others, 2014; Personius, 2002 (Fault 876); Pratt and others, 2001, Wells and others, 2020b.
SYLVAN-OATFIELD FAULT (SOF)	Considered part of the dextral-oblique Portland fault zone that, along with the Portland Hills and East bank faults, bound the Portland Hills anticlinal uplift (Beeson and others, 1990; Blakely and others, 1995). May be structurally linked to the Portland Hills fault at depth (Blakely and others, 1995; McPhee and others, 2014). SOF identified by mapped offsets of CRB, but no Quaternary surficial deposits have mapped offsets across SOF(Madin, 1990). SOF exposure in tunnel excavation revealed Miocene CRBG faulted against Quaternary Boring Lava (1 Ma); Slip rate estimated from tunnel exposure, 0.1-0.24 Walsh et al (2011) and Wells and other (2020b). Gravity data suggests 300 m vertical offset CRBG = 0.02 (McPhee, 2014)	No	QFFD (Fault 875) NSHM23v1	6.77	5	Beeson and others, 1991; Madin and others, 1990; McPhee and others, 2014; Personius, 2002 (Fault 875); Walsh and others, 2011; Wells and others, 2020b
GRANT BUTTE FAULT ZONE (GBFZ)	GBFZ (AKA Tickle Creek fault) comprised of zone of rnumerous enticulated short northeast- and northwest-trending faults that offset offset rocks of the Pliocene Troutdale Formation, Plio-Pleistocene Springwater Formation, and Pleistocene Boring Lava; 50-75 m escarpment across the fault (Madin, 1990; Wells and others, 2020). GBFZ strands are near-vertical reverse faults with a significant component of right-lateral strike-slip. In the subsurface, Boring Lava is offset up to 120 across fault (Unruh, 1994, in Personius, 2002). Based on available evidence of offset lava, the last rupture might have been mid-late Quaternary, but overlying Missoula Flood deposits not deformed (Madin, 1990). Due to no identified deformation of surficial late-Pleistocene deposits, Personius (2002) infers low slip rates (<0.2 mm/yr). NSHM14 uses slip rate (0.14) from geodetic data (Petersen and others, 2014).	No	QFFD (Fault 878, 879) NSHM14	6.21	11	Madin, 1990; Unruh, 1994; Personius, 2002 (Faults 878 and 879); Peterson and others, 2014; Wells and others, 2020b

Table 7-2 - Potential Quaternary-Active Faults Located Within 150 Kilometers of Burnside Bridge site

Fault	Geologic Evidence for Tectonic Activity in Quaternary and Fault Characteristics[1]	Significant Paleoseismic Evidence for Earthquakes <12,000 Yr	Fault included in USGS Model/Database?[2]	Estimated Maximum Magnitude[3]	Approximate Distance from EQRB (km)	Sources
BEAVERTON FAULT ZONE (BFZ)	Deformed CRBG and upper Hillsboro Fm (< 750 ka) mapped in subsurface explorations (Popowski, 1996; Wilson, 1998). Offset of CRBG yields long term slip rate: 200m offset of CRBG = 0.01 mm/yr (McPhee, 2014; Wilson, 1997), or 350m = 0.02 mm/yr (Popowski, 1997). Offset of Missoula or Holocene deposits across BFZ not observed. Blakely and others (2000) suggest, based on aeromagnetic-anomaly mapping, BFZ may be a compressional left-stepping fault between dextral Gales Creek fault and Canby-Molalla fault, but age control of motion is poorly-constrained (Wells and others, 2020a; 2020b).	No	QFFD (Fault 715) NSHM23v1	6.4	12	Madin, 1990; Popowski, 1996; Wilson, 1998; Blakely and others, 2000; Personius, 2002 (Fault 715); McPhee and others, 2014; Wells and others, 2020a; 2020b
BOLTON FAULT (BF)	Madin (1990) identifed a 150-m-high escarpment of CRBG as BF that offsets by 28 2.4-Ma Boring lava, but not Missoula deposits (Madin, 2009). Due to no identified deformation of surficial late-Pleistocene deposits, Personius (2002, Fault 874) infers low slip rates (<0.2 mm/yr).	No	QFFD (Fault 874) NSHM14 NSHM23v1	6.19	13	Madin, 1990; Personius, 2002 (Fault 874), Madin, 2009; Well and others, 2020b
HELVETIA FAULT (HF)	HF identified in subsurface exploration data as ~ 20 m offset CRB and overlying Plio-Pleistocene basin-fill deposits (Yeats and others, 1996; Wilson, 1997). Overlying Missoula Flood deposits do not appear to be deformed. Inferred very low slip rates (<0.2) due to lack of evidence for late Quaternary deformation (Personius, 2002).	No	QFFD (Class B, Fault 714) NSHM14	6.4	18	Popowski, 1996; Yeats and others, 1996; Personius, 2002 (Fault 714)
LACAMAS LAKE FAULT (LLF)	Beeson and Tolan (1990) and Blakely and others (1995) consider LLF to be a dextral fault system with dip slip motion, down to the west; may be component of Sandy River–Frontal fault extension that formed Portland Basin (Beeson and others, 1985; Blakely and others, 2000). Mapping by Evart and others (2008) suggests LLF now reactivated as reverse dextral-oblique. Columbia River morphology appears to have been influenced by LLF (Blakely and others, 1995). Subsurface well exploration data indicate offset across fault of Plio-Pleistocene (600 ka) Boring Lava (or 100 ka, as Personius (2002) notes), however, Missoula Flood deposits that overlie LLF appear to be undeformed. Thus, last activity may have been mid-late Quaternary.	No	QFFD (Fault 880) NSHM14	6.5	21	Beeson and others, 1985; Blakely and others, 1995; 2000; Personius, 2002 (Fault 880); Evarts, 2006; Anderson and others, 2013, Wells and others, 2020b
SANDY RIVER FAULT (SRF)	SRF identified in gravity data; no evidence for geomorphic deformation and offset of Quaternary deposits; considered possibly active because may be structurally and kinematically related to Lacamas fault as a right-stepping fault (Geomatrix, 1995). Peterson and others (2014) assign slip rate of 0.02 based on 245 m offset of CRBG mapped across fault. Considered component of Sandy River–Frontal fault, along with the Lacamas fault, that may have been involved in formation of Portland Basin (Beeson and others, 1985; Blakely and others, 2000).	No	QFFD (Class C) NSHM14	6.5	22	Beeson and others, 1985; Blakely and others, 2000;Geomatrix, 1995; Peterson and others, 2014;
GALES CREEK FAULT ZONE (GCFZ) (Chehalem Valley and Parsons Creek fault strands)	Wells and others (2020a) mapped 9 km of dextral offset of Siletzia-CRB bedrock and geological mapping and geophysical surveys along the GCFZ indicate long-term slip rate of 0.6 mm/yr. Quaternary deformation is recorded in right-laterally deflected streams, shutter ridges, scarps along GCFZ (Wells and others, 2020; Horst and others, 2020). Fault trenches along Parsons Creek strand reveal <200 ka offset in trenches (Bemis and Wells, 2012; Wells and others, 2020a). Subsequent studies documented Holocene-age deformation: 1) two trenches near Scoggins reservoir (Redwine and others, 2017) and 2) Horst and others, (2020) excavated across Parsons Creek fault strand and documented 3 Holocene- age earthquakes with last earthquake ~ 1000 yr BP, producing average recurrence of 4 ka. Long-term slip rate of Wells and others (2020a) generally consistent with rate of Horst and others (2020): 0.6 mm/yr; NSHM23 0.5-0.75 with 0.6 as preferred	Yes	QFFD (Fault 718) NSHM14 NSHM23v1	6.75	38	Bemis and Wells, 2012; Personius and Haller, 2017 (Fault 718); Redwine and others, 2017; Wells, and others, 2020a; Horst and others, 2020

Table 7-2 - Potential Quaternary-Active Faults Located Within 150 Kilometers of Burnside Bridge site

Fault	Geologic Evidence for Tectonic Activity in Quaternary and Fault Characteristics[1]	Significant Paleoseismic Evidence for Earthquakes <12,000 Yr	Fault included in USGS Model/Database?[2]	Estimated Maximum Magnitude[3]	Approximate Distance from EQRB (km)	Sources
MOUNT ANGEL FAULT (MAF)	Mapped as a high-angle, reverse fault (Yeats and others, 1996; Blakely and others 2000) and subsurface exploration data and gravity anomaly mapping show CRB offset across fault (Blakely and others, 2000). Late Pleistocene (< 125 ka) fluvial deposits might be uplifted across fault (Unruh and others, 1994; Givler and others, 2009). MAF location coincides with 1993 Scotts Mills earthquake swarm and may be the source (Thomas and others, 1996; Blakely and others, 2000). However, lidar-mapping has not identified prominent, post-Pleistocene, geomorphic deformation features; Based on lack of clear recent deformation and recent seismicity attributed to fault, Givler and others (2009) suggest MAF system might be a blind thrust. Based on gravity-anomaly mapping Blakey and others (2000) suggest MAF might be structurally connected to the Gales Creek fault zone.	No	QFFD (Fault 873) NSHM14 NSHM23v1	6.8	47	Unruh and others, 1994; Thomas and others, 1996; Yeats and others, 1996; Blakely and others, 2000; Givler and others, 2009; Personius and others, 2014 (Fault 873)
CLACKAMAS RIVER FAULT	Comprised of numerous northwest-striking normal and strike-slip faults (QFFD); fault strands may offset early Quaternary volcanic rocks, but inconclusive.	No	QFFD (Fault 864)	7.05	75	Personius, 2002 (Fault 864)
MT HOOD FAULT ZONE (Blue Ridge [BRF], Gate Creek fault [GCF], and Twin Lakes [TLF]-Multorpor Mountain Graben [MMG])	BRF and GCF scarps identified on lidar and offset glacial terrain (Madin and others, 2017; Bennett and others, 2021) Trenching across GCF by Bennett and others (2021 and pers. comm) suggested an event at AD 1350-1500 may have triggered large landslide in Hood River area. Trenching across BRF by Madin and others (2017) indicated most recent earthquake was 13,540 - 9,835 yr BP. TLF and MMG scarps identified on lidar (Madin and others, 2017; Bennett and others, 2021). Trenching across TLF by Bennett and others (2021 and pers. comm) suggested 2 earthquakes during the late Holocene: 3400 yr BP (2021) and possibly ~1500 -200 yr BP (pers comm).	Yes	QFFD (as Hood R. Fault Zone 866) NSHM23v1	7.05	75	Bennett, 2021; Madin and others, 2017; Personius, 2002 (Fault 866)
TURNER and MILLS CREEK FAULTS	100 m vertical offset of CRB observed across the Mills Creek fault, possible deformation of early Quaternary deposits, but no deformation of late Pleistocene or younger deposits observed (Yeats and others, 1996)	No	NSHM14 NSHM23v1	7.05	86	Yeats and others, 1996
HAPPY CAMP FAULT	Pleistocene channel deposits (200 ka - 1.6 Ma) appear to be offset by 9 m (Geomatrix, 1995)	No	QFFD (Fault 882) NSHM14 NSHM23v2	6.6	100	Geomatrix, 1995; Personius, 2002 (Fault 882)
WARWICK FAULT	Geomorphic mapping (offset loess, few ages, not detailed trench; youthful offset channels- no ages; offset <110ka loess (Woodring, 2020)	No	QFFD (as Faults near The Dalles, Fault 580) NSHM23v3	6.29	125	Personius and Lidke, 2003 (Fault 580); Woodring, 2020
DOTY FAULT ZONE (E and W strands)	Extensive field and shallow geophysical surveys of DFZ have not identified Quaternary activity. (Anderson, 2021; Lau, 2021); infer DFZ slipping slowly leading to poor preservation of scarps, etc.	No	QFFD (2020 Update)	7.05	130	Personius, 2002 (Fault 864)
METOLIUS FAULT	Multiple faults part of eastern boundary of the Cascades graben. Fault strands offset pyroclastic rocks of middle and late Pleistocene age, and glacial outwash and/or alluvial deposits of middle and late (?) Pleistocene age; Holocene deformation not observed (Personius and Haller, 2002 (Fault 853c)	No	QFFD (Fault 853b) NSHM14 NSHM23v1	7.05	130	Personius, 2002 (Fault 853b)
WHITE BRANCH FAULT ZONE	Surficial mapping with cosmogenic-nucleide dating suggests normal offsets of glacial deposits with max age of 20 ka, slip rates = 0.5 - 1.0 Alexander (2020)	Maybe	QFFD (Fault 1809) NSHM23v1	6.8	140	Alexander, 2020; Personius, 2002 (Fault 1809)
WILLAPA BAY FAULT ZONE	Based on seismic and field study, northern strands offset erosional surface estimated to have been cut less than 20 ka (C14 ages); aso offsets late Quaternary marine terrace deposits (McCrory, 2002; 2003)	No	QFFD (Fault 592) NSHM23v2	6.6	100	McCrory, 2002; 2003

NOTES:

1 QFFD = USGS Quaternary Fault and Fold Database (USGS, 2006); NSHM14 = US National Seismic Hazard Map (Peterson and others 2014); NSHM23v1 = U.S. National Seismic Hazard Model 2023, version 1.0 (Hatem and others, 2021)

2 Specific fault parameters used in PSHA are listed in Table 3-3; Fm = Geologic Formation; CRB = Columbia River Basalt, approx. 15 Ma; Missoula Flood Deposits approx. 20 ka- 12 ka; Holocene approx. < 12 ka

3 Earthquake magnitudes are from 2014 NSHMP, or determined using fault length and Magnitude relationships of Wells and Coppersmith (1994)

Table 7-3 - Seismic Source Parameters for Crustal Faults Within 150 Kilometers of EQRB

Source (Probability of Activity)	Maximum Mw	Inferred Max Slip Rate (mm/year)	Slip Sense	Dip Angle (degrees)	Dip Direction	Fault Strike Direction	Thickness (km)	Length (km)	Source for Fault Geometry
Portland Hills fault [0.8]	7	0.05 [0.3], 0.1 [0.4], 0.2 [0.3]	Oblique (Reverse-Right-lateral)	60 [.4] 70 [0.4] 80 [0.2]	SW	N37°W	15	46	Wells and others, 2020
East Bank fault [0.7]	6.8	0.05 [0.3], 0.1 [0.4], 0.2 [0.3]	Oblique (Reverse-Right-lateral)	70 [0.5] 80 [0.5]	NE	N46°W	15	27	Wells and others, 2020/NSHM23
Sylvan-Oatfield fault [0.9]	6.8	0.05 [0.3], 0.1 [0.4], 0.2 [0.3]	Oblique (Reverse-Right-lateral)	60 [0.4], 70 [0.4], 80 [0.2]	E	N41°W	15	34	Wells and others, 2020
Beaverton fault [0.7]	6.4 [0.3], 6.8 [0.7]	0.01 [0.4], 0.1 [0.4], 0.2 [0.2]	Reverse	60 [0.5] 70 [0.5]	S	N86°E	15	15 [0.3, 31 [0.7]	NSHM23 and Wells 2020
Canby-Molalla fault [0.7]	7	0.05 [0.3], 0.1 [0.4], 0.2 [0.3]	Oblique (Reverse-Right-lateral)	70 [0.5] 80 [0.5]	NE	N34°W	15	50	QFFD/NSHM23/ Wells 2020
Damascus-Tickle Creek-Grant Butte (Grant Butte) fault zone [0.8]	6.2	0.01 [0.3], 0.05 [0.4], 0.1 [0.3]	Normal	60 [0.6] 80 [0.4]	NW for N75E, NE for N60W	N75°E [0.6], N60°W [0.4]	15	10 (NW and NE striking strands)	NSHM14/Wells2020
Bolton fault [0.7]	6.2 [0.3], 6.7 [0.7]	0.01 [0.5], 0.5 [0.3], 0.1 [0.2]	Reverse	60 [0.5] 70 [0.5]	SW	N53°W	15	9 [0.3], 20 [0.7]	NSHM14
Helvetia fault [0.5]	6.5	0.01	Reverse	60	SW	N26°W	15	14	NSHM14
Lacamas Lake fault [0.7]	6.5	0.03 [0.3], 0.1 [0.4], 0.2 [0.3]	Dextral Strike Slip	90	V	N43°W	15	16	NSHM14/Wells2020
Sandy River fault zone [0.2]	6	0.016	Strike Slip	90		N32°W	15	6	NSHM14/Wells2020
Gales Creek (Chehalem Valley and Parsons Creek fault strands) [1.0]	6.8 - 7.1	0.6 [0.5] 0.5 [0.2] 0.75 [0.3]	Dextral Strike Slip	90		N25°W	15	Segmented, 30 km; Unsegmented 60 km	NSHM23/Wells (2020)
Mount Angel fault [0.8]	6.6 - 7.1	0.05 [0.5] 0.5 [0.3] 1.0 [0.2]	Oblique (Reverse-Right-lateral)	60 [0.5] 70 [0.3] 80 [0.2]	NE	N43°E	15	20 [0.5] 30 [0.3] 55 [0.2]	NSHM23 (20km); Blakely and others 2000 (55km)
Clackamas fault zone [0.2]	6.4	0.05 [0.3], 0.1 [0.4], 0.2 [0.3]	Oblique (normal-Right-lateral)	70 [0.6] 80 [0.4]	E [0.5], W [0.5]	N19°W	15	14	QFFD
Mt Hood faults (Blue Ridge-Gate Creek fault zone and Twin Lakes-Multorpor Mountain Graben) [1.0]	6.3 - 7.1	0.05 [0.2] 0.1 [0.4] 0.2 [0.4]	Normal	50 [0.2] 70 [0.4] 80 [0.4]	E [0.5] W [0.5]	N10°W	15	Unsegmented: 55 km (GCF + BRF +TLF) [0.5], 30 km (GCF+BRF) [0.5]; Segmented: 12 km (GCF or BRF or TLF)	NSHM23 (merged S strands together)
Turner & Mill Creek fault [0.5]	6.5	0.08	Reverse	60 [0.5], 70 [0.5]	SE	N66°E	15	18	NSHM23
Happy Camp fault [0.5]	5.6 - 6.6	0.05 [0.3], 0.1 [0.4], 0.2 [0.3]	Reverse	35 [0.3] 50 [0.4] 60 [0.3]	N	N73°W	15	3 [0.5] 20 [0.5]	NSHM23

Table 7-3 - Seismic Source Parameters for Crustal Faults Within 150 Kilometers of EQRB

Source (Probability of Activity)	Maximum Mw	Inferred Max Slip Rate (mm/year)	Slip Sense	Dip Angle (degrees)	Dip Direction	Fault Strike Direction	Thickness (km)	Length (km)	Source for Fault Geometry
Warwick fault [0.8]	6.9 - 7.1	0.01 [0.4] 0.05 [0.3] 1.0 [0.3]	Strike Slip	90 [0.6], 80 [0.3], 60 [0.1]	NE	305 [.6] (6), 320 [.4] (change to Azimuth notation with the same wt of lengths)	15	35 [0.3], 54 [0.7]	Woodring (2020)/NSHM23
Doty fault (W and E strands) [0.6]	6.8 - 7.2	0.05 [0.3] 0.07 [0.4] 0.09 [0.3]	Reverse	50 [0.3] 60 [0.4] 75 [0.3]	N	N88°E	15	Unsegmented, 72; Segmented, 32 km (West strand) or 40 km (East strand)	Steely and others, 2021
Metolius fault [0.9]		0.05 [0.3], 0.1 [0.4], 0.2 [0.3]	Normal	50 [0.6] 70 [0.4]	SW	N23°W	15	70	
White Branch fault zone [1.0]	6.8	0.5 [0.4] 0.7 [0.3] 1.0 [0.3]	Normal	50	E	N	15	33	NSHM23 & Alexander (2020)
Willapa Bay fault [0.8]	6.9	0.5 [0.2] 0.3 [0.6] 0.1 [0.2]	Oblique	30 [0.2] 60 [0.6] 80 [0.2]	E [0.5] W [0.5]	N22°W	15	25	NSHM23

Table 8-1 - 1,000-year Probabilistic Hazard Level Recommended Design Response Spectrum

Period (seconds)	Spectral Response Acceleration Site Class D Bents (g)	Site Class E Bents (g)
PGA	0.49	0.31
0.015	0.51	0.35
0.02	0.54	0.40
0.03	0.70	0.50
0.04	0.90	0.65
0.05	1.20	0.85
0.07	1.70	1.25
0.1	1.70	1.25
0.2	1.70	1.25
0.25	1.70	1.25
0.3	1.55	1.25
0.35	1.33	1.25
0.5	0.93	0.92
0.6	0.77	0.77
0.7	0.67	0.66
0.8	0.51	0.58
0.9	0.41	0.51
1	0.33	0.46
1.1	0.29	0.42
1.2	0.26	0.38
1.3	0.24	0.35
1.4	0.22	0.33
1.5	0.21	0.31
1.6	0.20	0.29
1.7	0.18	0.27
1.8	0.17	0.26
1.9	0.17	0.24
2	0.16	0.23
2.75	0.11	0.17
3	0.10	0.15
4	0.079	0.12
5	0.051	0.072
6	0.035	0.050
7	0.026	0.037
8	0.020	0.028
9	0.016	0.022
10	0.013	0.018

NOTES:

1 The recommended design spectrum was developed using site response analysis per AASHTO (2020) and the ODOT GDM (ODOT, 2019).

Table 8-2 - Deterministic CSZ Hazard Level Recommended Design Response Spectrum

Period (seconds)	Spectral Response Acceleration Site Class D Bents (g)	Site Class C Bents (g)
PGA	0.18	0.15
0.015	0.19	0.16
0.02	0.20	0.16
0.03	0.23	0.19
0.04	0.26	0.22
0.05	0.30	0.27
0.07	0.40	0.37
0.1	0.62	0.50
0.2	0.62	0.50
0.25	0.62	0.50
0.3	0.62	0.50
0.35	0.62	0.50
0.45	0.48	0.50
0.6	0.36	0.50
0.7	0.31	0.43
0.8	0.27	0.37
0.9	0.24	0.33
1	0.22	0.30
1.1	0.20	0.27
1.2	0.18	0.25
1.3	0.17	0.23
1.4	0.16	0.21
1.5	0.15	0.19
1.6	0.14	0.18
1.7	0.13	0.17
1.8	0.12	0.16
1.9	0.11	0.15
2	0.11	0.14
2.5	0.087	0.11
3	0.073	0.090
3.5	0.062	0.066
4	0.054	0.050
5	0.035	0.032
6	0.024	0.022
7	0.018	0.016
8	0.014	0.013
9	0.011	0.010
10	0.009	0.008

NOTES:

1 The recommended design spectrum was developed using site response analysis per AASHTO (2020) and the ODOT GDM (ODOT, 2019).

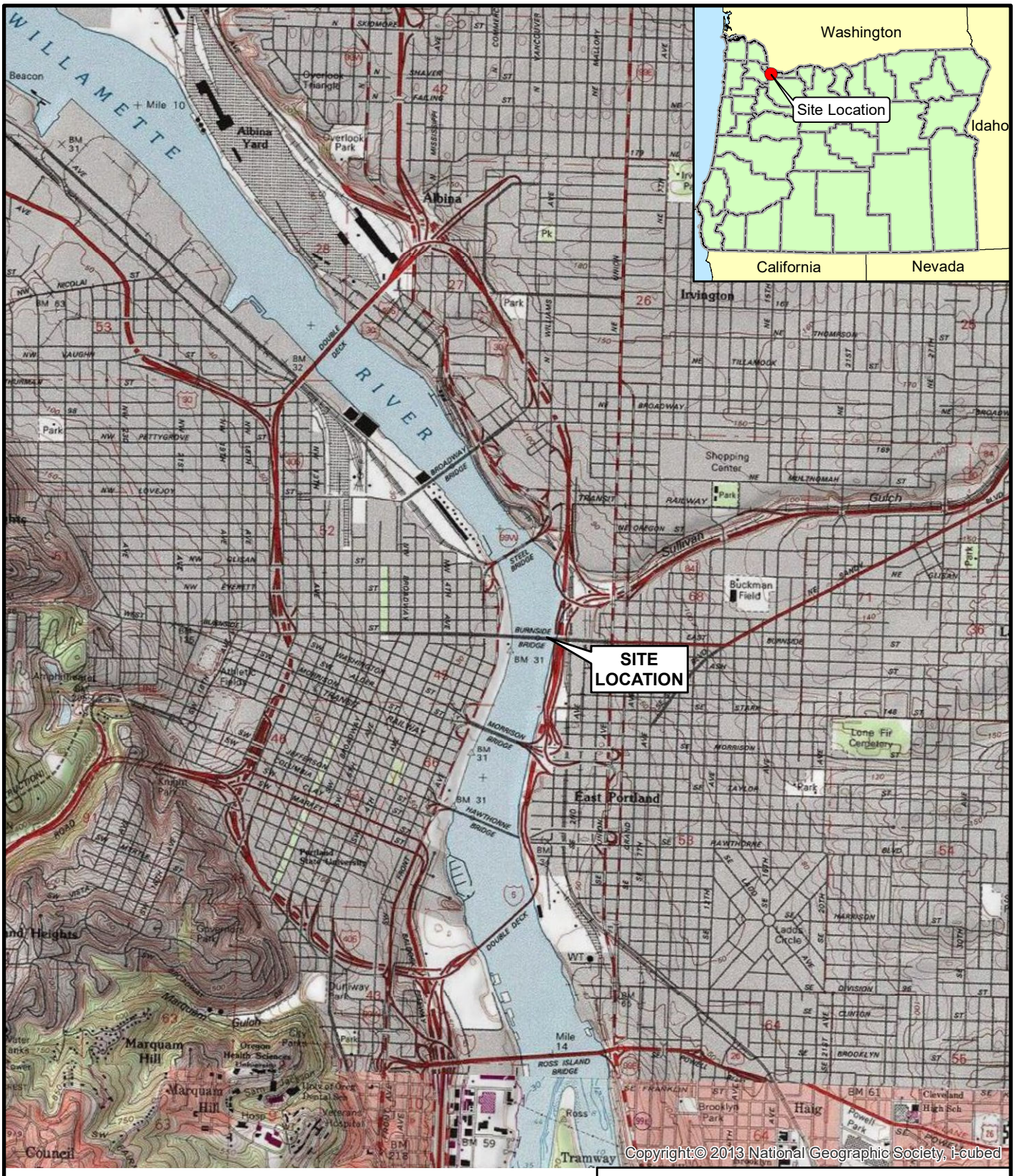

0 0.25 0.5 1

Scale in Miles

N

Earthquake Ready Burnside Bridge
Portland, Oregon

VICINITY MAP

January 2022 102636-009

SHANNON & WILSON, INC.
GEOTECHNICAL AND ENVIRONMENTAL CONSULTANTS

FIG. 1-1

Filename: T:\Projects\PDX\102000s\102636_Burnside Bridge\Avmxd\VicinityMap_10.6.mxd Date: 1/7/2022 Login: AEH

LEGEND

Quaternary Faults

⋯ middle and late Quaternary (<750,000 years), inferred location

⋯ undifferentiated Quaternary(<1.6 million years), inferred location

▨ Qaf - Artificial Fill

▨ Qal - Alluvium

▨ Qfch - Catastrophic Flood Deposits, Channel Facies

▨ Qff - Catastrophic Flood Deposits, Fine-grained Facies

▨ QTs - Troutdale Formation

▨ Tfg - Basalt of Ginko

▨ Tgsb - Columbia River Basalt Group, Sentinel Bluffs Member

▨ Tgww - Columbia River Basalt Group, Winter Water Member

0 500 1,000 2,000

Scale in Feet

NOTES

1. Geologic mapping from Oregon Geologic Data Compilation, Release 6 (OGDC-6) by DOGAMI.
2. Quaternary faults from the USGS Quaternary Fault and Fold Database of the United States, downloaded October 26, 2021.
3. Aerial imagery obtained through Google Maps Satellite.

Earthquake Ready Burnside Bridge
Portland, Oregon

PUBLISHED GEOLOGIC MAPPING

January 2022 102636-009

SHANNON & WILSON, INC.
GEOTECHNICAL AND ENVIRONMENTAL CONSULTANTS

FIG. 2-1

Filename: T:\Projects\PDX\102000s\102636_Burnside Bridge\Avmxd\Geology_10.6.mxd Date: 1/7/2022 Login: AEH

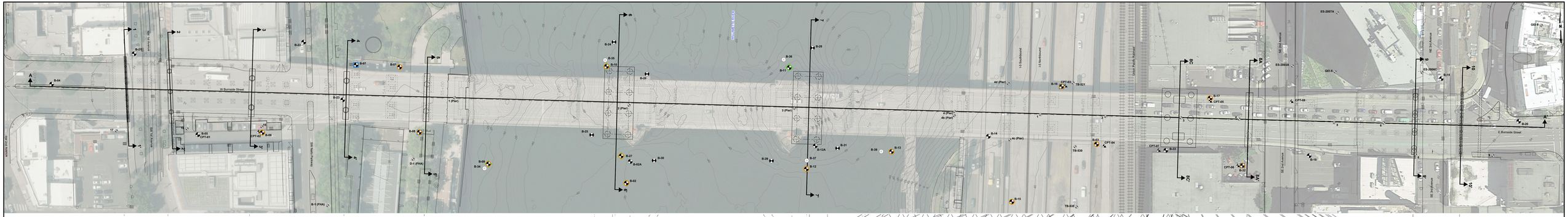

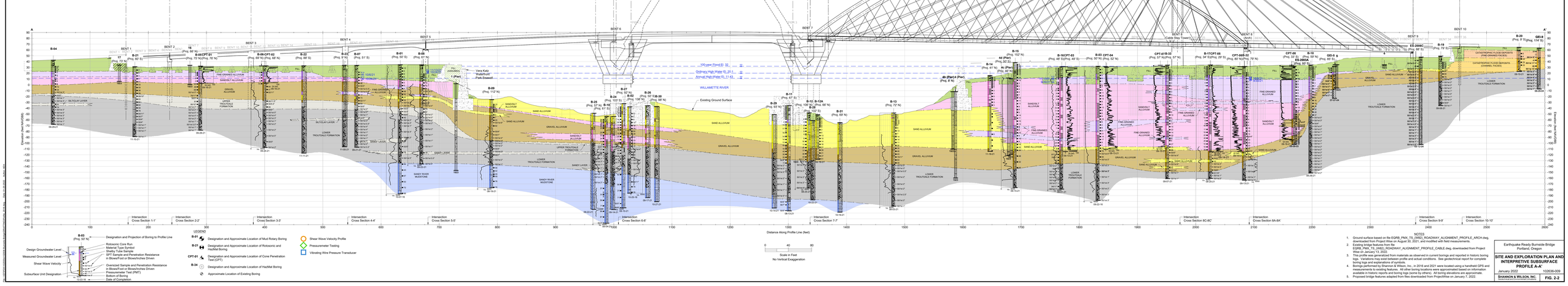

LEGEND

- B-02 (Proj. 50' N) — Designation and Projection of Boring to Profile Line
- Rotosonic Core Run
- Hollow Stem Auger
- Shelby Tube Sample
- SPT Sample and Penetration Resistance in Blows/Foot or Blows/Inches Driven
- Oversized Sample and Penetration Resistance in Blows/Foot or Blows/Inches Driven
- Pressuremeter Test (PMT)
- Bottom of Boring
- 12-22-16 — Date of Completion
- Design Groundwater Level
- Measured Groundwater Level
- Shear Wave Velocity
- Subsurface Unit Designation
- B-01 — Designation and Approximate Location of Mud Rotary Boring
- B-21 — Designation and Approximate Location of Rotosonic and HazMat Boring
- CPT-01 — Designation and Approximate Location of Cone Penetration Test (CPT)
- B-34 — Designation and Approximate Location of HazMat Boring
- Approximate Location of Existing Boring
- Shear Wave Velocity Profile
- Pressuremeter Testing
- Vibrating Wire Pressure Transducer

Scale in Feet
No Vertical Exaggeration

NOTES

1. Ground surface based on file EGRB_PMX_TS_(WB2)_ROADWAY_ALIGNMENT_PROFILE_ARCH.dwg, downloaded from Project Wise on August 30, 2021, and modified with field measurements.
2. Existing bridge features from file EGRB_PMX_TS_(WB2)_ROADWAY_ALIGNMENT_PROFILE_CABLE.dwg, downloaded from Project Wise on January 13, 2022.
3. This profile was generalized from materials as observed in current borings and reported in historic boring logs. Variations may exist between profile and actual conditions. See geotechnical report for complete boring logs and explanations of symbols.
4. Borings performed by Shannon & Wilson, Inc. in 2016 and 2021 were located using a handheld GPS and measuring tape and/or taping methods. All other boring locations were approximated based on information available in historic reports and boring logs (some by others). All boring elevations are approximate.
5. Proposed bridge features adapted from files downloaded from ProjectWise on January 7, 2022.

Earthquake Ready Burnside Bridge
Portland, Oregon

SITE AND EXPLORATION PLAN AND INTERPRETIVE SUBSURFACE PROFILE A-A'

January 2022 | 102636-009

SHANNON & WILSON, INC.
Geotechnical and Environmental Consultants

FIG. 2-2

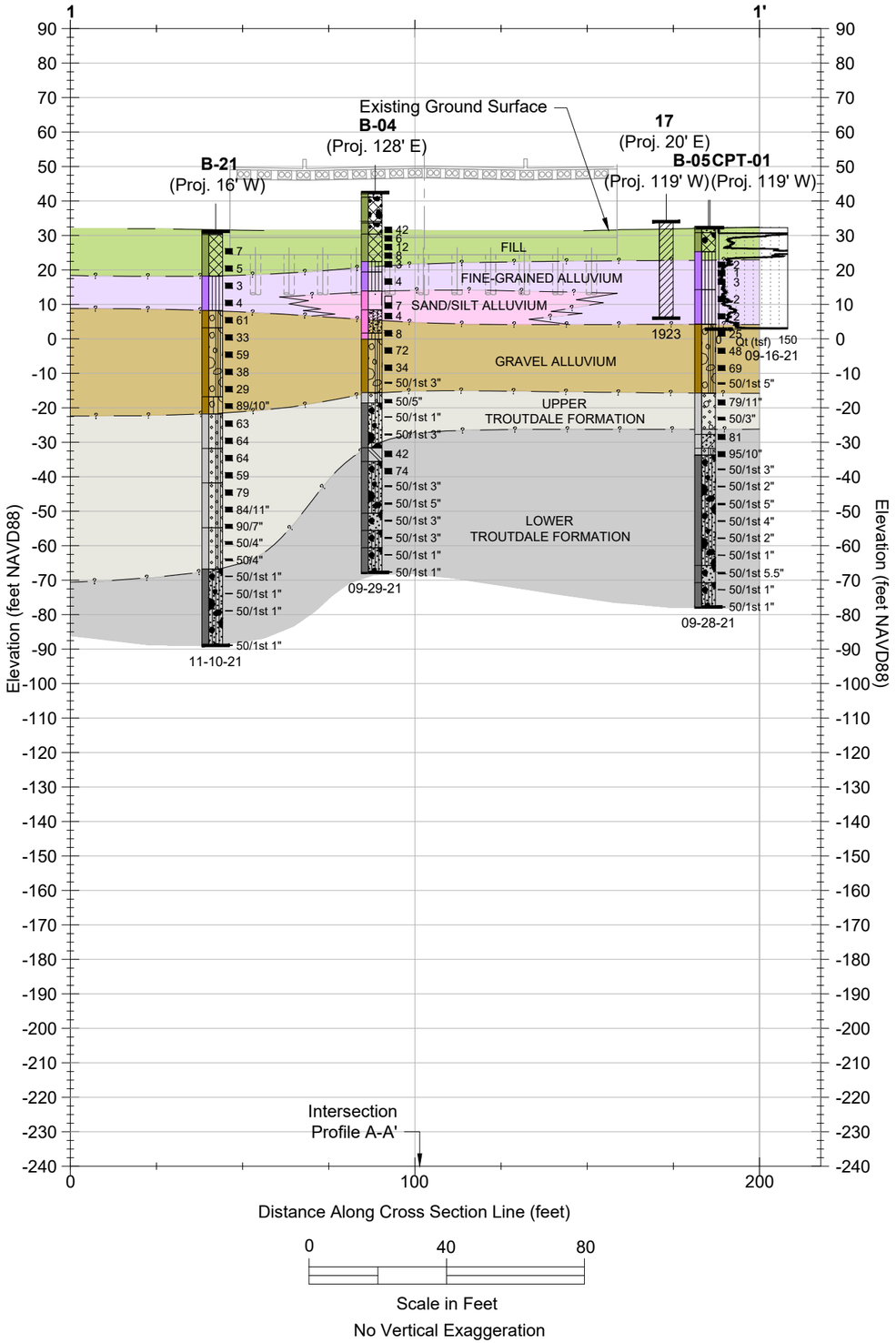

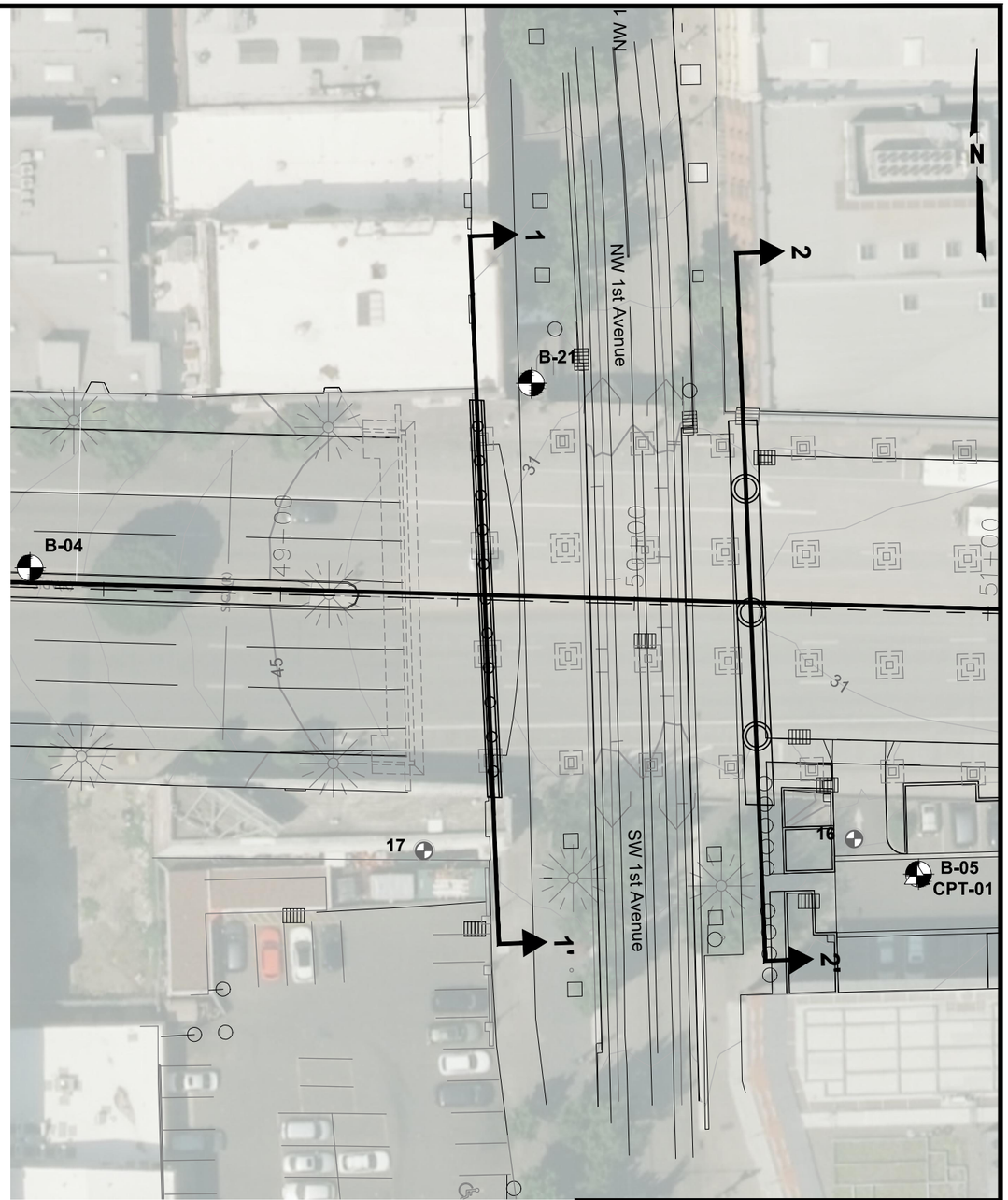

NOTES

1. See Figure 2-2 for legend, complete plan view, and applicable notes.

Earthquake Ready Burnside Bridge
Portland, Oregon

INTERPRETIVE SUBSURFACE CROSS SECTION 1-1'

January 2022 102636-009

SHANNON & WILSON, INC.
Geotechnical and Environmental Consultants

FIG. 6-1

File: I:\EF\PDX\102000s\102636 Burnside Bridge\DRAFTING\Profile_2018.dwg Date: 01-25-2022 Author: AEH

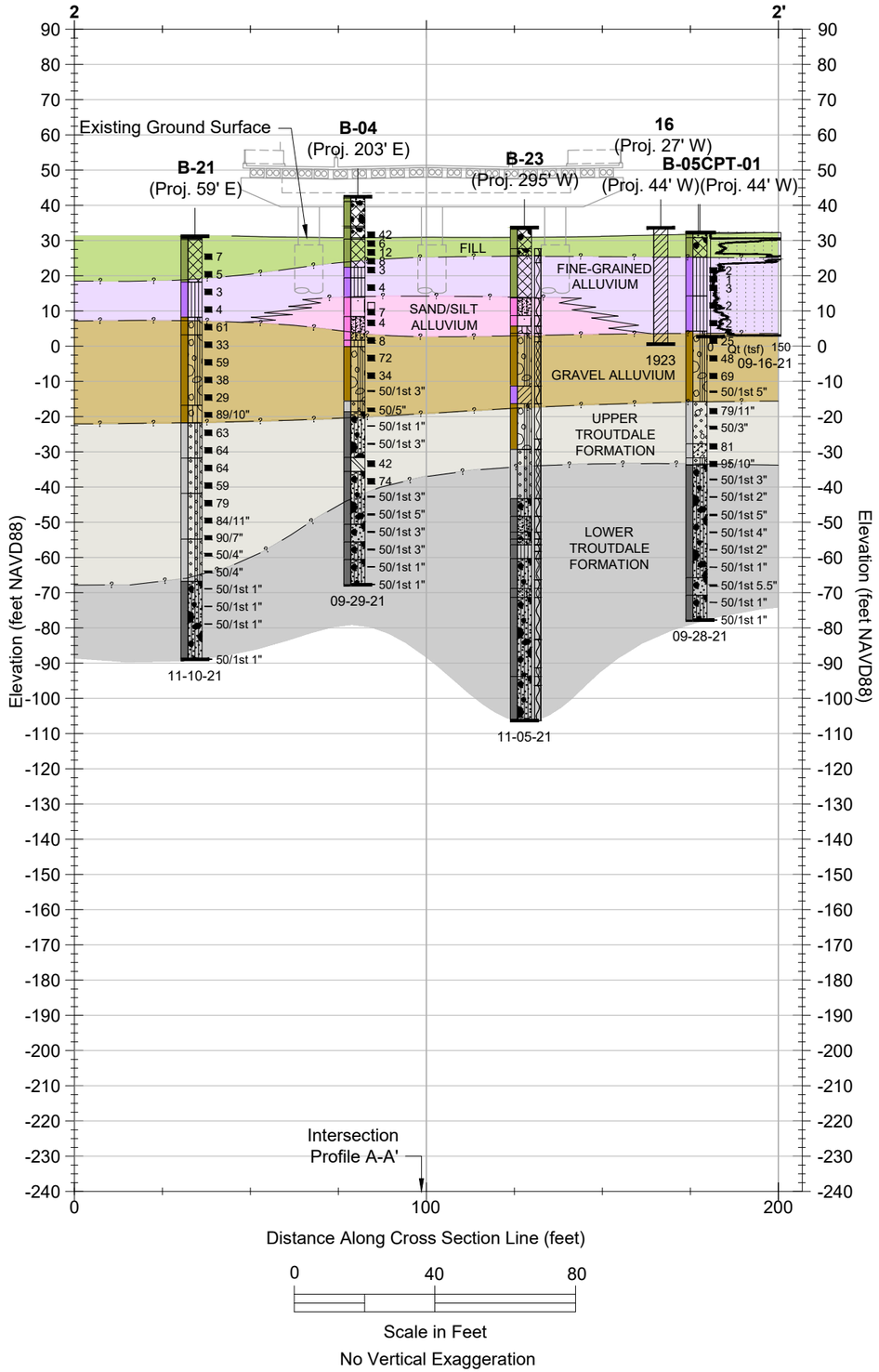

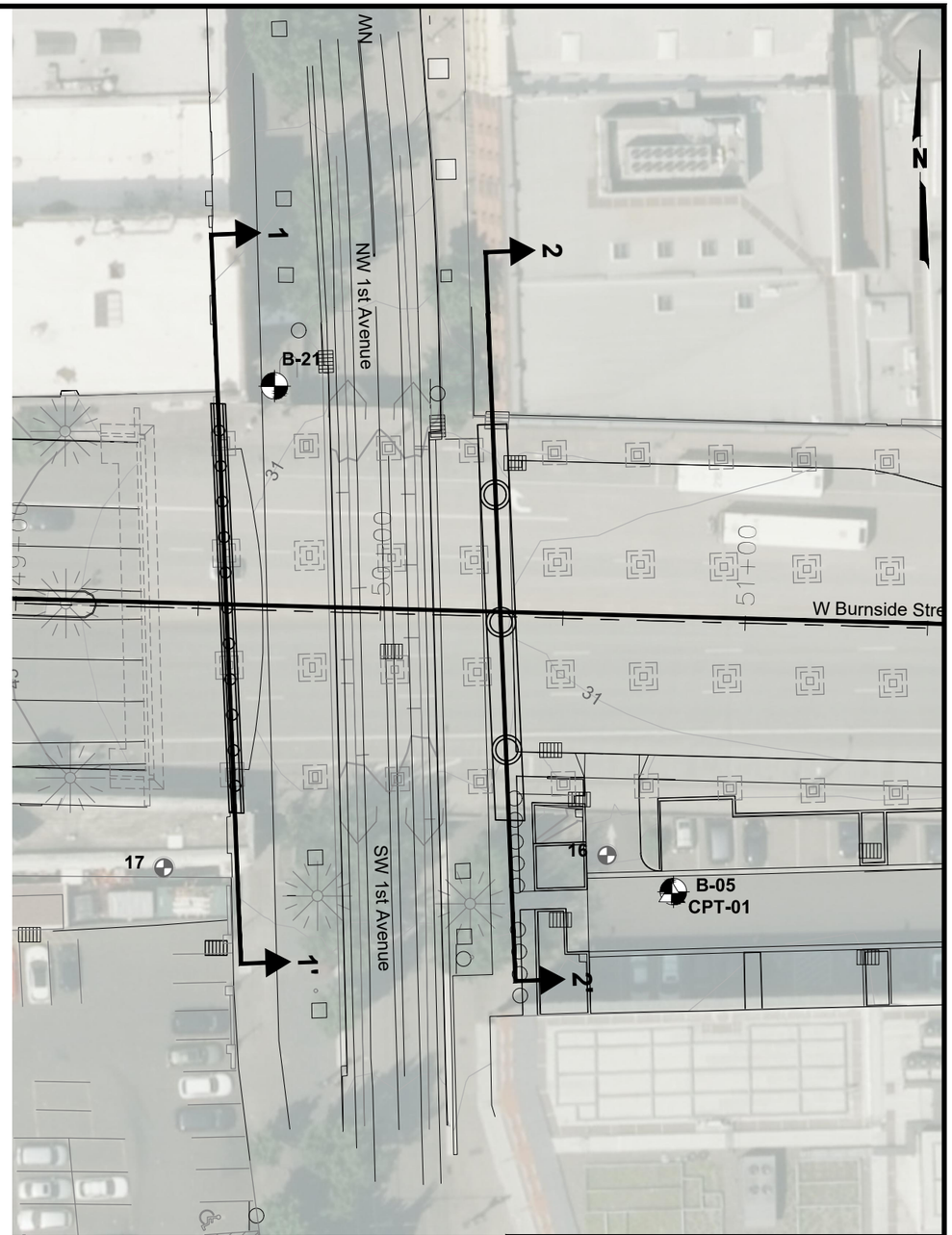

NOTES

1. See Figure 2-2 for legend, complete plan view, and applicable notes.

Earthquake Ready Burnside Bridge
Portland, Oregon

INTERPRETIVE SUBSURFACE CROSS SECTION 2-2'

January 2022 102636-009

SHANNON & WILSON, INC.
Geotechnical and Environmental Consultants

FIG. 6-2

File: I:\EF\PDX\102000s\102636 Burnside Bridge\DRAFTING\Profile_2018.dwg Date: 01-25-2022 Author: AEH

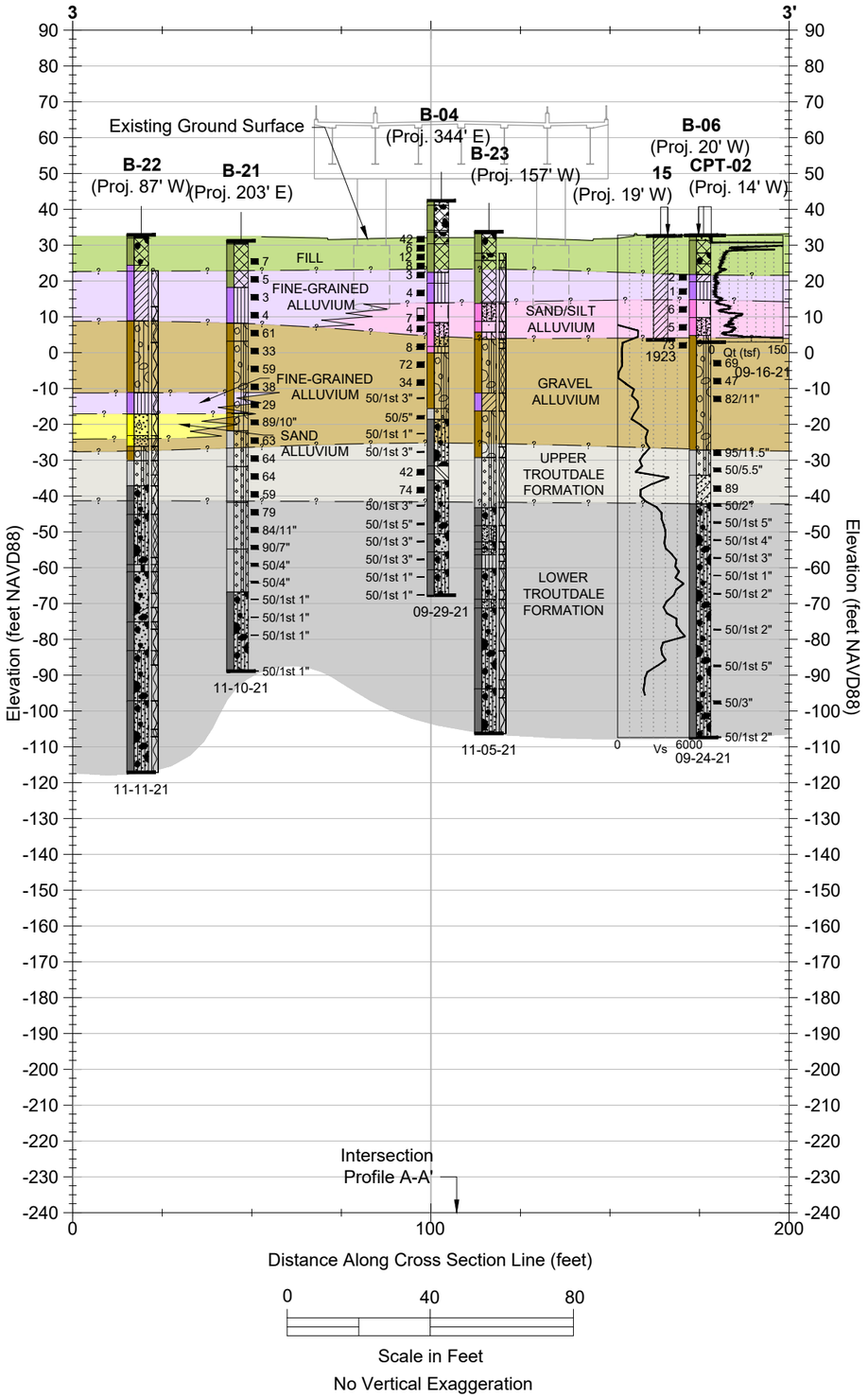

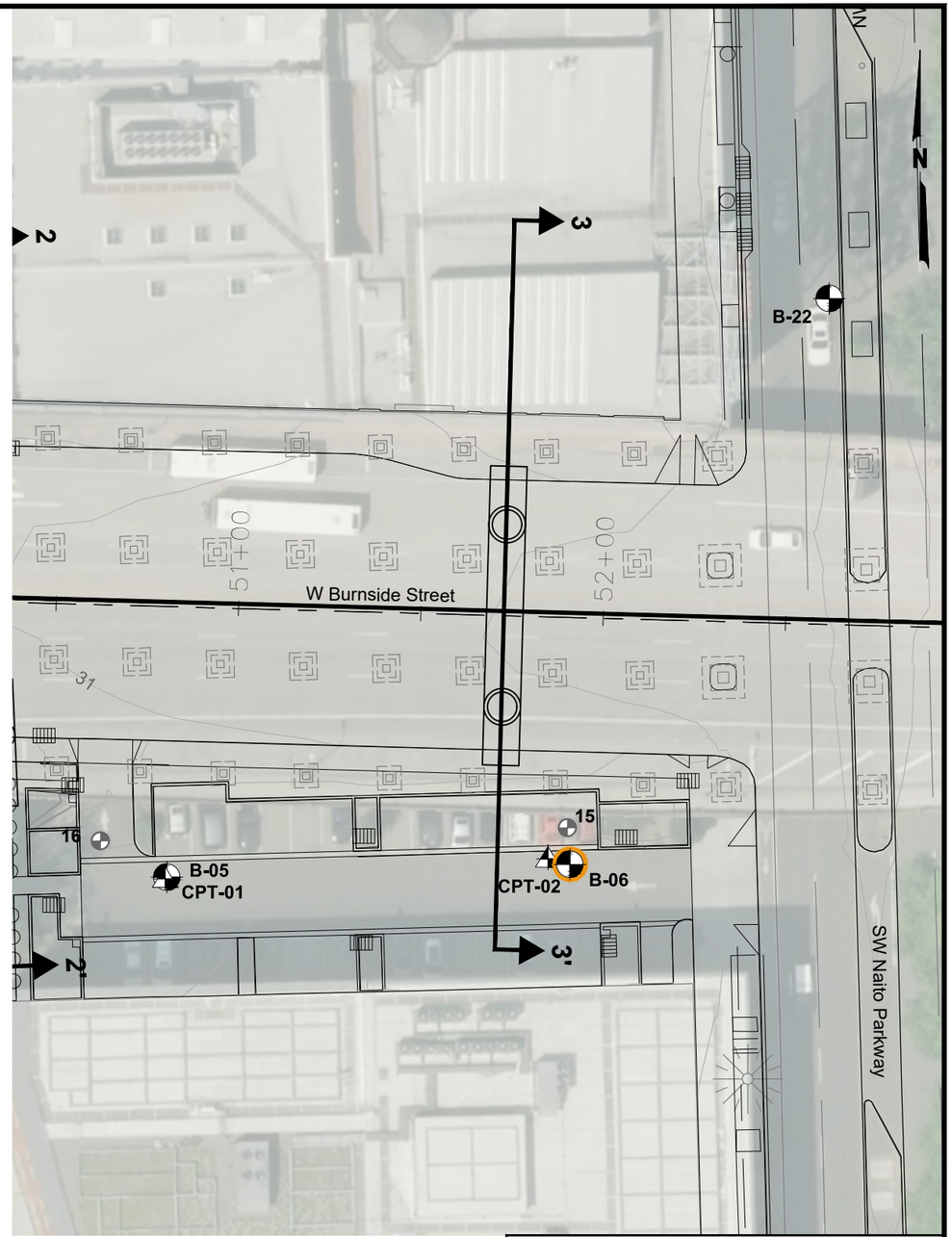

NOTES

1. See Figure 2-2 for legend, complete plan view, and applicable notes.

Earthquake Ready Burnside Bridge
Portland, Oregon

INTERPRETIVE SUBSURFACE CROSS SECTION 3-3'

January 2022 | 102636-009

SHANNON & WILSON, INC.
Geotechnical and Environmental Consultants

FIG. 6-3

File: I:\EF\PDX\102000s\102636 Burnside Bridge\DRAFTING\Profile_2018.dwg Date: 01-25-2022 Author: AEH

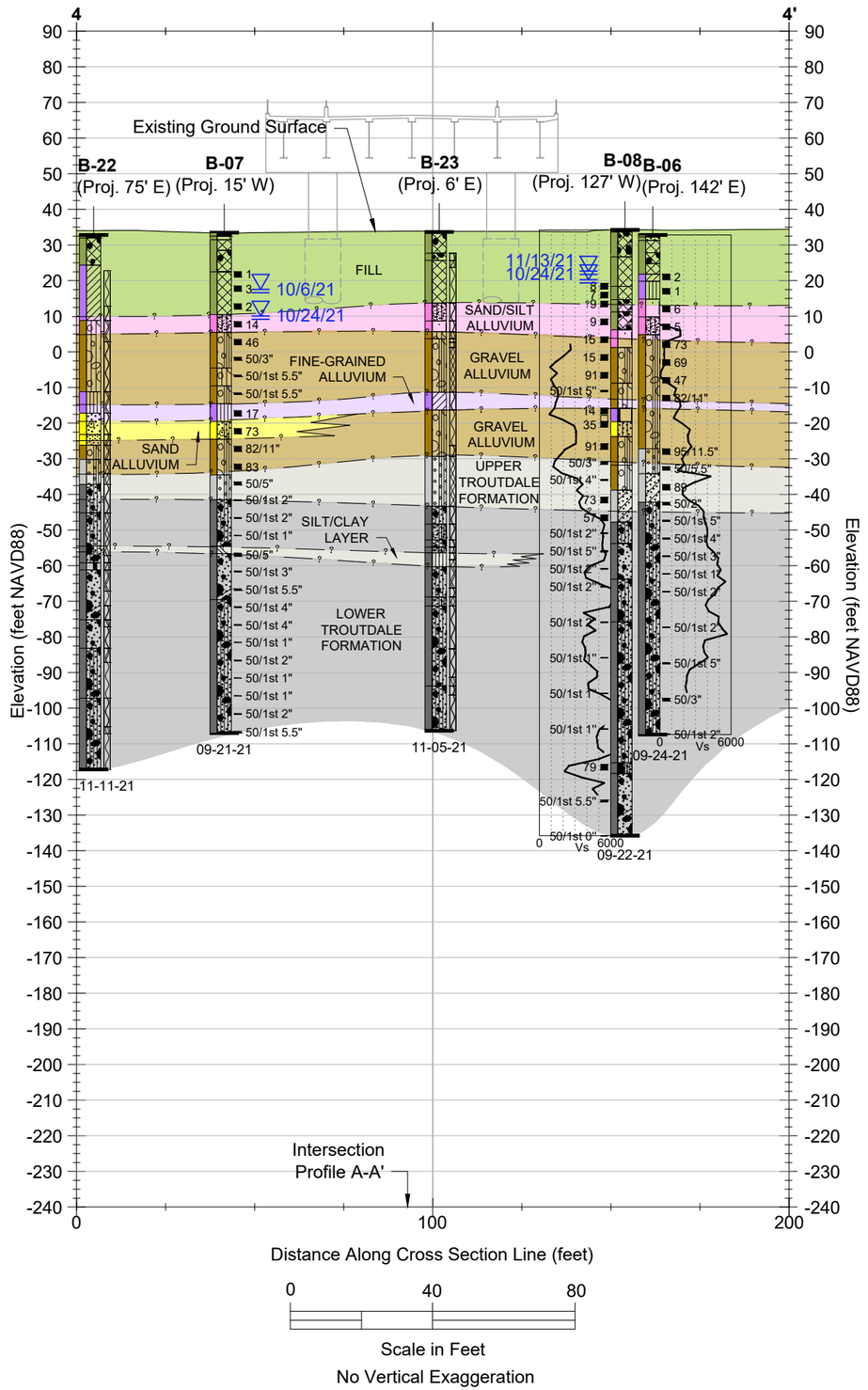

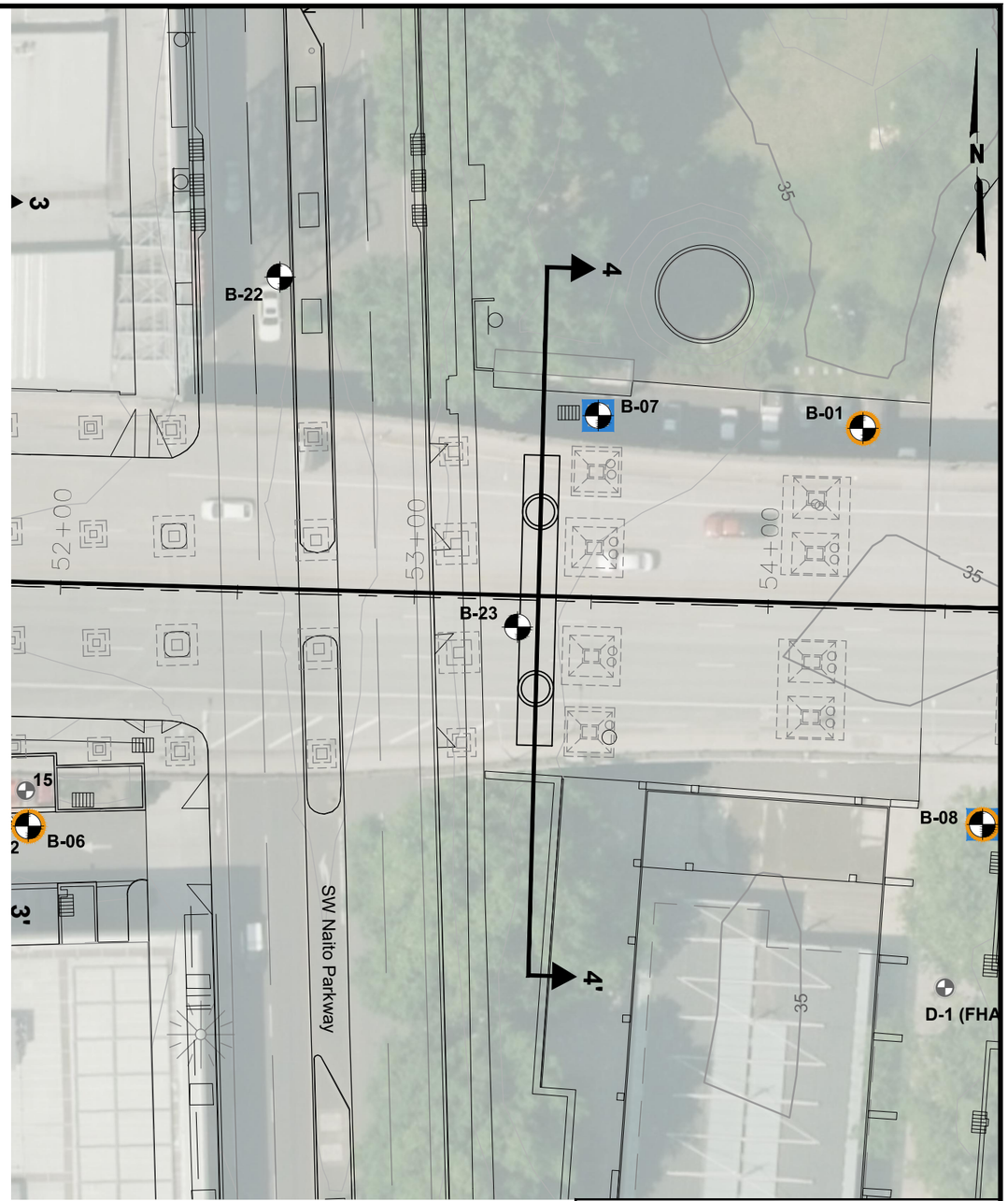

NOTES

1. See Figure 2-2 for legend, complete plan view, and applicable notes.

Earthquake Ready Burnside Bridge
Portland, Oregon

INTERPRETIVE SUBSURFACE CROSS SECTION 4-4'

January 2022 102636-009

SHANNON & WILSON, INC.
Geotechnical and Environmental Consultants

FIG. 6-4

File: I:\EF\PDX\102000s\102636 Burnside Bridge\DRAFTING\Profile_2018.dwg Date: 01-25-2022 Author: AEH

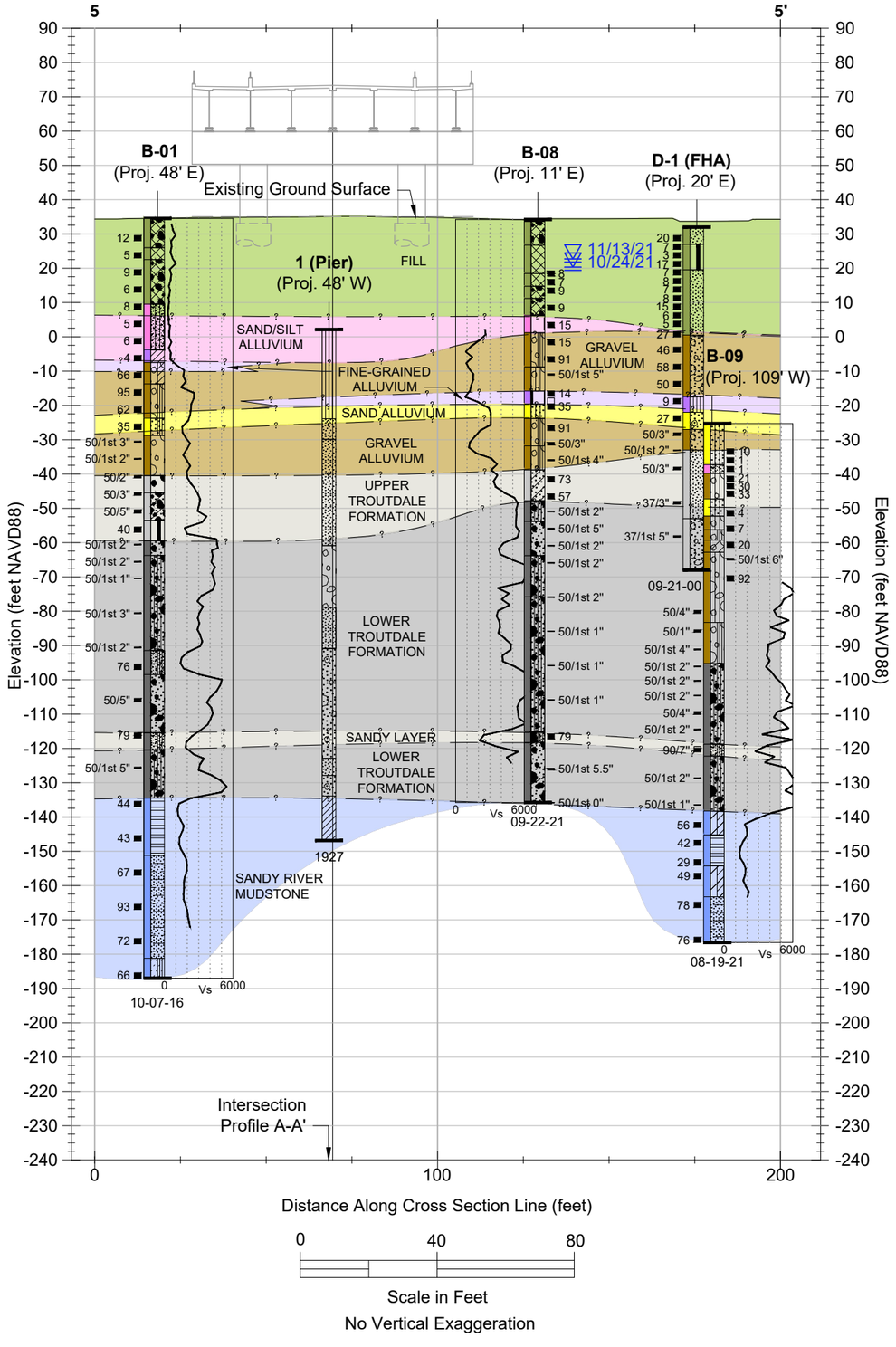

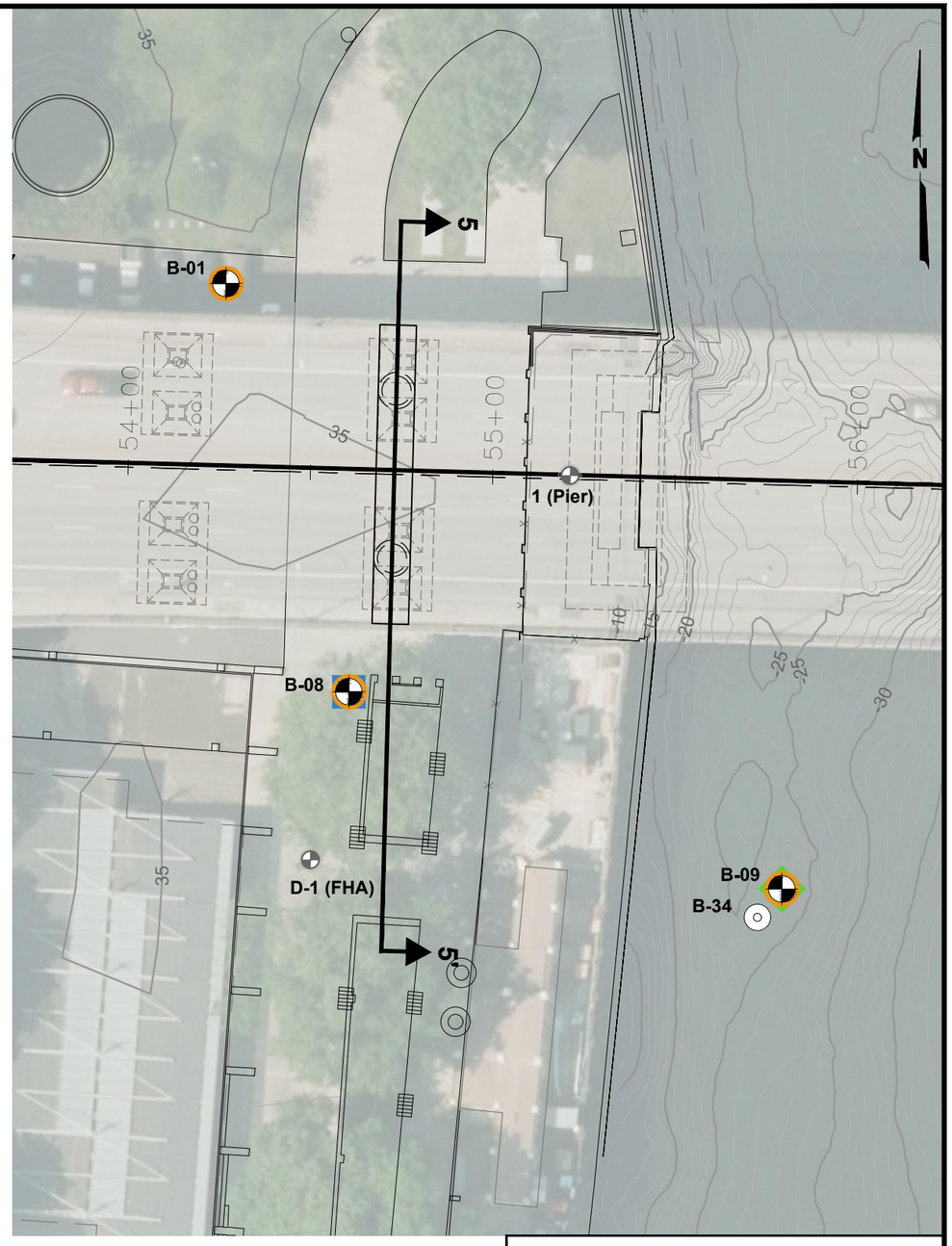

NOTES

1. See Figure 2-2 for legend, complete plan view, and applicable notes.

Earthquake Ready Burnside Bridge
Portland, Oregon

INTERPRETIVE SUBSURFACE CROSS SECTION 5-5'

January 2022 102636-009

SHANNON & WILSON, INC.
Geotechnical and Environmental Consultants

FIG. 6-5

File: I:\ER\PDX\102000s\102636 Burnside Bridge\DRAFTING\Profile_2018.dwg Date: 01-21-2022 Author: AEH

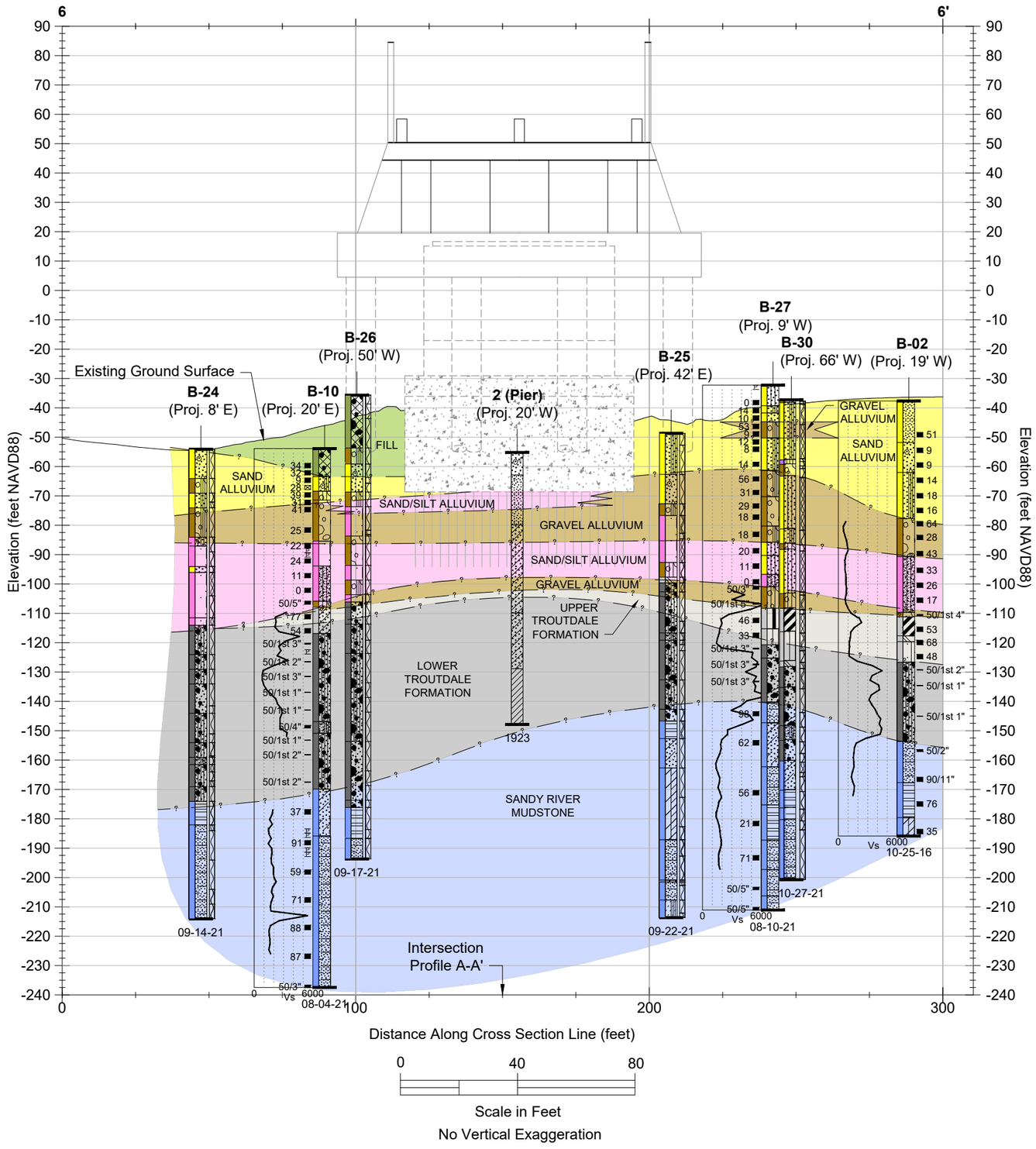

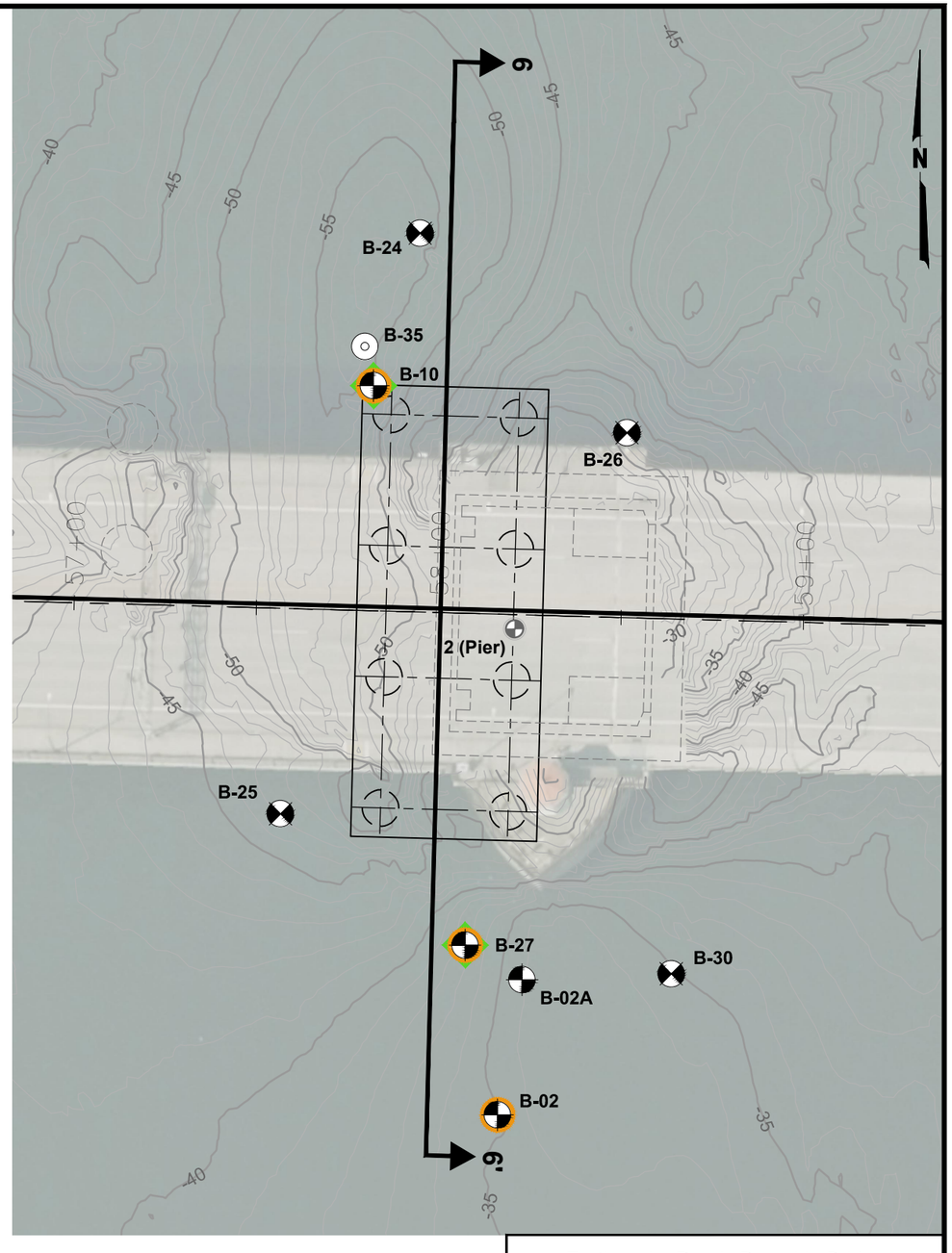

NOTES

1. See Figure 2-2 for legend, complete plan view, and applicable notes.

Earthquake Ready Burnside Bridge
Portland, Oregon

INTERPRETIVE SUBSURFACE CROSS SECTION 6-6'

January 2022 102636-009

SHANNON & WILSON, INC.
Geotechnical and Environmental Consultants

FIG. 6-6

File: I:\EF\PDX\102000s\102636 Burnside Bridge\DRAFTING\Profile_2018.dwg Date: 01-21-2022 Author: AEH

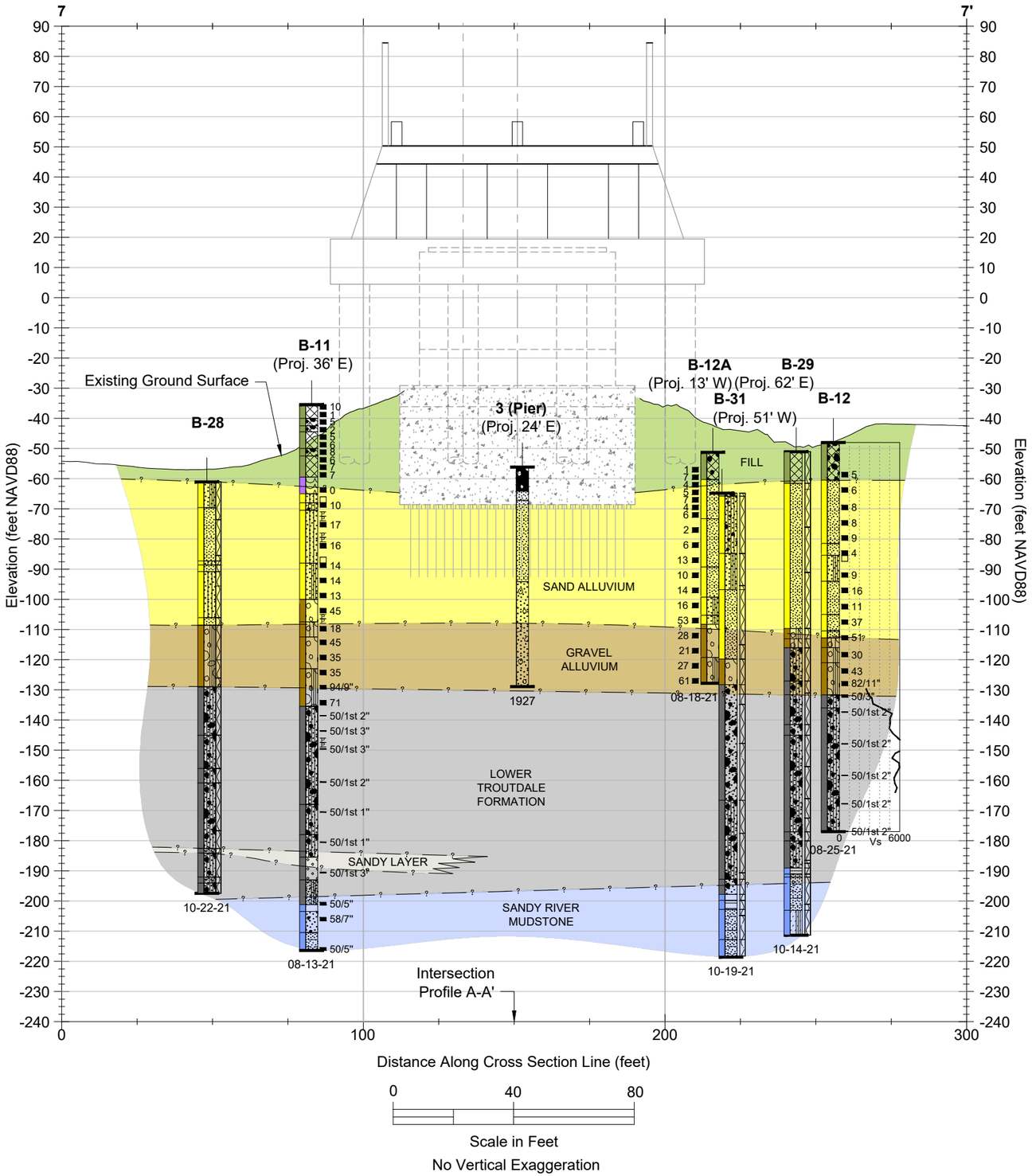

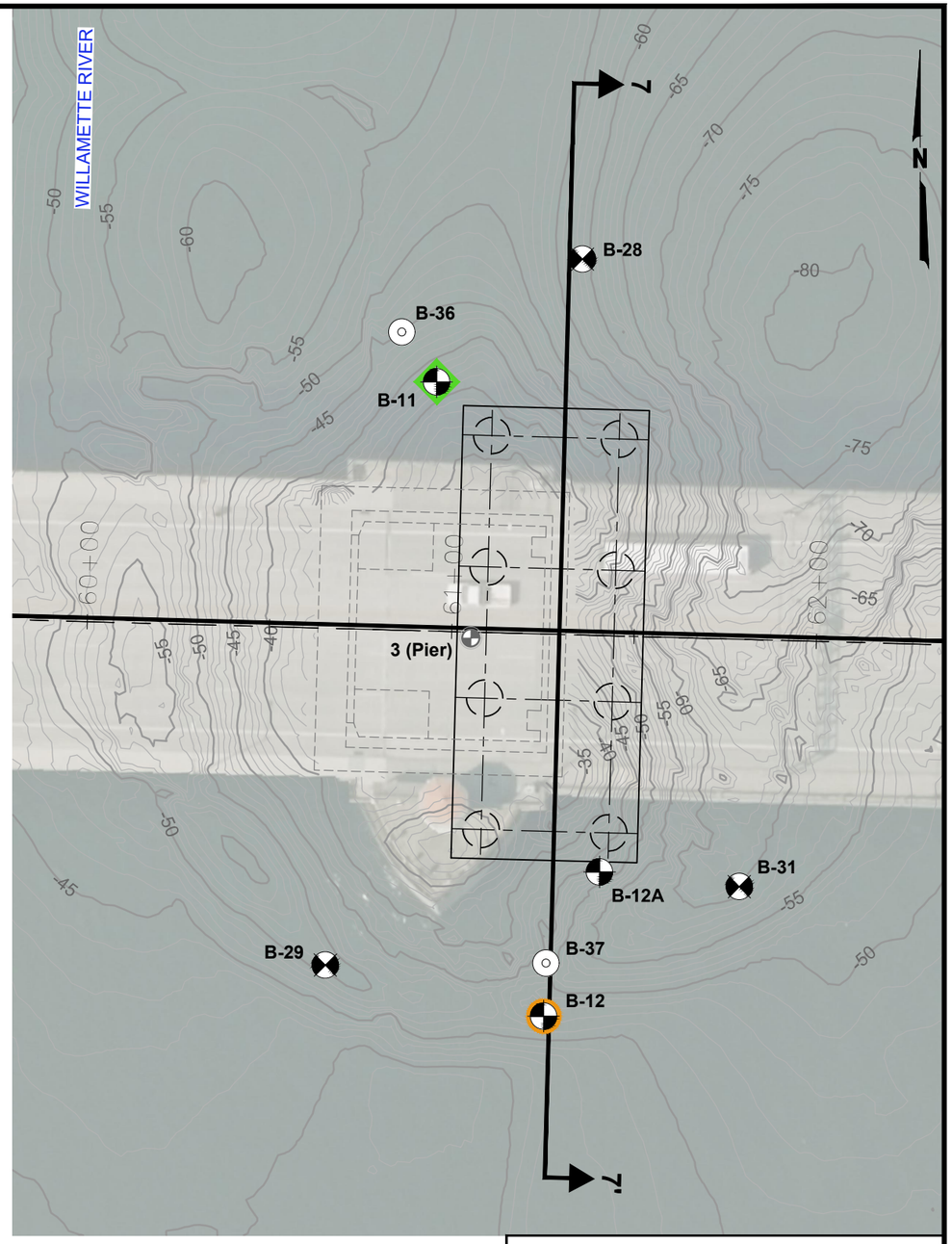

NOTES

1. See Figure 2-2 for legend, complete plan view, and applicable notes.

Earthquake Ready Burnside Bridge
Portland, Oregon

INTERPRETIVE SUBSURFACE CROSS SECTION 7-7'

January 2022 102636-009

SHANNON & WILSON, INC.
Geotechnical and Environmental Consultants

FIG. 6-7

File: I:\ER\PDX\102000s\102636 Burnside Bridge\DRAFTING\Profile_2018.dwg Date: 01-21-2022 Author: AEH

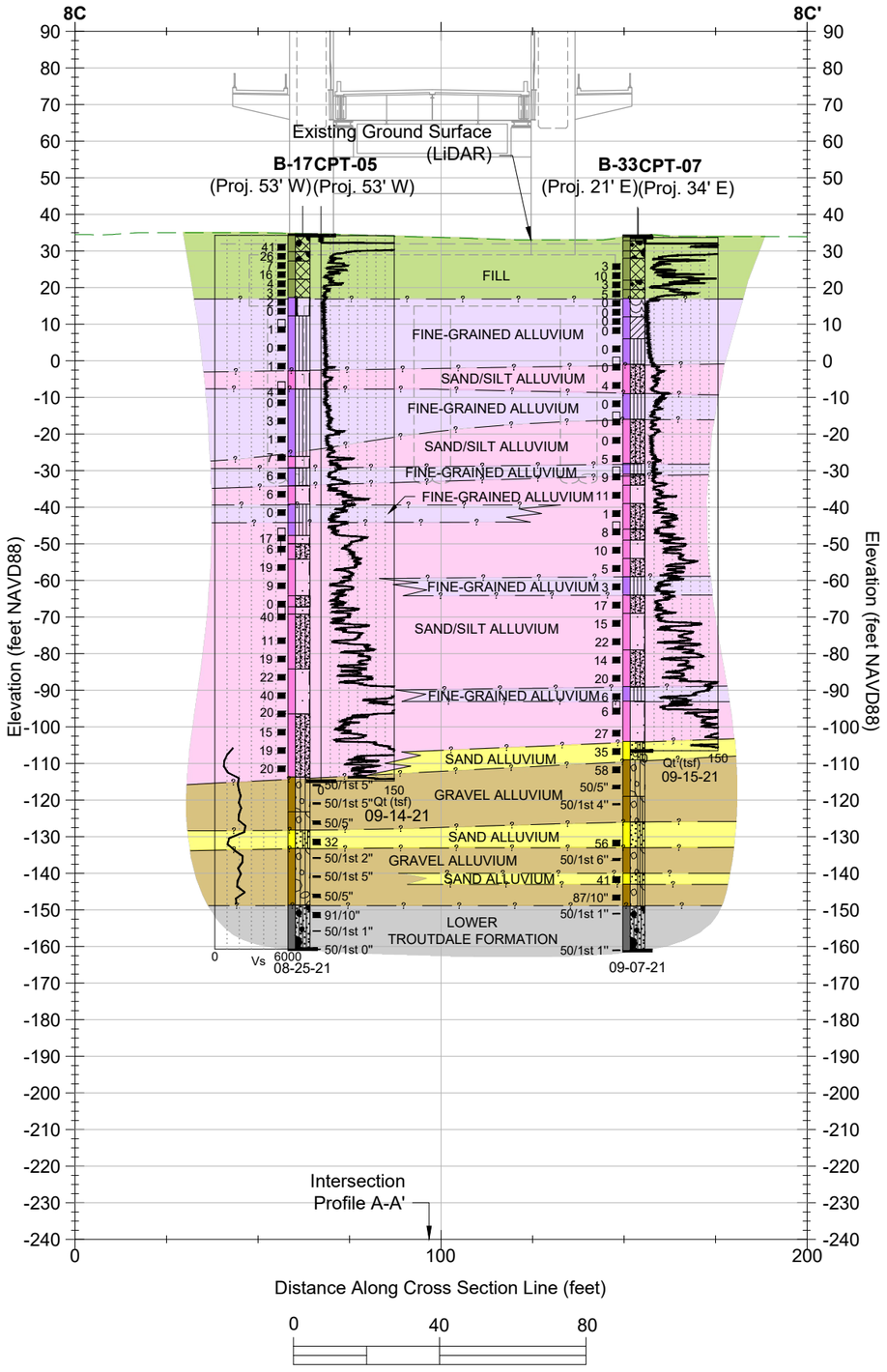

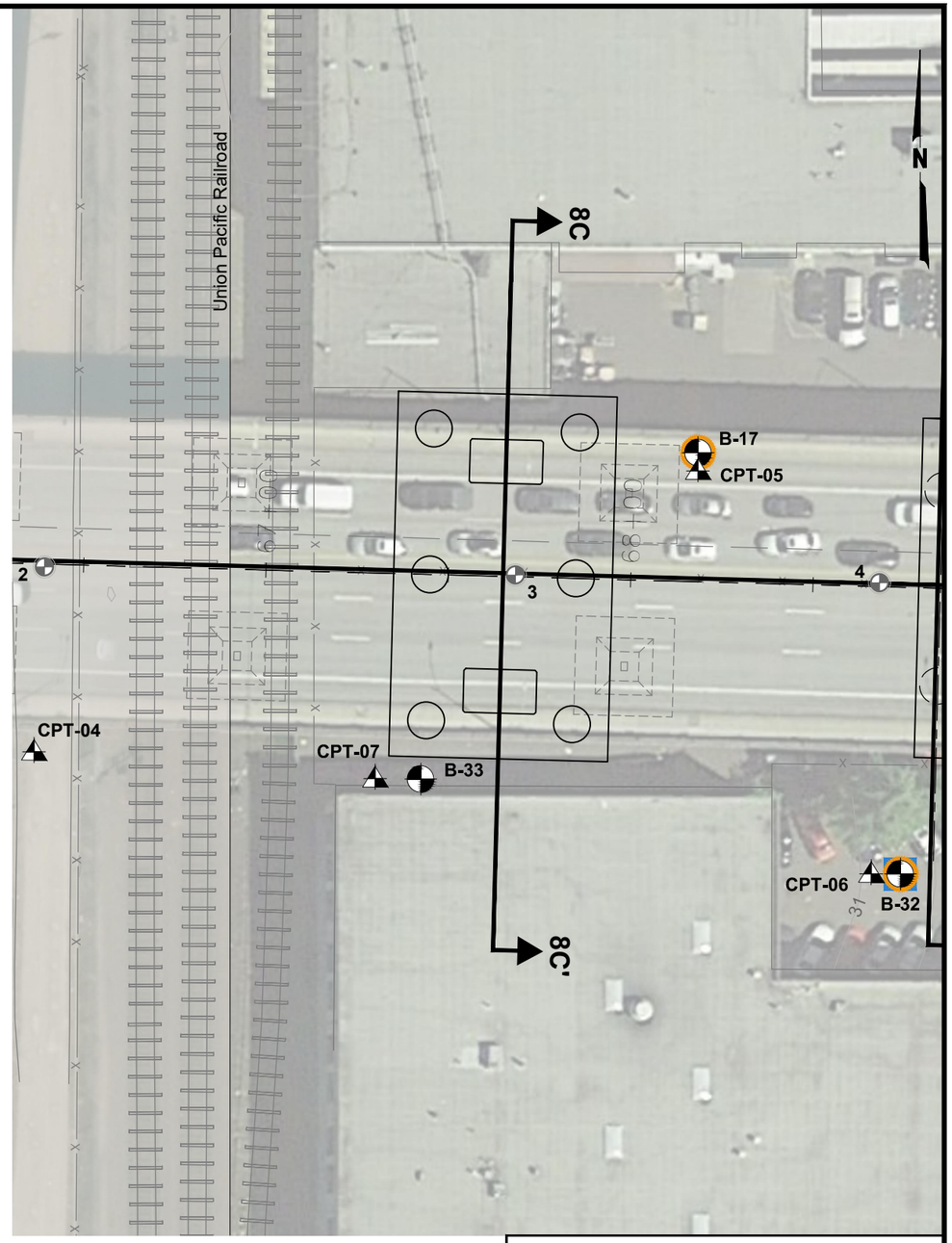

NOTES

1. See Figure 2-2 for legend, complete plan view, and applicable notes.

Earthquake Ready Burnside Bridge
Portland, Oregon

INTERPRETIVE SUBSURFACE CROSS SECTION 8C-8C'

January 2022 102636-009

SHANNON & WILSON, INC.
Geotechnical and Environmental Consultants

FIG. 6-8

File: I:\EF\PDX\102000s\102636 Burnside Bridge\DRAFTING\Profile_2018.dwg Date: 01-21-2022 Author: AEH

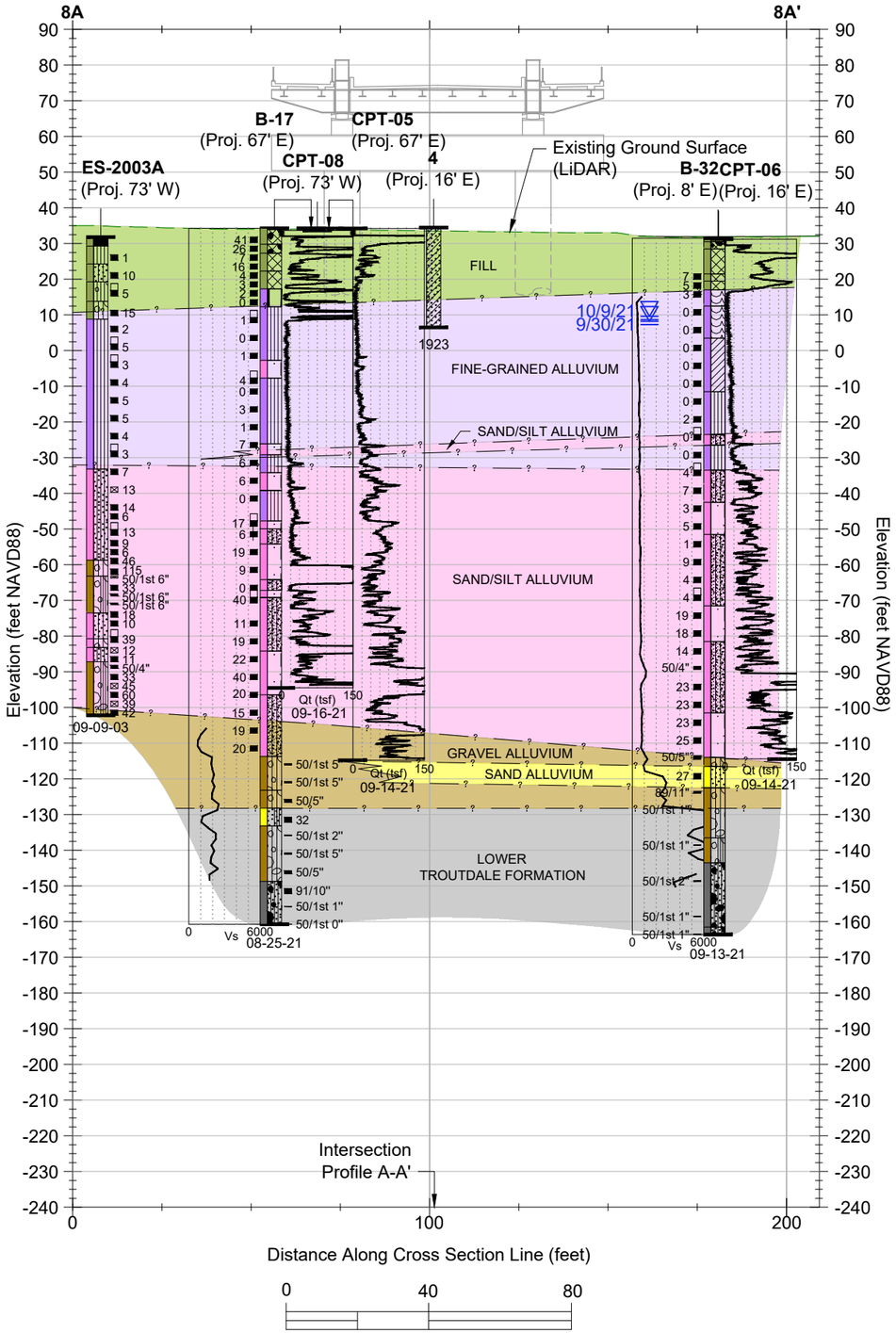

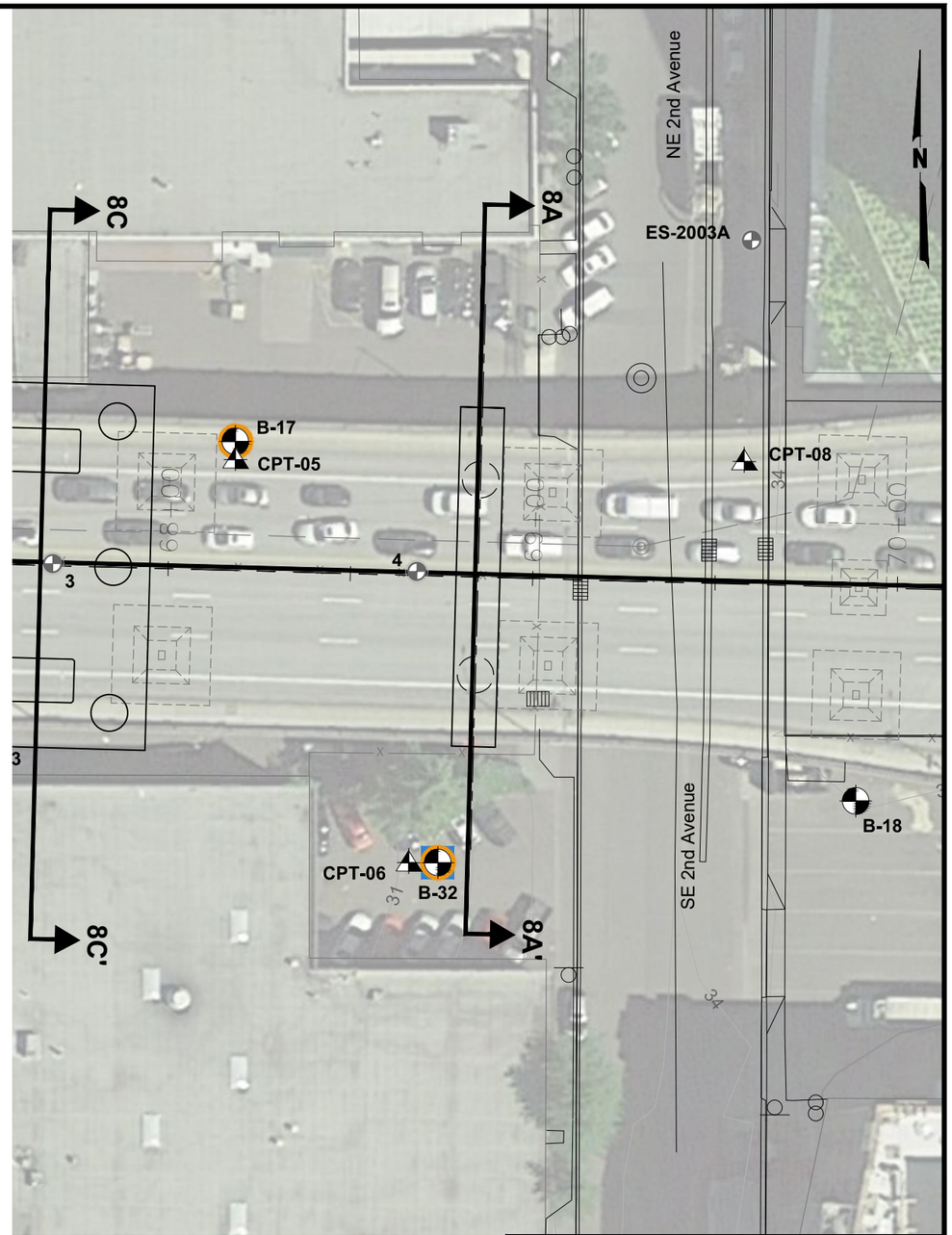

NOTES

1. See Figure 2-2 for legend, complete plan view, and applicable notes.

Earthquake Ready Burnside Bridge
Portland, Oregon

INTERPRETIVE SUBSURFACE CROSS SECTION 8A-8A'

January 2022 102636-009

SHANNON & WILSON, INC.
Geotechnical and Environmental Consultants

FIG. 6-9

File: I:\EF\PDX\102000s\102636 Burnside Bridge\DRAFTING\Profile_2018.dwg Date: 01-25-2022 Author: AEH

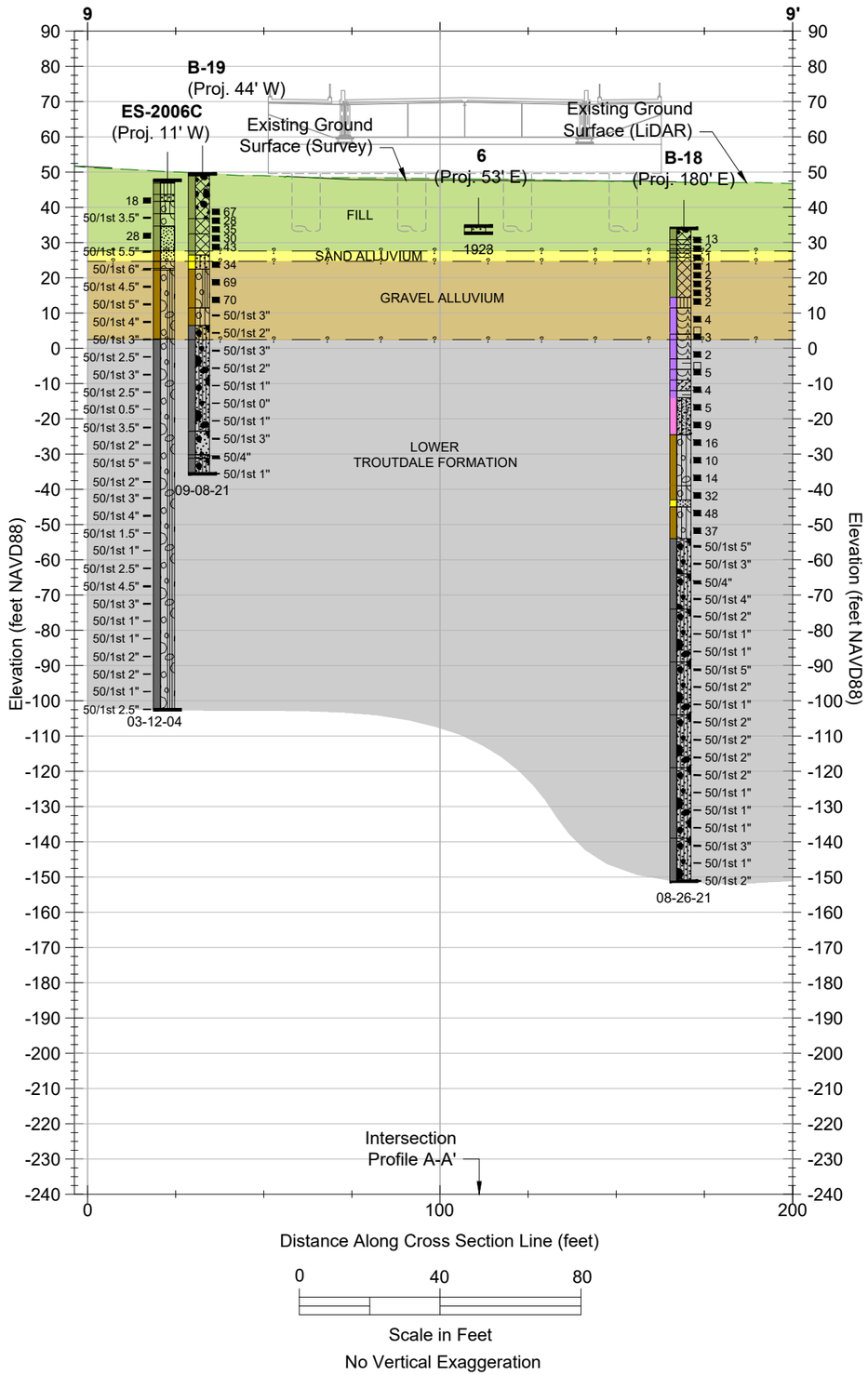

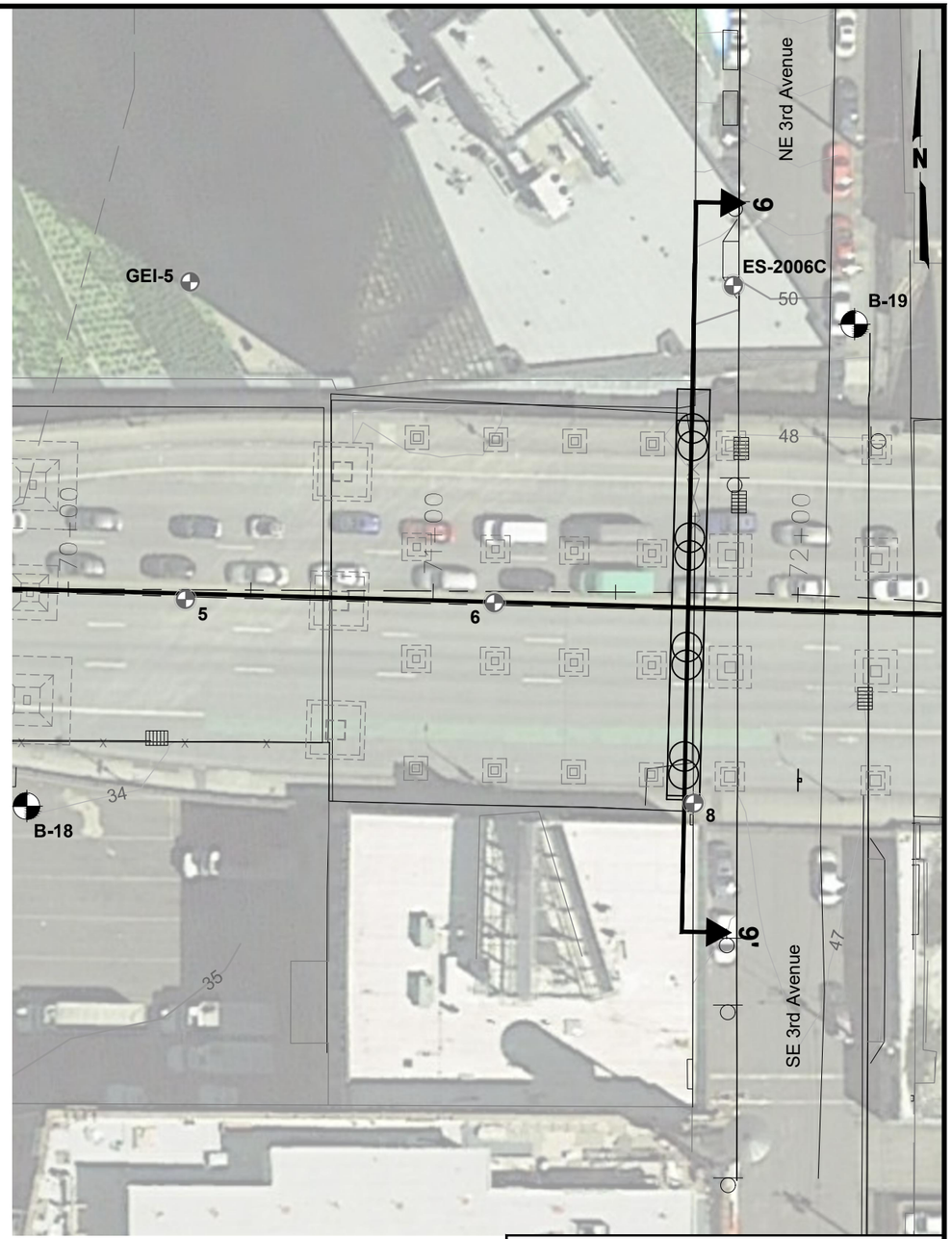

NOTES

1. See Figure 2-2 for legend, complete plan view, and applicable notes.

Earthquake Ready Burnside Bridge
Portland, Oregon

INTERPRETIVE SUBSURFACE CROSS SECTION 9-9'

January 2022 102636-009

SHANNON & WILSON, INC.
Geotechnical and Environmental Consultants

FIG. 6-10

File: I:\EF\PDX\102000s\102636 Burnside Bridge\DRAFTING\Profile_2018.dwg Date: 01-25-2022 Author: AEH

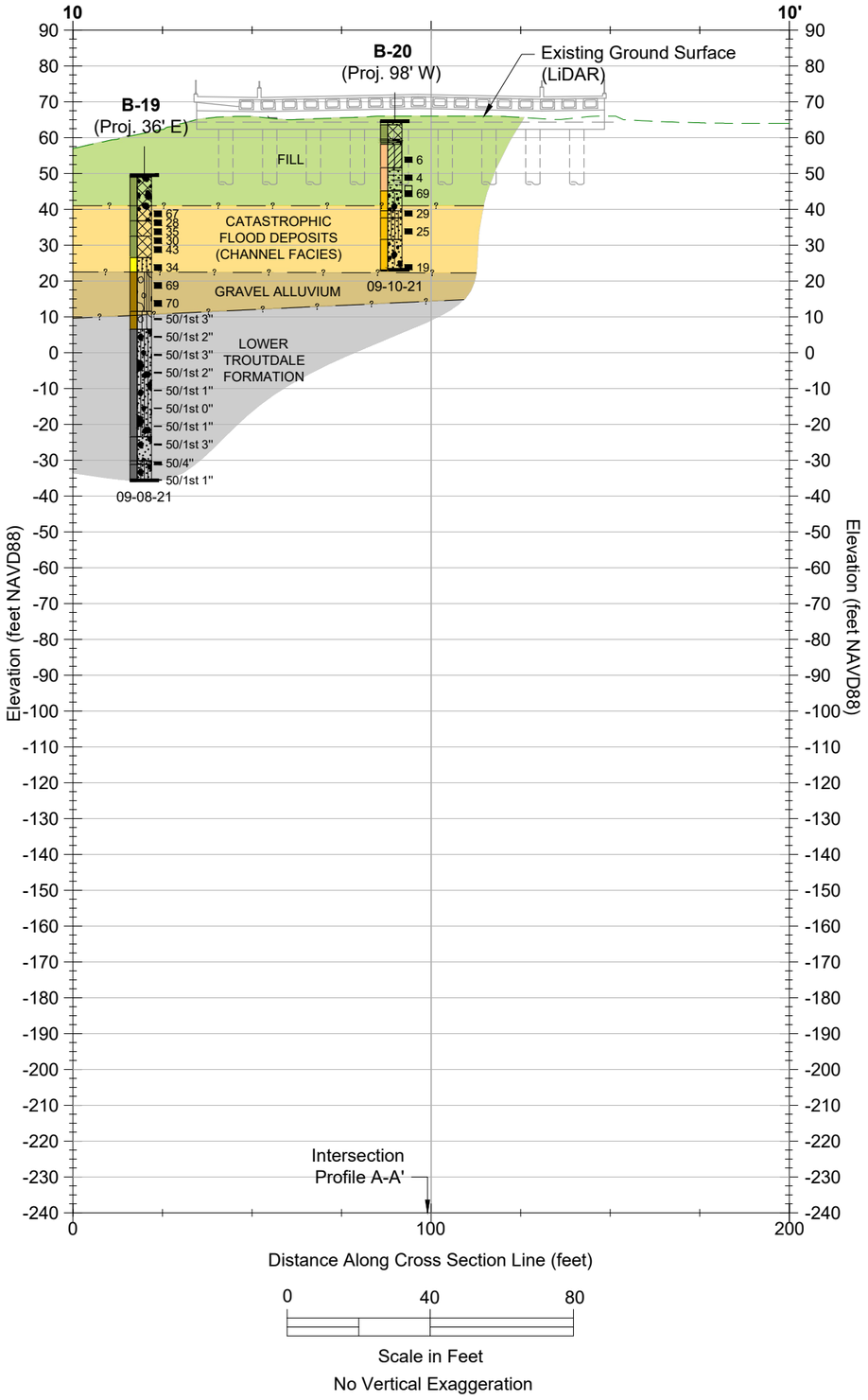

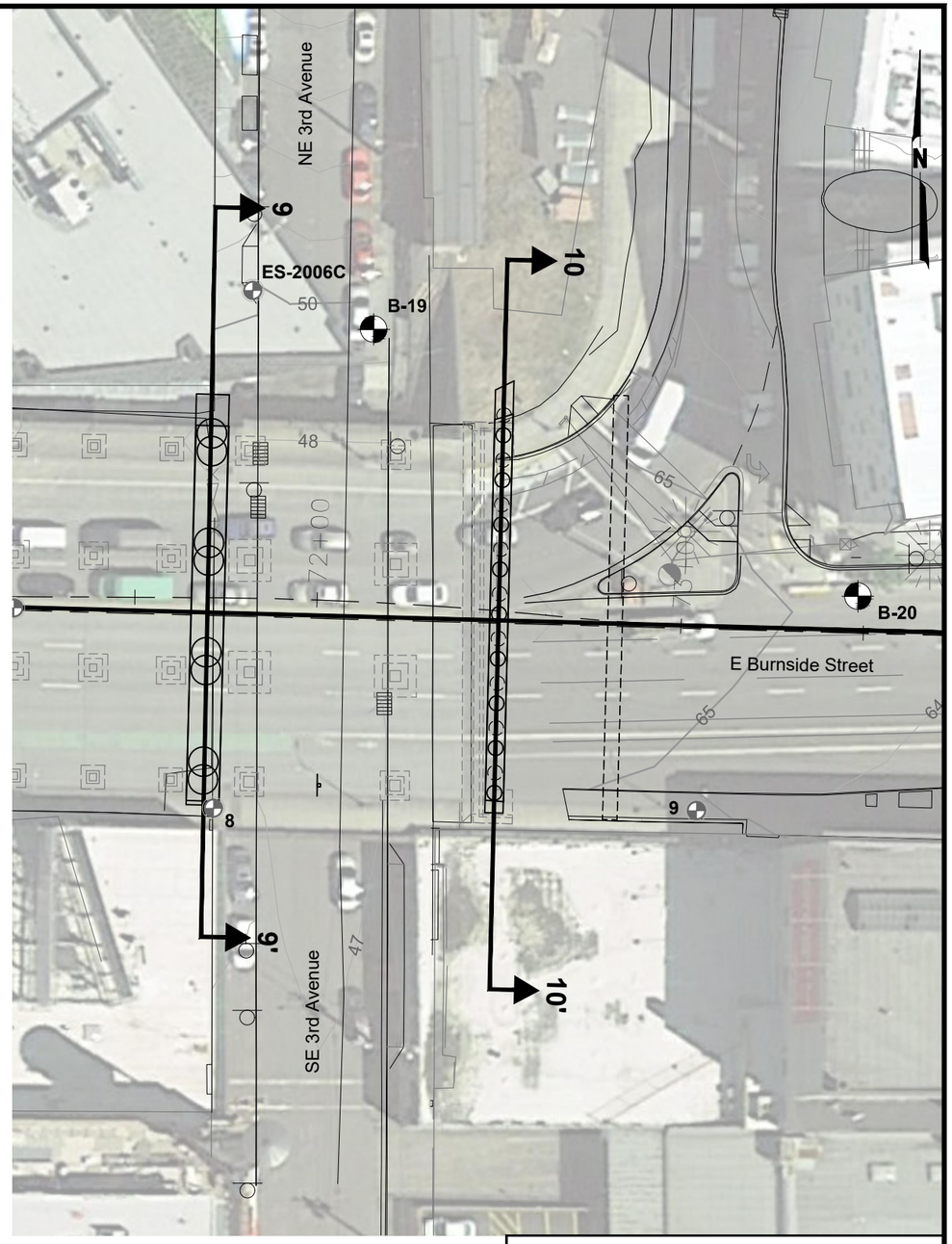

NOTES

1. See Figure 2-2 for legend, complete plan view, and applicable notes.

Earthquake Ready Burnside Bridge
Portland, Oregon

INTERPRETIVE SUBSURFACE CROSS SECTION 10-10'

January 2022 102636-009

SHANNON & WILSON, INC.
Geotechnical and Environmental Consultants

FIG. 6-11

File: I:\EP\PDX\102000s\102636 Burnside Bridge\DRAFTING\Profile_2018.dwg Date: 01-25-2022 Author: AEH

A

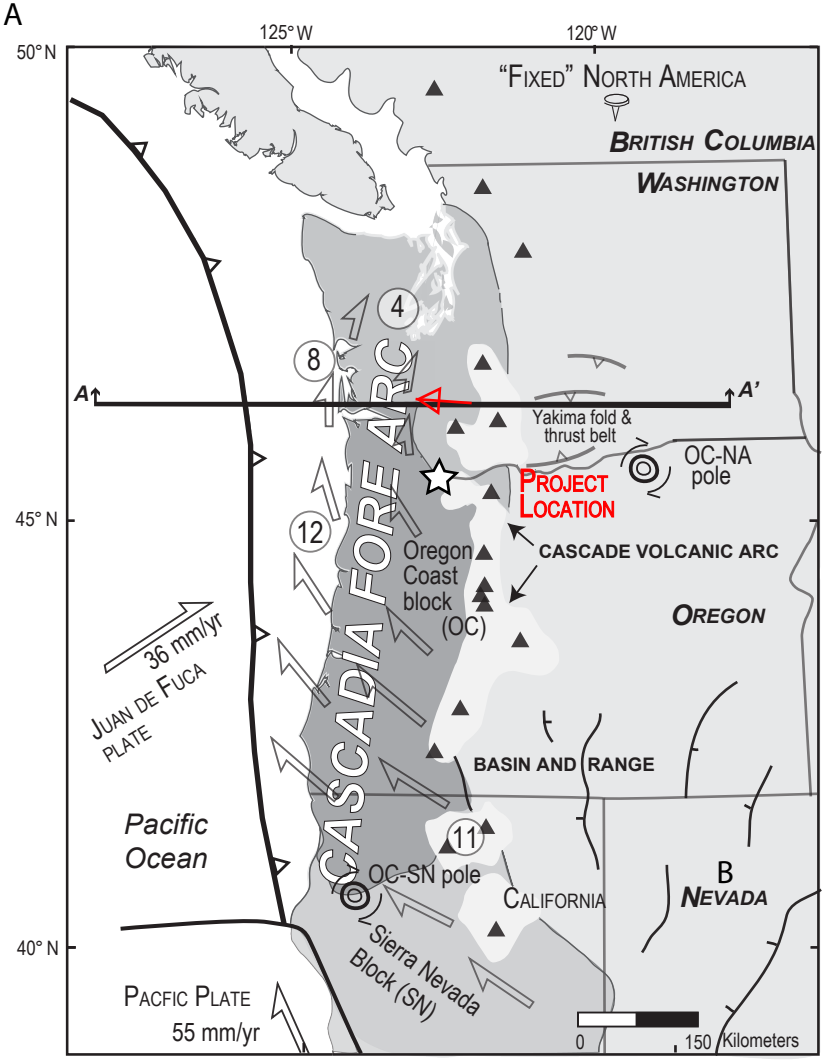

B

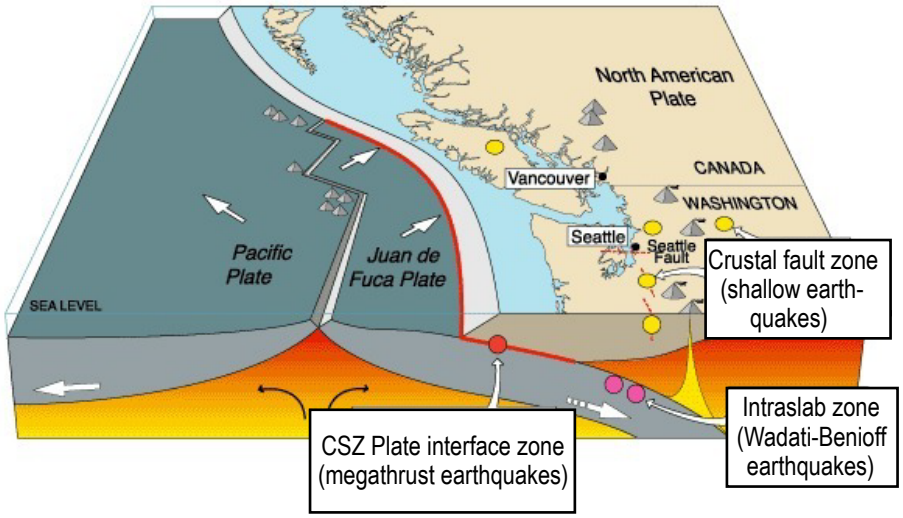

IDEALIZED CROSS SECTION AND SEISMIC SOURCE ZONES

NOT TO SCALE

NOTES

1. Figure A modified from Wells and Simpson (2001). Gray-outlined arrows indicate relative plate motions. Block motions (circled numbers) are in mm/yr.

2. Figure B adapted from Wells and others (2000).

FIG. 7-1

Earthquake Ready Burnside Bridge
Portland, Oregon

TECTONIC BLOCK MODEL OF CASCADIA FORE-ARC TERRANES

January 2022 102636-009

SHANNON & WILSON, INC.
Geotechnical and Environmental Consultants

FIG. 7-1

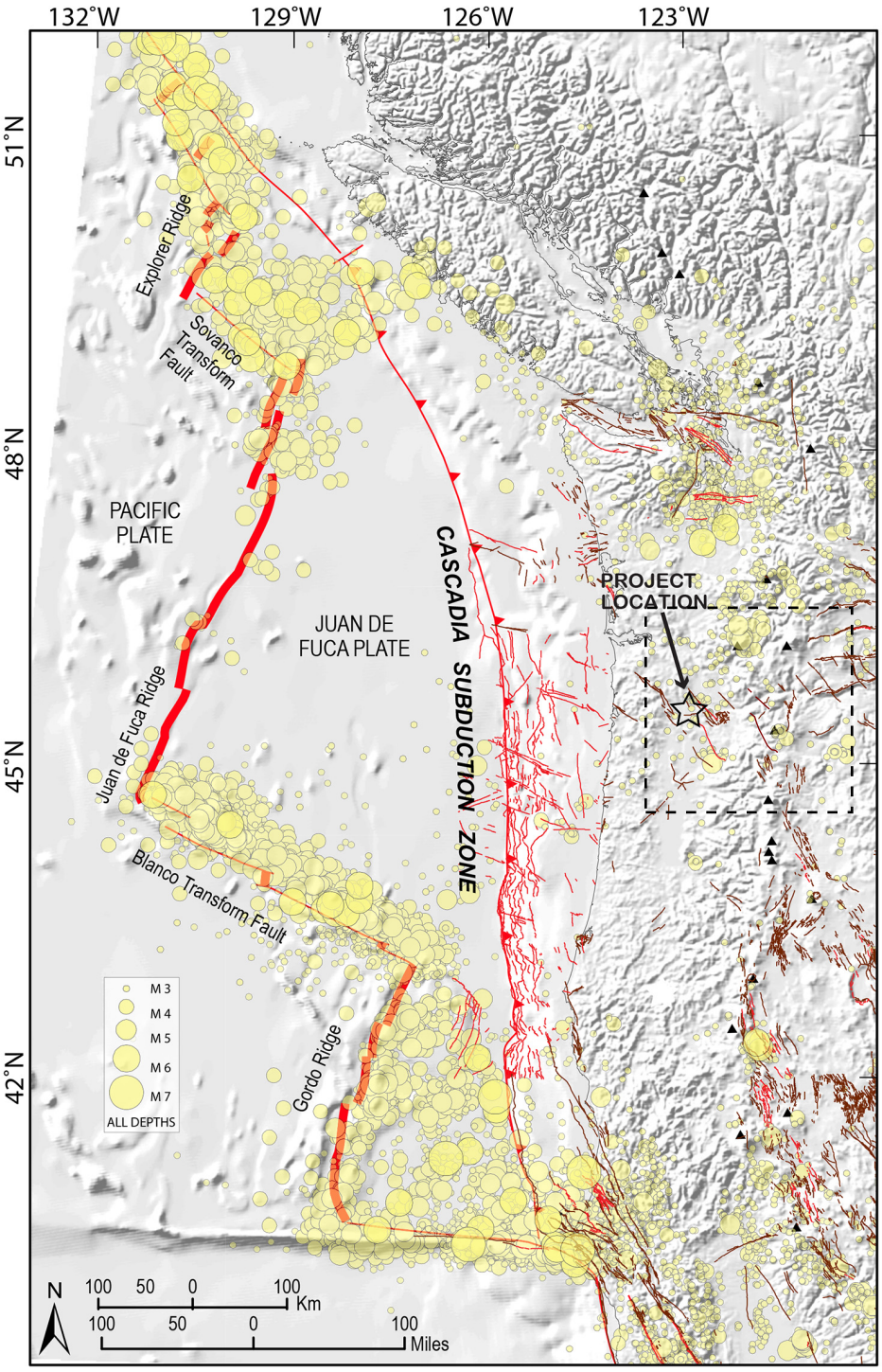

CASCADIA SUBDUCTION ZONE SEISMICITY

NOTES

1. Red lines on Figure A indicate active faults, brown lines denote faults with uncertain ages. Black triangles indicate locations of volcanoes. Fault traces from U.S.G.S Quaternary Fault and Fold Database, accessed 10/2015. Red triangles note upthrown block over fault.

2. Earthquake data accessed through the Northern California Earthquake Data Center (NCEDC).

Earthquake Ready Burnside Bridge
Portland, Oregon

PACIFIC NORTHWEST SEISMIC SOURCE ZONES

January 2022 102636-009

SHANNON & WILSON, INC.
Geotechnical and Environmental Consultants

FIG. 7-2

FIG. 7-2

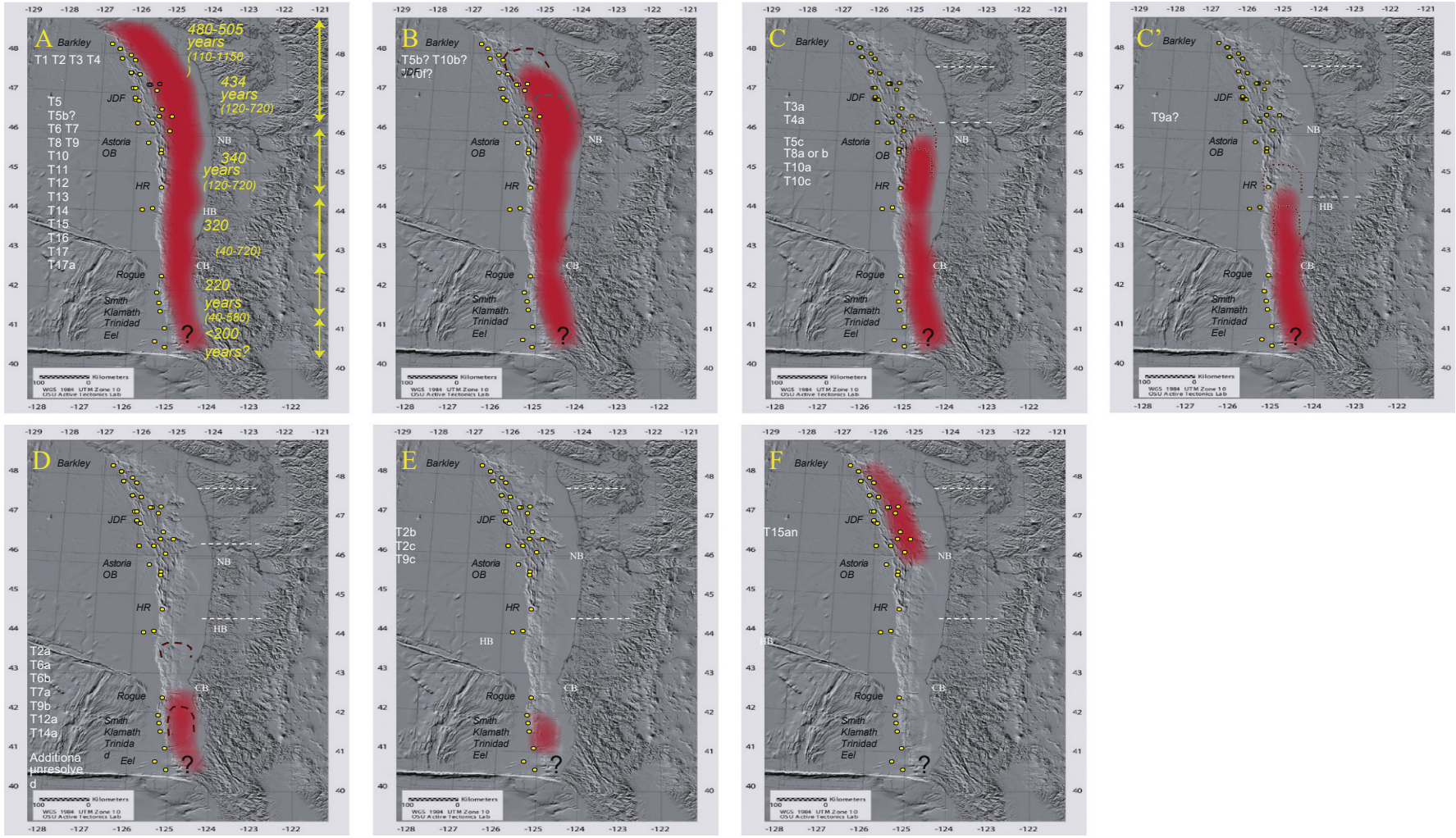

NOTES

1 Figure from Goldfinger and others (2017). Recurrence intervals in yellow. See the original paper for notation on this figure.

2 Seven rupture models for CSZ Interface inferred from turbidite stratigraphic correlation: Full or nearly full rupture (A), Mid-northern rupture from northern Washington southward (B), Mid rupture from northern or mid Oregon southward (C and C'), Southern Oregon/northern California rupture (D), Nothern California rupture (E), and Northern rupture from northern Oregon northward (F).

Earthquake Ready Burnside Bridge
Portland, Oregon

CSZ RUPTURE MODELS DERIVED FROM PALEOSEISMIC EVIDENCE GOLDFINGER AND OTHERS (2017)

January 2022 102636-009

SHANNON & WILSON, INC.
Geotechnical and Environmental Consultants

FIG. 7-3

FIG. 7-3

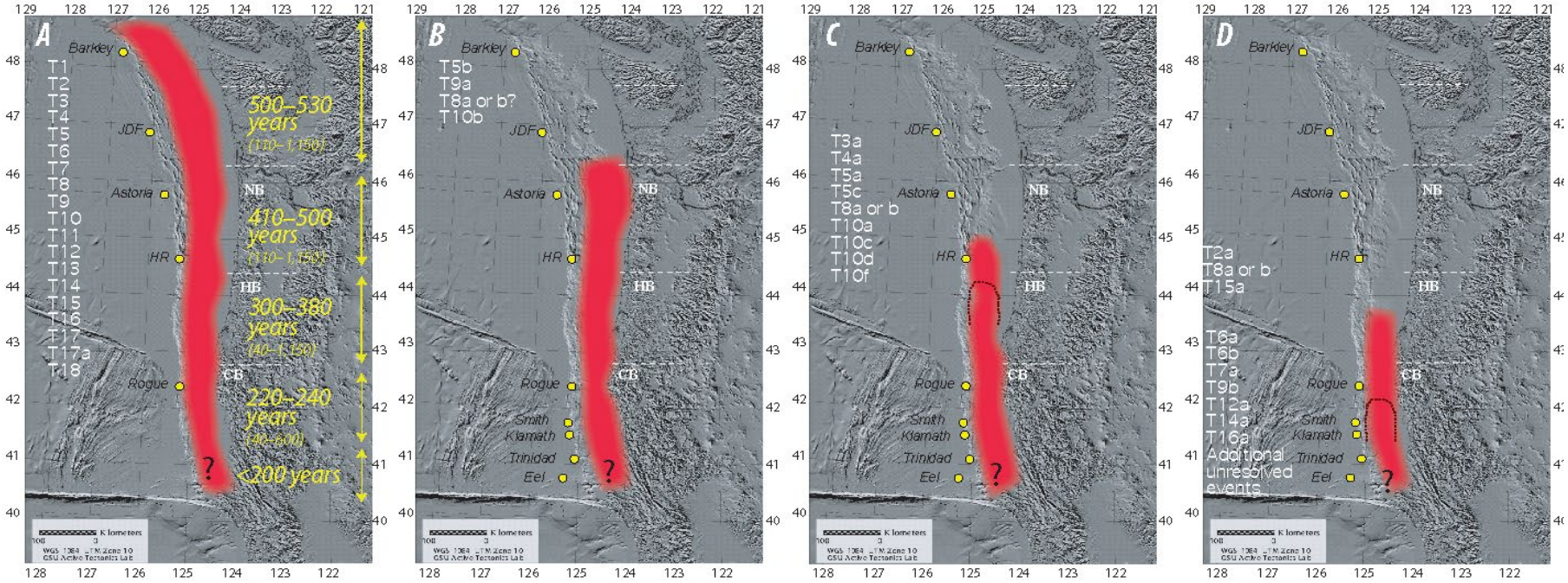

NOTES

1 Figure from Goldfinger and others (2012). Recurrence intervals in yellow. See the original paper for notation on this figure.

2 Four rupture modes for CSZ Interface inferred from turbidite stratigraphic correlation: Full or nearly full rupture (A), Mid-southern rupture from northern Oregon southward (B), Southern rupture from central Oregon southward (C), and Southern Oregon/northern California rupture (D).

Earthquake Ready Burnside Bridge
Portland, Oregon

CSZ RUPTURE MODELS DERIVED FROM PALEOSEISMIC EVIDENCE GOLDFINGER AND OTHERS (2012)

January 2022 102636-009

SHANNON & WILSON, INC.
Geotechnical and Environmental Consultants

FIG. 7-4

FIG. 7-4

Fig 7-5 CSZ-Interface Logic Tree.xlsx

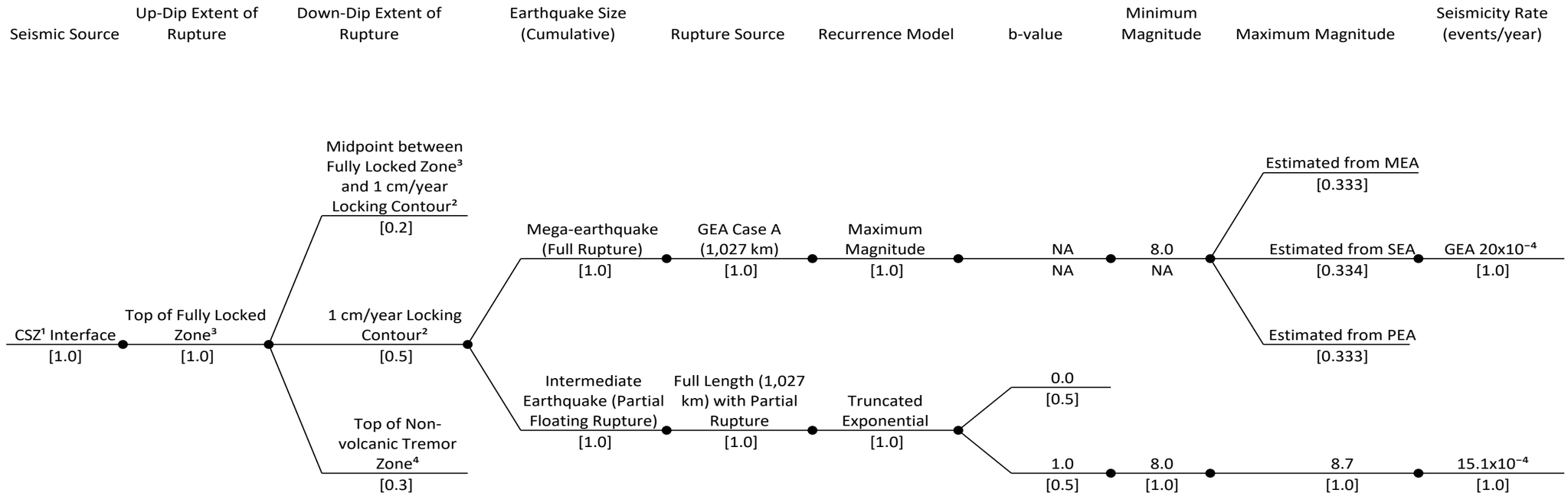

NOTES

[1]CSZ = Cascadia subduction zone
[2]Average of McCaffrey and others (2012) and Schmidt and others (2012), and Wang and others (2003) model
[3]Flück and others (1997)
[4]Gomberg and others (2010) and Wech (2011)
GEA = Goldfinger and others (2017)
MEA = Murotani and others (2008)
SEA = Strasser and others (2010)
PEA = Papazachos and others (2004)
km = kilometers

NA = not applicable
b-value = seismicity rate slope in recurrence relationship model

References cited in this figure are from Petersen and others (2014) and include personal communication. See Petersen and others (2014) for more information.

Earthquake Ready Burnside Bridge
Portland, Oregon

CSZ INTERFACE LOGIC TREE

January 2022 102636-009

SHANNON & WILSON, INC.
GEOTECHNICAL AND ENVIRONMENTAL CONSULTANTS

FIG. 7-5

Document Path: L:\Users\eab\CSZ_DDModel_14.mxd

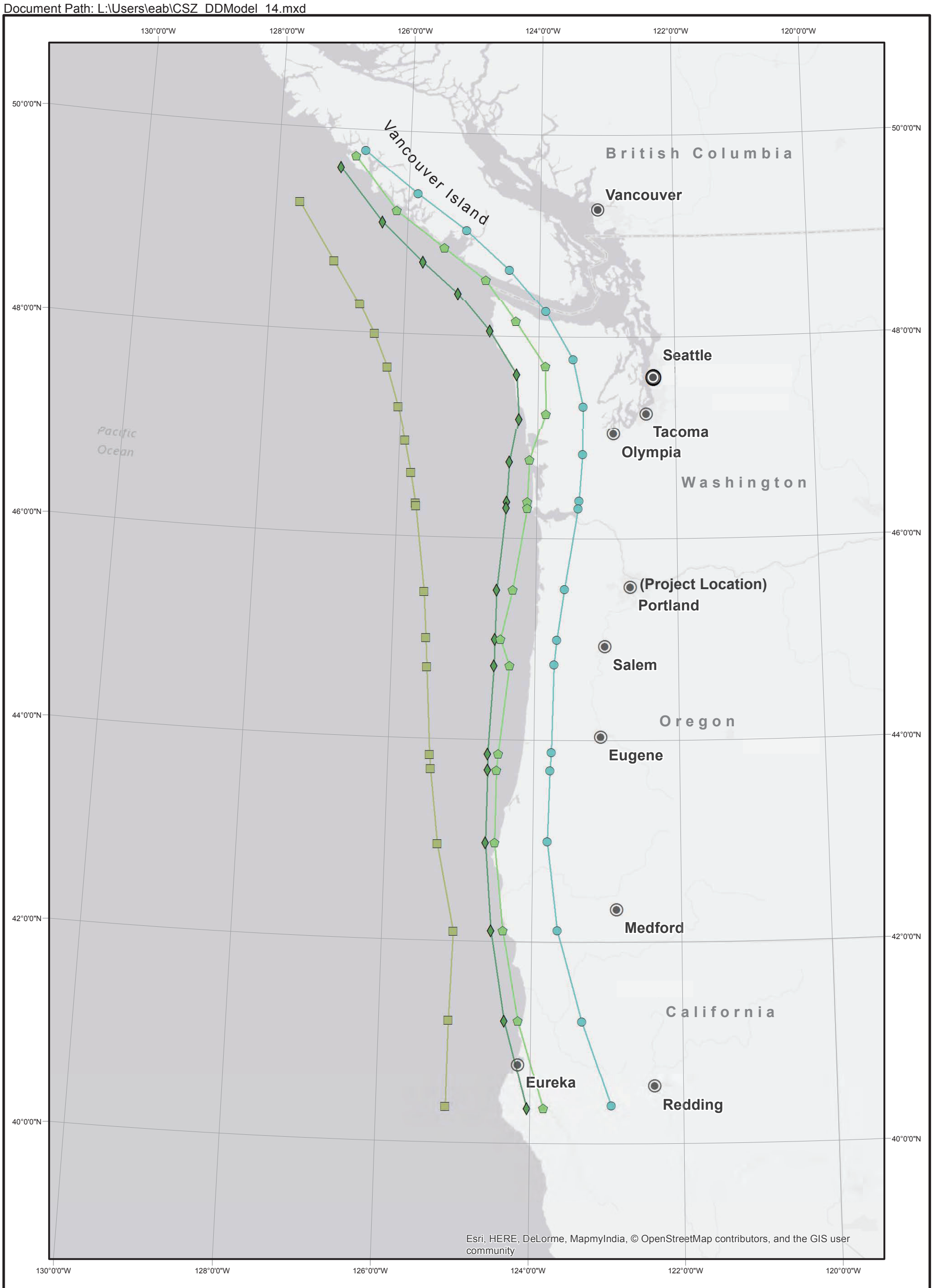

CSZ Models

- Deformation Front
- Midpoint Between Fully Locked Zone and 1 cm/yr (centimeters per year) Locking Contour
- 1 cm/yr Locking Contour
- Top of Episodic Non-Volcanic Tremor Slip Zone

N
W E
S

0 100
Kilometers

Earthquake Ready Burnside Bridge
Portland, Oregon

CSZ DOWNDIP MODELS

April 2022 102636-009

SHANNON & WILSON, INC.
Geotechnical and Environmental Consultants

FIG. 7-6

FIG. 7-6

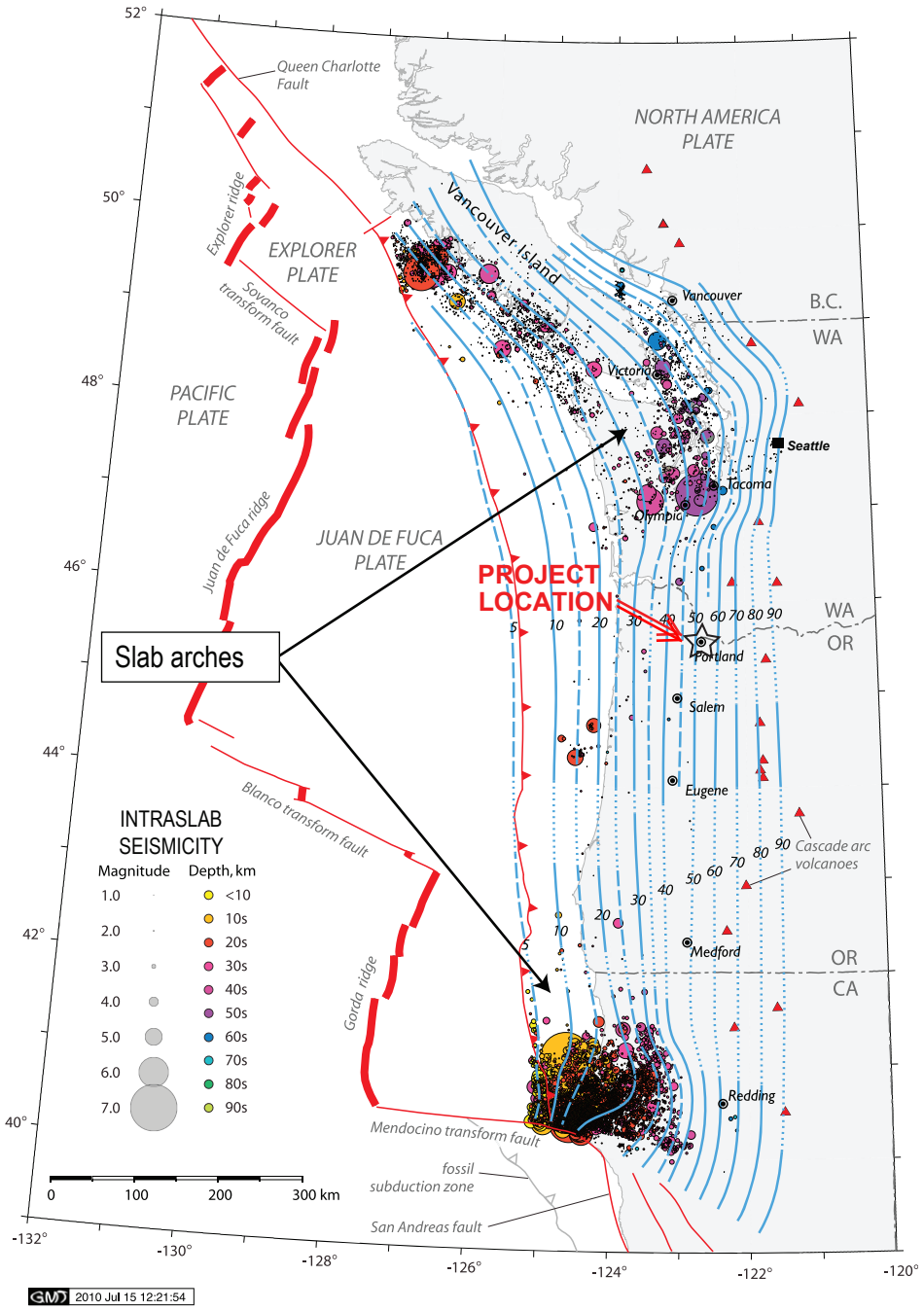

Subducting Slab Geometry and Intraslab Seismicity

NOTES

1. Figures adapted from McCrory and others (2012).

2. Circles show location of epicenters interpreted to be intraslab earthquakes, colored by depth range. Contour lines represent depth, in kilometers, to the top of the subducting Juan de Fuca slab surface. Red triangles show locations of active volcanoes.

Earthquake Ready Burnside Bridge
Portland, Oregon

SUBDUCTED JUAN DE FUCA SLAB SURFACE CONTOURS

April 2022 102636-009

SHANNON & WILSON, INC.
Geotechnical and Environmental Consultants

FIG. 7-7

Fig 7-8 CSZ-Intraslab Logic Tree.xlsx

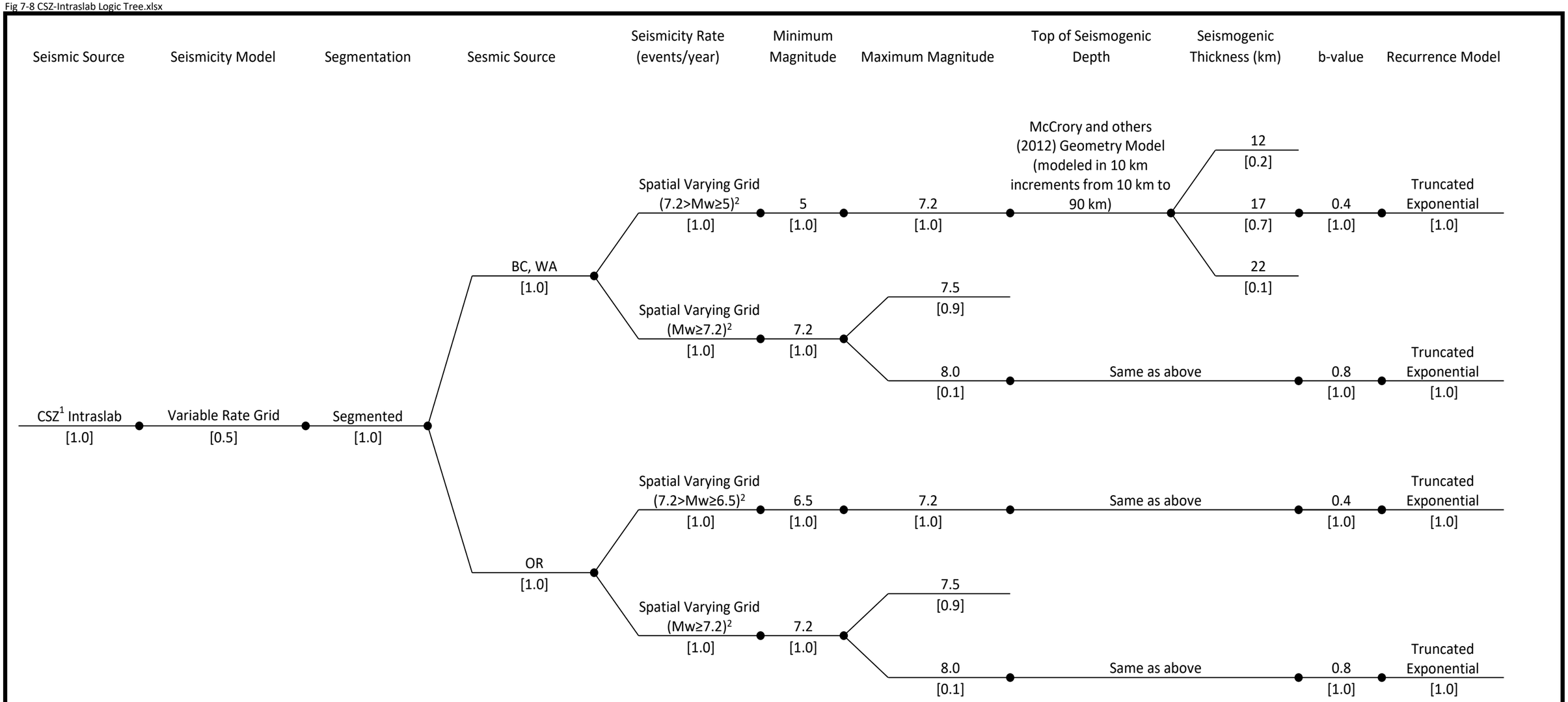

NOTES

[1] CSZ = Cascadia subduction zone
[2] The 2014 NSHM grid was limited to between 124.6°W and 120.7°W and between 44.1°N and 46.9°N.
NSHM = national seismic hazard model
BC = British Columbia
WA = Washington
OR = Oregon
km = kilometers

b-value = seismicity rate slope in recurrence relationship model
M_W = moment magnitude

Earthquake Ready Burnside Bridge
Portland, Oregon

CSZ INTRASLAB LOGIC TREE

January 2022 102636-009

SHANNON & WILSON, INC.
GEOTECHNICAL AND ENVIRONMENTAL CONSULTANTS

FIG. 7-8

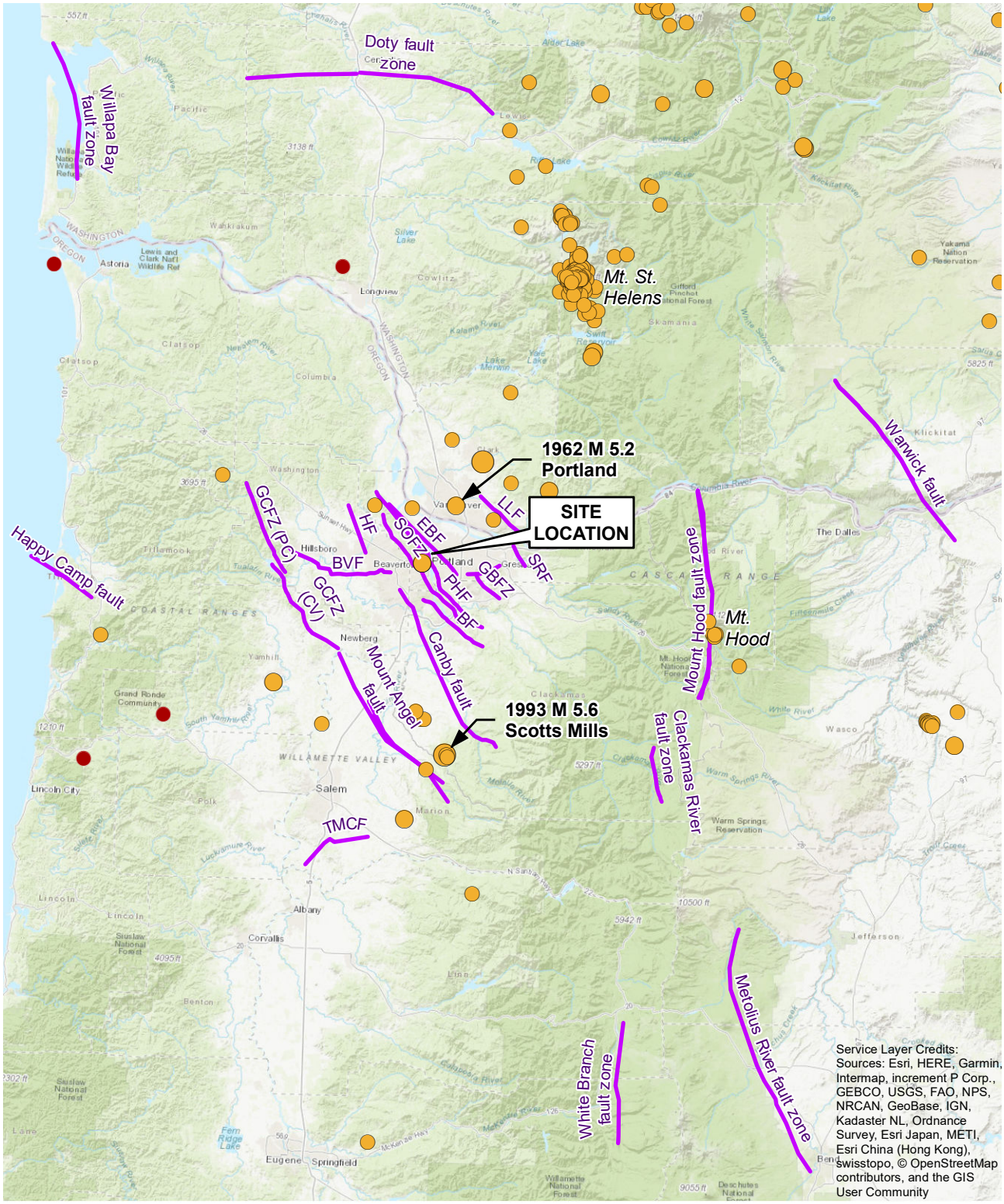

BVF = Beaverton fault; BF = Bolton fault; EBF = East Bank fault; GBFZ = Grant Butte fault zone; GCFZ (CV) = Gales Creek fault zone (Chehalem Valley); GCFZ (PC) = Gales Creek fault zone (Parsons Creek); HF = Helvetia fault; LLF = Lacamas Lake fault; PHF = Portland Hills fault; SOFZ = Sylvan-Oatfield fault zone; SRF = Sandy River fault; TMCF = Turner & Mill Creek fault

LEGEND

35 km < Depth < 35 km

4
5
6

Magnitude

Fault Included in Probabilistic Seismic Hazard Analysis (PSHA)

0 12.5 25 50

Scale in Miles

0 20 40 80

Scale in Kilometers

Earthquake Ready Burnside Bridge
Portland, Oregon

REGIONAL FAULTS AND HISTORIC EARTHQUAKES MAGNITUDE 4+

January 2022 102636-009

SHANNON & WILSON, INC.
GEOTECHNICAL AND ENVIRONMENTAL CONSULTANTS

FIG. 7-9

Filename: T:\Projects\PDX\102000s\102636_Burnside Bridge\Avmxd\PSHAfaults_10.6.mxd Date: 1/25/2022 Login: AEH

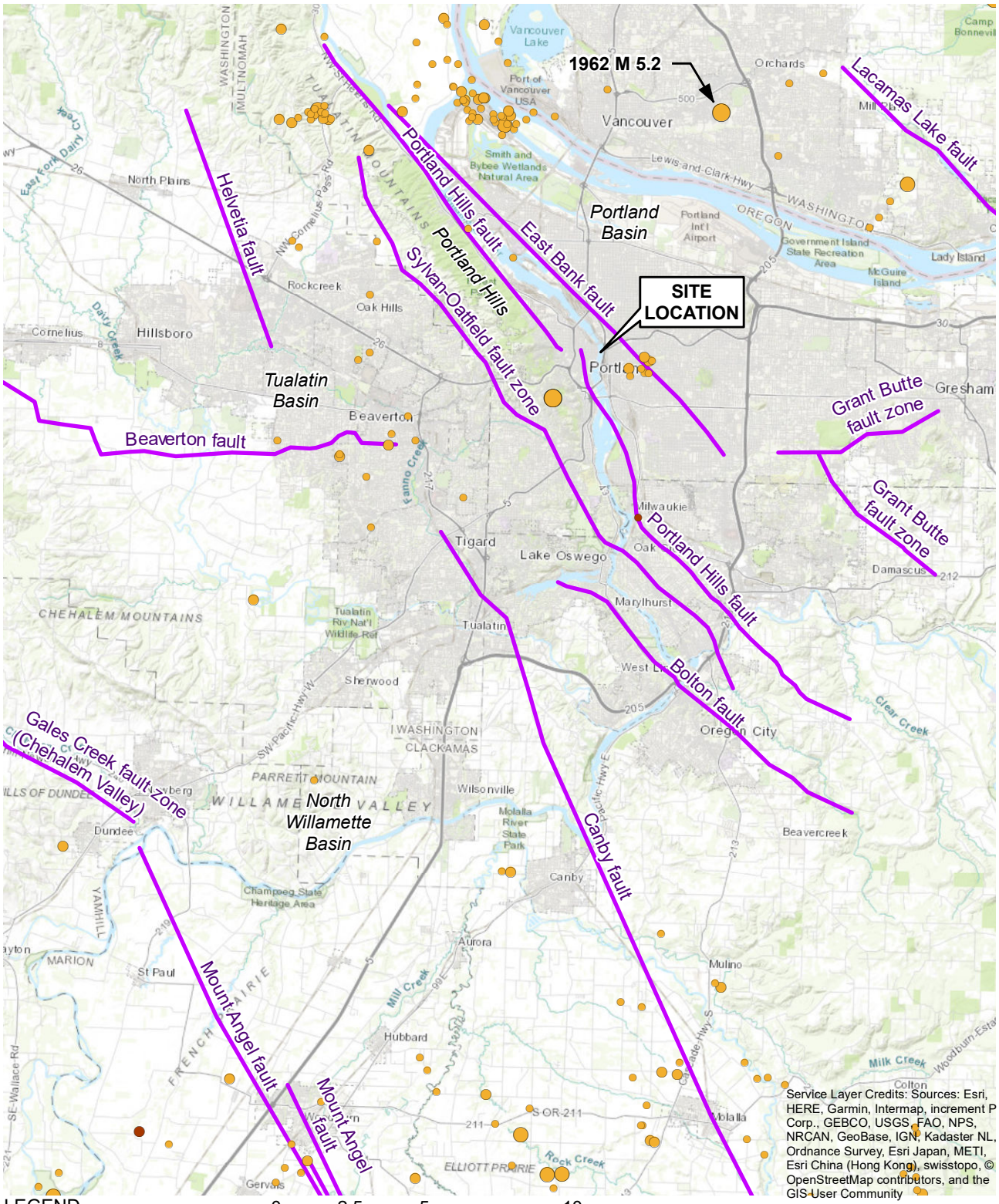

LEGEND

35 km < Depth < 35 km

2
3
4
5
6

Magnitude

Fault Included in Probabilistic Seismic Hazard Analysis (PSHA)

0 2.5 5 10

Scale in Miles

0 4 8 16

Scale in Kilometers

Earthquake Ready Burnside Bridge
Portland, Oregon

LOCAL FAULTS AND HISTORIC EARTHQUAKES MAGNITUDE 2+

January 2022 102636-009

SHANNON & WILSON, INC.
GEOTECHNICAL AND ENVIRONMENTAL CONSULTANTS

FIG. 7-10

Filename: T:\Projects\PDX\102000s\102636_Burnside Bridge\Avmxd\Localfaults_10.6.mxd Date: 1/25/2022 Login: AEH

Fig 7-11 Crustal Background Logic Tree.xlsx

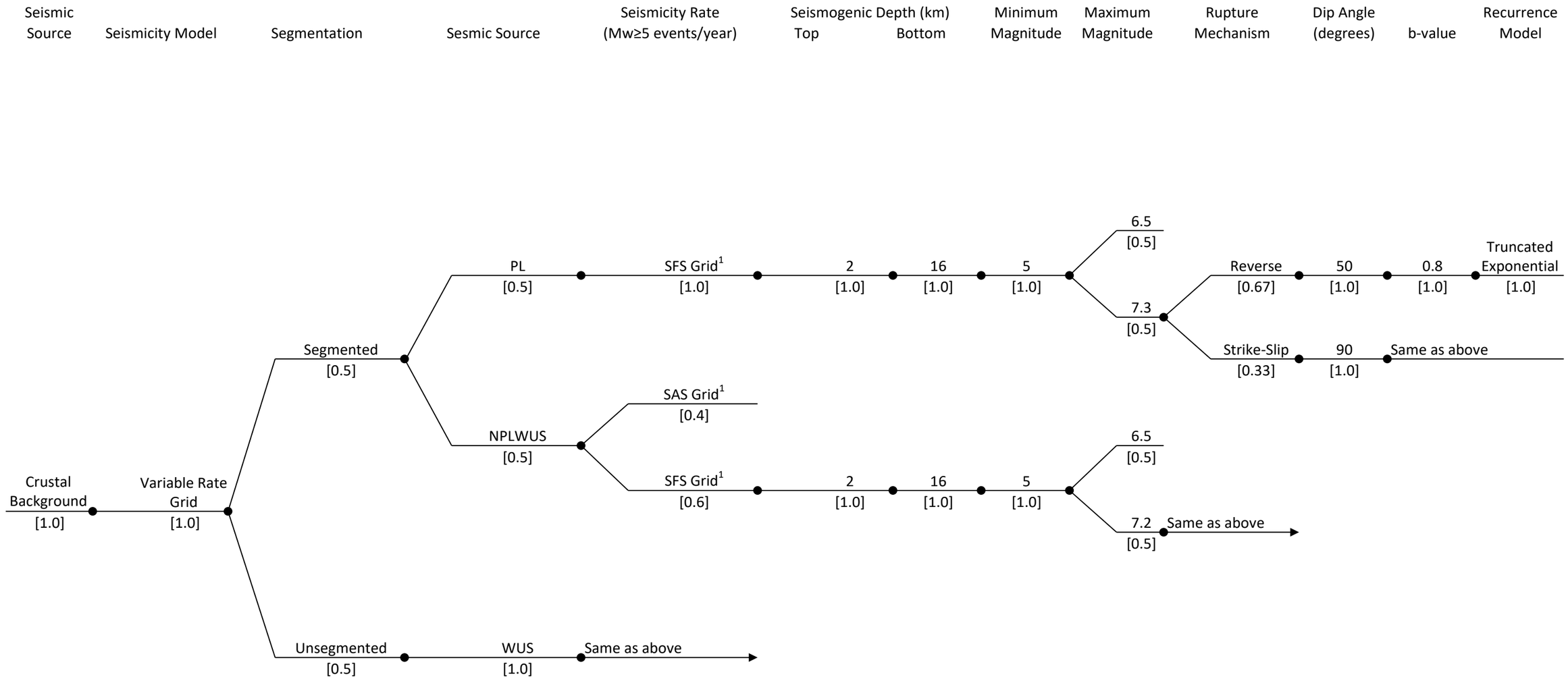

NOTES

[1]The 2014 NSHM grid was limited to between 124.6°W and 120.7°W and between 44.1°N and 46.9°N.
NSHM = national seismic hazard model
WUS = western United States
PL = Puget lowland
NPWUS = no-Puget lowland WUS
SFS = spatial fixed smoothing
SAS = spatial adaptive smoothing
km = kilometers

b-value = seismicity rate slope in recurrence relationship model
M_W = moment magnitude

Earthquake Ready Burnside Bridge
Portland, Oregon

CRUSTAL BACKGROUND LOGIC TREE

January 2022 102636-009

SHANNON & WILSON, INC.
GEOTECHNICAL AND ENVIRONMENTAL CONSULTANTS

FIG. 7-11

Fig 7-12 & 7-13 GMM Logic Tree.xlsx

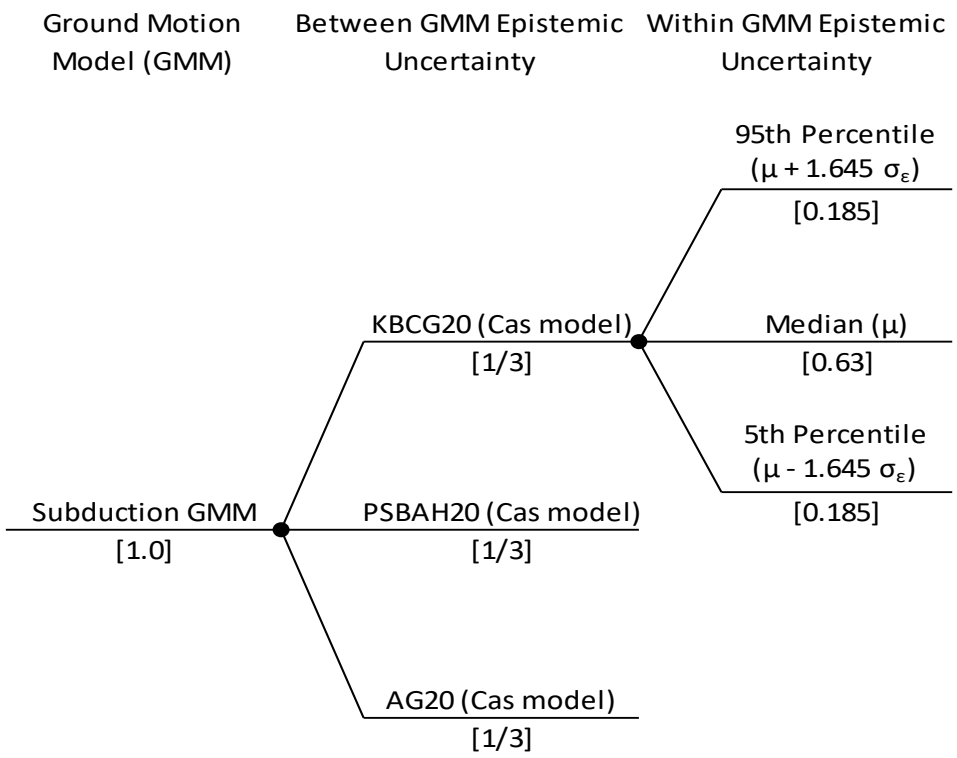

NOTES:

Values in brackets are weight factors.
μ = median spectral acceleration in log scale
σ_ε = within-model epistemic standard deviation of spectral acceleration in natural log scale
AG20 = Abrahamson and Gülerce (2020)
Cas = Cascadia
GMM = ground motion model
KBCG20 = Kuehn and others (2020)
PSBAH20 = Parker and others (2020)

Earthquake Ready Burnside Bridge
Portland, Oregon

SUBDUCTION GROUND MOTION MODEL LOGIC TREE

January 2022 102636-009

SHANNON & WILSON, INC.
GEOTECHNICAL AND ENVIRONMENTAL CONSULTANTS

FIG. 7-12

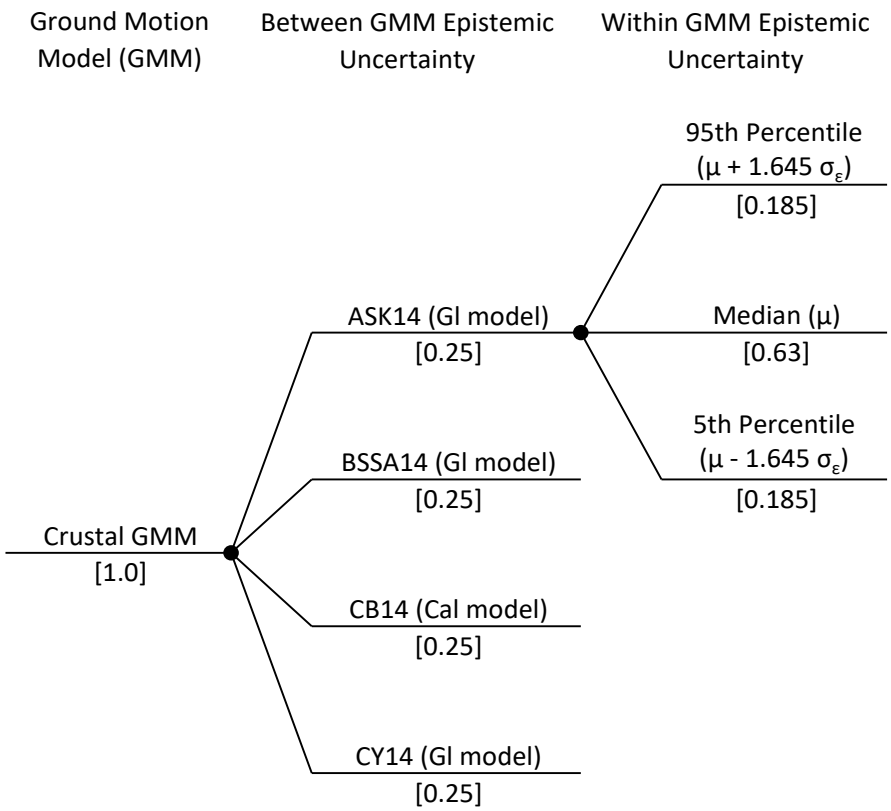

NOTES:

Values in brackets are weight factors.
μ = median spectral acceleration in log scale
σ_ε = within-model epistemic standard deviation of spectral acceleration in natural log scale
ASK14 = Abrahamson and others (2014)
BSSA14 = Boore and others (2014)
Cal = California
CB14 = Campbell and Bozorgnia (2014)
CY14 = Chiou and Youngs (2014)
GI = global

Earthquake Ready Burnside Bridge
Portland, Oregon

CRUSTAL GROUND MOTION MODEL LOGIC TREE

January 2022 102636-009

SHANNON & WILSON, INC.
GEOTECHNICAL AND ENVIRONMENTAL CONSULTANTS

FIG. 7-13

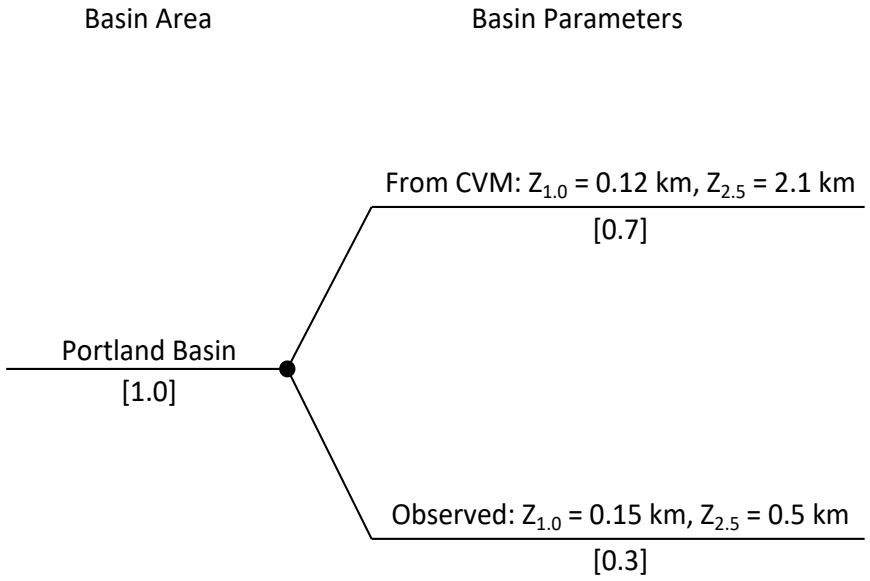

NOTES:

Values in brackets are weight factors.
CVM = community velocity model (stephenson and others, 2017)
$Z_{1.0}$ = depth to subsurface material with a shear wave velocity of 1 km/sec
$Z_{2.5}$ = depth to subsurface material shear wave velocity of 2.5 km/sec.

Earthquake Ready Burnside Bridge
Portland, Oregon

BASIN TERM PARAMETERS LOGIC TREE

January 2022 102636-009

SHANNON & WILSON, INC.
GEOTECHNICAL AND ENVIRONMENTAL CONSULTANTS

FIG. 7-14

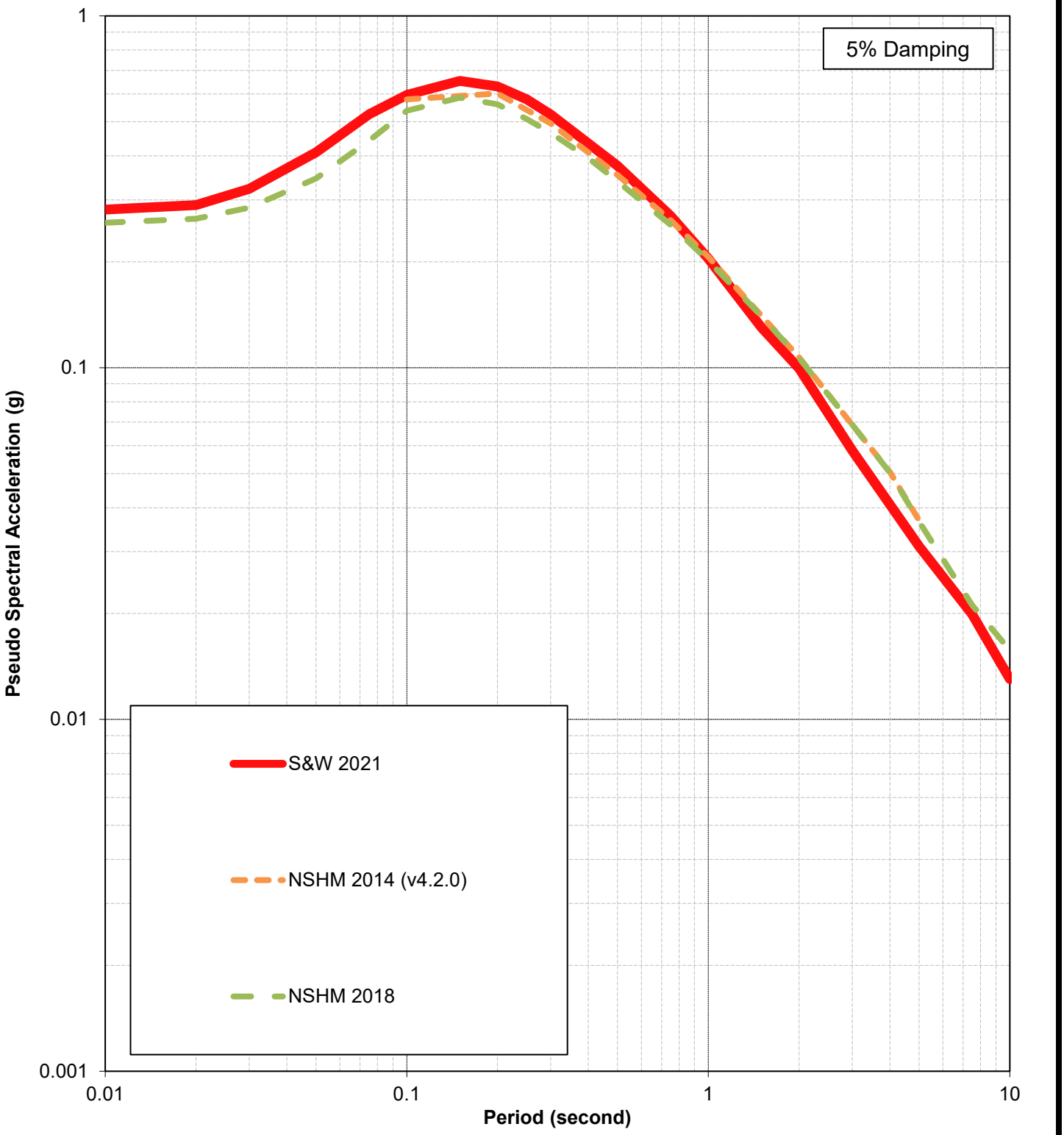

NOTES

1. Spectra correspond to Site Class B/C Boundary VS30 of 760 meters per second.
2. g = standard gravitational acceleration
   NSHM = national seismic hazard model
   S&W = Shannon & Wilson
   VS30 = time-averaged shear wave velocity for 30 meters of soil below soil profile base

Earthquake Ready Burnside Bridge
Portland, Oregon

1,000-YEAR RETURN PERIOD MEAN UNIFORM HAZARD SPECTRA

January 2022 102636-009

SHANNON & WILSON, INC.
GEOTECHNICAL AND ENVIRONMENTAL CONSULTANTS

FIG. 7-15

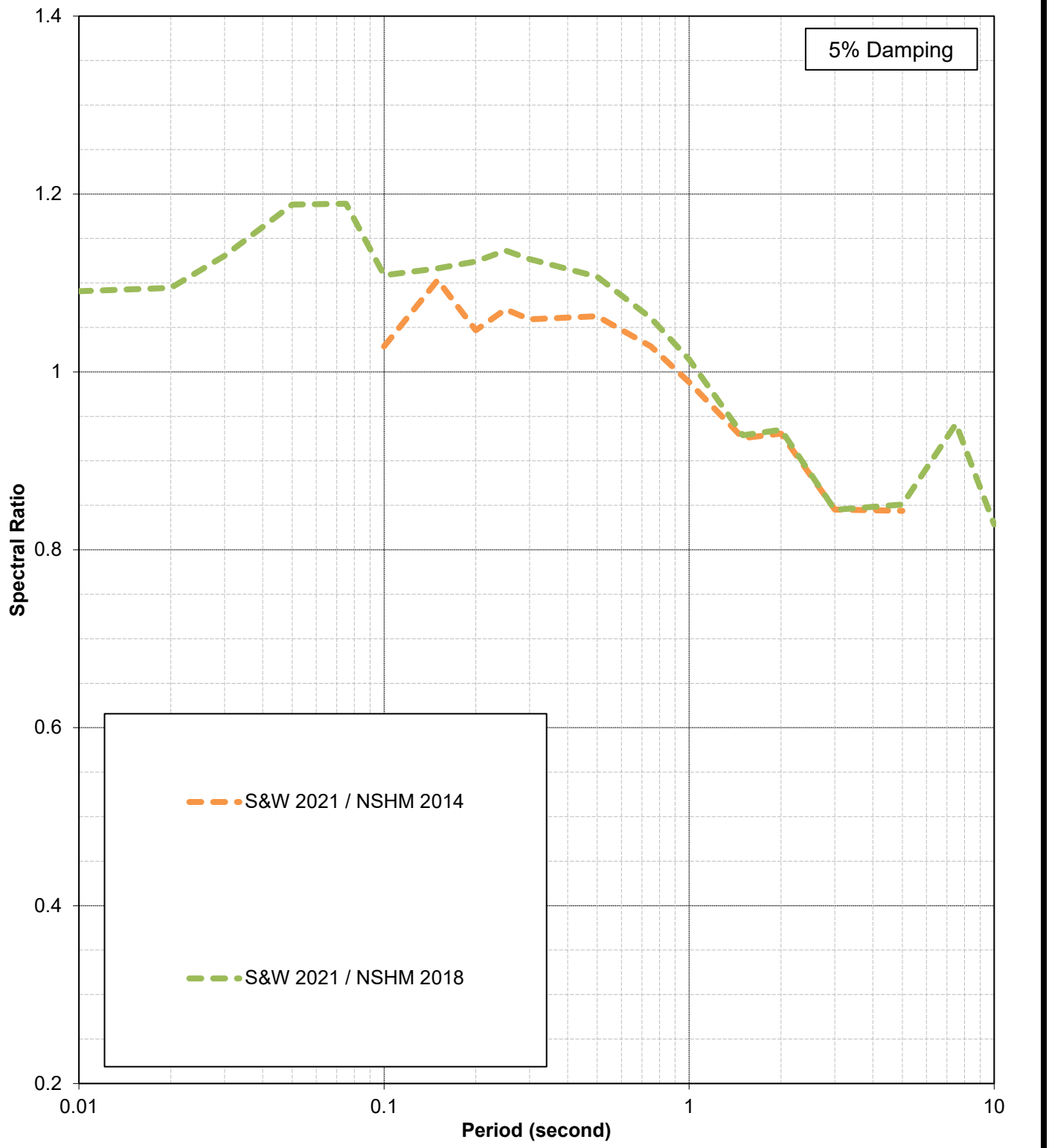

NOTES

1. Spectra correspond to Site Class B/C Boundary VS30 of 760 meters per second.
2. g = standard gravitational acceleration
   NSHM = national seismic hazard model
   S&W = Shannon & Wilson
   VS30 = time-averaged shear wave velocity for 30 meters of soil below soil profile base

Earthquake Ready Burnside Bridge
Portland, Oregon

1,000-YEAR RETURN PERIOD MEAN UNIFORM HAZARD SPECTRAL RATIO

January 2022 102636-009

SHANNON & WILSON, INC.
GEOTECHNICAL AND ENVIRONMENTAL CONSULTANTS

FIG. 7-16

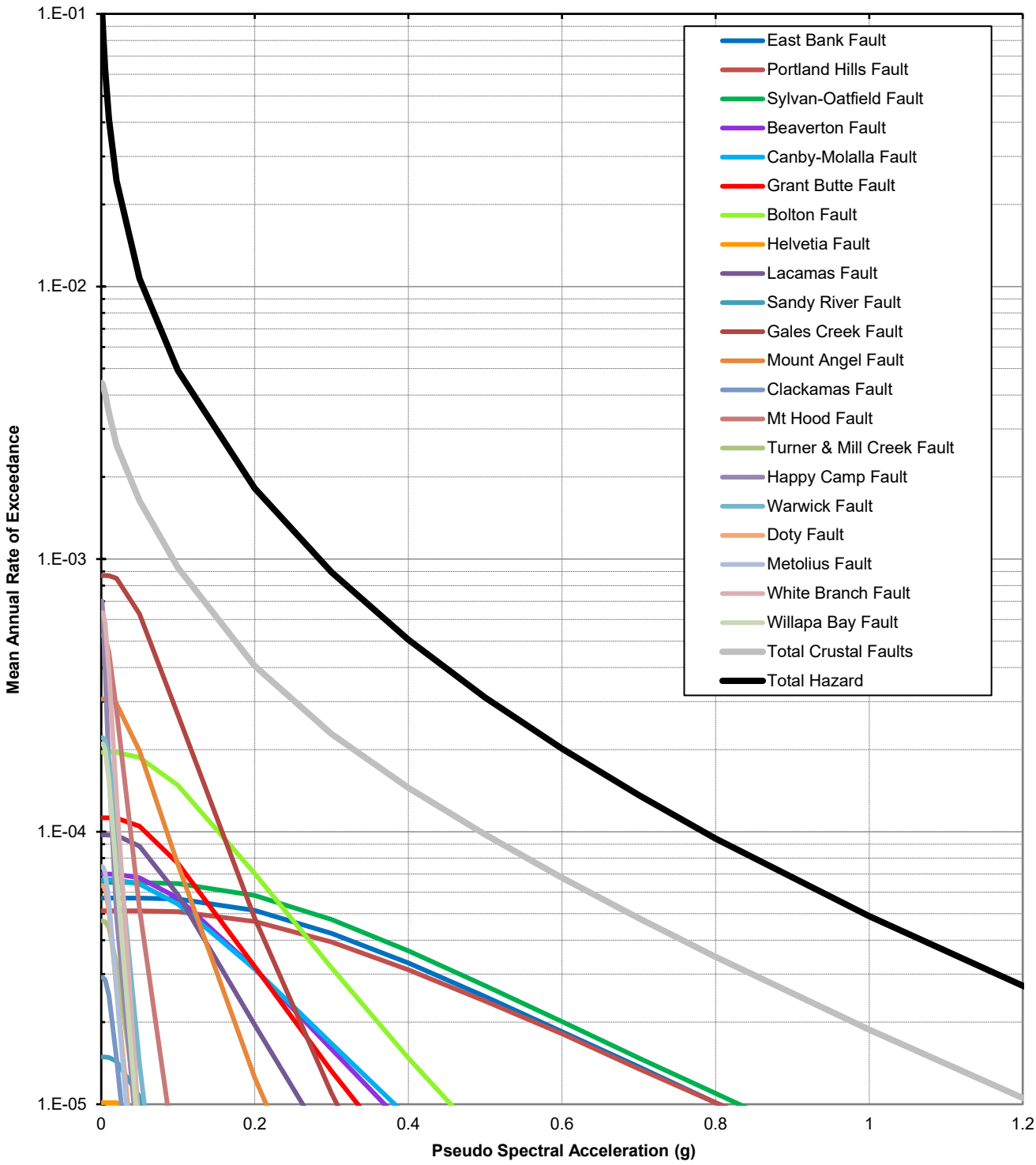

NOTES

1. g = acceleration due to gravity

Earthquake Ready Burnside Bridge
Portland, Oregon

HORIZONTAL FAULT HAZARD CURVES
PEAK GROUND ACCELERATION

April 2022 102636-009

SHANNON & WILSON, INC.
GEOTECHNICAL AND ENVIRONMENTAL CONSULTANTS

FIG. 7-17

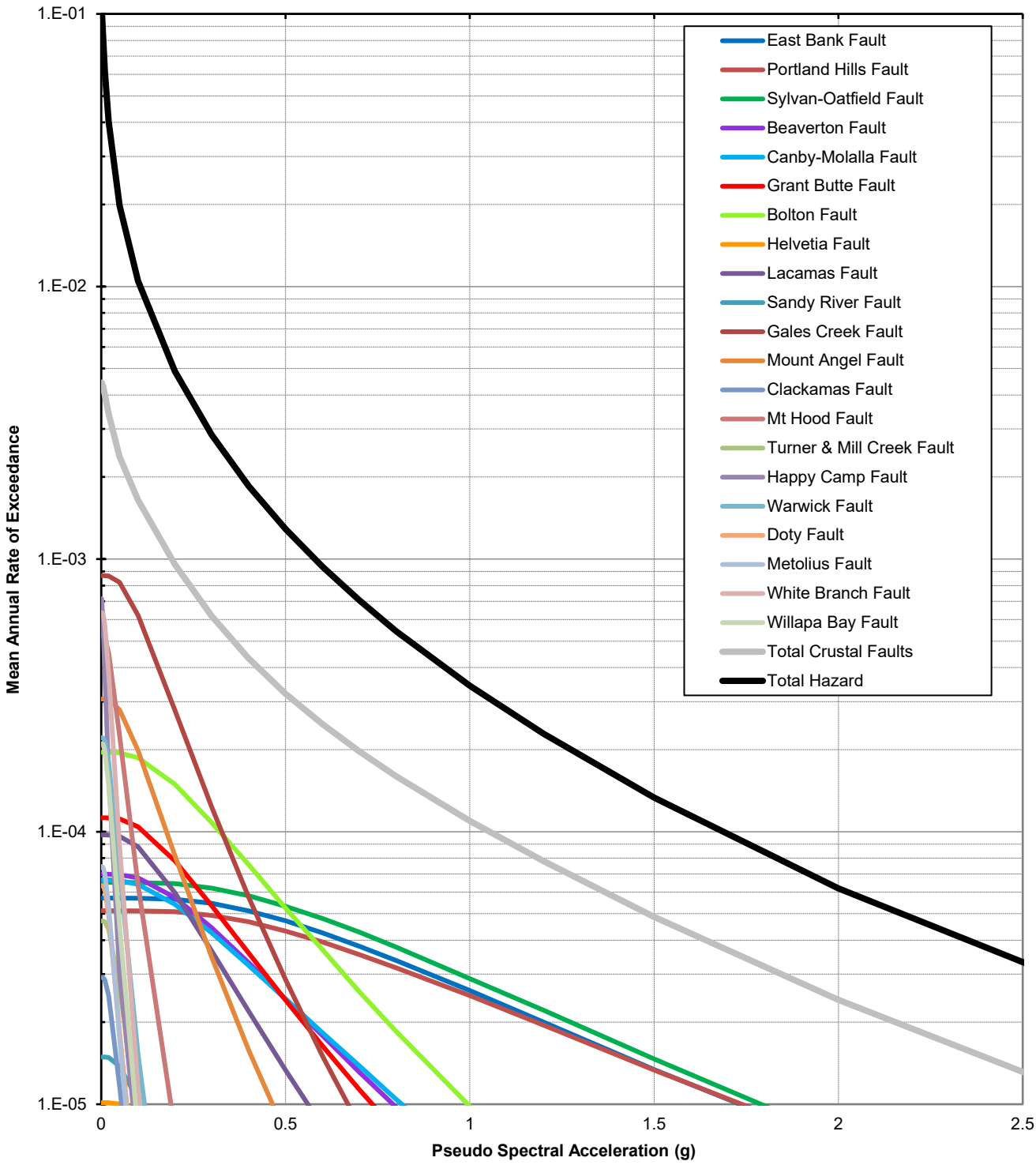

NOTES

1. g = acceleration due to gravity

Earthquake Ready Burnside Bridge
Portland, Oregon

HORIZONTAL FAULT HAZARD CURVES
0.25 SECOND PERIOD

April 2022 102636-009

SHANNON & WILSON, INC.
GEOTECHNICAL AND ENVIRONMENTAL CONSULTANTS

FIG. 7-18

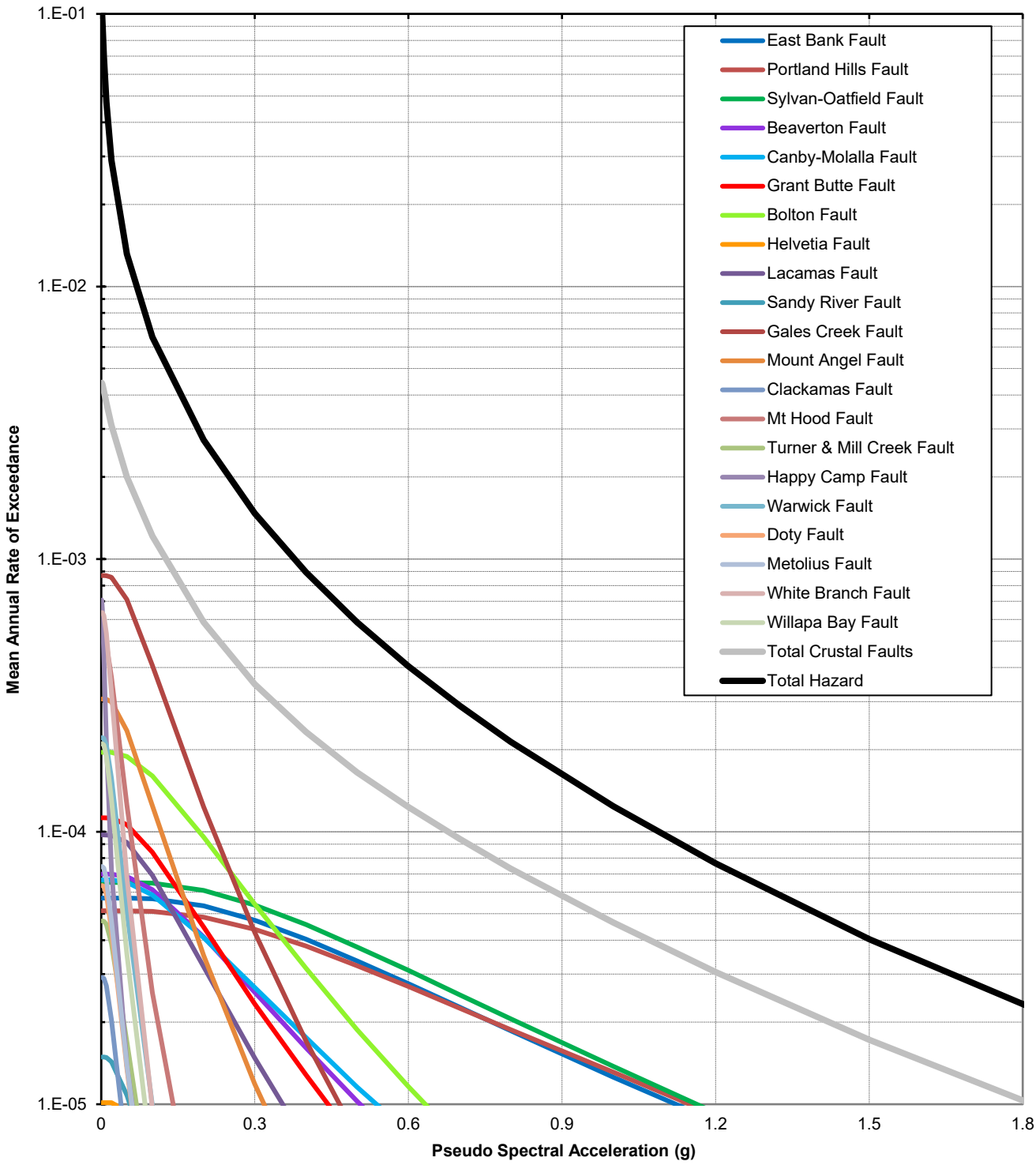

NOTES

1. g = acceleration due to gravity

Earthquake Ready Burnside Bridge
Portland, Oregon

HORIZONTAL FAULT HAZARD CURVES
0.5 SECOND PERIOD

April 2022 102636-009

SHANNON & WILSON, INC.
GEOTECHNICAL AND ENVIRONMENTAL CONSULTANTS

FIG. 7-19

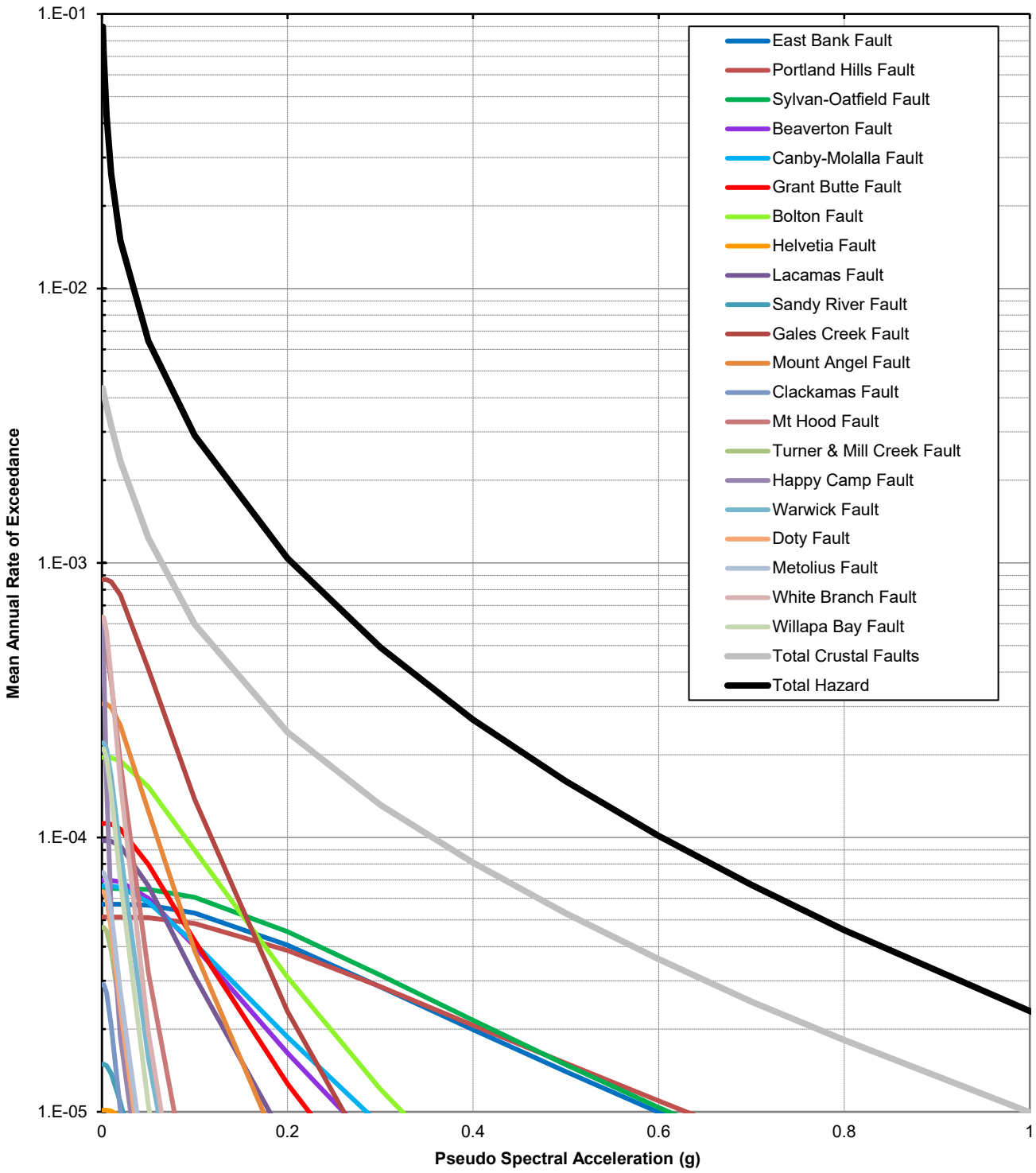

NOTES

1. g = acceleration due to gravity

Earthquake Ready Burnside Bridge
Portland, Oregon

HORIZONTAL FAULT HAZARD CURVES
1.0 SECOND PERIOD

April 2022 102636-009

SHANNON & WILSON, INC.
GEOTECHNICAL AND ENVIRONMENTAL CONSULTANTS

FIG. 7-20

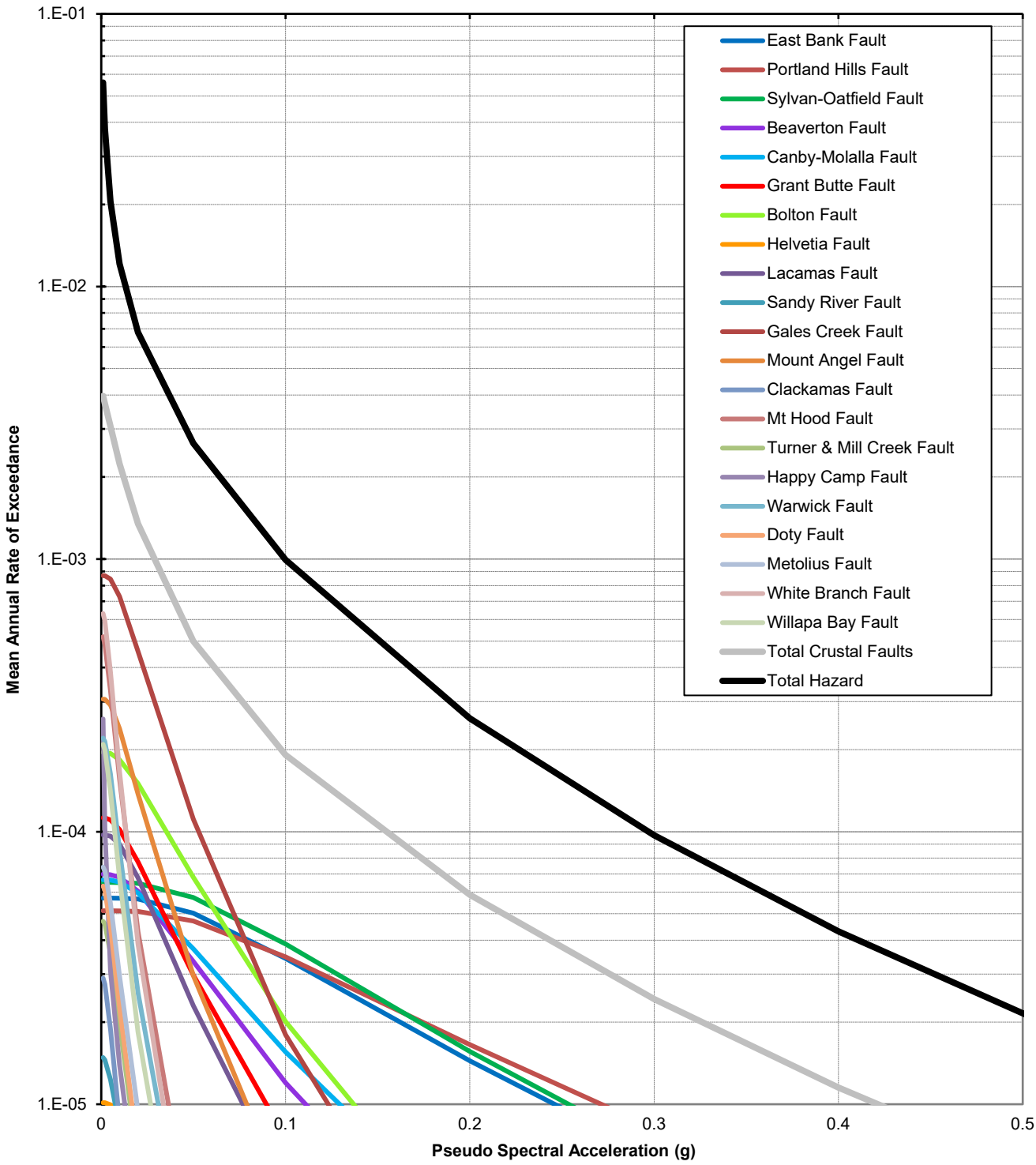

NOTES

1. g = acceleration due to gravity

Earthquake Ready Burnside Bridge
Portland, Oregon

HORIZONTAL FAULT HAZARD CURVES
2.0 SECOND PERIOD

April 2022 102636-009

SHANNON & WILSON, INC.
GEOTECHNICAL AND ENVIRONMENTAL CONSULTANTS

FIG. 7-21

BSB Hazard Curves.xlsm 4/7/2022

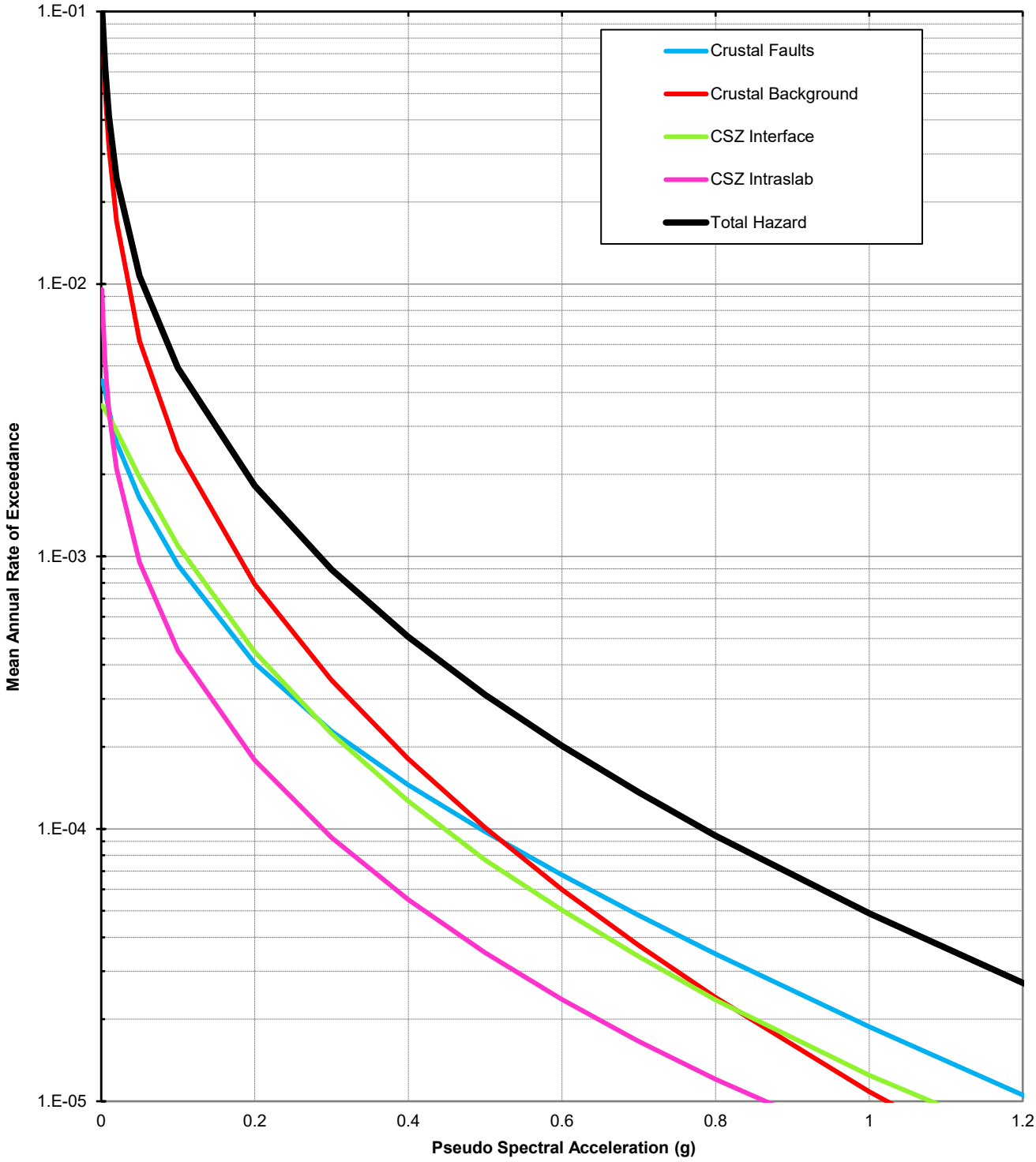

NOTES

1. g = acceleration due to gravity
   CSZ = Cascadia subduction zone

Earthquake Ready Burnside Bridge
Portland, Oregon

HORIZONTAL HAZARD CURVES
PEAK GROUND ACCELERATION

April 2022 102636-009

SHANNON & WILSON, INC.
GEOTECHNICAL AND ENVIRONMENTAL CONSULTANTS

FIG. 7-22

BSB_Hazard Curves.xlsm 4/7/2022

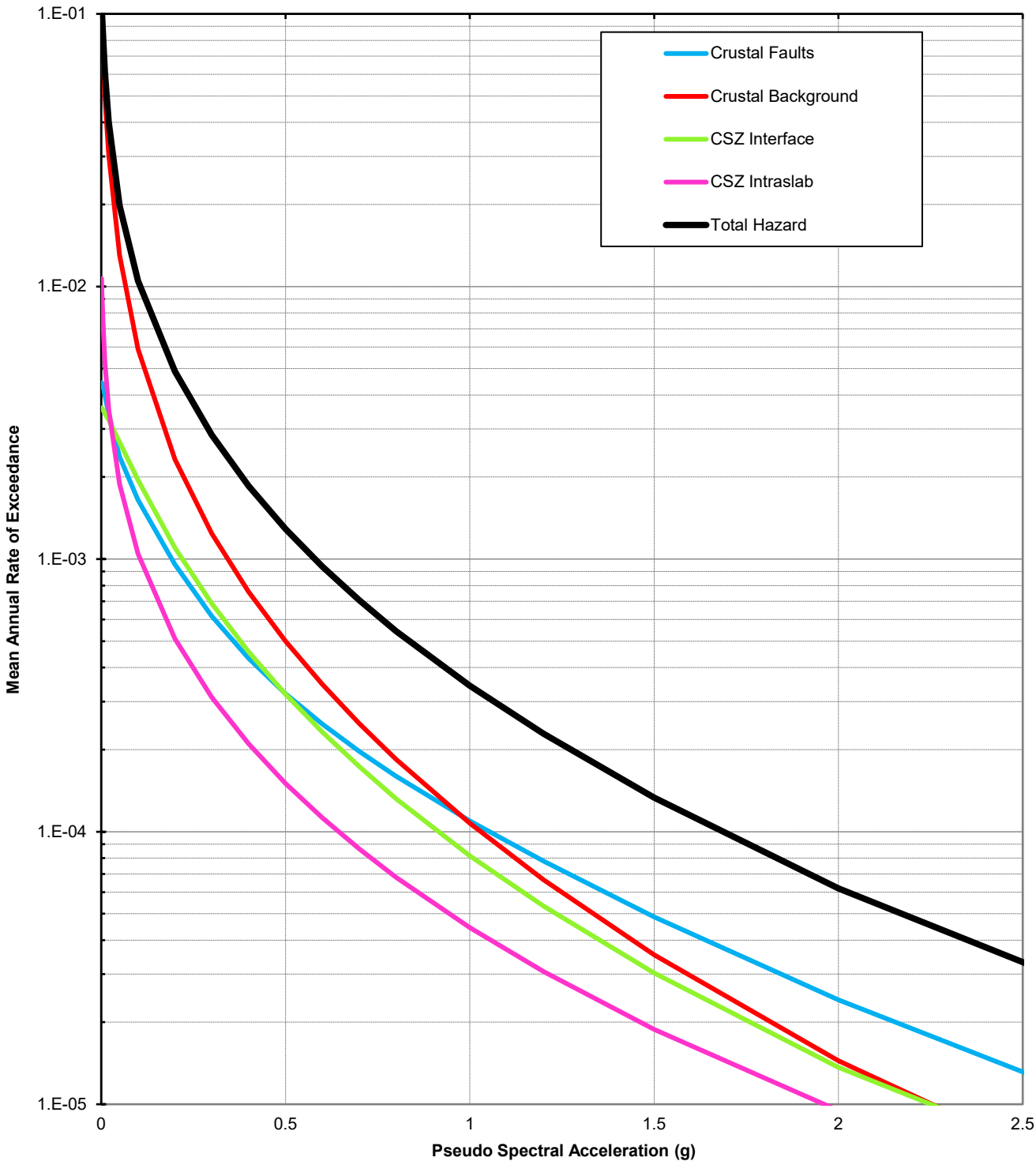

NOTES

1. g = acceleration due to gravity
   CSZ = Cascadia subduction zone

Earthquake Ready Burnside Bridge
Portland, Oregon

HORIZONTAL HAZARD CURVES
0.25 SECOND PERIOD

April 2022 102636-009

SHANNON & WILSON, INC.
GEOTECHNICAL AND ENVIRONMENTAL CONSULTANTS

FIG. 7-23

BSB_Hazard Curves.xlsm 4/7/2022

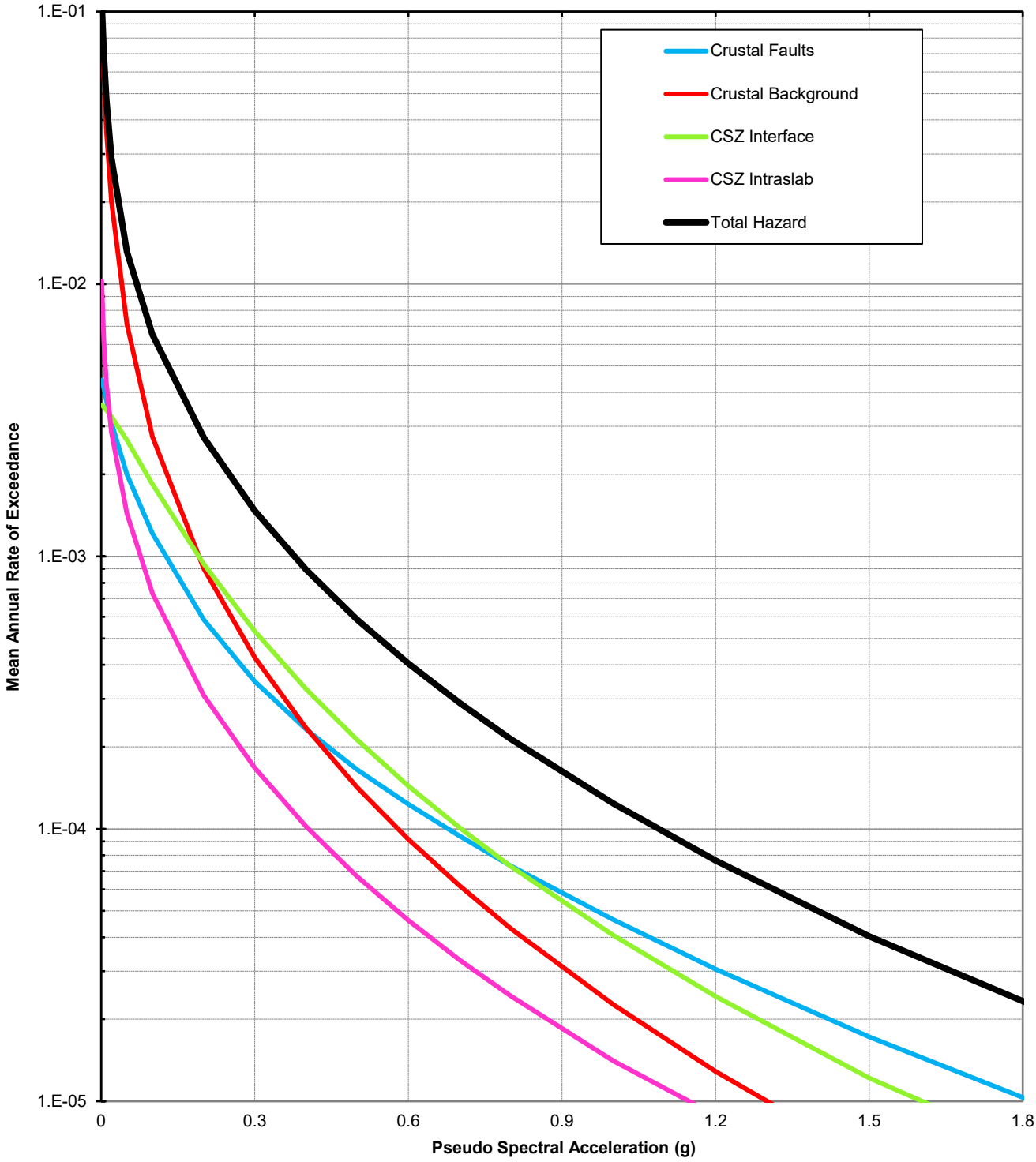

NOTES

1. g = acceleration due to gravity
   CSZ = Cascadia subduction zone

Earthquake Ready Burnside Bridge
Portland, Oregon

HORIZONTAL HAZARD CURVES
0.5 SECOND PERIOD

April 2022 102636-009

SHANNON & WILSON, INC.
GEOTECHNICAL AND ENVIRONMENTAL CONSULTANTS

FIG. 7-24

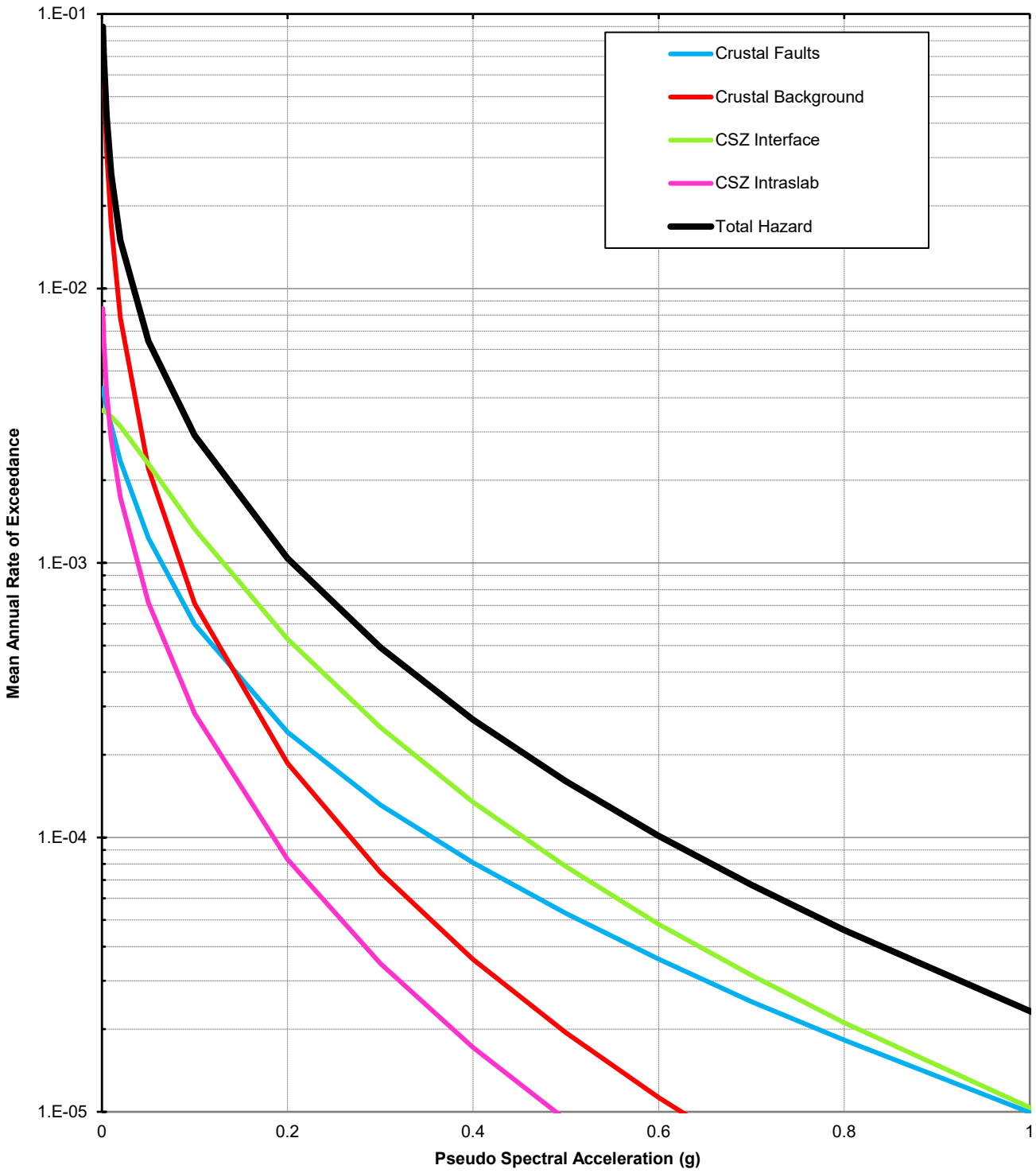

NOTES

1. g = acceleration due to gravity
   CSZ = Cascadia subduction zone

Earthquake Ready Burnside Bridge
Portland, Oregon

HORIZONTAL HAZARD CURVES
1.0 SECOND PERIOD

April 2022 102636-009

SHANNON & WILSON, INC.
GEOTECHNICAL AND ENVIRONMENTAL CONSULTANTS

FIG. 7-25

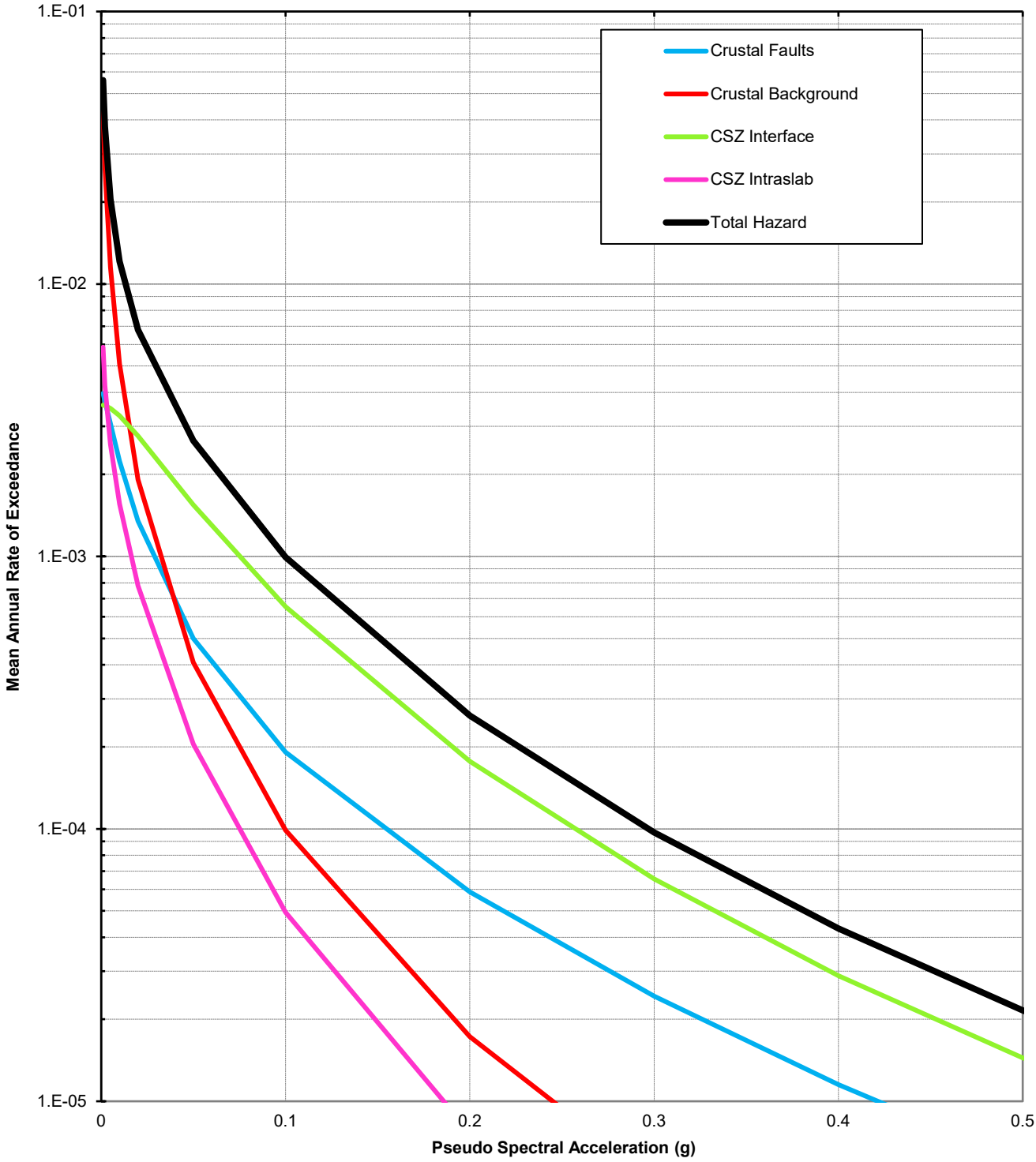

NOTES

1. g = acceleration due to gravity
   CSZ = Cascadia subduction zone

Earthquake Ready Burnside Bridge
Portland, Oregon

HORIZONTAL HAZARD CURVES
2.0 SECOND PERIOD

April 2022 102636-009

SHANNON & WILSON, INC.
GEOTECHNICAL AND ENVIRONMENTAL CONSULTANTS

FIG. 7-26

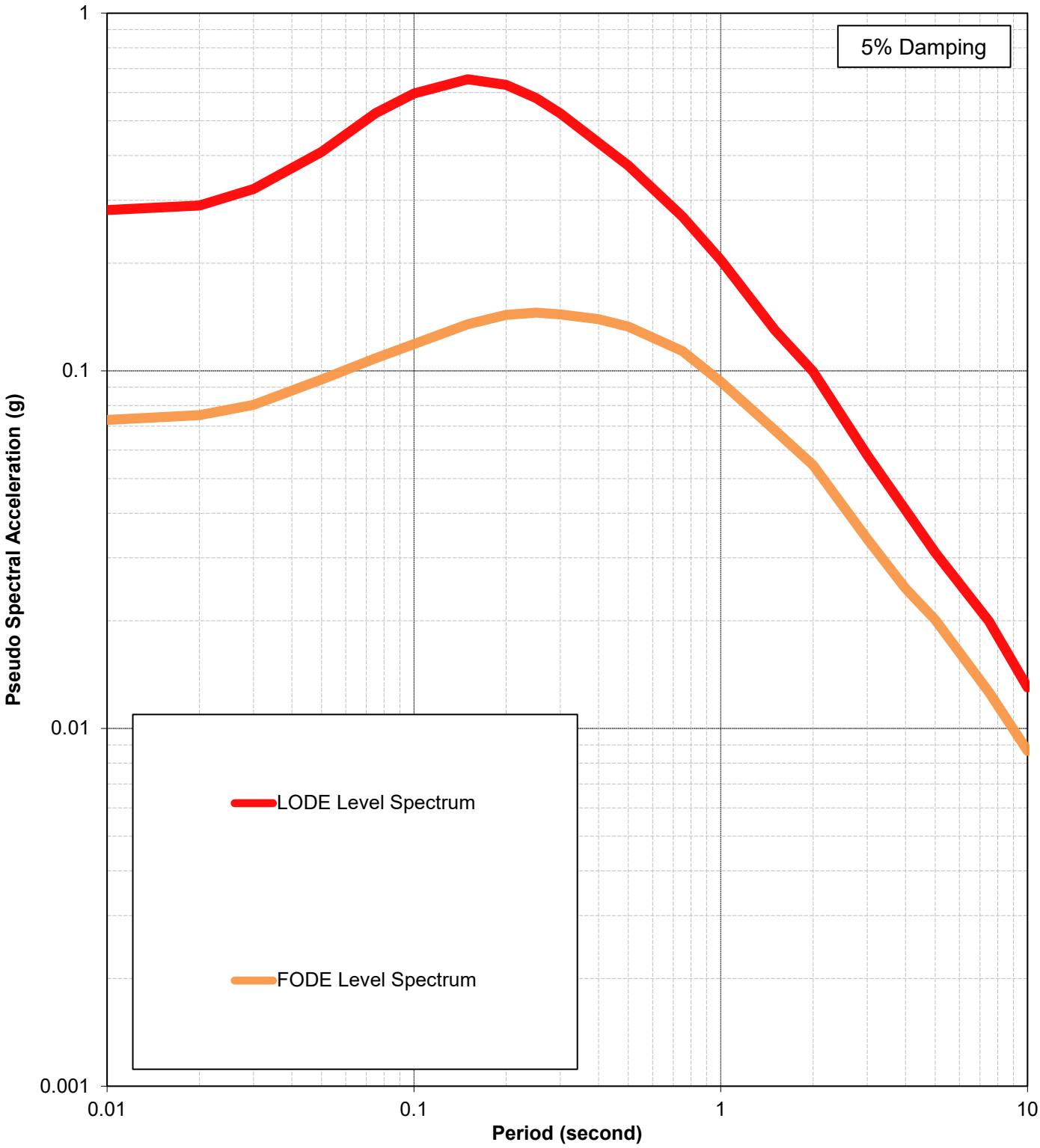

NOTES

1. Spectra correspond to Site Class B/C Boundary V_{S30} of 760 meters per second.
2. Limited Operation Design Earthquake (LODE) level spectrum is equivalent to 1,000-year return period mean UHS. Full Operation Design Earthquake (FODE) level spectrum in equivalent to 50th percentile deterministic CSZ interface full rupture event.
3. g = standard gravitational acceleration; UHS = Uniform Hazard Spectrum; V_{S30} = time-averaged shear wave velocity for 30 meters of soil below soil profile base

Earthquake Ready Burnside Bridge
Portland, Oregon

GROUND MOTION HAZARD LEVEL SPECTRA

April 2022 102636-009

SHANNON & WILSON, INC.
GEOTECHNICAL AND ENVIRONMENTAL CONSULTANTS

FIG. 7-27

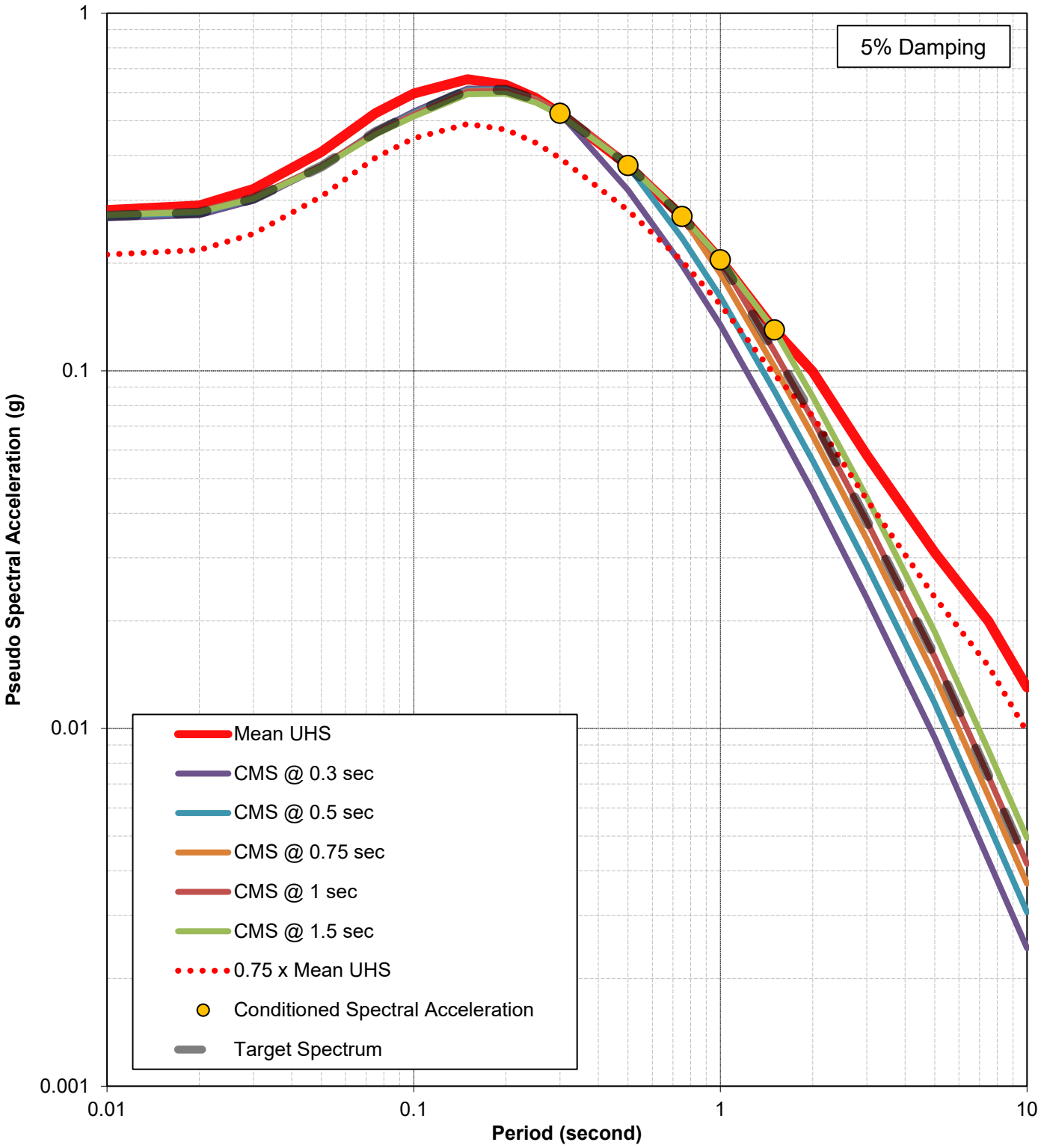

NOTES

1. Spectra correspond to Site Class B/C Boundary V_{S30} of 760 meters per second.
2. CMS = conditional mean spectrum; g = standard gravitational acceleration; sec = second; UHS= uniform hazard spectrum; V_{S30} = time-averaged shear wave velocity for 30 meters of soil below soil profile base

Earthquake Ready Burnside Bridge
Portland, Oregon

HORIZONTAL CMS
1,000-YEAR RETURN PERIOD
CRUSTAL

April 2022 102636-009

SHANNON & WILSON, INC.
GEOTECHNICAL AND ENVIRONMENTAL CONSULTANTS

FIG. 7-28

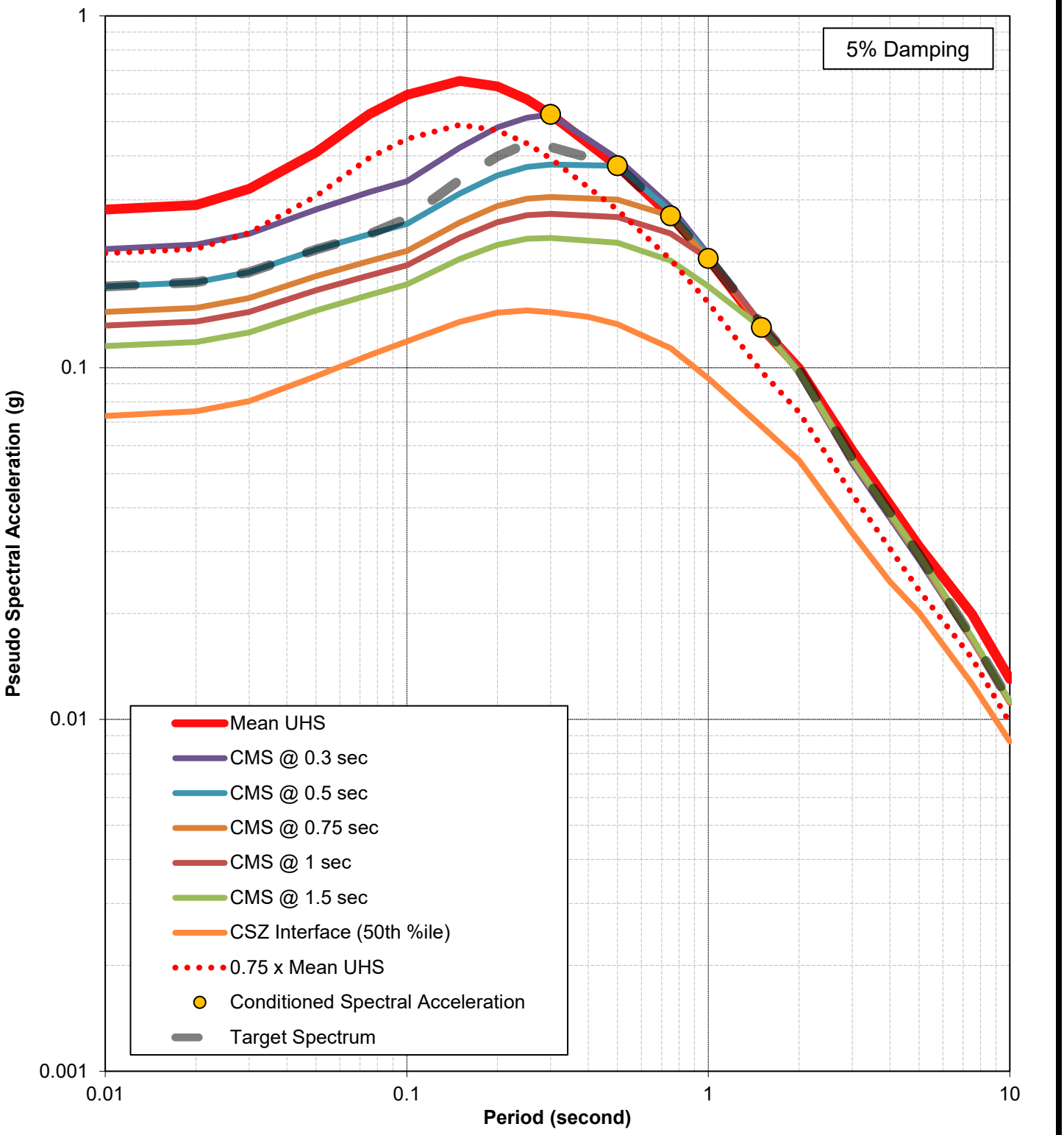

NOTES

1. Spectra correspond to Site Class B/C Boundary V_{S30} of 760 meters per second.
2. CSZ = Cascadia subduction zone; CMS = conditional mean spectrum; DS = deterministic spectrum; g = standard gravitational acceleration; sec = second; UHS= uniform hazard spectrum; V_{S30} = time-averaged shear wave velocity for 30 meters of soil below soil profile base

Earthquake Ready Burnside Bridge
Portland, Oregon

HORIZONTAL CMS VS DS
1,000-YEAR RETURN PERIOD
CSZ INTERFACE

April 2022 102636-009

SHANNON & WILSON, INC.
GEOTECHNICAL AND ENVIRONMENTAL CONSULTANTS

FIG. 7-29

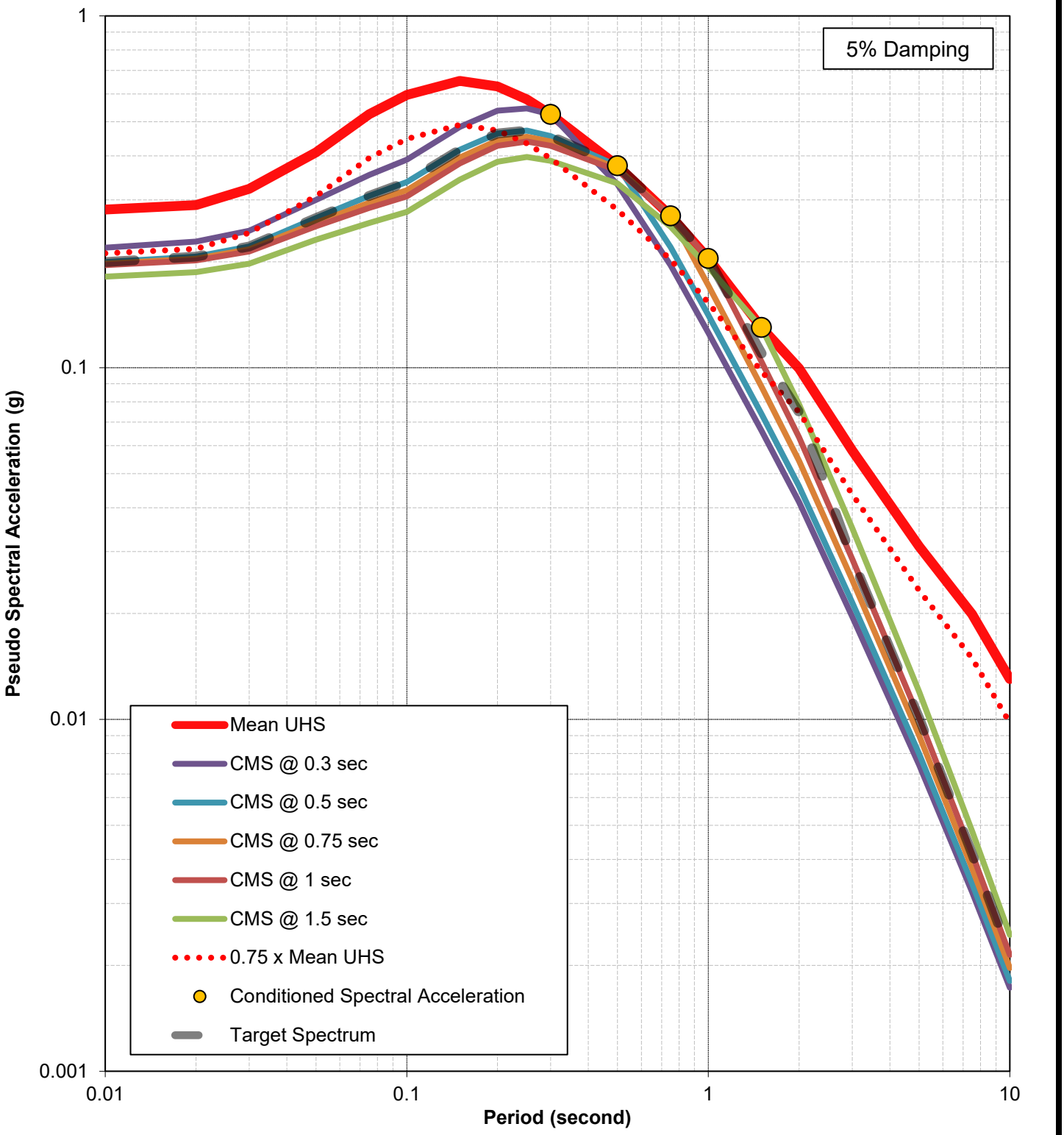

NOTES

1. Spectra correspond to Site Class B/C Boundary V_{S30} of 760 meters per second.
2. CSZ = Cascadia subduction zone; CMS = conditional mean spectrum; g = standard gravitational acceleration; sec = second; UHS= uniform hazard spectrum; V_{S30} = time-averaged shear wave velocity for 30 meters of soil below soil profile base

Earthquake Ready Burnside Bridge
Portland, Oregon

HORIZONTAL CMS
1,000-YEAR RETURN PERIOD
CSZ INTRASLAB

April 2022 102636-009

SHANNON & WILSON, INC.
GEOTECHNICAL AND ENVIRONMENTAL CONSULTANTS

FIG. 7-30

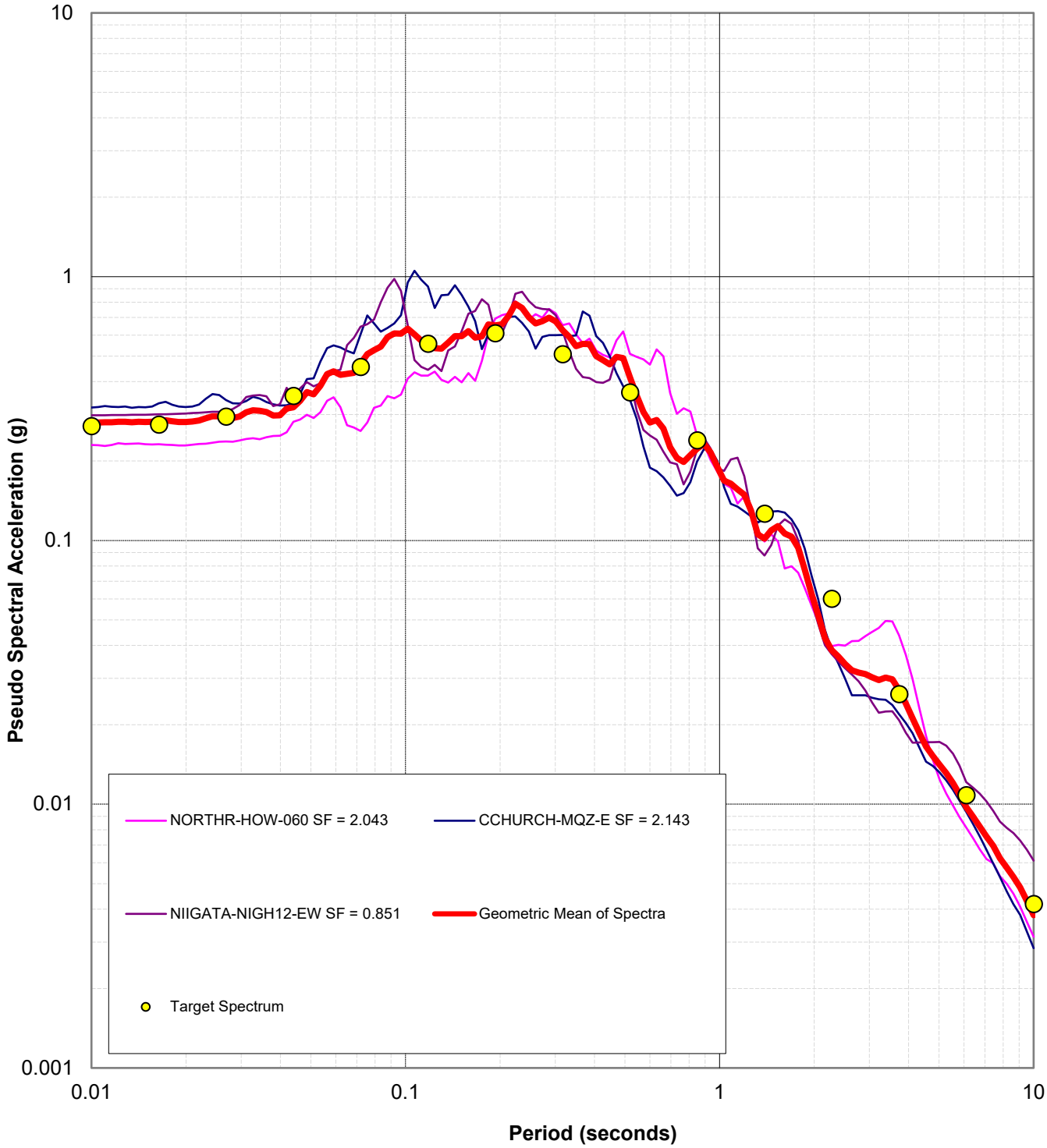

NOTES

1. LODE = Limited Operation Design Earthquake
   SF = Scale Factor

Earthquake Ready Burnside Bridge
Portland, Oregon

SCALED RESPONSE SPECTRA
CRUSTAL
LODE LEVEL

April 2022 102636-009

SHANNON & WILSON, INC.
GEOTECHNICAL AND ENVIRONMENTAL CONSULTANTS

FIG. 7-31

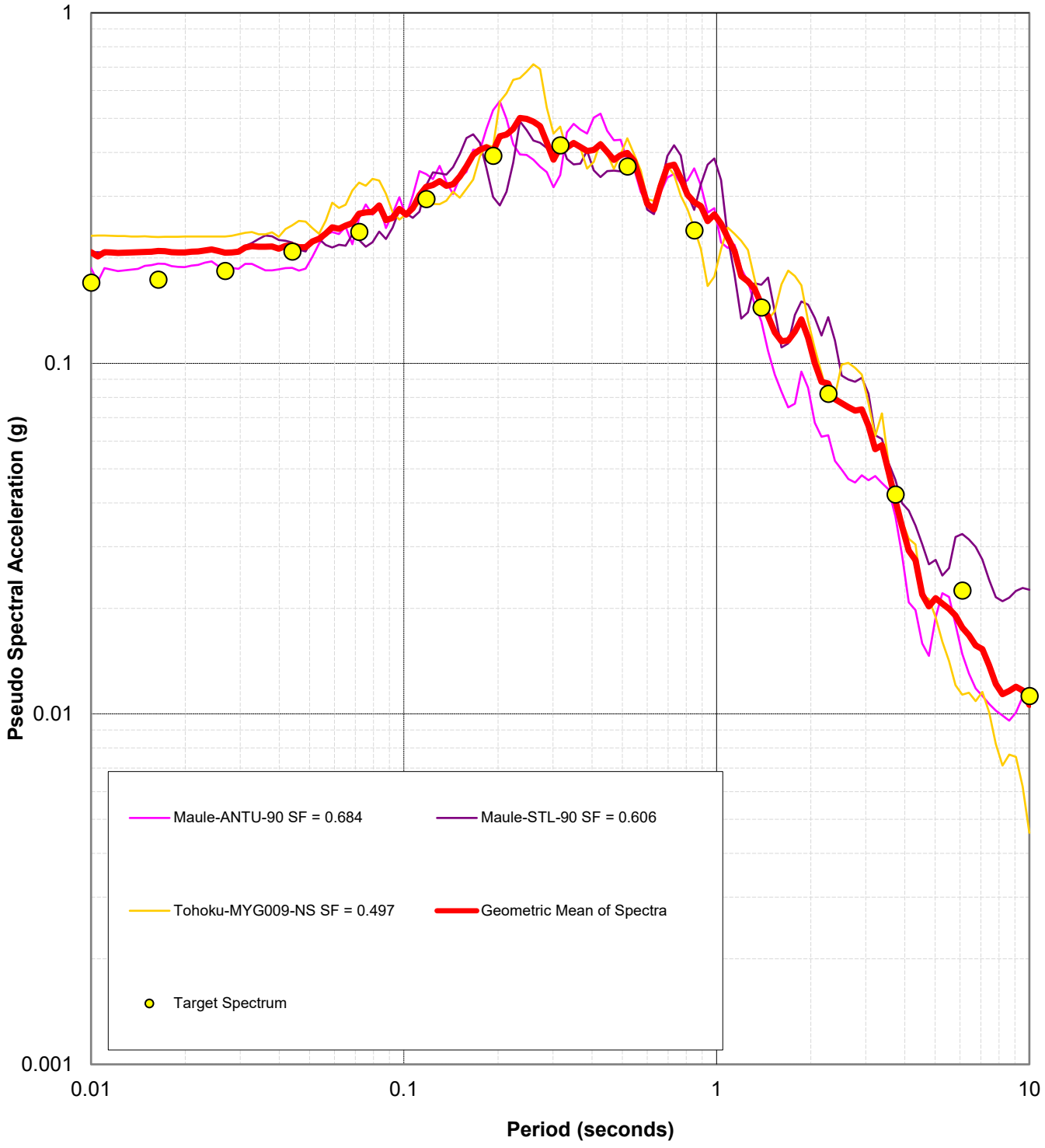

NOTES

1. LODE = Limited Operation Design Earthquake
   SF = Scale Factor

Earthquake Ready Burnside Bridge
Portland, Oregon

SCALED RESPONSE SPECTRA
CSZ SUBDUCTION INTERFACE
LODE LEVEL

April 2022 102636-009

SHANNON & WILSON, INC.
GEOTECHNICAL AND ENVIRONMENTAL CONSULTANTS

FIG. 7-32

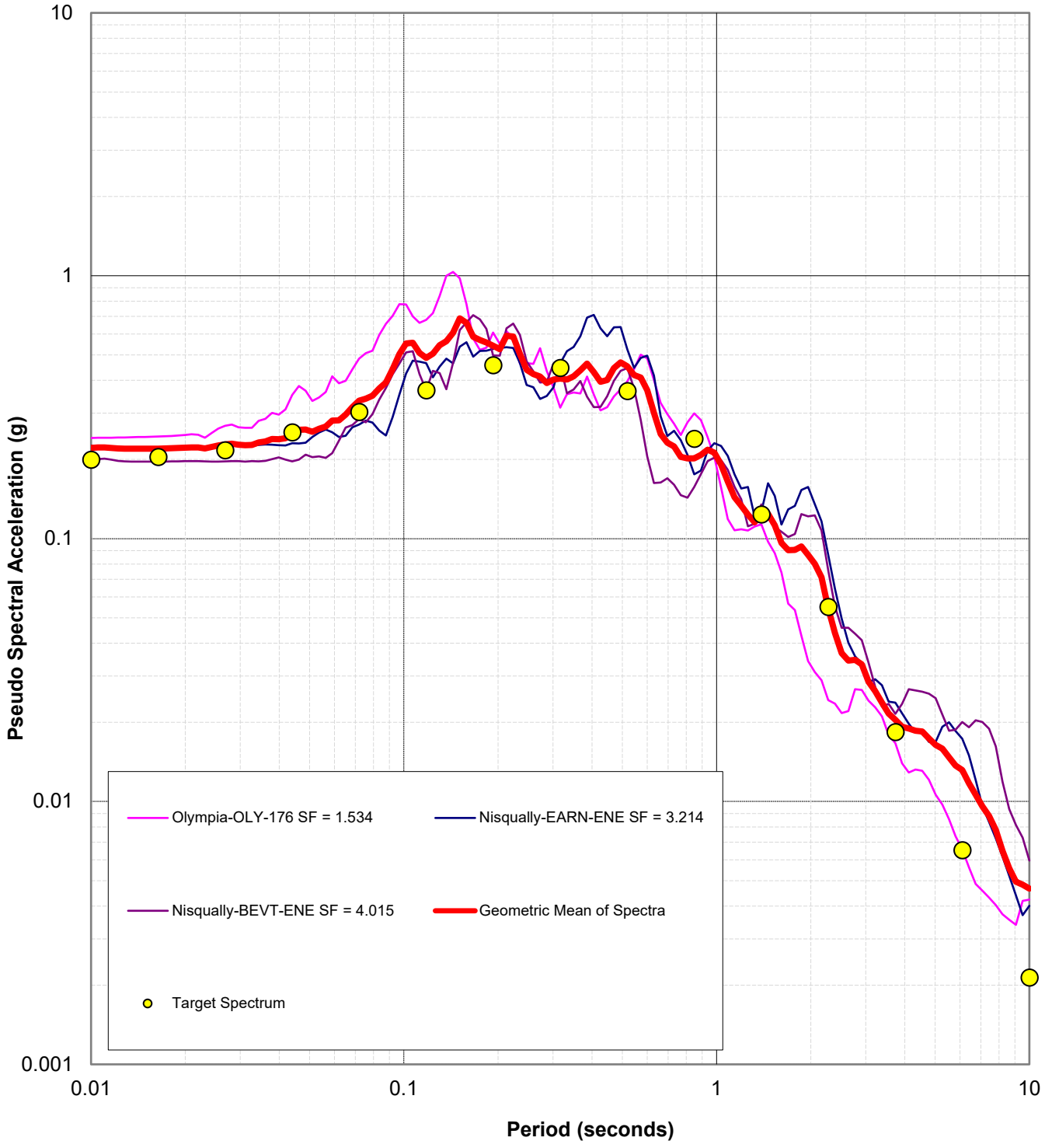

NOTES

1. LODE = Limited Operation Design Earthquake
   SF = Scale Factor

Earthquake Ready Burnside Bridge
Portland, Oregon

SCALED RESPONSE SPECTRA
CSZ SUBDUCTION INTRASLAB
LODE LEVEL

April 2022 102636-009

SHANNON & WILSON, INC.
GEOTECHNICAL AND ENVIRONMENTAL CONSULTANTS

FIG. 7-33

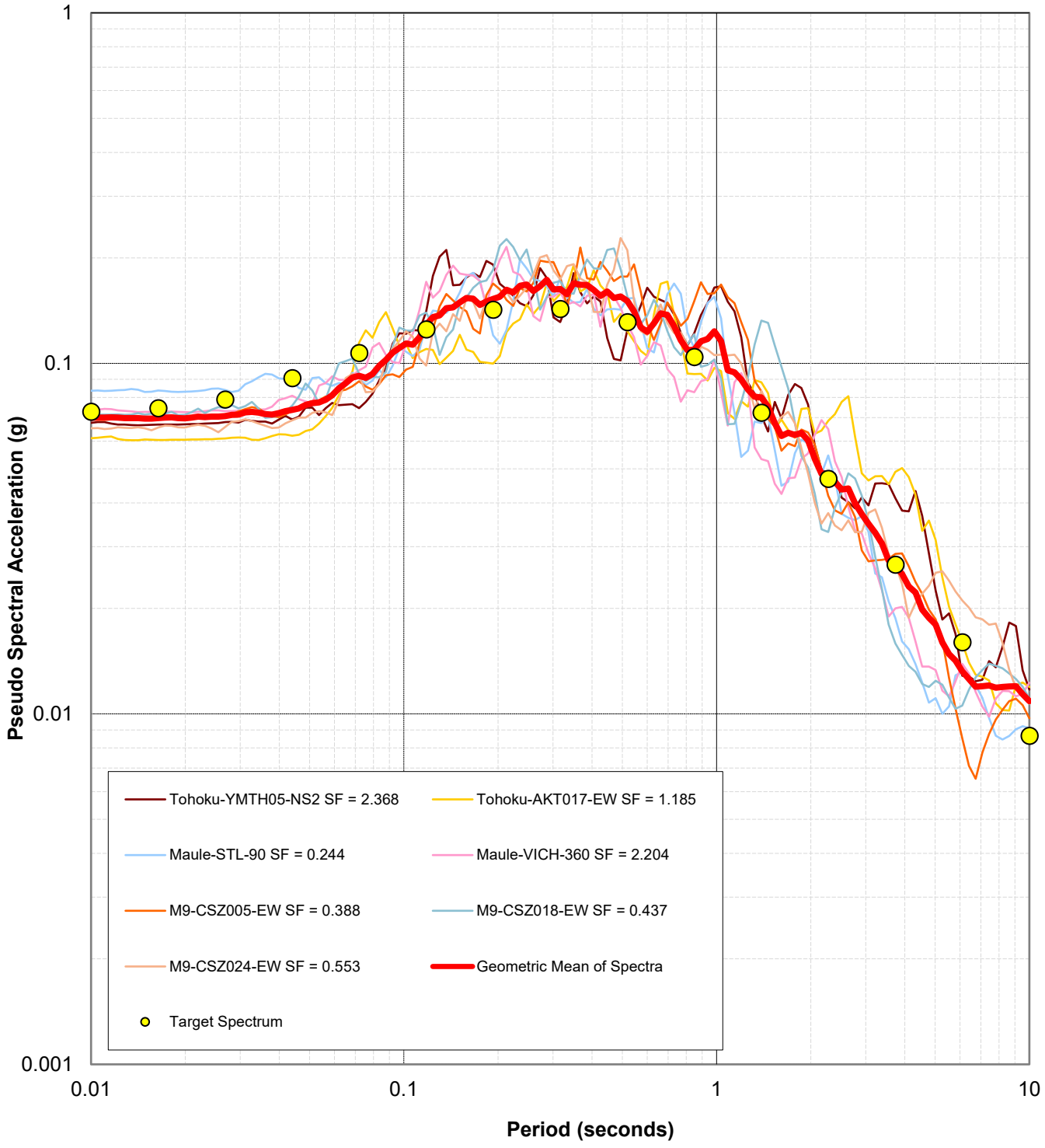

NOTES

1. FODE = Full Operation Design Earthquake
   SF = Scale Factor

Earthquake Ready Burnside Bridge
Portland, Oregon

SCALED RESPONSE SPECTRA
SUBDUCTION INTERFACE
FODE LEVEL

April 2022 102636-009

SHANNON & WILSON, INC.
GEOTECHNICAL AND ENVIRONMENTAL CONSULTANTS

FIG. 7-34

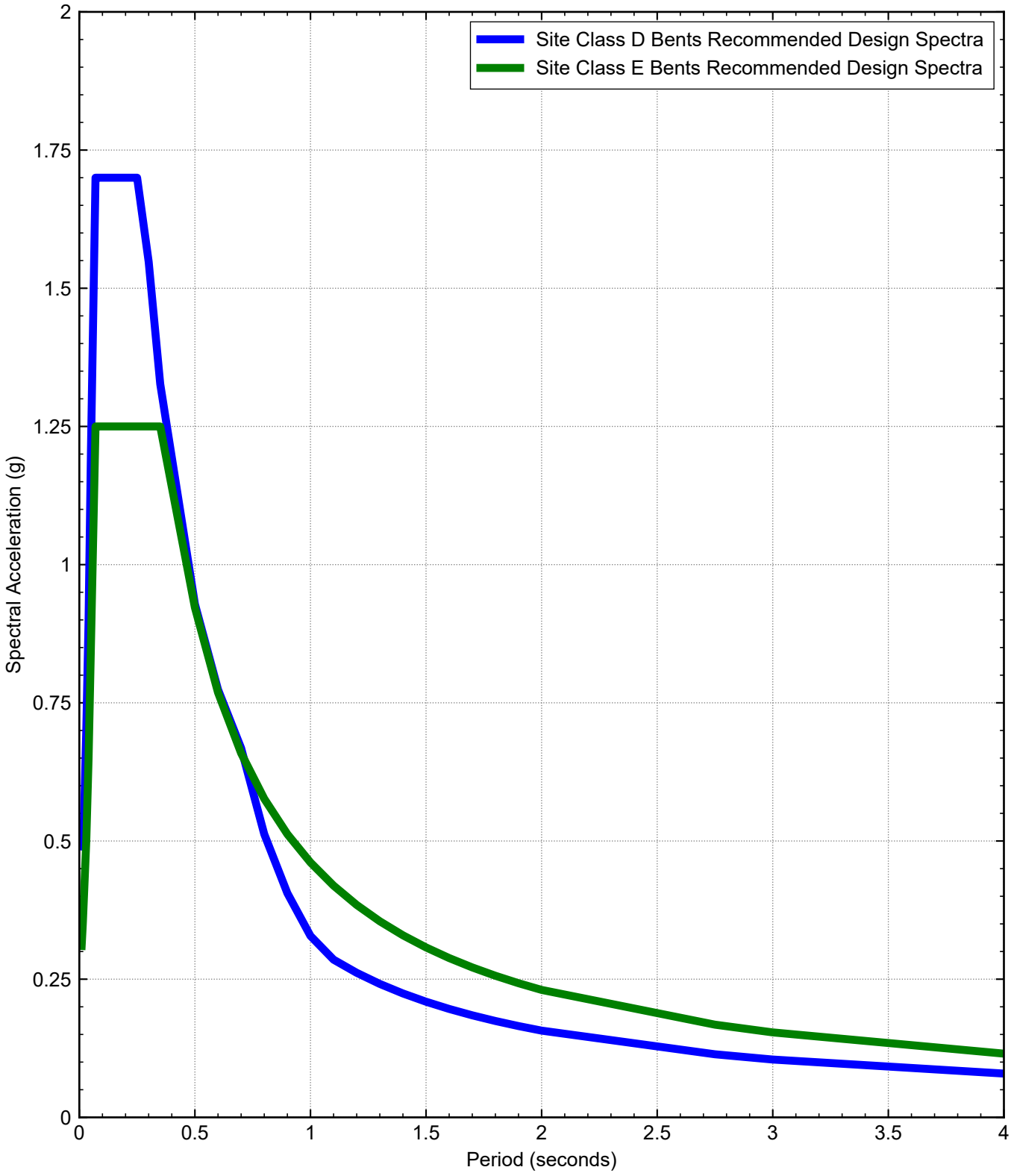

Note:
1. Our recommended design spectrum were evaluated based on AASHTO and the GDM and the results of our site response analysis.

Earthquake Ready Burnside Bridge
Portland, Oregon

RECOMMENDED DESIGN SPECTRUM 1,000-YEAR PROBABILISTIC HAZARD LEVEL

January 2022 102636-009

SHANNON & WILSON, INC.
Geotechnical and Environmental Consultants

FIG. 8-1

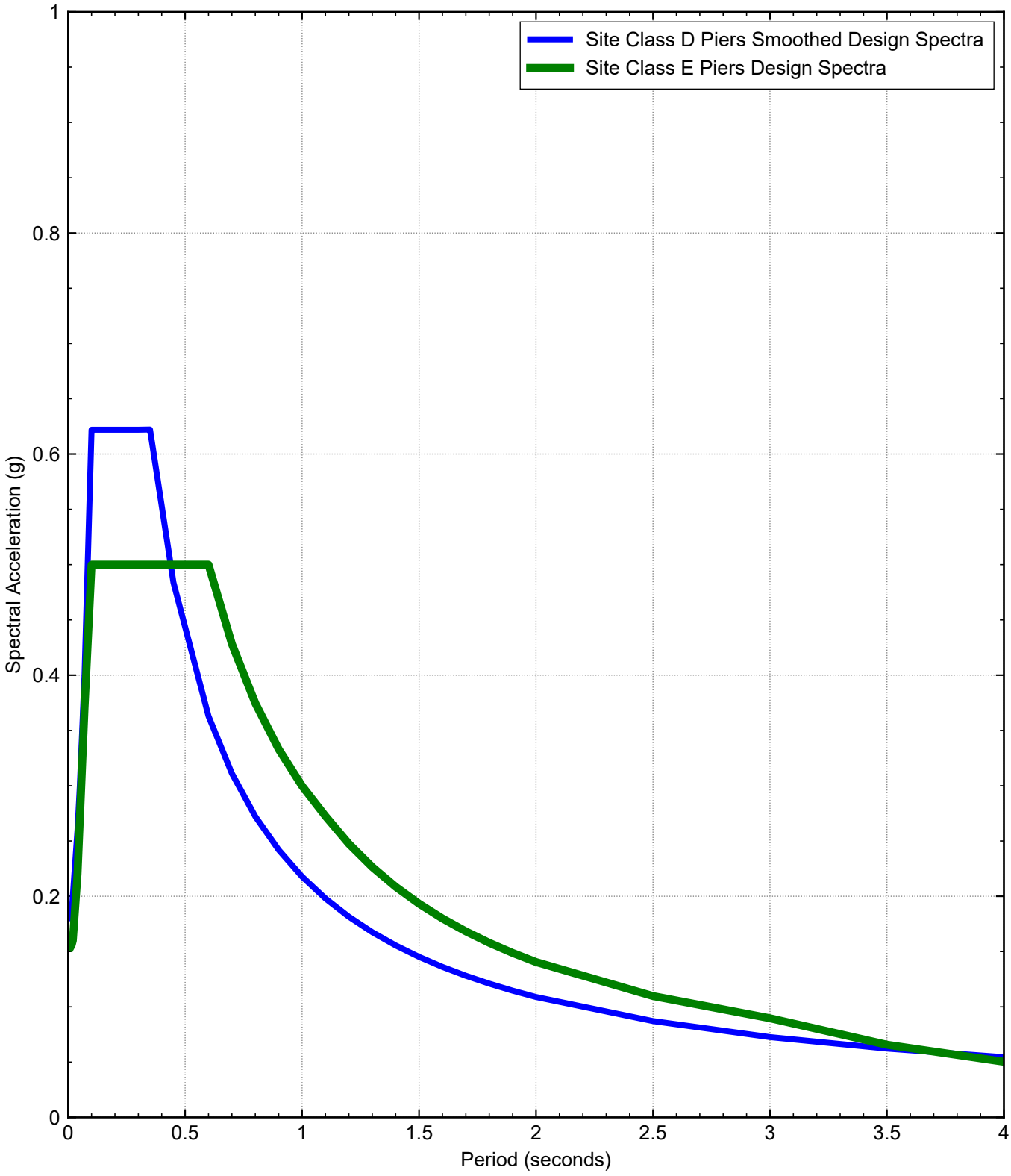

Note:
1. Our recommended design spectrum were evaluated based on AASHTO and the GDM and the results of our site response analysis.

Earthquake Ready Burnside Bridge
Portland, Oregon

RECOMMENDED DESIGN SPECTRUM
DETERMINISTIC CSZ HAZARD LEVEL

January 2022 102636-009

SHANNON & WILSON, INC.
Geotechnical and Environmental Consultants

FIG. 8-2

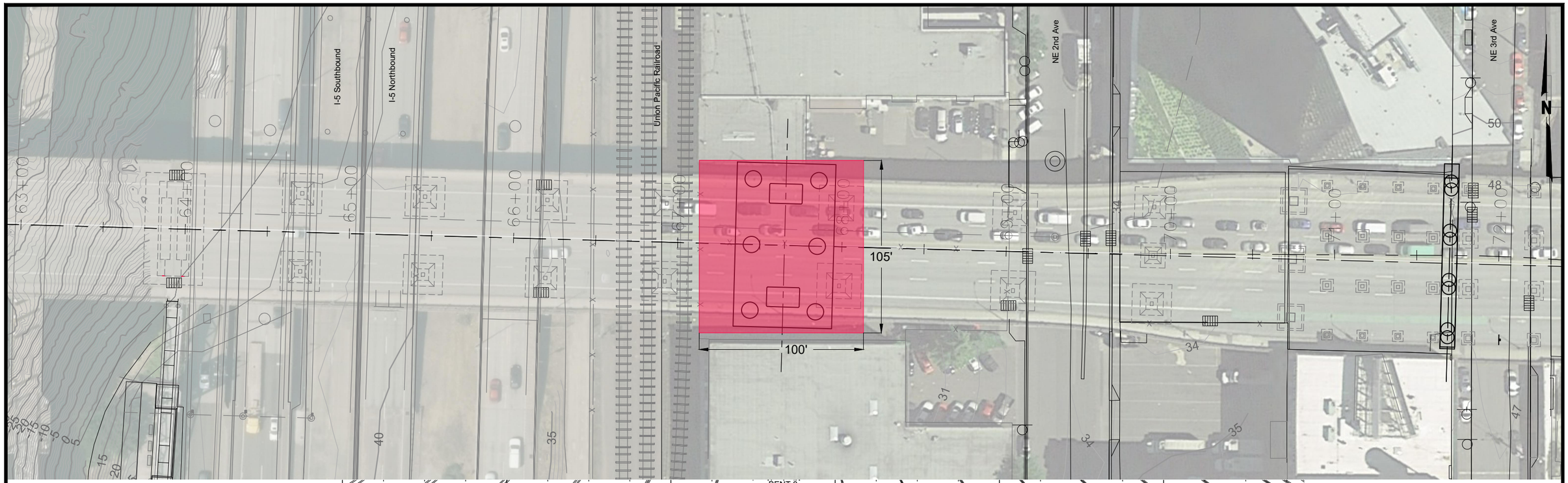

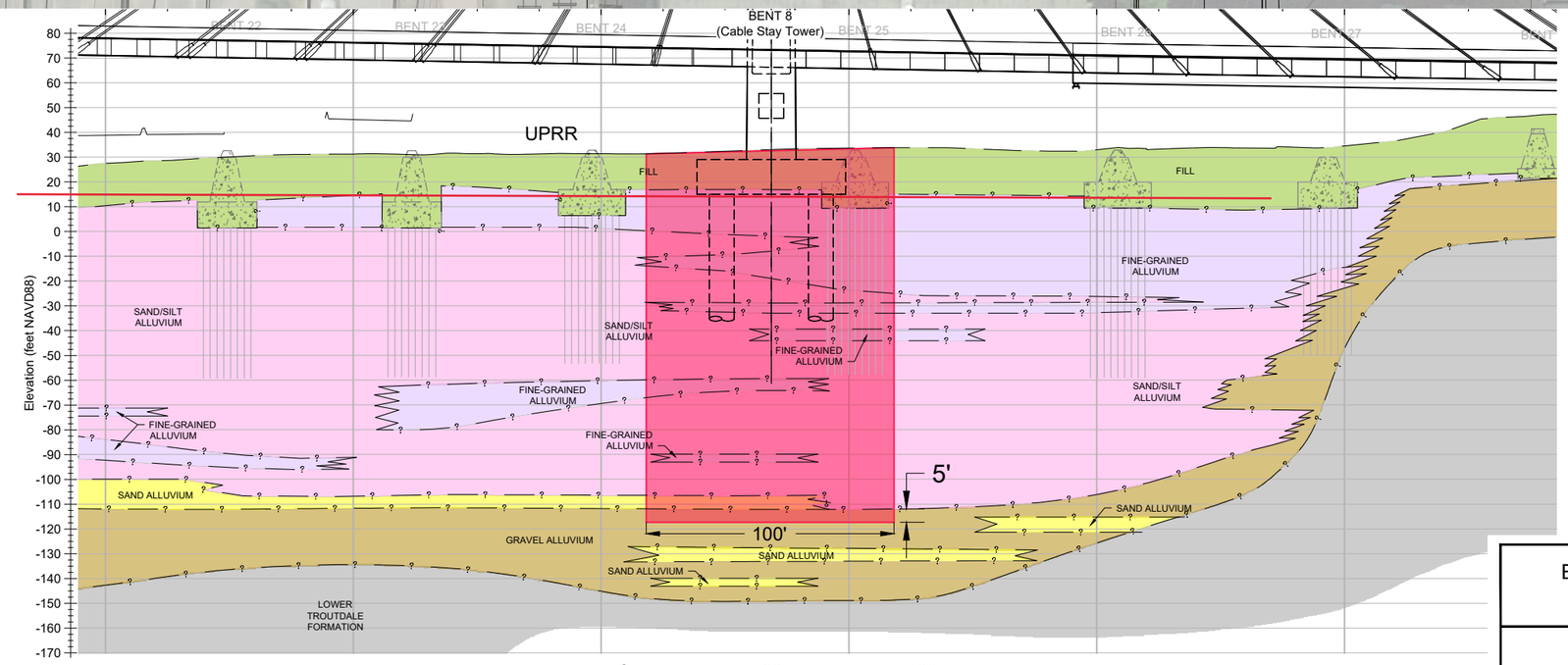

Approximate Cellular Soil-Cement Ground Improvement Zones

NOTES

1. See Figure 2-2 for legend, complete plan view, and applicable notes.

Earthquake Ready Burnside Bridge
Portland, Oregon

CONCEPTUAL GROUND IMPROVEMENT EXTENTS

January 2022 102636-009

SHANNON & WILSON, INC.
Geotechnical and Environmental Consultants

FIG. 9-1

File: I:\EF\PDX\102000s\102636 Burnside Bridge\DRAFTING\Profile_2018.dwg Date: 01-18-2022 Author: AEH